

MAGNETOM Flash

The Magazine of MRI

Issue Number 2/2012
RSNA Edition

SIEMENS

Artifact Reduction

3D MSK MRI with
syngo SPACE
Page 6

Oncology

Bone and soft tissue
tumor imaging
Page 50

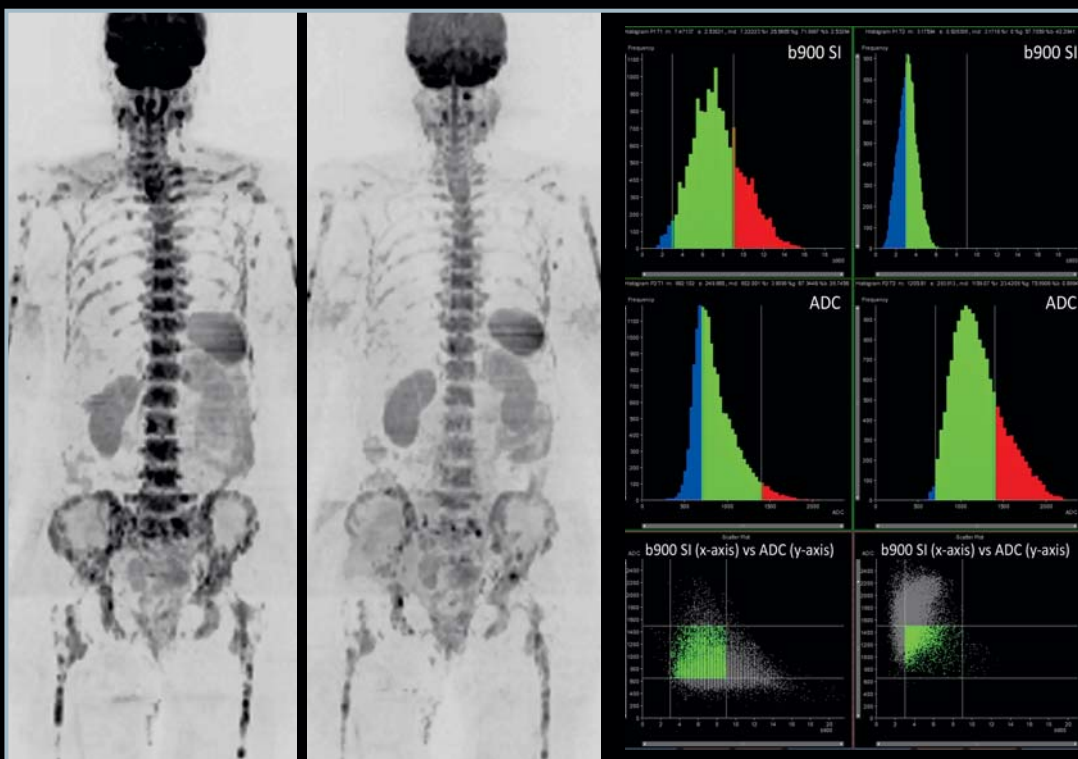
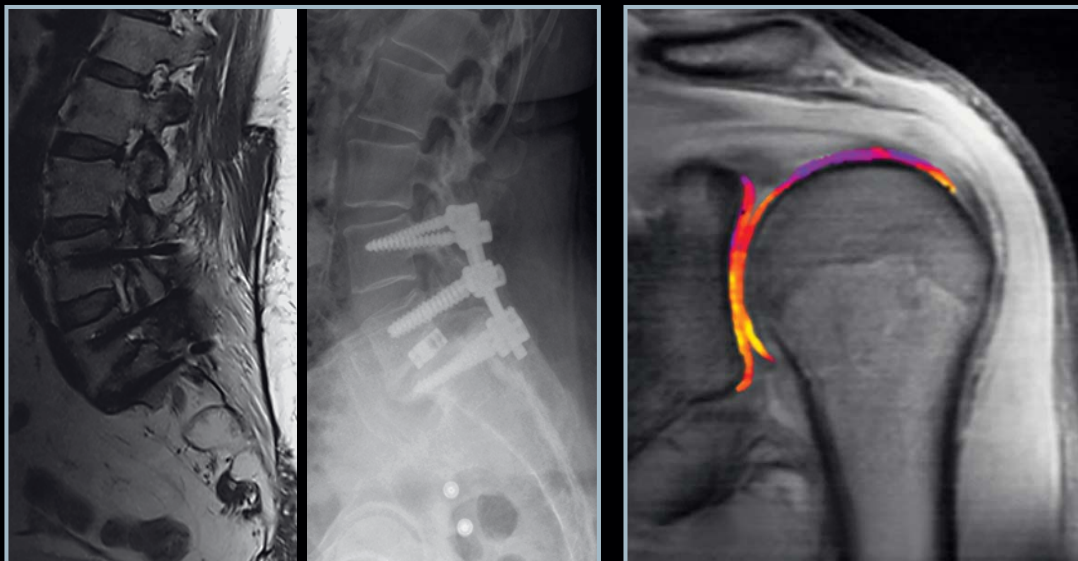
Whole-body DWI
of Bone Marrow
Page 60

How I do it

MSK imaging
Tips and Tricks
Page 58

Technology

7T MRI for MSK
Applications
Page 98



50



John A. Carrino, M.D., M.P.H.

Associate Professor of Radiology and
Orthopedic Surgery

Section Chief, Musculoskeletal Radiology

The Russel H. Morgan Department of
Radiology and Radiological Science

Johns Hopkins University
School of Medicine
Baltimore, Maryland, USA

Dear MAGNETOM users,

It is truly an honor and a privilege for me to edit this 2012 RSNA edition of MAGNETOM Flash. This issue focuses on the imaging of musculoskeletal diseases/disorders – a substantial source of morbidity worldwide. Without any radiation, MR imaging depicts occult bone injuries and soft tissue, such as meniscal, ligament and tendon tears with unparalleled tissue contrast. Providers who are eager for advanced diagnostic and therapeutic techniques to prevent end-stage joint damage and preserve quality of life will find a good variety of technical, experiential and clinical information available in this issue spanning the spectrum of bone, joint and soft tissue topics.

The variety of musculoskeletal anatomy at numerous locations throughout the body lends itself to 3D imaging. The orientation of many articulations and adjacent supporting soft tissue structures are not in the traditional cardinal planes and can be difficult to evaluate with routine coronal, axial and sagittal sections. 3D imaging using SPACE¹ empowers the user to create arbitrary multi-planar reconstructions in the contrasts that are best suited for musculoskeletal imaging. Furthermore, whilst MR imaging can be limited by metal artifact for post-operative patients, the development of new techniques encompassed in syngo WARP¹ reduces the susceptibility effects and signal pile ups to produce an improved visualization of peri-implant complications.

Exciting developments in this area include:

- Cartilage imaging – the 'holy grail' to an understanding of joint internal derangement. High spatial resolution is key for morphological tasks. However, an ability to probe the biochemical

milieu of chondroid matrix can reveal early degeneration for pre-structural changes of arthritis and regeneration of normal cartilage constituents after biological repair.²

- Oncology applications – diffusion-weighted imaging shows an increased potential for differentiating benign from malignant processes based on restricted diffusion [1]. The ability for time-effective whole-body acquisition now means that MRI can rival other techniques for total disease surveillance.
- Increased signal-to-noise ratio (SNR) through (a) high field strength to acquire improved spatial, contrast, temporal or spectral resolution to better depict infrastructural details, gain a more direct evaluation of sodium present within cartilage, capture real-time kinematic joint motion as for cardiac imaging and improve the detection of smaller quantity metabolites, and (b) the use of coils. For extremity work we now have an increased number of channels and extended field-of-view coils suitable for high resolution imaging of the entire foot and hand.
- The application of MR protocols – greatly facilitated by the workflow developed within Dot (day optimized throughput) engines.

Special thanks to all our contributors. These contributions are a valuable resource to assist other MAGNETOM users in making optimum use of their systems at the cutting edge of daily practice and to enhance the medical imaging objectives of visualization, recognition and interpretation.

John A. Carrino, M.D., M.P.H.

[1] Spuentrup E, Buecker A, Adam G, van Vaals JJ, Guenther R W. Diffusion-weighted MR imaging for differentiation of benign fracture edema and tumor infiltration of the vertebral body. Am J Roentgenol 2001; 176(2):351 - 381.

¹The software is pending 510(k) clearance, and is not yet commercially available in the United States.

²A licensed physician may choose to use FDA-approved contrast agents in conjunction with an MRI examination, based on his/her medical opinion and discretion and in accordance with the instructions for use and indication for use supplied by the pharmaceutical manufacturer for the contrast agents.

Editorial Board

We appreciate your comments.

Please contact us at magnetomworld.med@siemens.com



Antje Hellwich
Associate Editor



Wellesley Were
MR Business Development
Manager Australia and New
Zealand



Dr. Sunil Kumar S.L.
Senior Manager Applications,
Mississauga, ON, Canada



Ralph Strecker
MR Collaboration Manager,
São Paulo, Brazil



Christiane Bernhardt
Head Outbound Marketing
Erlangen, Germany



Milind Dhamankar, M.D.
Sr. Director, MR Product
Marketing, Malvern, PA, USA



Gary R. McNeal, MS (BME)
Advanced Application Specialist,
Cardiovascular MR Imaging
Hoffman Estates, IL, USA



Peter Kreisler, Ph.D.
Collaborations & Applications,
Erlangen, Germany

Review Board

Lisa **Chua**, Ph.D., Clinical Collaboration Manager

Wilhelm **Horger**, Application Development Oncology

Michelle **Kessler**, US Installed Base Manager

Berthold **Kiefer**, Ph.D., Oncological and Interventional Applications

Ferdinand **Lipps**, Ph.D., Global Marketing Manager Orthopedics

Heiko **Meyer**, Ph.D., Neuro Applications

Silke **Quick**, Global Marketing Manager Women's Health

Raphael **Schwarz**, Ph.D., Orthopedic Applications

Ignacio **Vallines**, Ph.D., Global Marketing Manager Neurology

Heike **Weh**, Clinical Data Manager

Sven **Zühlsdorff**, Clinical Collaboration Manager

Editorial Board

We appreciate your comments.

Please contact us at magnetomworld.med@siemens.com



Antje Hellwich
Associate Editor



Wellesley Were
MR Business Development
Manager Australia and New
Zealand



Dr. Sunil Kumar S.L.
Senior Manager Applications,
Mississauga, ON, Canada



Ralph Strecker
MR Collaboration Manager,
São Paulo, Brazil



Christiane Bernhardt
Head Outbound Marketing
Erlangen, Germany



Milind Dhamankar, M.D.
Sr. Director, MR Product
Marketing, Malvern, PA, USA



Gary R. McNeal, MS (BME)
Advanced Application Specialist,
Cardiovascular MR Imaging
Hoffman Estates, IL, USA



Peter Kreisler, Ph.D.
Collaborations & Applications,
Erlangen, Germany

Review Board

Lisa **Chua**, Ph.D., Clinical Collaboration Manager

Wilhelm **Horger**, Application Development Oncology

Michelle **Kessler**, US Installed Base Manager

Berthold **Kiefer**, Ph.D., Oncological and Interventional Applications

Ferdinand **Lipps**, Ph.D., Global Marketing Manager Orthopedics

Heiko **Meyer**, Ph.D., Neuro Applications

Silke **Quick**, Global Marketing Manager Women's Health

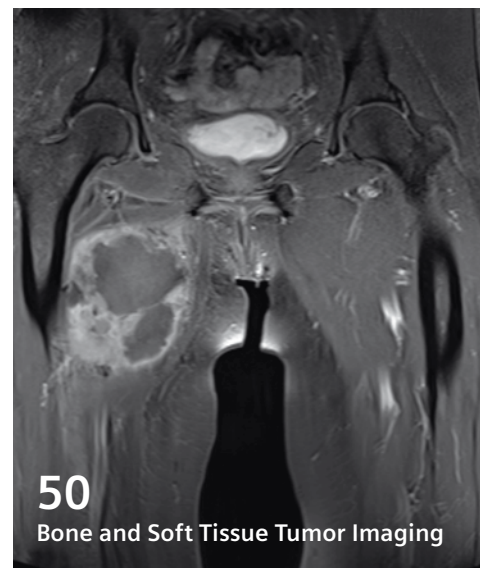
Raphael **Schwarz**, Ph.D., Orthopedic Applications

Ignacio **Vallines**, Ph.D., Global Marketing Manager Neurology

Heike **Weh**, Clinical Data Manager

Sven **Zühlsdorff**, Clinical Collaboration Manager

Content



With the first issue published in 1993 we now celebrate issue number 50. From the very beginning MAGNETOM Flash was a cooperation of Siemens Healthcare with MAGNETOM users.

We welcome your feedback, questions and comments – please contact us at magnetomworld.med@siemens.com

The information presented in MAGNETOM Flash is for illustration only and is not intended to be relied upon by the reader for instruction as to the practice of medicine. Any health care practitioner reading this information is reminded that they must use their own learning, training and expertise in dealing with their individual patients. This material does not substitute for that duty and is not intended by Siemens Medical Solutions to be used for any purpose in that regard. The treating physician bears the sole responsibility for the diagnosis and treatment of patients, including drugs and doses prescribed in connection with such use. The Operating Instructions must always be strictly followed when operating the MR System. The source for the technical data is the corresponding data sheets.

MR scanning has not been established as safe for imaging fetuses and infants under two years of age. The responsible physician must evaluate the benefit of the MRI examination in comparison to other imaging procedures.

The MRI restrictions (if any) of the metal implant must be considered prior to patient undergoing MRI exam. MR imaging of patients with metallic implants brings specific risks. However, certain implants are approved by the governing regulatory bodies to be MR conditionally safe. For such implants, the previously mentioned warning may not be applicable. Please contact the implant manufacturer for the specific conditional information. The conditions for MR safety are the responsibility of the implant manufacturer, not of Siemens.

Clinical 3D Imaging and Artifact Reduction

- 6 3D Musculoskeletal MRI with syngo SPACE
Mike Notohamiprodjo
- 12 Imaging of Metallic Prostheses Using Novel Sequences
Leon Rybak, et al.
- 20 Experience with the MAGNETOM Verio system in Spine Imaging: Benefit of 3D Sequences and Reduction of Metal-Related Artifacts with syngo WARP¹
Marcel Wolf, Marc-André Weber

Product News

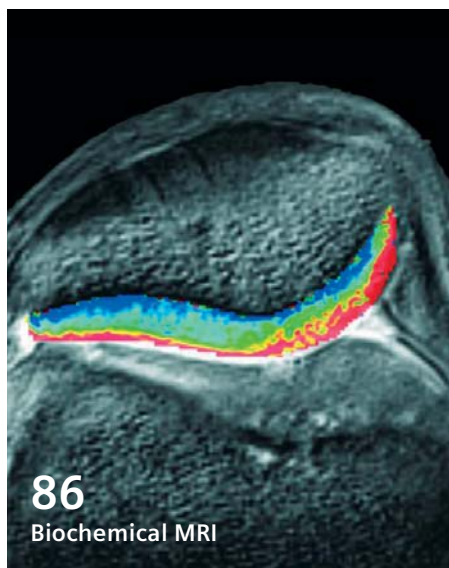
- 24 syngo WARP¹: Metal Artifact Reduction Techniques in MRI
Theresa Bachschmidt, et al.

Clinical Cartilage Imaging

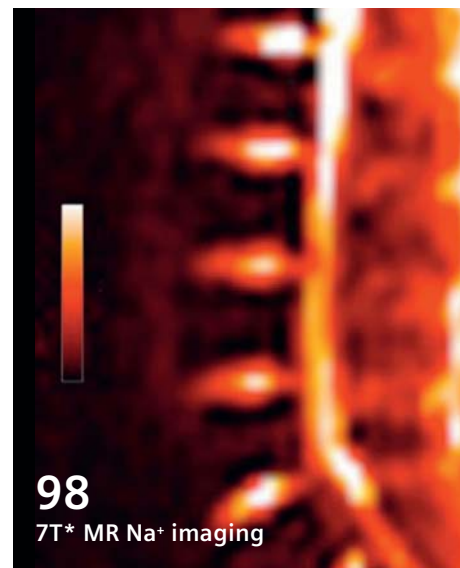
- 26 MRI Assessment of Articular Cartilage Repair
Darshana Sanghvi



60
Whole-Body DWI



86
Biochemical MRI



98
7T* MR Na⁺ imaging

Clinical Sports and Trauma Imaging

- 30** Case Series Sports and Trauma Imaging including:
- Chondral Delamination in the Knee
 - Melorheostosis
 - Glenohumeral Joint Dislocation
- Eric K. Fitzcharles, Charles P. Ho*

Clinical Case Report

- 42** Job's Syndrome
G. Hadjidekov, et al.

How I do it

- 46** MRI of the Shoulder: Utilizing the Glenoid Clockface Orientation
Steven D. Needell

Clinical Oncology

- 50** Bone and Soft Tissue Tumor Imaging
Marcus Pianta, et al.
- 58** **How I do it**
MSK Imaging Tips & Tricks
Mark Lourensz, et al.
- 60** Whole-Body Diffusion-Weighted MRI of the Bone Marrow in Health and Disease
Anwar Padhani, et al.
- 66** Knee MR Imaging of an Osteochondroma in Combination with Melorheostosis
Paul Flechsig, Marc André Weber

Clinical Pediatric Imaging

- 70** Sinding-Larsen-Johansson Disease
Axel Goldmann
- 72** MRI of the Fetal Skeleton.
Tips for Sequence Parameters and Post-Processing Protocol
Marcio Bernardes, et al.

Technology Tissue Function

- 74** Implementation of Quantitative MRI Evaluation of Tissue Health into Clinical Practice
Charles P. Ho, et al.
- 80** T1_ρ MRI: A Potential Biomarker of Cartilage Physiology
Arijitt Borthakur, et al.
- 86** Biochemical MR in Musculoskeletal Applications
Siegfried Trattnig, et al.

Technology Image Gallery

- 98** Ultra High Field (7 Tesla*) MRI for Musculoskeletal Applications
Siegfried Trattnig, et al.

*The 7T system is a research system only. It cannot be used outside of a research study.

¹syngo WARP and syngo RESOLVE are pending 510(k) clearance. The software is not yet commercially available in the United States and in other countries.

Three-Dimensional Musculoskeletal MR Imaging with *syngo* SPACE

Mike Notohamiprodjo, M.D.

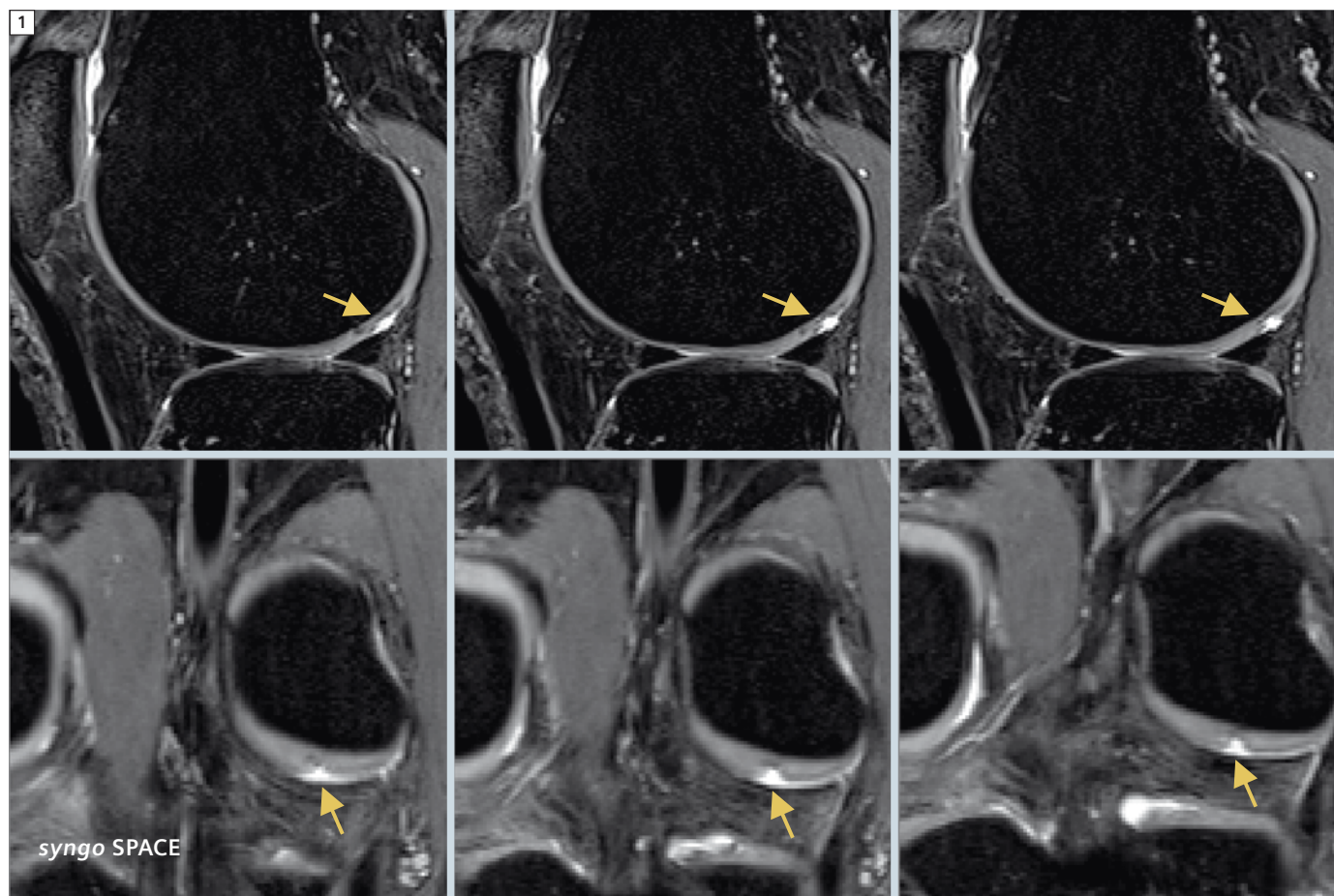
Department of Clinical Radiology, University Hospitals Munich, Munich, Germany

Background

Due to the excellent soft-tissue contrast MRI is the primary modality in musculoskeletal (MSK) imaging. It offers excellent direct depiction of bone marrow,

fibrous, ligamentous and cartilaginous structures as well as of the periarticular soft tissue. However, many anatomical structures such as ligaments and tendons are obliquely oriented. These struc-

tures and lesions / signal alterations are hence difficult to assess with two-dimensional (2D) sequences oriented in the standard planes. At a standard slice thickness of 3–5 mm [1], depiction is



1 Subtle III°-cartilage defect of the dorsal lateral femoral condyle.

Left knee of a 52-year-old female patient: The cartilage defect is mostly obscured and was missed in the 2D TSE reading (upper row, arrow) because of partial volume effects. While only visible on 1 2D FSE slice, the defect is clearly visible in *syngo* SPACE (bottom row).

(With permission from [8].)

also often comprised by partial volume effects, which may mimic signal alteration. Three-dimensional (3D) reconstructions of the standard planes are an alternative to additional sequences [2], although image quality is limited due to the anisotropic voxel-dimensions and interslice gaps of conventional 2D sequences. Acquisition of an isotropic source-dataset reducing partial volume effects and eliminating interslice gaps is therefore desirable and has been shown feasible and useful in previous studies [3–9]. Anatomical understanding and depiction of small lesions may particularly benefit from this approach.

Multi-channel extremity coils and higher field strengths facilitate time-efficient acquisition and allow to acquire isotropic 3D Turbo Spin Echo (TSE) sequences [10, 11], such as *syngo* SPACE (Sampling Perfection with Application optimized Contrasts using different flip angle Evolutions). With these 3D sequences, the whole area of interest is covered by an isotropic volume, which can be subsequently reconstructed in any desired orientation and slice thickness. Such a primary 3D approach for MSK imaging has been performed in several studies with a T2 or Proton Density-weighted 3D TSE sequence [7–9]. However, a T1-weighted (T1w) contrast is still required for a comprehensive MSK protocol. This article demonstrates our experiences with *syngo* SPACE in musculoskeletal MR examinations, also in combination with a T1-weighted protocol.

Technical considerations

An exemplary isotropic *syngo* SPACE-protocol is provided in Table 1. The 3D blocks cover the whole area of interest, so that exact orientation along important anatomical structures, e.g. the supraspinatus tendon or anterior cruciate ligament, is not required with these isotropic sequences [8]. The acquisition time of 3D sequences would have to be the same or at least similar to conventional 2D sequences, so that implementation of these sequences is justifiable. The compromise between acquisition

time and image quality is fundamental to all MRI approaches, and 3D TSE techniques have been struggling with either long acquisition times or low resolution. Longer acquisition times improve image quality but increase the susceptibility for motion artifacts. To shorten acquisition time we have performed parallel imaging with the *k*-space based technique *syngo* GRAPPA. The average examination time was 6–10 minutes per sequence depending on the organ of interest and the size of the joint [7–9]. This is

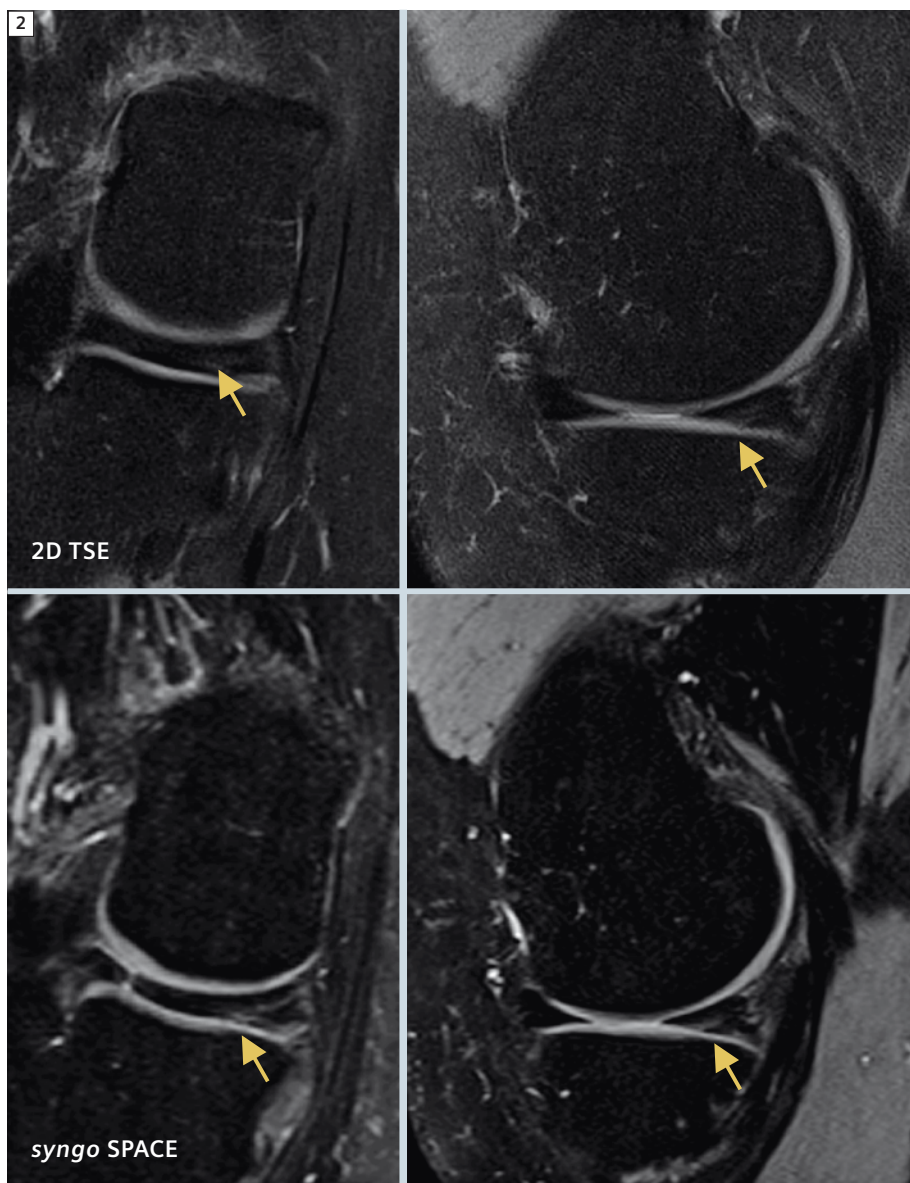
approximately 2–5 minutes longer than the acquisition of a single conventional anisotropic 2D sequence but still considerably faster than acquisition of three separate sequences. We observed motion artifacts similarly in both conventional and 3D sequences [7–9]. Compared to Gradient Echo sequences metal artifacts did not negatively affect image quality.

The isotropic resolution of *syngo* SPACE allows for free arbitrary online reconstruction. However, because of signal-

Table 1: Sequence parameters

Parameter	T1w <i>syngo</i> SPACE	T2w <i>syngo</i> SPACE
Orientation	Coronal	Coronal
TR (ms)	700	1100
TE (ms)	26	37
FA (°)	130	120-100-80
Matrix	230 x 230	256 x 256
FOV (mm)	160 x 160	160 x 160
Slice thickness (mm)	0.6	0.6
Number of slices (n=)	120	120
Bandwidth (Hz/pixel)	543	430
Echo train length	142	30
PAT (R=)	2	3
Number of averages	1	1
Acquisition time (min)	6:24	6:43

TR = repetition time; TE = echo time; FA = flip angle; FOV = field-of-view; PAT = parallel acquisition technique (GRAPPA).



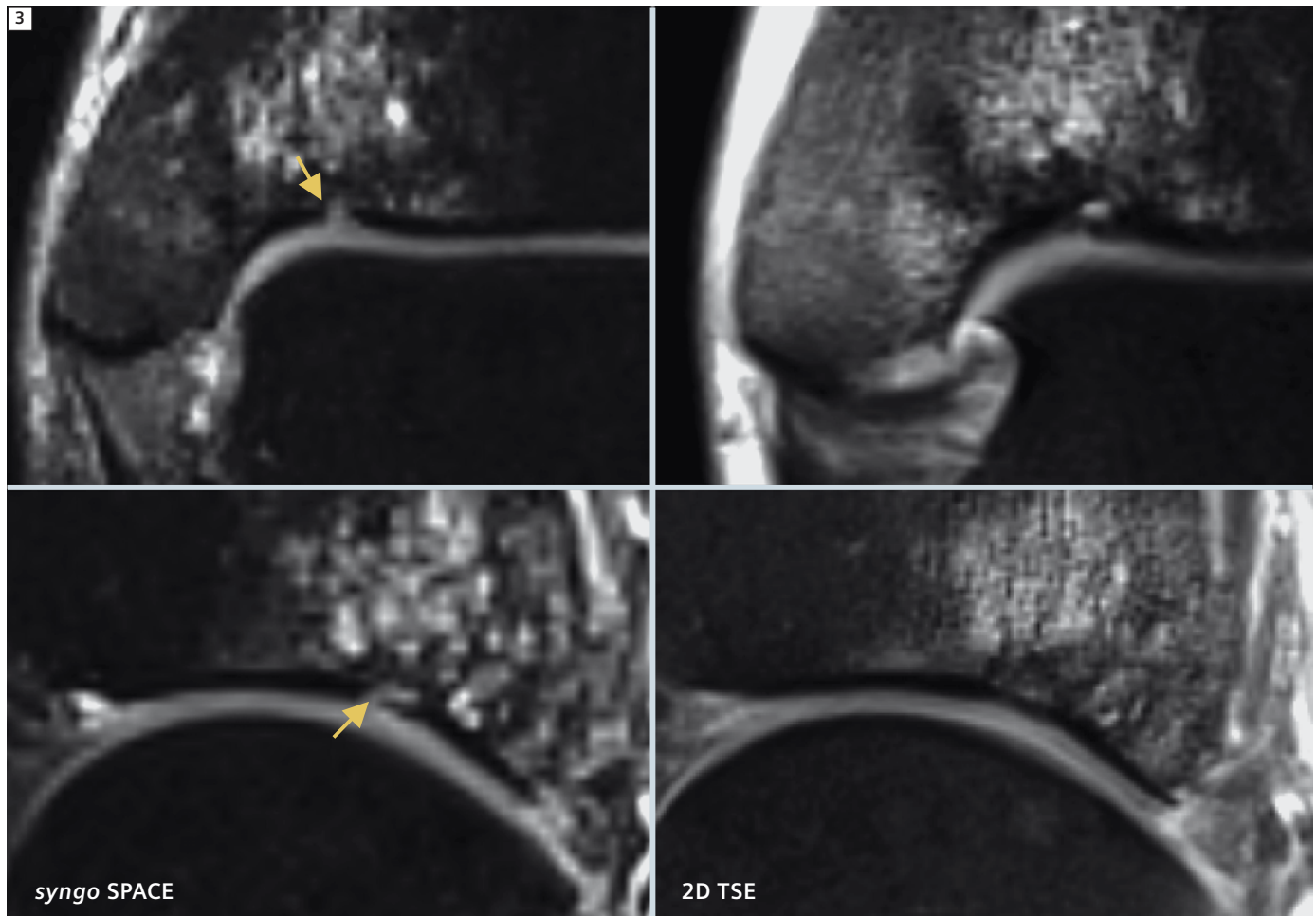
2 III°-lesion of the dorsal portion of the medial meniscus. Left knee of a 21-year-old female patient: The III°-tear of the dorsal portion of the medial meniscus is clearly visible in *syngo SPACE* (bottom row). The involvement of the meniscus surface is obscured in 2D TSE (upper row) and was regarded as a II° degeneration. (With permission from [8].)

related constraints or missing 3D reconstruction abilities of the PACS system, several previous studies featured time-consuming, standardized, retrospective reconstructions of the isotropic source data set in thicker slices, sacrificing the major asset of this sequence technique [3, 8]. Radial k-space acquisition and elliptical scanning were recently introduced in *syngo SPACE*, so that it provides excellent signal and contrast [7, 9]. In our department we now use the online 3D reconstruction capabilities of the PACS-integrated imaging software *syngo.via* to assess the original 3D data-set, so that no additional reconstruction time is required [9].

Clinical application

We primarily use *syngo SPACE* protocols at 3T (MAGNETOM Verio, Siemens Healthcare, Erlangen, Germany) in combination with dedicated multi-channel coils for the MRI-examination of joints, such as the knee, shoulder and ankle, but also for the assessment of bone marrow changes of the jaw (here only T1w). In previously published studies we have shown that a moderately T2-weighted sequence is feasible for time-efficient isotropic assessment of the knee and ankle [7-9]. In the knee, *syngo SPACE* has been shown superior to conventional 2D sequences for the depiction of the cartilage of the femoral trochlea and the meniscus root ligaments [7, 8]. Small lesions of femoral trochlea or peripheral condyles or talus can be readily depicted with *syngo SPACE* with a higher diagnostic confidence than for conventional sequence (Fig. 1). However, a small additional number of cartilage and meniscus lesions were detected with *syngo SPACE*, which was mainly attributed to a reduction of through-plane partial volume effects. Sensitivity for meniscus lesions was higher for *syngo SPACE* compared to conventional 2D sequences (Fig. 2).

The ankle is one of the most complex human joints and most ligaments and tendons are oriented obliquely, so that



3 Osteochondral abnormalities. A small osteochondral lesion of the medial tibia can be clearly delineated in *syngo* SPACE (arrow). In the 2D TSE sequence the discontinuity of the subchondral bone cannot be detected. Depiction of bone marrow edema is similar in both sequences. (With permission from [9]).

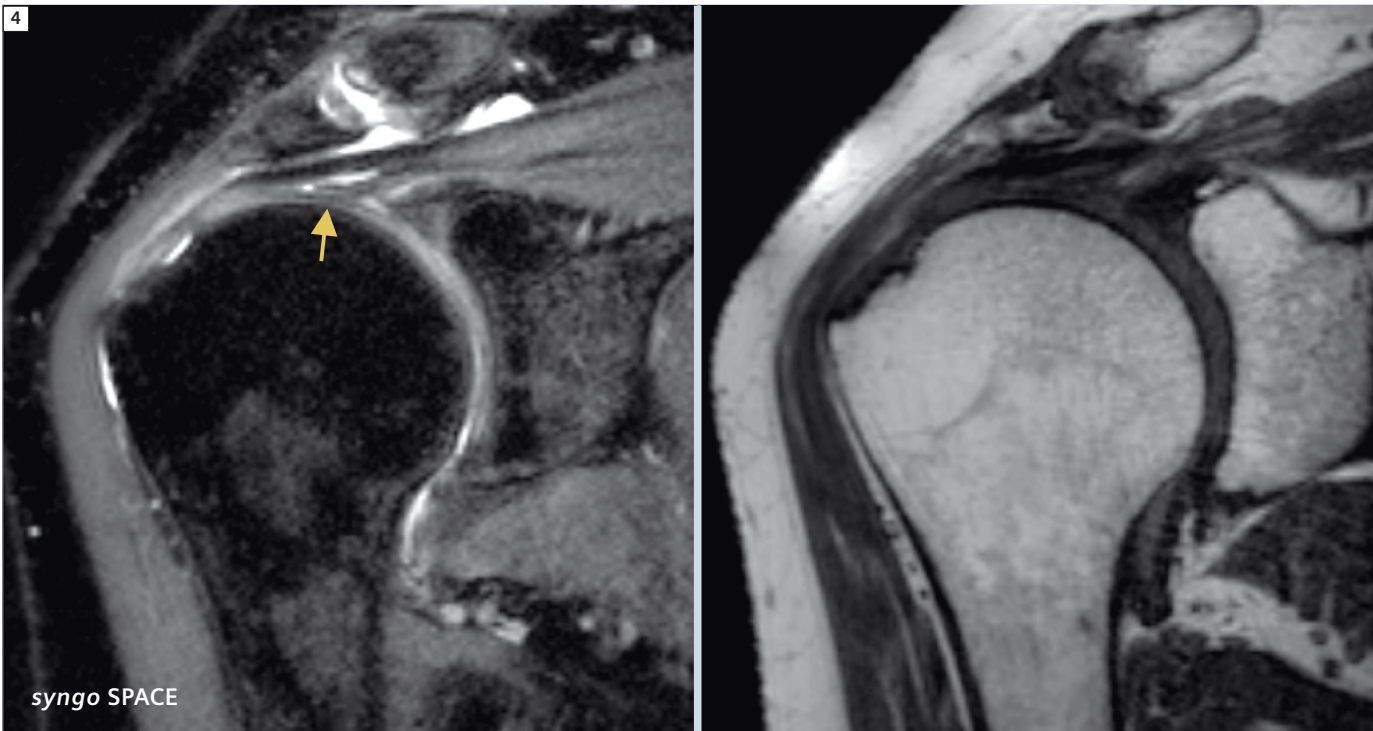
syngo SPACE appears particularly promising. Indeed *syngo* SPACE was superior to 2D sequences for the depiction of the spheric tibial and talar cartilage (Fig. 4) as well as for the spring ligament complex. The complete three-dimensional approach facilitated good depiction of those ligaments usually difficult to assess with standard 2D sequences. No abnormality detected with conventional 2D TSE was missed when using *syngo* SPACE and intersequence- and inter-reader correlation showed no significant differences, so that implementation of *syngo* SPACE in clinical routine protocols appears justified [9].

A T1-weighted 3D approach appears particularly promising to achieve a complete 3D protocol. Our first results show that T1w *syngo* SPACE yields a very similar contrast to conventional 2D SE sequences, so that a need for any significant adjustment of the radiologist's reading and interpretation habits to the new sequence is unlikely. Assessment of tendons and the subchondral bone is readily possible with T1w *syngo* SPACE. The T1w contrast allows for an improved anatomical understanding and is useful for verification of findings in the T2w sequence (Fig. 5). The anatomically complex jaw appears particularly promising for the application of the T1w sequence. T1w sequences show the

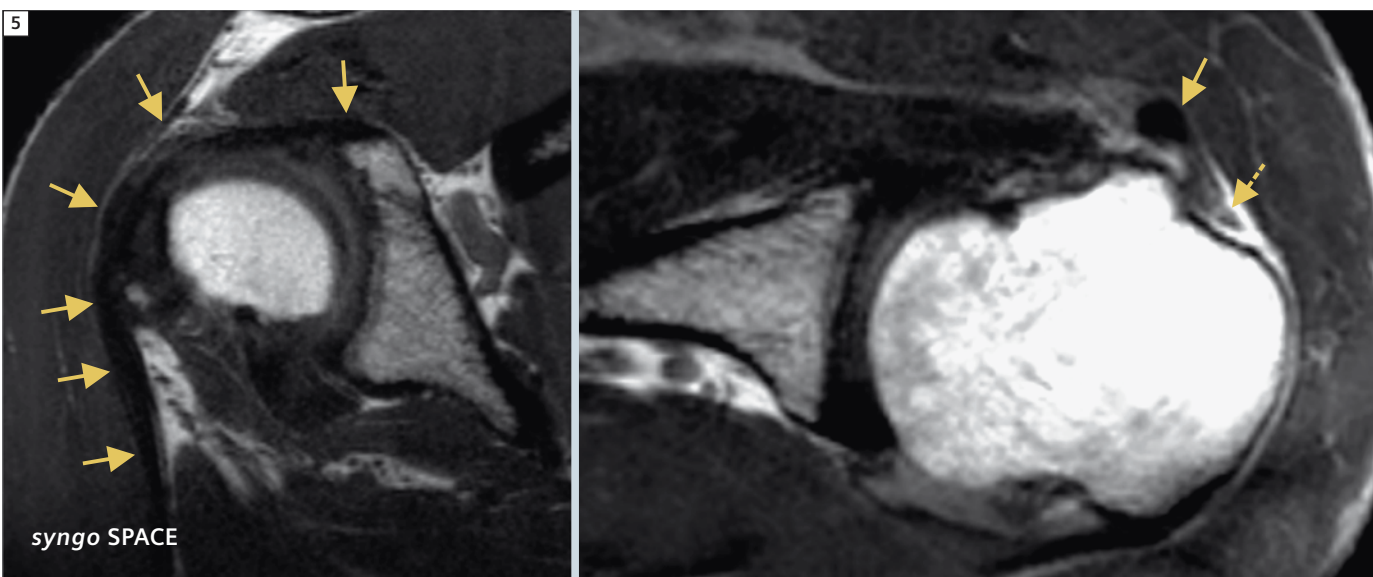
highest sensitivity for diseases affecting the structures of the bone, which are commonly found in the jaw bone [12]. The isotropic resolution allows for a convenient analysis of the jaw bone, even with curved multiplanar reconstructions (MPRs) very similar to an orthopantomogram (Fig. 6).

Conclusion

Isotropic 3D imaging with *syngo* SPACE is a promising approach to assess musculoskeletal pathologies. Previous technical constraints such as low SNR, CNR and blurring have been compensated by flip angle optimization and radial



4 Combined T1w and T2w syngo SPACE dataset of the shoulder. T1w and moderately T2w syngo SPACE can be combined for a comprehensive 3D protocol. Right shoulder of a 45-year-old male patient: Small partial tear of the supraspinatus tendon (arrow). syngo SPACE provides excellent contrast between joint fluid and tendons/muscle.



5 Luxation of the biceps tendon. 46-year-old male patient with tear of the subscapularis muscle and consecutive anteromedial luxation of the biceps tendon (arrows). The biceps sulcus is empty (dotted arrow) syngo SPACE allows to conveniently display the full course of the tendon in one slice.



6 Curved MPR of the jaw.

62-year-old female patient with osteonecrosis of the jaw. A curved MPR along the oral midline was created to display the mandible and maxilla in one slice. The large osteonecrosis of the right mandibular ramus (arrows) can be readily depicted in this T1w syngo SPACE sequence.

k-space sampling. The theoretical susceptibility of this technique to motion artifacts did not become evident in our experience. The identification of anatomical structures at least equals the conventional sequence and allows superior discrimination of relevant small ligamentous and cartilaginous structures. The image contrast is comparable to conventional 2D sequences, so that no considerable adjustment by the radiologist is necessary.

A combined isotropic T1w and moderately T2w 3D protocol will take approximately 12–16 minutes. In combination with arbitrary multiplanar reformation, no other additional sequences are necessary. Therefore, syngo SPACE has become an appropriate alternative for substantially shortened routine MSK protocols.

References

- 1 Resnick, D., H.S. Kang, and M.L. Pretterklieber, *Internal derangements of joints*. 2nd ed 2006, Philadelphia: Saunders/Elsevier. 2 v. (xvi, 2284, liv p.).
- 2 Duc, S.R., et al., *Improved visualization of collateral ligaments of the ankle: multiplanar reconstructions based on standard 2D turbo spin-echo MR images*. *Eur Radiol*, 2007. **17**(5): p. 1162-71.
- 3 Gold, G.E., et al., *Isotropic MRI of the knee with 3D fast spin-echo extended echo-train acquisition (XETA): initial experience*. *AJR Am J Roentgenol*, 2007. **188**(5): p. 1287-93.
- 4 Gold, G.E., et al., *Balanced SSFP imaging of the musculoskeletal system*. *J Magn Reson Imaging*, 2007. **25**(2): p. 270-8.
- 5 Kijowski, R., et al., *Vastly undersampled isotropic projection steady-state free precession imaging of the knee: diagnostic performance compared with conventional MR*. *Radiology*, 2009. **251**(1): p. 185-94.
- 6 Kijowski, R., et al., *Knee joint: comprehensive assessment with 3D isotropic resolution fast spin-echo MR imaging--diagnostic performance compared with that of conventional MR imaging at 3.0 T*. *Radiology*, 2009. **252**(2): p. 486-95.
- 7 Notohamiprodjo, M., et al., *3D-imaging of the knee with an optimized 3D-FSE-sequence and a 15-channel knee-coil*. *European journal of radiology*, 2012.
- 8 Notohamiprodjo, M., et al., *MRI of the knee at 3T: first clinical results with an isotropic PDfs-weighted 3D-TSE-sequence*. *Investigative radiology*, 2009. **44**(9): p. 585-97.
- 9 Notohamiprodjo, M., et al., *3D-MRI of the ankle with optimized 3D-SPACE*. *Investigative radiology*, 2012. **47**(4): p. 231-9.
- 10 Alsop, D.C., *The sensitivity of low flip angle RARE imaging*. *Magn Reson Med*, 1997. **37**(2): p. 176-84.
- 11 Hennig, J., *Multiecho imaging sequences with low refocusing flip angles*. *J Magn Reson.*, 1988. **1988**(78): p. 397-407.
- 12 Arce, K., et al., *Imaging findings in bisphosphonate-related osteonecrosis of jaws*. *Journal of oral and maxillofacial surgery : official journal of the American Association of Oral and Maxillofacial Surgeons*, 2009. **67**(5 Suppl): p. 75-84.

Contact

Mike Notohamiprodjo, M.D.
Section Chief Conventional Radiology
Department of Clinical Radiology
University Hospitals Munich
Campus Großhadern
Marchioninistrasse 15
81377 Munich
Germany
Phone: +49-89-7095-3620
Fax: +49-89-7095-8832
mike.notohamiprodjo@med.lmu.de

Imaging of Metallic Prostheses Using Novel Sequences: Early Experience

Leon D. Rybak, M.D.¹; Mary Bruno, B.S.¹; Mathias Nittka, Ph.D.²; Christian Geppert, Ph.D.³; Holly Delaney, M.D.¹; Park Jong, M.D.¹

¹New York University Medical Center, Department of Radiology, New York, NY, USA

²Siemens Healthcare, Erlangen, Germany

³Siemens US R&D Collaborations, New York, NY, USA

Introduction

For many years, diagnostic imaging in patients with metallic implants had been limited to plain X-rays and nuclear medicine studies. Although there have been advancements with regards to imaging of hardware using computed tomography, many of the changes involve increasing the radiation dose at a time when the public has become increasingly sensitive to reported long term risk of carcinogenesis posed by this exposure. With recent technical developments, magnetic resonance imaging (MRI) in the presence of metal is quickly becoming a reality with the added benefits of excellent soft tissue resolution and contrast. This could not come at a better time considering that new methods of hip and knee arthroplasty have led to unique complications which require timely diagnosis and treatment to prevent implant failure, damage to the surrounding soft tissues and, possibly, carcinogenesis [1, 2]. This article outlines some of these advances and describes the author's early experiences in regards to the clinical use of these techniques.

The clinical incentive

Initial attempts at arthroplasty involved the interposition of various substances including fascia lata, porcine bladder, gold foil, glass, rubber and Vitallium [3–5]. Early versions of hip arthroplasties were marred by flawed design and poor materials resulting in early failure. It was not until the 1960s that Sir John Charnley of the Manchester Royal Infir-

mary developed the initial prototype of what would become a long line of modern hip arthroplasties. It soon became apparent, however, that the longevity of these devices was limited, in large part to wear of the various components. It was also discovered that the particles which resulted from this wear could incite an inflammatory response that led to areas of bone destruction. This process was given several names over the years, some of which included 'cement disease', 'particle disease', 'foreign body granuloma formation' or, simply, 'osteolysis' [6, 7]. Although most cases were limited, more florid cases resulting in widespread and extensive bone loss were noted. This 'aseptic' form of loosening which, though not without consequence, would have to be differentiated from septic or infectious loosening. Infected arthroplasties, require removal and, in many cases, a two staged procedure with a period of antibiotic therapy prior to re-implantation. Though the gold standard in these cases has remained joint aspiration and culture, imaging has played a role with certain plain film findings and nuclear imaging studies helping to confirm the diagnosis.

Initial reports of osteolysis around arthroplasties implicated methacrylate (cement) as the inciting factor. However, with the advent of non-cemented components, the majority of cases have been attributed to wear of the polyethylene components [6]. Regardless of the presence of bone destruction, the inevitable loss of the polythene weight-bearing surfaces

has led to a limited lifespan of the prosthesis and the need for revision surgery. In an effort to increase the longevity of the components, much research has centered on the creation of new, more durable plastics included cross-linked ultrahigh-molecular-weight polyethylene as well as the use of other substances such as ceramic [4, 5]. Though initially explored in the 1960s, metal-on-metal systems had not met with success and were abandoned. In an effort to prevent the complications resulting from component wear, the feasibility of such a system was revisited in the past decade. Theoretically, metal-on-metal systems would eliminate the need for plastic altogether, reduce the rate of wear and allow for the use of larger femoral heads providing for greater stability and range of motion [5] (Fig. 1). Though these new systems showed early promise, they have created a new set of problems and complications. Metal wear resulting in 'metallosis' with elevated blood levels of ions has been noted, creating a fear of possible carcinogenesis [1, 2]. More recently, a new form of perivascular lymphocytic infiltration involving the soft tissues of the hip girdle referred to as aseptic lymphocyte-dominated vasculitis-associated lesions (ALVAL), has been described [8–13]. In addition to areas of osteolysis, this pathologic entity has been noted to manifest as synovitis, peri-prosthetic soft tissue masses and bursal fluid collections. Like osteolysis, ALVAL needs to be discriminated and has even been implicated as a risk factor for infection [14, 15].

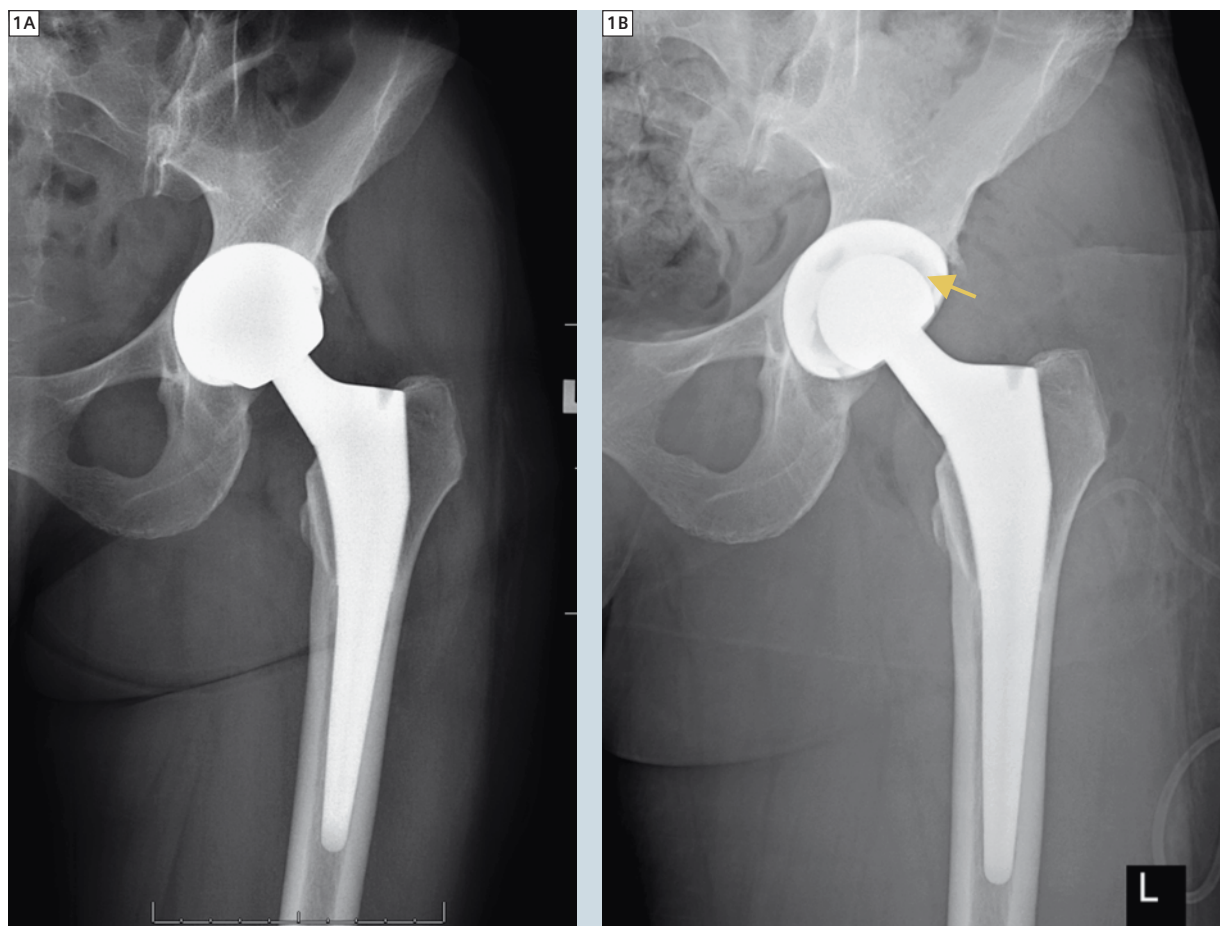
These developments have created an additional incentive to find a safe and effective mechanism of non-invasively evaluating both the prosthetic components themselves, but also the joint space and surrounding soft tissues. Recent advances in magnetic resonance imaging have made this possible.

The physics

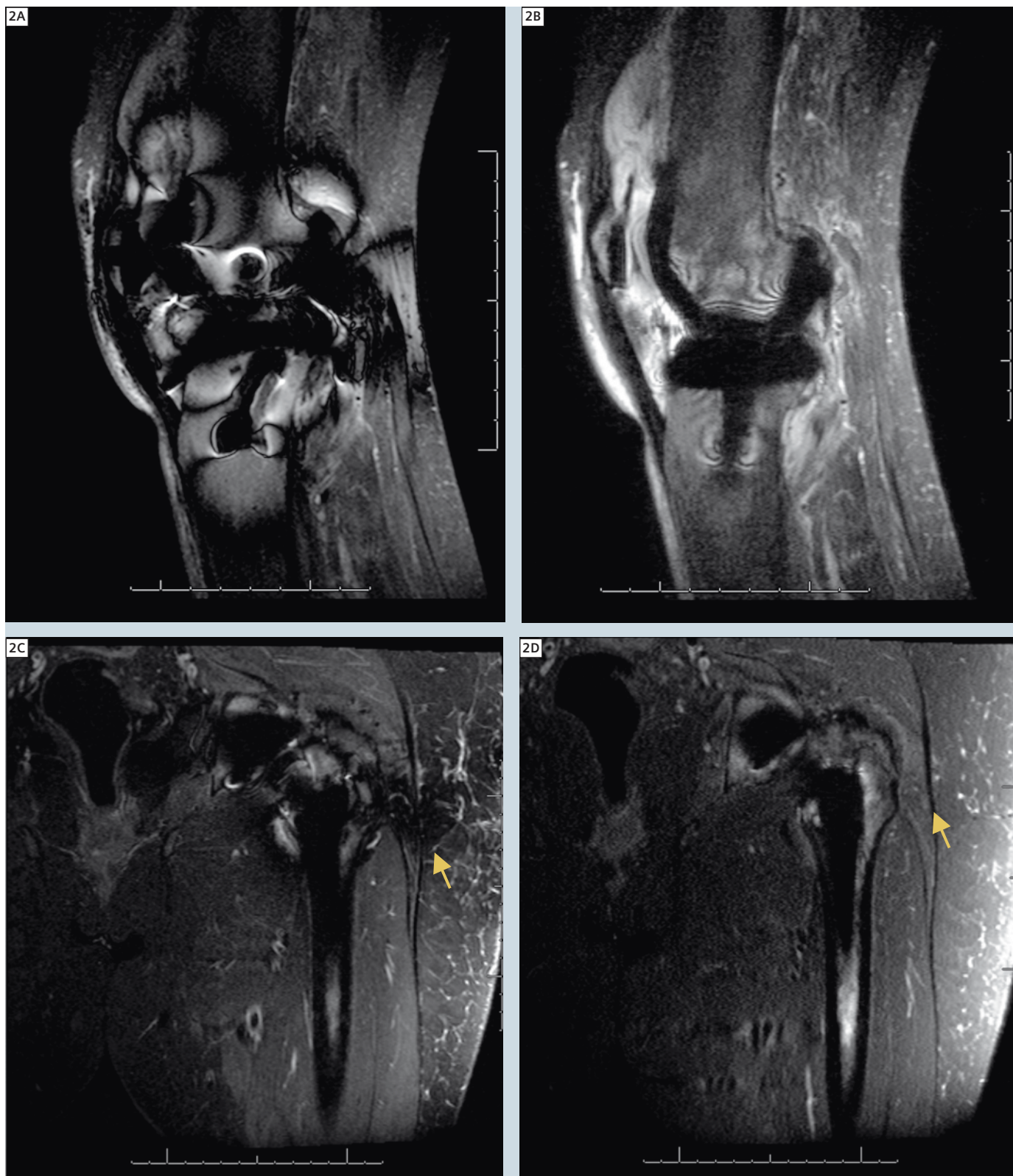
In order to be able to fix a problem, one must first be familiar with the issues. When a patient with an arthroplasty is placed in the magnetic field, the relatively easily magnetized metallic components of the arthroplasty are in direct apposition to poorly magnetized soft

tissues creating large localized fluctuations of the static magnetic field. The result is either spatial mismapping or even complete signal loss. One should be aware that the mismapping takes place in two dimensions: one is the in-plane signal misregistration in the frequency direction which occurs during readout, closely related to the well known chemical shift effect. The second effect is a through-plane distortion due to warping that occurs at the time of slice selection. Metal artifacts are strongly dependent on the type and shape of the metal used and the orientation of the metal within the magnetic field. Titanium implants, being less

magnetic, tend to pose the least problem for the imager, with stainless steel causing more perturbation of the field and cobalt chrome presenting the greatest challenge. As the susceptibility artifact occurs in the frequency direction, orienting the metallic components with the longest axis in the frequency direction will allow optimal resolution of changes along the greatest proportion of the metal soft tissue interface. Alternatively, two acquisitions with a swap of phase and frequency will optimize resolution around all portions of the prosthetic components. Finally, curved or rounded portions of the metal components like the femoral head tend to



1 AP radiographs of the hip in the same patient before (1A) and after (1B) revision arthroplasty. The original prosthesis in (1A) consists of a metal on metal device with no interposed plastic component. Note the large size of the metallic femoral head which articulates directly with the acetabular cup. In the more traditional revised prosthesis in (1B), note the lucent zone (arrow) between the femoral head and acetabulum which reflects the interposed polyethylene liner.

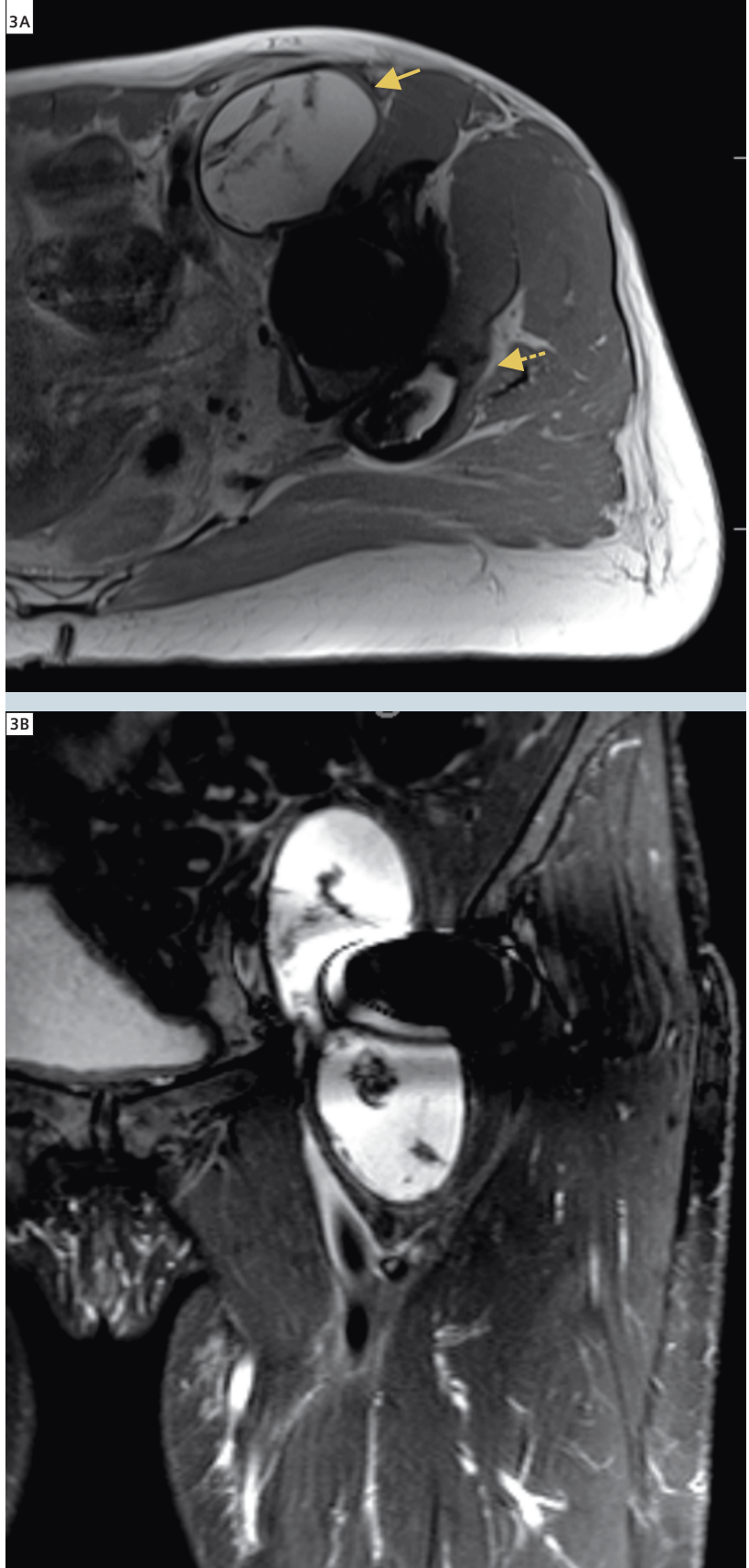


2 STIR contrast images of a total knee prosthesis in the sagittal plane (2A, 2B) and a total hip prosthesis in the coronal plane (2C, 2D) obtained on a 1.5T magnet (MAGNETOM Avanto, Siemens Healthcare). In each case, the left sided image was obtained with routine technique and the right image, with the SEMAC* sequence. The imaging times were between 3–4.5 minutes for the conventional and 9–12 minutes for the SEMAC sequences. Arrow pointing to the lateral soft tissue.

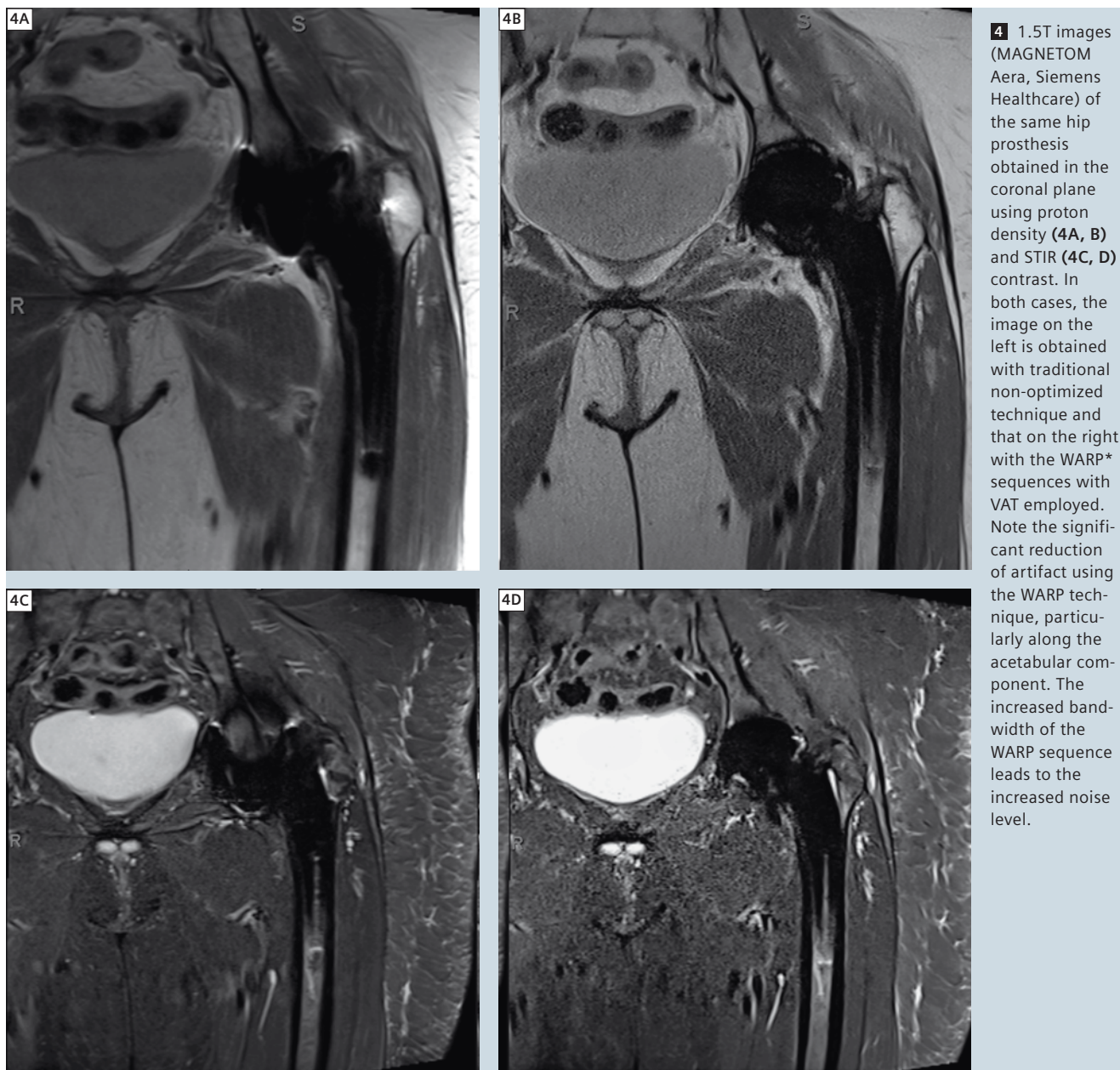
cause more disturbance of the magnetic field than the linear portions [16–20]. It is, thus, possible to eliminate a certain amount of artifact making changes in several of the basic sequence parameters. First, turbo spin echo (TSE) techniques are used to take advantage of the multiple 180 degree refocusing pulses which result in rephasing of the signal. Second, receiver bandwidth is increased to reduce the shift in the frequency encoding direction in the area of the metal. Third, spatial resolution is increased by using a finer matrix to decrease the conspicuity of the artifact. Last, if fat suppression is required, inversion recovery is favored over frequency selective techniques which may suffer as a result of field inhomogeneity. In addition, there are more sophisticated approaches to metal reduction which change the actual acquisition scheme of the conventional TSE sequence. One of these which is referred to as view angle tilting* (VAT) involves applying an additional readout gradient with the same amplitude as that employed during slice select, thereby re-phasing the spins in the x-axis and correcting for in-plane distortion [21]. Slice Encoding for Metal Artifact Reduction¹ (SEMAC) is a novel technique which is presently being tested for clinical applications. With SEMAC, additional phase encoding steps are applied in the z-direction, correcting through plane distortions. This method is used in conjunction with VAT [22, 23]. Though artifact reduction has been demonstrated, there is a significant time cost with SEMAC and much of the research at this time is focused on increasing the speed of image acquisition with this technique.

Early clinical results

Several groups using various methods of metal reduction have reported good to excellent results in visualization of both the prosthetic bone interface as well as the surrounding soft tissue envelope in patients [20, 24, 25]. Using their standard protocol with simple parameter modifications designed for optimization of metal artifact reduction, White et al.



3 1.5T MR images (MAGNETOM Avanto, Siemens Healthcare) from a surgically proven case of metallosis with ALVAL status post metal on metal hip replacement in a 48-year-old female. Both the optimized proton density-weighted image in the axial plane (**3A**) and the STIR image in the coronal plane using SEMAC¹ (**3B**) demonstrate a large bilobed fluid-like collection extending both along the posterior joint margin (dashed blue arrow) as well as into the iliopsoas bursa anteriorly (solid blue arrow) with areas of low signal internal debris. This is the same patient whose plain films are depicted in figure 1.



reported on MRI of 14 total hip arthroplasties and found depiction of the periprosthetic structures to be of diagnostic quality for all of the femoral components and 36% of the acetabular components [20]. They found abnormalities in 11 cases and correctly diagnosed pathology in all 7 cases in which surgical correlation was available. Potter et al., using a similar technique, found good delineation of the bone-implant interface and surrounding soft tissues in 100% of 28

hip prostheses and correctly diagnosed areas of osteolysis in 15 patients with surgical correlation.

The NYU experience

At NYU, between August of 2011 and August of 2012, we imaged 39 consecutive patients with painful hip (28 hips in 29 patients) and knee (11 knees in 10 patients) prostheses. Early in our experience, we used a combination of routine, routine optimized for metal

reduction, VAT only and SEMAC¹ sequences, the latter two being a prototype provided by Siemens (WARP WIP#648, works in progress package*). All patients were imaged on the same 1.5 Tesla magnet (MAGNETOM Avanto, Siemens Healthcare, Erlangen, Germany). There was significant reduction of metal artifact both with the use of the optimized and VAT only sequences in scan times comparable to those used in routine imaging studies. The best result

using STIR contrast was with SEMAC at a time cost. An example of the conventional and SEMAC sequences using STIR contrast in a hip and knee in two different patients is provided in figure 2. Our clinical results were similarly encouraging with significant findings diagnosed in 26 of the 39 cases and confirmation of the findings in all 11 cases with surgical correlation. These surgically confirmed findings included 5 cases of metallosis/ALVAL, 2 cases of patellar tendon rupture, 1 case of an infected bursal collection, 1 case of patellar component loosening, 1 case of acetabular osteolysis from polyethylene wear and 1 case of marked capsular thickening resulting in contracture in a knee. A case of metallosis/ALVAL is provided in figure 3.

More recently, we compared conventional imaging to *syngo* WARP*, an 'out of the box' optimized metal reduction sequence which can be used with or without the addition of VAT. Imaging was performed at 1.5T (MAGNETOM Aera, Siemens Healthcare, Erlangen, Germany). A side by side comparison of conventional and *syngo* WARP sequences of the same hip prosthesis in the coronal plane using proton density (Fig. 4A) and STIR (Fig. 4B) contrasts demonstrates significant improvement in image quality with similar imaging times. The increased noise in the images is caused by the increased readout bandwidth.

Conclusion

Excellent reduction of metal artifact can be achieved through the use of optimized traditional sequences as well as novel techniques such as VAT and SEMAC¹. At NYU, we have decided to adapt a protocol which consists of *syngo* WARP imaging with VAT obtained in all three planes using a combination of contrasts suited to answering the particular clinical questions being posed in each case (Table 1). The SEMAC sequence was used with STIR contrast in the coronal plane in the hip and the sagittal plane in knees in patients who appear to be able to tolerate the longer imaging time. Further enhancements to the SEMAC sequence with reductions in imaging time are being explored.

*510(k) pending. Not for sale in the US and in other countries.

¹Works in Progress in the USA. The information about this product is preliminary. The product is under development and is not commercially available in the USA and its future availability cannot be ensured.

Table 1: 1.5T MAGNETOM Aera protocols.

		TA [min]	Ma- trix	resolution [mm]	FOV [mm]	phase encoding direction	slices	TR [ms]	TE [ms]	TI [ms]	BW [Hz/ Pixel]	PAT accel. factor	VAT	turbo factor
Hip	COR STIR	3:46	320	0.9x0.9x3.0	280	RL	36	4680	39	145	504	off	on	17
	AX PD	5:29	320	0.7x0.7x3.0	220	AP	78	5450	31		521	off	off	9
	COR PD	5:07	512	0.5x0.5x4.0	280	RL	28	5000	31		514	off	on	33
	SAG PD	4:35	512	0.5x0.5x4.0	280	AP	40	4590	27		514	2	on	21
Knee	SAG STIR	3:42	384	0.5x0.5x3.0	200	HF	36	4800	45	150	383	off	on	19
	AX PD	2:10	320	0.5x0.5x3.0	160	AP	58	5580	21		504	off	on	12
	COR T1	1:34	320	0.6x0.6x4.0	200	RL	30	600	12		401	1	on	3
	SAG PD	2:18	448	0.4x0.4x4.0	200	HF	30	4000	25		558	off	on	32

The protocols we developed for hip and knee implants based on the new *syngo* WARP* sequence on 1.5T MAGNETOM Aera. Note that all protocols apply VAT*, except for the axial hip, where the difference with or without VAT was not considered significant.

Disclaimer:

MR imaging of patients with metallic implants brings specific risks. However, certain implants are approved by the governing regulatory bodies to be MR conditionally safe. For such implants, the previously mentioned warning may not be applicable. Please contact the implant manufacturer for the specific conditional information. The conditions for MR safety are the responsibility of the implant manufacturer, not of Siemens.

References

- 1 Afolaranmi GA, Tettey J, Meek RM, Grant MH. Release of chromium from orthopaedic arthroplasties. *The open orthopaedics journal*. 2008;2:10-18.
- 2 Delaunay C, Petit I, Learmonth ID, Oger P, Vendittoli PA. Metal-on-metal bearings total hip arthroplasty: the cobalt and chromium ions release concern. *Orthopaedics & traumatology, surgery & research* : OTSR. Dec 2010; 96(8):894-904.
- 3 Gomez PF, Morcuende JA. Early attempts at hip arthroplasty--1700s to 1950s. *The Iowa orthopaedic journal*. 2005;25:25-29.
- 4 Knight SR, Aujla, R., Biswas, S.P. Total Hip Arthroplasty – over 100 years of operative history. *Orthopedic Reviews*. 2011;3:e16:72-74.
- 5 Learmonth ID, Young C, Rorabeck C. The operation of the century: total hip replacement. *Lancet*. Oct 27 2007;370(9597):1508-1519.
- 6 Goodman S. Wear particulate and osteolysis. *The Orthopedic clinics of North America*. Jan 2005;36(1):41-48, vi.
- 7 Kadoya Y, Kobayashi A, Ohashi H. Wear and osteolysis in total joint replacements. *Acta orthopaedica Scandinavica. Supplementum*. Feb 1998;278:1-16.
- 8 Anderson H, Toms AP, Cahir JG, Goodwin RW, Wimhurst J, Nolan JF. Grading the severity of soft tissue changes associated with metal-on-metal hip replacements: reliability of an MR grading system. *Skeletal radiology*. Mar 2011;40(3):303-307.
- 9 Campbell P, Ebramzadeh E, Nelson S, Takamura K, De Smet K, Amstutz HC. Histological features of pseudotumor-like tissues from metal-on-metal hips. *Clinical orthopaedics and related research*. Sep 2010;468(9):2321-2327.
- 10 Counsell A, Heasley R, Arumilli B, Paul A. A groin mass caused by metal particle debris after hip resurfacing. *Acta orthopaedica Belgica*. Dec 2008;74(6):870-874.
- 11 Hart AJ, Satchithananda K, Liddle AD, et al. Pseudotumors in association with well-functioning metal-on-metal hip prostheses: a case-control study using three-dimensional computed tomography and magnetic resonance imaging. *The Journal of bone and joint surgery. American volume*. Feb 15 2012;94(4):317-325.
- 12 Natsu S, Sidaginamale RP, Gandhi J, Langton DJ, Nargol AV. Adverse reactions to metal debris: histopathological features of periprosthetic soft tissue reactions seen in association with failed metal on metal hip arthroplasties. *Journal of clinical pathology*. May 2012;65(5):409-418.
- 13 Watters TS, Cardona DM, Menon KS, Vinson EN, Bolognesi MP, Dodd LG. Aseptic lymphocyte-dominated vasculitis-associated lesion: a clinicopathologic review of an underrecognized cause of prosthetic failure. *American journal of clinical pathology*. Dec 2010;134(6):886-893.
- 14 Donaldson JR, Miles J, Sri-Ram K, Poullis C, Muirhead-Allwood S, Skinner J. The relationship between the presence of metallosis and massive infection in metal-on-metal hip replacements. *Hip international : the journal of clinical and experimental research on hip pathology and therapy*. Apr-Jun 2010;20(2):242-247.
- 15 Galbraith JG, Butler JS, Browne TJ, Mulcahy D, Harty JA. Infection or metal hypersensitivity? The diagnostic challenge of failure in metal-on-metal bearings. *Acta orthopaedica Belgica*. Apr 2011;77(2):145-151.
- 16 Cahir JG, Toms AP, Marshall TJ, Wimhurst J, Nolan J. CT and MRI of hip arthroplasty. *Clinical radiology*. Dec 2007;62(12):1163-1171; discussion 1172-1163.
- 17 Potter HG, Foo, L.F., Nestor, B.J. What is the Role of Magnetic Resonance Imaging in the Evaluation of Total Hip Arthroplasty? *HSSJ*. 2005;1(1):89-93.
- 18 Potter HG, Foo LF. Magnetic resonance imaging of joint arthroplasty. *The Orthopedic clinics of North America*. Jul 2006;37(3):361-373, vi-vii.
- 19 Sofka CM, Potter HG. MR imaging of joint arthroplasty. *Seminars in musculoskeletal radiology*. Mar 2002;6(1):79-85.
- 20 White LM, Kim JK, Mehta M, et al. Complications of total hip arthroplasty: MR imaging-initial experience. *Radiology*. Apr 2000;215(1):254-262.
- 21 Cho ZH, Kim DJ, Kim YK. Total inhomogeneity correction including chemical shifts and susceptibility by view angle tilting. *Medical physics*. Jan-Feb 1988;15(1):7-11.
- 22 Ai T, Padua A, Goerner F, et al. SEMAC-VAT and MSVAT-SPACE sequence strategies for metal artifact reduction in 1.5T magnetic resonance imaging. *Investigative radiology*. May 2012;47(5):267-276.
- 23 Lu W, Pauly KB, Gold GE, Pauly JM, Hargreaves BA. SEMAC: Slice Encoding for Metal Artifact Correction in MRI. *Magnetic resonance in medicine : official journal of the Society of Magnetic Resonance in Medicine / Society of Magnetic Resonance in Medicine*. Jul 2009;62(1):66-76.
- 24 Potter HG, Nestor BJ, Sofka CM, Ho ST, Peters LE, Salvati EA. Magnetic resonance imaging after total hip arthroplasty: evaluation of periprosthetic soft tissue. *The Journal of bone and joint surgery. American volume*. Sep 2004;86-A(9):1947-1954.
- 25 Toms AP, Marshall TJ, Cahir J, et al. MRI of early symptomatic metal-on-metal total hip arthroplasty: a retrospective review of radiological findings in 20 hips. *Clinical radiology*. Jan 2008;63(1):49-58.

Contact

Leon D. Rybak
Assistant Professor,
Vice Chair of
Operations in Radiology
New York University
Langone Medical Center
301 East 17th Street
New York, NY 10003
USA
Phone: +1 212-598-6655
Leon.Rybak@nyumc.org

Product News

Spine Dot Engine

Complete spine examinations with ease and fewer errors

- Fast and standardized scanning for consistent and robust image quality with AutoAlign and AutoCoverage
- Automatic detection of intervertebral disc planes and display of suggested vertebrae labelling
- Automatic curved reconstruction of 3D datasets for optimal visualization
- *syngo* WARP* for reduction of susceptibility artifacts, such as from MR conditional metal implants

*510(k) pending. Not for sale in the U.S. and in other countries.



Vertebrae labelling in the Spine Dot Engine

Experience a Dot workflow yourself and hear about other user's favourite Dot feature at:
www.siemens.com/Dot

Experience with the 3 Tesla MAGNETOM Verio system in Spine Imaging: Benefit of 3D Sequences and Reduction of Metal-Related Artifacts with the *syngo* WARP WIP-package

Marcel Wolf, M.D.¹; Marc-André Weber, M.D., M.Sc.²

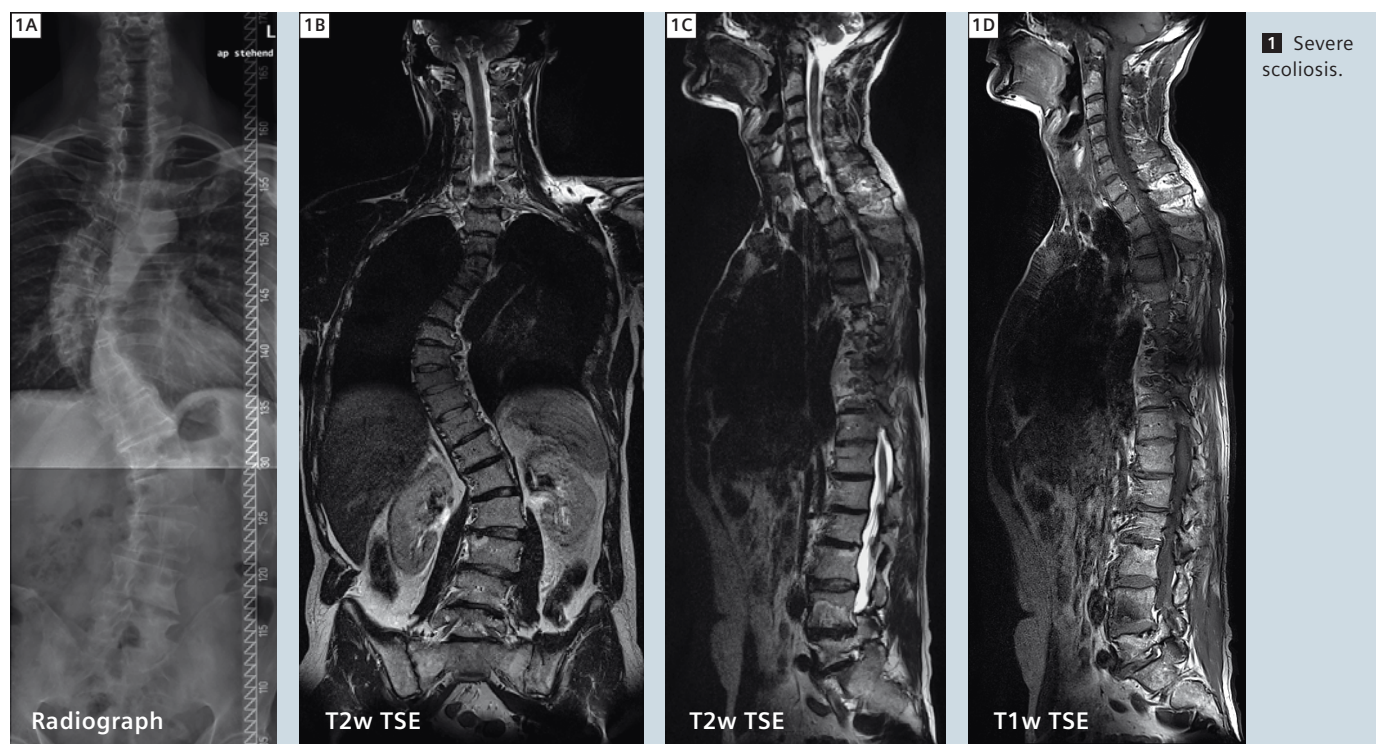
¹Department of Neuroradiology, University Hospital Heidelberg, Germany

²Department of Diagnostic and Interventional Radiology, University Hospital Heidelberg, Germany

Spine imaging in posttraumatic and paraplegic patients has great demands on the MRI scanner and pulse sequences. At our institution, the Department of Diagnostic and Interventional Radiology within the Department of Orthopedics, Traumatology and Spinal Cord Injury Center, MR imaging of the spine is paramount in daily routine. We use the 3 Tesla MAGNETOM Verio system, offer-

ing several advantages for patient comfort and radiological requirements. The advantages of 3 Tesla especially for orthopedic imaging are well known: increase in signal-to-noise ratio (SNR) and less prominent effect of B₁ inhomogeneity on image quality results in clearly improved image quality and/or faster scan times. Visualizing the whole spine in a single examination requires

relatively fast protocols, facilitated by the short acquisition times. The relatively wide 70 cm open-bore of the 3 Tesla MAGNETOM Verio system enables a very flexible positioning of patients, being crucial for those suffering from hemi- or paraplegia, scoliosis, contractions and/or obesity (Fig. 1). 3D sequences like *syngo* SPACE (Sampling Perfection with Application



optimized Contrasts using different flip angle Evolution) (Figs. 2 and 3) or CISS (Constructive Interference in Steady State (Fig. 4) allow for depiction of delicate anatomic structures and reconstruction in all directions. A high percentage of our patients underwent surgery with spinal fusion. As orthopedic hardware causes metal-related artifacts in MRI, adjacent structures may be difficult to evaluate. Thus special pulse sequences that are insensitive, or at least less sensitive to susceptibility changes are important in these cases. In our experience, the use of *syngo* WARP* WIP-package reduced susceptibility artifacts in the presence of orthopedic hardware (Fig. 5). In this article we report on our experience in spine imaging using 3D sequences, and demonstrated reduction of metal-related susceptibility by using the *syngo* WARP* WIP-package.

3D-sequences

3D-sequences like *syngo* SPACE (Figs. 2 and 3) or CISS (Fig. 4) allow for 3-dimensional reconstruction with high resolution in every direction and curved reconstructions. We find the later especially

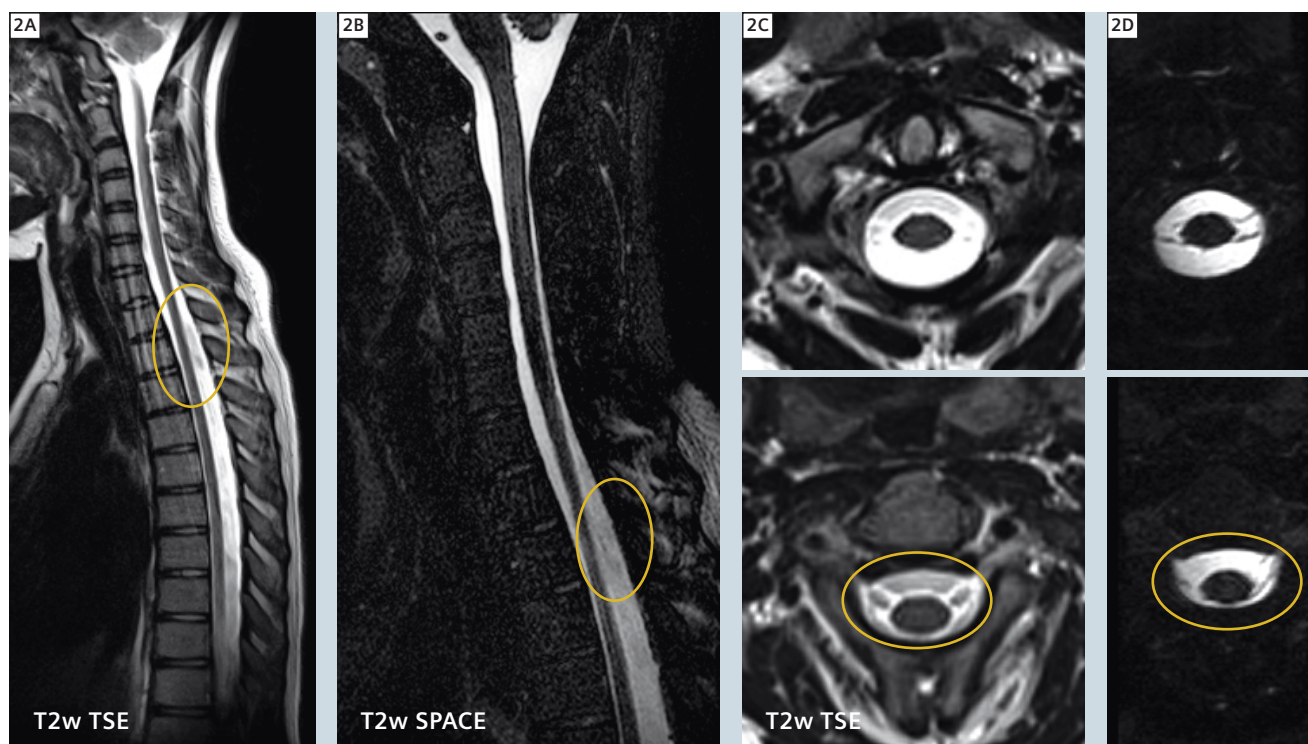
helpful in cases of severe scoliosis to fully assess the spinal cord for cleft formations and tethering, because the myelon can be 'flattened out' as shown in the example of figure 3. The SPACE-sequence is based on, but faster than turbo spin echo and acquires more echoes after excitation. *syngo* SPACE helps reduce SAR (Specific Absorption Rate). Compared to turbo spin echo (TSE) the soft tissue contrast of SPACE is less sensitive, and SPACE is more vulnerable to susceptibility artifacts.

The *syngo* SPACE sequence is, however, less vulnerable to pulsation artifacts than a T2-weighted TSE (Fig. 2). Pulsation artifacts especially occur in the cervical subarachnoid space due to CSF motion. Even delicate anatomical structures like the ventral and dorsal nerve root can be delineated by the *syngo* SPACE- and CISS sequence (Figs. 2 and 4).

Reduction of susceptibility artifacts

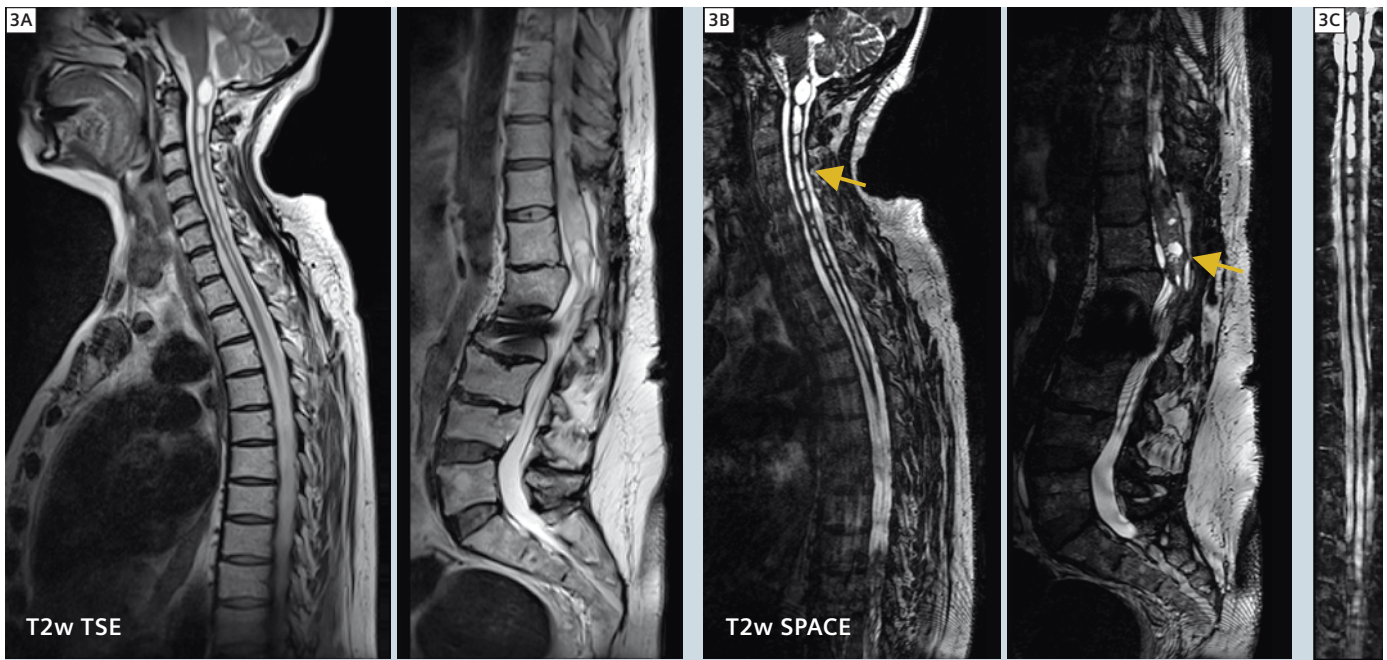
In the presence of metallic implants, for instance after spinal fusion surgery, adjacent structures may not be assessable due to metal-related artifacts. The

extent of the artifacts is determined by several factors, such as size and composition of the implant, orientation of the implant within the main magnetic field, the strength of the magnetic field, the type and parameters of the pulse sequence, and other imaging parameters like echo train length, slice thickness, and voxel size. The metallic composition of the implant has a major influence on the extent of the susceptibility artifact, with e.g. non-ferromagnetic titanium alloy producing significantly less artifacts than stainless steel. Of course, the size of the implant affects the extent of the artifacts, with small implants producing fewer artifacts than large ones. The position of the patient and thus of the implant within the main magnetic field (B_0) should be considered as the long axis of the implant and the direction of the main magnetic field should be parallel. The choice of an adequate pulse sequence is important. Instead of gradient echo (GRE) sequences, spin echo (SE) sequences should be used. The 180° refocusing pulse applied in SE sequences corrects for large magnetic field inhomogene-



2 Pulsation artifacts: T2w TSE vs. T2w *syngo* SPACE.

*510(k) pending. Not for sale in the U.S.



3 Posttraumatic syringomyelia: T2w TSE vs. T2w syngo SPACE.

ities. Higher magnetic field strengths produce larger susceptibility artifacts. But with consequently higher gradient pulses used in high-field MRI, the increased distortion effects of higher main magnetic fields can be reduced. Field-of-view (FOV), image matrix, and section thickness determine the voxel size. Small voxel sizes increase the spatial resolution. Thus using a small FOV, a high resolution matrix, thin sections, and high gradient strengths reduce susceptibility artifacts.

Case 1

For an MRI examination of patients with severe scoliosis, a flexible positioning is mandatory, facilitated by the great 70 cm bore of the MAGNETOM Verio scanner. In Figure 1, radiographic (1A), T2-weighted (1B, C) and T1-weighted images (1D) of a 51-year-old man with severe scoliosis are shown.

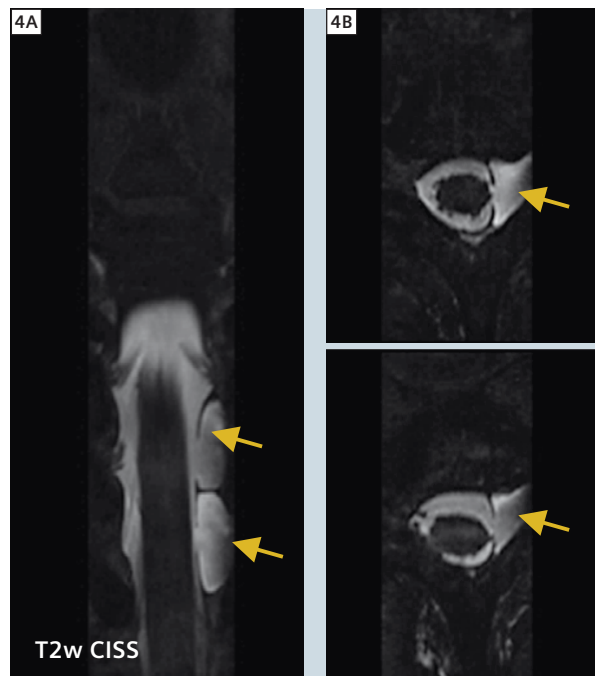
Case 2

17-year-old woman with unspecific non-radicular pain of the middle thoracic spine for 3 years. MRI did not reveal any pathologic finding. Compared to TSE sequences, syngo SPACE produces lesser pulsation artifacts in the subarachnoid space, and allows for a more defined delineation of delicate structures like the

ventral and dorsal nerve roots. In Figure 2 the pulsation artifacts in the subarachnoid space using a T2-weighted TSE (2A) and a syngo SPACE sequence (2B) are compared. For delineation of nerve roots, a T2-weighted TSE sequence (2C) is opposed to a syngo SPACE sequence (2D).

Case 3

51-year-old woman, who had a traumatic fracture of the second lumbar vertebral body 25 years ago. Since the accident, she suffered from paraplegia, but in the meantime neurologic status further deteriorated resulting in tetraplegia.



4 Avulsion of nerve roots and avulsion pseudo-meningoceles: Multiplanar reconstruction of T2w CISS.

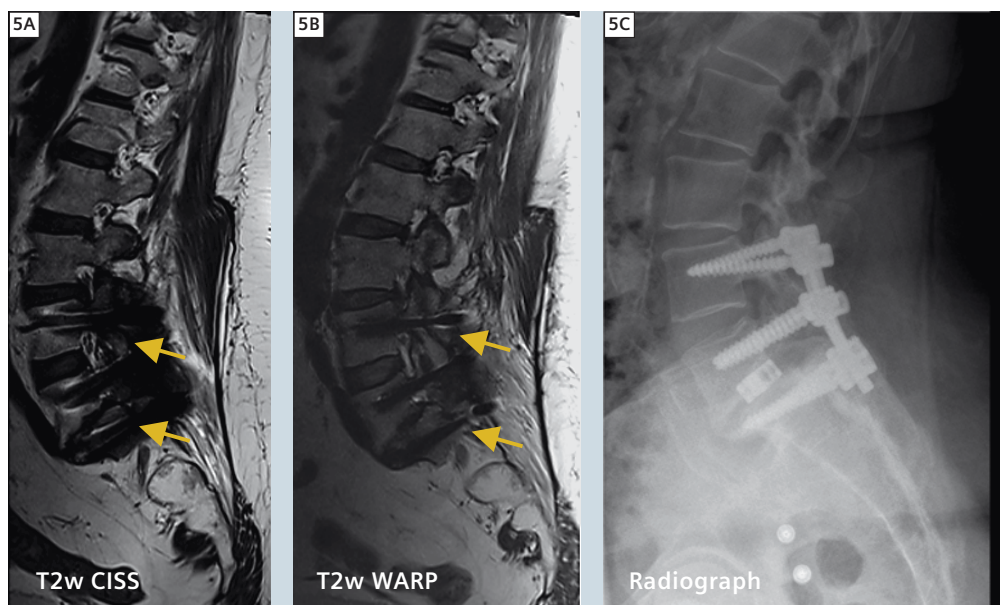
Image 3 shows the posttraumatic syringomyelia ascending from the medullary conus to the medulla oblongata causative for the patient's increasing symptoms. Contrary to T2-weighted TSE (3A), the arachnopathic adhesions (arrows) are clearly visible using a *syngo* SPACE sequence (3B). Another advantage of 3D-sequence is the potential of multiplanar and curved reconstructions (3C).

Case 4

24-year-old man with a posttraumatic plegia of his left arm. The MRI performed 3 months after the accident demonstrates avulsion of the nerve roots C8 and T1 and consecutive avulsion pseudo-meningoceles (arrows). In Figure 4, coronal (4A) and transversal (4B) reconstruction of the CISS sequence are shown.

Case 5

55-year-old female suffering from pseudoradicular pain of both legs. The patient underwent surgical implantation of a cage in the lumbosacral transition and spinal fusion from the fourth lumbar to the first sacral vertebral body. As MRI is compromised in the presence of metallic hardware due to metal-related artifacts, we observed a reduction of metal-related susceptibility artifacts when using the *syngo* WARP* WIP-package. The *syngo* WARP* WIP-package provides a set of modified sequences, which are designed to reduce imaging artifacts when scanning patients with metal implants. Main source of artifacts are susceptibility induced changes of the main magnetic field B_0 near metallic objects, leading to severe geometric distortions, contrast changes, signal pile-ups, as well as signal voids. In Figure 5, the potential of the *syngo* WARP



5 Metal implant imaging using *syngo* WARP*.

sequences (5B) in reducing metal-related susceptibility artifacts is shown in comparison to a standard TSE sequence (5A).

Acknowledgements

The excellent cooperation regarding brain and spine imaging with Prof. Dr. Stefan Hähnel from the Department of Neuroradiology at the University Hospital Heidelberg (Head: Prof. Dr. Martin Bendszus) is gratefully acknowledged.

Disclaimer:

MR imaging of patients with metallic implants brings specific risks. However, certain implants are approved by the governing regulatory bodies to be MR conditionally safe. For such implants, the previously mentioned warning may not be applicable. Please contact the implant manufacturer for the specific conditional information. The conditions for MR safety are the responsibility of the implant manufacturer, not of Siemens.

*510(k) pending. Not for sale in the U.S. and in other countries.

References

- 1 Gasparotti R, Ferraresi S, Pinelli L, Crispino M, Pavia M, Bonetti M, Garozzo D, Manara O, Chiesa A. Three-dimensional MR myelography of traumatic injuries of the brachial plexus. *AJNR Am J Neuroradiol.* 1997, 18(9):1733-42.
- 2 Lee MJ, Kim S, Lee SA, Song HT, Huh YM, Kim DH, Han SH, Suh JS: Overcoming artifacts from metallic orthopedic implants at high-field-strength MR imaging and multi-detector CT. *Radiographics* 2007, 27:791-803.
- 3 Lichy MP, Wietek BM, Mugler JP 3rd, Horger W, Menzel MI, Anastasiadis A, Siegmann K, Niemeyer T, Königsrainer A, Kiefer B, Schick F, Claussen CD, Schlemmer HP. Magnetic resonance imaging of the body trunk using a single-slab, 3-dimensional, T2-weighted turbo-spin-echo sequence with high sampling efficiency (SPACE) for high spatial resolution imaging: initial clinical experiences. *Invest Radiol.* 2005, 40(12):754-60.



Marc-André Weber, M.D., M.Sc.



Marcel Wolf, M.D.

Contact

Marc-André Weber, M.D., M.Sc.
Professor of Radiology
Heidelberg University
Diagnostic and Interventional Radiology
Im Neuenheimer Feld 110
69120 Heidelberg
Germany
MarcAndre.Weber@med.uni-heidelberg.de

Marcel Wolf, M.D.
Radiology Resident
Heidelberg University
Department of Neuroradiology
Im Neuenheimer Feld 400
69120 Heidelberg
Germany
Marcel.Wolf@med.uni-heidelberg.de

syngo WARP – Metal Artifact Reduction Techniques in Magnetic Resonance Imaging

Theresa Bachschmidt; Ferdinand Lipps, Ph.D.; Mathias Nittka, Ph.D.

Siemens Healthcare, Erlangen, Germany

The term WARP summarizes methods to minimize the impact of metal implants on image quality.

Challenges

Metals have highly different susceptibility constants compared to tissue. When metallic implants are present in the MRI examination, the static magnetic field in their vicinity is manipulated by strong local off-resonances induced by the implants. The degree of field distortions depends on the shape, the location and the material properties of the metal implant.

Distortions of the static magnetic field result in:

- Intra-voxel dephasing: Signal voids are visible as black areas in the image.

- Changes in tissue contrast: Failure of fat suppression and saturation bands.
- In-plane distortion: The local field offset leads to a shift of image pixels in the readout encoding (i.e. frequency encoding) direction.
- Through-plane distortion: The local field offset leads to curved and frayed slices instead of the expected flat image plane (Fig. 1).

Since both in-plane and through-plane distortions shift image pixels away from their real positions, image geometry appears to be distorted. In both cases, regions with severe field changes will lead to signal voids visible as black spots and signal pileups visible as bright spots. However, it makes sense to distinguish between in- and through-plane artifacts, since different techniques are needed to reduce these types of artifacts.

Approaches to avoid metal artifacts

Imaging in the presence of metal implants is mostly based on (turbo) spin echo sequences due to its high immunity with regard to signal dephasing induced by local off-resonances. In the following, three approaches to reduce metal artifacts are presented, that have shown promising results in clinical settings. Figure 2 depicts their effects *in-vivo* compared to imaging with standard protocols. Although other techniques exist, they are often constrained by excessive scan times or special hardware requirements.

High bandwidth sequence parameters

Basic acquisition parameters are adjusted to what is called high bandwidth (BW) parameters to make the MR sequence less sensitive to field distortions.

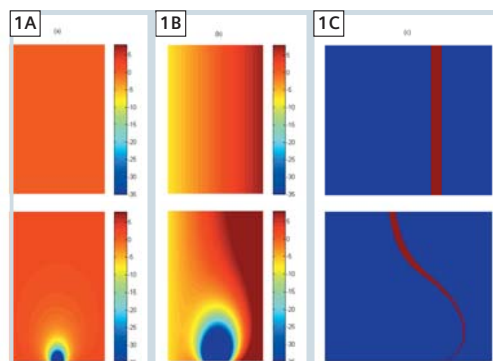
What is done:

The bandwidth of both the excitation pulse and the signal readout is increased.

What it effects:

A high bandwidth sequences reduces the through-plane distortion of the slice profile. This implies less severe variations of the apparent slice thickness, i.e. the amount of signal voids and pileups is reduced compared to standard protocols with a low bandwidth.

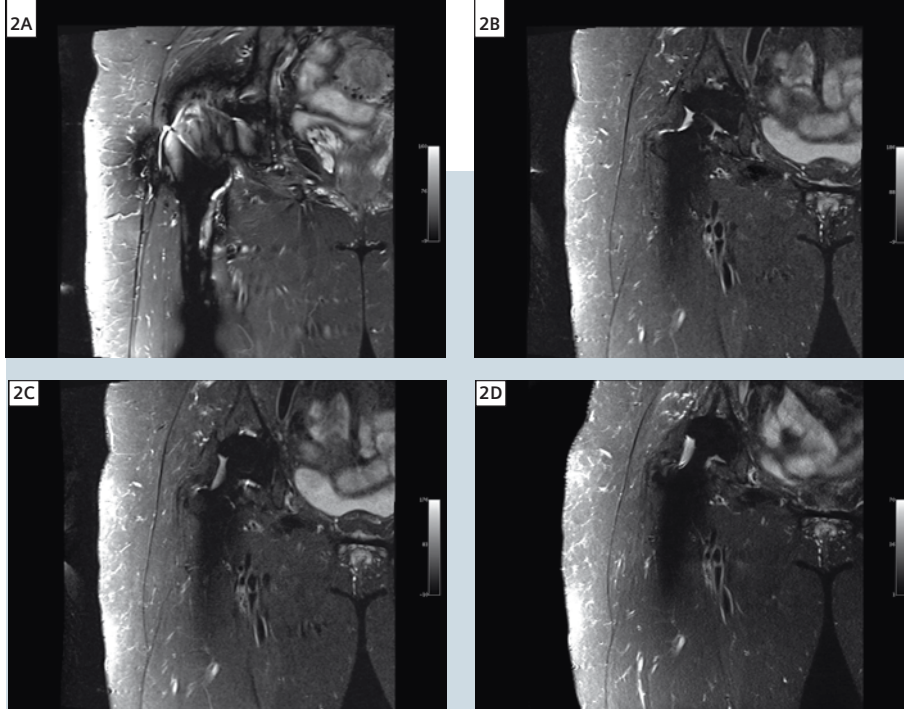
A high signal readout bandwidth



1 The upper row visualizes the ideal case of slice selection, while the lower row displays the effects on the slice selection by a distorted background field: (1A) B_0 field map in slice select direction, (1B) B_0 field map in direction of slice encoding with superimposed magnetic gradient field for excitation, and (1C) position of the excited slice.

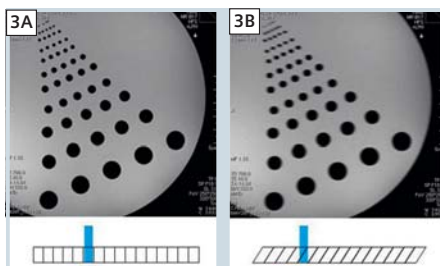
Implant imaging at 3T:

There is a significant difference between MR imaging at 3T and 1.5T. In contrast to common clinical imaging, higher field strength does not necessarily imply better image quality for patients with metal implants. Apart from increased safety concerns, the level of image distortions scales with the strength of the static field, i.e. the level of artifacts is higher at 3T than at 1.5T. Additionally, the efficiency of artifact reduction techniques is reduced by the increased SAR constraints at 3T.



2 Image comparison: (2A) standard protocol, (2B) high BW, (2C) VAT* and (2D) SEMAC**.

addresses in-plane distortions: Intra-voxel signal dephasing and geometrical shift in the readout encoding direction are reduced. Consequently, the image has less signal voids and less pileup artifacts related to in-plane distortions. The main drawback of high bandwidth protocols is reduced signal-to-noise ratio (SNR) and increased specific absorption rate (SAR). High bandwidth sequences are very demanding in terms of scanner hardware, mainly gradient and RF power performance. Ultimately, the RF power applied by high bandwidth RF pulses is limited by the patient (SAR). Hence, the RF pulse bandwidth is more affected by these restrictions and in-plane artifact reduction is more efficient.



3 VAT* blurring caused by the shearing of the slice: (3A) Image without VAT: the signal of a vertical structure (vertical blue line) is well localized in a pixel (horizontal blue line); (3B) blurred image with VAT: The vertical structure appears smeared over multiple pixels.

VAT* (View Angle Tilting)

VAT is a modified sequence acquisition scheme that is able to compensate for in-plane distortions. It can be easily implemented into a turbo spin echo (TSE) sequence.

What is done:

Simultaneously with the conventional readout gradient, an additional readout gradient is applied along the slice selective direction. Its amplitude equals the one applied during the excitation RF pulse.

What it means:

The additional gradient causes shearing of the imaged pixels, as if the slice were viewed at an angle. From a different point-of-view, the VAT gradient brings back all excited spins within the RF bandwidth and local off-resonances are cancelled exactly. Hence, the pixel shift in readout direction is fully compensated.

What it effects:

In-plane distortions, more precisely those along the readout direction, are corrected. However, VAT may cause blurring of the image caused by two separate effects. One cause is the geometric slice shear, causing edges to be smeared out along the shearing direction (Fig. 3). This effect can be reduced by using thin slices and a high resolution. The second source of blurring is a low-pass filter

superimposed on the signal readout by the additional VAT gradient. This can be reduced by a short readout duration.

SEMAC** (Slice Encoding for Metal Artifact Correction)

SEMAC is based on a 2D TSE sequence. An additional encoding dimension is introduced to enable the correction of through-plane distortions.

What is done:

Each slice is additionally phase-encoded in the third dimension, very similar to a 3D scan. This provides information on how the slice profile is distorted, such that signal shifted perpendicular to the image plane can be corrected by post-processing during image reconstruction.

What it effects:

Gross through-plane artifacts, which usually cannot be handled efficiently by high bandwidth parameters, can be corrected. In particular, imaging of large metal structures like full knee or hip replacements is being studied. This method is very time-consuming. Despite the use of advanced undersampling techniques, such as partial Fourier and parallel imaging, it is challenging to achieve scan times acceptable for routine examinations.

**510(k) pending. Not for sale in the U.S. and in other countries.*

***WIP: Work in progress. SEMAC is currently under development; is not for sale in the U.S. Its future availability cannot be guaranteed.*

Disclaimer:

MR imaging of patients with metallic implants brings specific risks. However, certain implants are approved by the governing regulatory bodies to be MR conditionally safe. For such implants, the previously mentioned warning may not be applicable. Please contact the implant manufacturer for the specific conditional information. The conditions for MR safety are the responsibility of the implant manufacturer, not of Siemens.

Contact

Mathias Nittka, Ph.D.
Siemens Healthcare
MR PI ORTH
Postbox 32 60
91050 Erlangen
Germany
Phone: +49 (9131) 84-4460
mathias.nittka@siemens.com

MRI Assessment of Articular Cartilage Repair

Darshana Sanghvi, M.D., D.N.B.

Kokilaben Dhirubhai Ambani Hospital, Mumbai, India

Introduction

Articular cartilage lesions in the young population predispose to the development of precocious osteoarthritis. Poor healing of cartilage damaged by trauma or degeneration has been ascribed to avascularity. Cartilage lesions are associated with significant morbidity, including lifestyle restrictions, especially in individuals engaged in sports. The past decade has seen the evolution of a number of sophisticated surgical repair procedures for the treatment of isolated, focal traumatic or degenerative cartilage lesions. The evolution of these surgeries

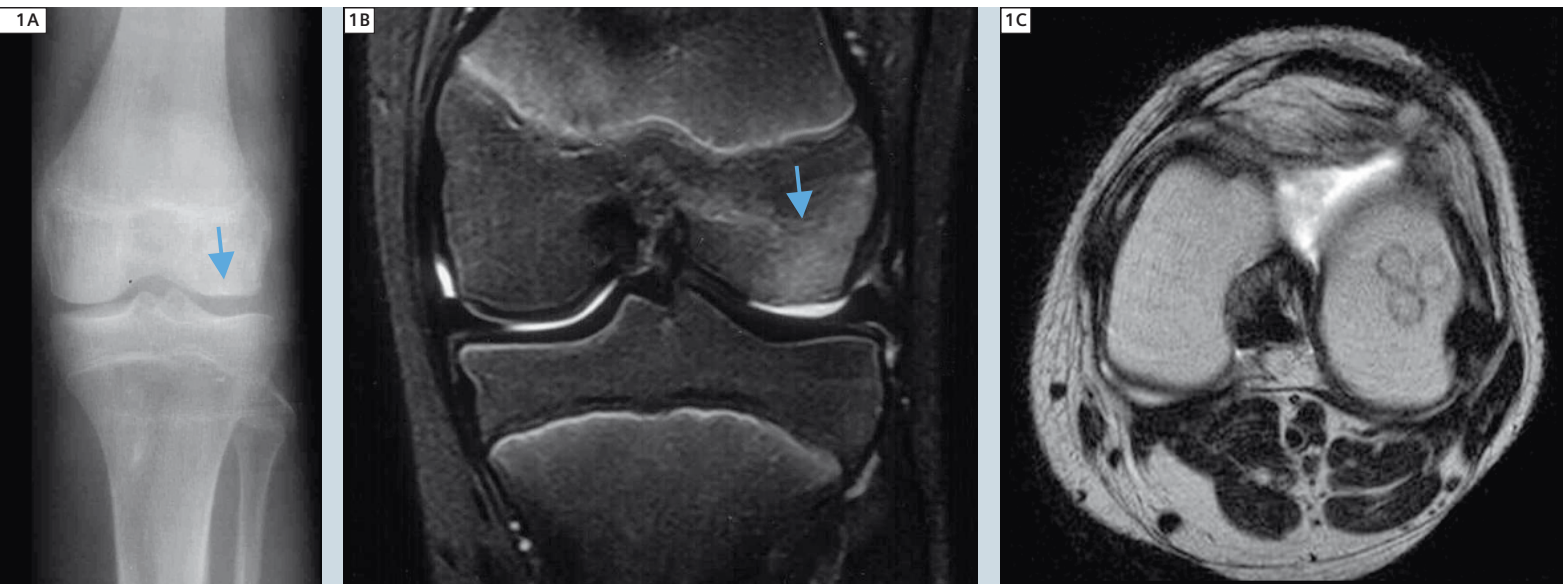
has created the need for accurate, non-invasive assessment of the repair tissue. The current generation of MR magnets and dedicated pulse sequences allow for structural and biochemical assessment of the repair tissue. This information is useful for prognostication and for comparing the effectiveness of various types of surgical procedures.

Articular cartilage repair procedures

The bone marrow stimulation surgeries include microfracture technique, drilling and abrasion arthroplasty. The goal of all of these procedures is to expose the pluripotent stem cells in the subchon-

dral bone which then migrate to the site of the chondral lesion. A fibrin clot is formed at the site of the microfractures or drilling, which serves as a scaffold for the formation of fibro cartilaginous repair tissue.

Osteochondral autologous transfer (OATS) technique or mosaicplasty involves the removal of osteochondral plugs from the non-weight-bearing part of the joint, often the trochlea. The plugs are then transferred to the chondral lesion along the weight-bearing part of the articular surface. It thus transplants autologous hyaline tissue to



the articular lesion. The osteochondral plugs should be perpendicular to the articular chondral defect.

Autologous chondrocyte implantation (ACI) technique involves transplanting chondrocytes harvested and replicated from a non-weight-bearing part of the articular surface into the lesion at the weight-bearing site. In the initial part of this two stage procedure, the chondrocytes are harvested and cultured in vitro for approximately five weeks. In the second part of the procedure, the harvested chondrocytes are injected into the articular chondral lesion and covered with a periosteal flap.

MRI assessment

The aim of imaging is to examine the success of surgery and assess the quality of the repair tissue.

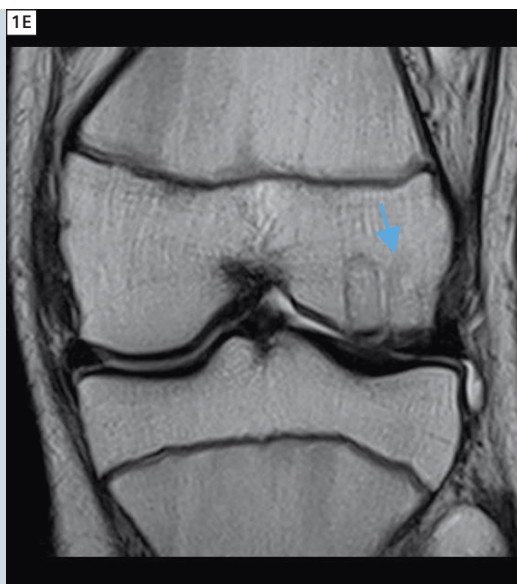
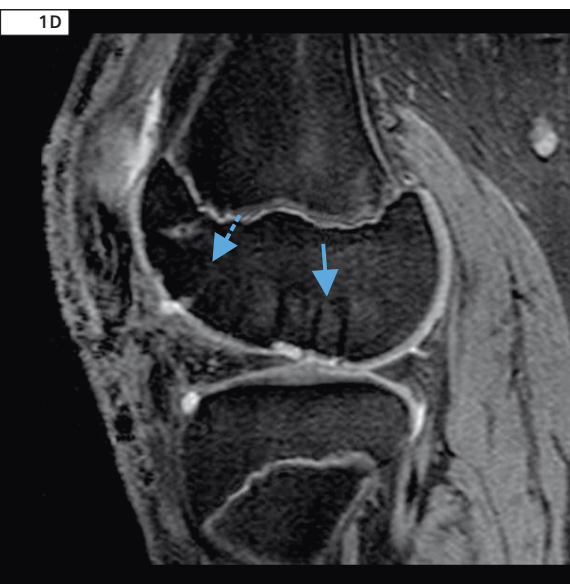
In a successful mosaicplasty procedure, the cartilage caps of plugs should be flushed with the adjacent native cartilage. The aim is to have the plugs placed perpendicular to the articular surface. MRI after the mosaicplasty procedure involves assessment of graft incorporation, graft congruity and examination of the repair tissue characteristics. The donor site may also be assessed. In the first four weeks after the procedure, the

Table 1: The 8 parameters assessed by the MOCART scoring system.

1	Degree of defect repair and defect filling
2	Integration with border zone
3	Quality of repair tissue surface
4	Structure of repair tissue
5	Signal characteristics of repair tissue
6	Status of subchondral lamina
7	Integrity of subchondral bone
8	Presence of complications (adhesions and effusion)

plugs and surrounding marrow have altered marrow signal. By 12 months, the plugs and the surrounding marrow return to normal fatty marrow signal (Fig. 1). Persistent edema like subchondral bone marrow signal and cyst formation indicates graft failure and poor incorporation.

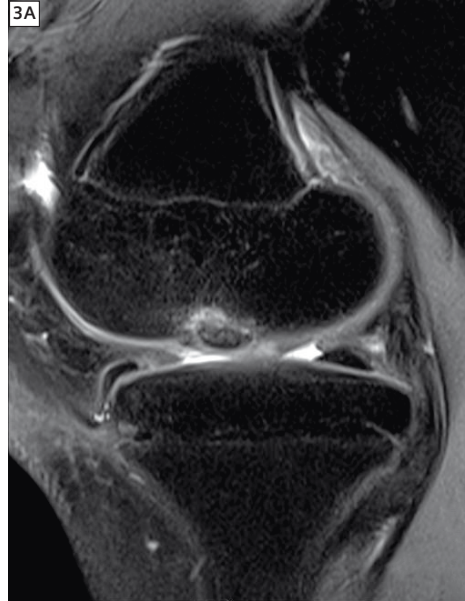
The MOCART (MR observations of cartilage repair tissue) system (Table 1) is an efficient scoring method for consistent reporting of the radiological features of autologous chondrocyte implants and has impressive interobserver reproducibility. MOCART scoring may be useful for objective follow-up of articular carti-



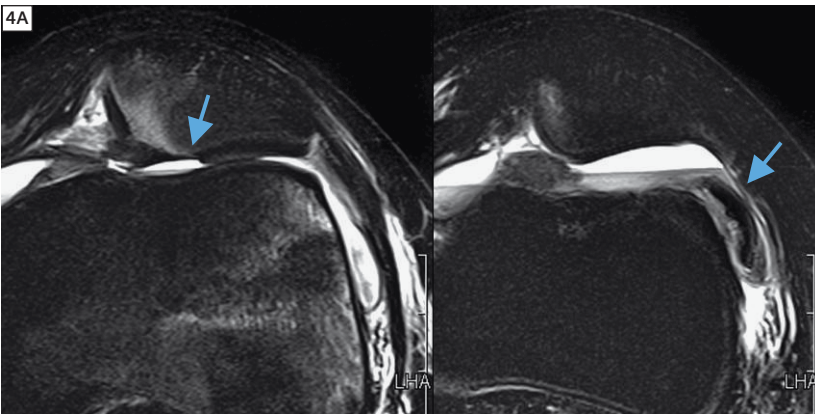
1 An 18-year-old was involved in a motorcycle accident. **(1A)** Frontal knee radiograph shows flattening of the articular surface of the lateral femoral condyle (arrow). **(1B)** Corresponding coronal MR STIR image shows a traumatic osteochondral lesion of the lateral femoral condyle. **(1C)** The biopsy site from the non-weight-bearing part of the lateral femoral condyle is seen in the trans-axial image. **(1D and 1E)** Sagittal DESS and coronal T2w images show the biopsy site (dotted arrow) from the non-weight-bearing lateral femoral condyle and the site of the graft (solid arrow). There is excellent congruity of the osteochondral plugs with the parent bone. The patient remained symptom free at one year clinical follow up.



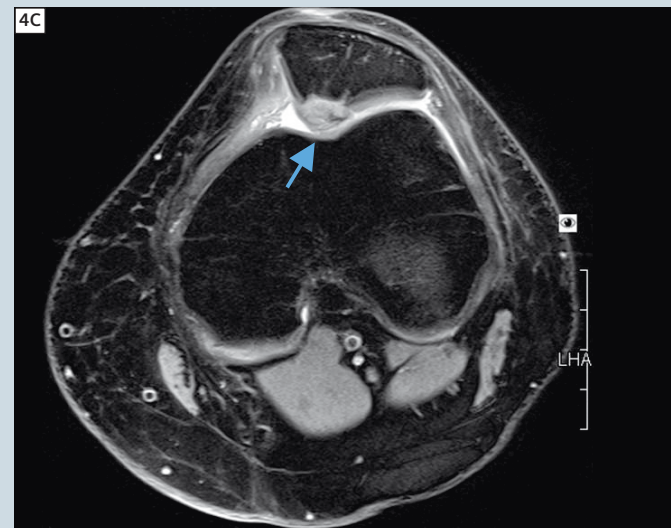
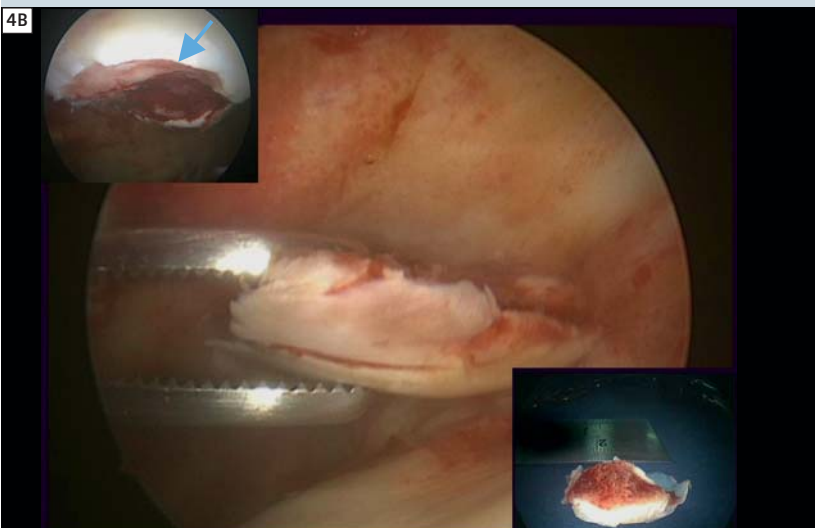
2 Post ACI follow up MRI shows satisfactory fill of the lesion. The articular surface of the graft is smooth. The signal is similar to native cartilage. There is no defect between the graft and parent bone, no subchondral marrow edema, adhesions or effusion.



3 Sagittal PD-weighted images of the knee joint (**3A**) – unstable osteochondritis dissecans of the medial femoral condyle. (**3B**) Post ACI MRI shows adequate fill by the graft (arrow).



4 15-year-old girl with first episode of patellar dislocation. (**4A**) Axial STIR MR images show trochlear dysplasia with marrow contusions at patellar apex and outer aspect of lateral femoral condyle and also a large osteochondral defect at the patellar apex (arrow). The corresponding osteochondral fragment is seen in the lateral patellofemoral recess (arrow). (**4B**) In the first stage of surgery, arthroscopic loose body removal was done with cartilage biopsy. Left knee open ACI (stage 2) was done for the patellar osteochondral defect. (**4C**) Follow up MRI showed graft hypertrophy. The patient had mechanical symptoms after surgery.



lage repair, as it allows prospective multicenter studies in which results of cartilage repair surgeries are compared [1]. An additional advantage over arthroscopy for post operative assessment is the ability of MRI to demonstrate subchondral marrow.

The margins of the repair tissue should be continuous [2] and have equivalent thickness when compared with adjacent native cartilage and the articular surface should be even (Figs. 2, 3).

Adverse events after ACI include graft failure, which is the commonest, followed by delamination, tissue hypertrophy and local infection. Two common complications of the ACI technique are graft hypertrophy and delamination. Graft hypertrophy (Figs. 4, 5) may occur 3 to 7 months after autologous chondrocyte implantation and has been reported as a complication in 10% to 63% of cases [3–5]. Delamination refers to separation of the graft from the parent bone.

It appears as a linear fluid signal undermining the graft. When significant, both delamination and graft hypertrophy may require repeat surgery, either debridement in the case of hypertrophy or repeat ACI in both cases.

Conclusions

Articular cartilage injury is frequent, documented in almost 63% of arthroscopies [6]. It is even more common in conjunction with ACL tears; about 79% of patients with ACL deficient knees have chondral lesions of varying severity [7]. The introduction of novel cartilage repair procedures that transplant hyaline cartilage to the injured area or have the potential to form hyaline-like repair tissue, has lead to an increased requirement for a non-invasive but accurate technique to assess the outcome of such repair surgeries. MR imaging is currently the optimal technique for such assessment [8]. The ability of MR imaging to directly depict subchondral bone and bone marrow represents an advantage over arthroscopy MRI is also accurate for examination of the repair tissue and its interface with parent cartilage and complications of repair surgeries such as graft hypertrophy and delamination.



5 Graft hypertrophy after ACI.

Acknowledgement for arthroscopy images:
Dr. Dinshaw Pardiwala, M.S.,
Consultant Arthroscopy and Sports Medicine,
Kokilaben Dhirubhai Ambani Hospital, Mumbai,
India.

References

- 1 Choi YS, Potter HG, Chun TJ. MR imaging of cartilage repair in the knee and ankle. *Radiographics*. 2008 Jul-Aug;28(4):1043-59. Review.
- 2 Henderson IJ, Tuy B, Connell D, Oakes B, Hettwer WH. Prospective clinical study of autologous chondrocyte implantation and correlation with MRI at three and 12 months. *J Bone Joint Surg Br* 2003; 85(7):1060-1066.
- 3 Peterson L, Minas T, Brittberg M, Nilsson A, Sjogren-Jansson E, Lindahl A. Two- to 9-year outcome after autologous chondrocyte transplantation of the knee. *Clin Orthop Relat Res* 2000;374: 212-234.
- 4 Henderson I, Gui J, Lavigne P. Autologous chondrocyte implantation: natural history of postimplantation periosteal hypertrophy and effects of repair-site debridement on outcome. *Arthroscopy* 2006;22(12):1318-1324.
- 5 Brown WE, Potter HG, Marx RG, Wickiewicz TL, Warren RF. Magnetic resonance imaging appearance of cartilage repair in the knee. *Clin Orthop Relat Res* 2004;422:214-223.
- 6 Curl WW, Krume J, Gordon ES, et al. Cartilage injuries: a review of 31,576 knee arthroscopies. *Arthroscopy* 1997; 13:456-460.
- 7 Noyes FR, Stabler CC. A system for grading articular cartilage lesions at arthroscopy. *Am J Sports Med* 1989; 17:505-513.
- 8 Recht MP, Kramer J. MR imaging of the post-operative knee: a pictorial essay. *Radiographics*. 2002 Jul-Aug;22(4):765-74. Review.



Darshana Sanghvi,
M.D., D.N.B.

Contact

Darshana Sanghvi, M.D., D.N.B.
Kokilaben Dhirubhai Ambani Hospital
Mumbai
India
sanghvidarshana@gmail.com

Case Series Sports and Trauma Imaging

Eric K. Fitzcharles, M.D.; Charles P. Ho, Ph.D., M.D.

Steadman Philippon Research Institute, Vail, CO, USA

Case 1: Chondral delamination in the knee

Patient history

Patient is a professional basketball player, 13 months after left knee medial femoral condyle microfracture, and approximately 5 months after left knee hardware removal from prior patellar fracture. He reports no symptoms in either knee. There is a history of progressive cartilage degeneration in the right knee.

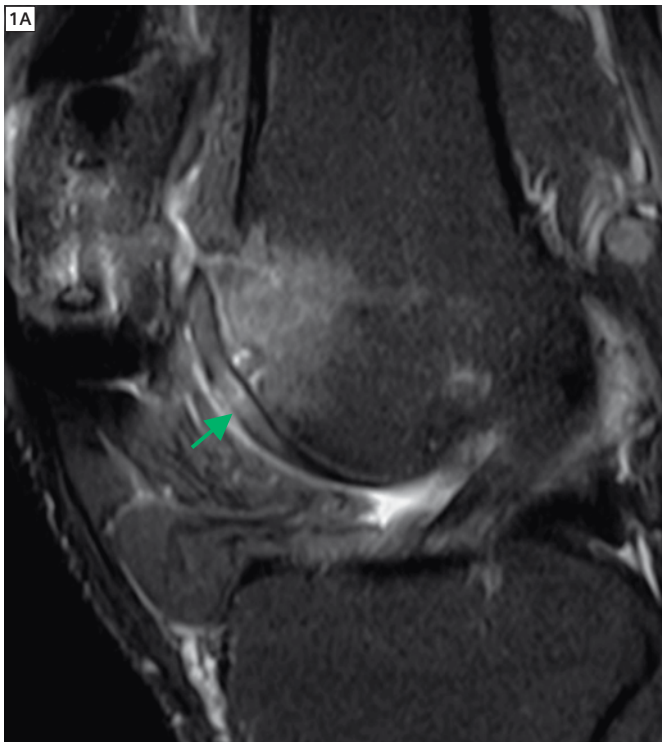
Physical examination

Examination of the left knee reveals a mild joint effusion. There is good patellar mobility and minimal crepitus under the patella. Range of motion is from full extension to 135 degrees. Negative tests include Lachman, McMurray, anterior drawer, posterior drawer and pivot-shift. The knee is stable to varus and valgus stresses. He has no focal

point tenderness. There is normal patellar tracking. There is mild atrophied quadriceps on the left as compared to the right.

Imaging findings

X-rays demonstrate no changes in his joint space and there is no acute fracture identified.



1 (1A) Initial study: Sagittal fat suppressed proton density-weighted image showing a new area of chondral thinning and fissuring with irregularity, areas to bone, delamination, and flap, with marked underlying osseous edema (arrow). (1B) 43 days later: Sagittal fat suppressed proton density-weighted image, showing a more focal sharply marginated 1.0 cm full thickness chondral defect and with areas of undermining and possible flap at the inferior margin. This appears more severe than on the prior exam.

MRI initial study:

(Figs. 1A, 2A and Table 1)

1. Trochlea: In the central and medial aspects, there is an area of chondral thinning and fissuring with irregularity, areas to bone, delamination, and flap, with marked underlying osseous edema. This is new since the prior outside examination.
2. Medial femoral condyle: Slight interval progression of irregularity, increased signal, and edema in the vicinity of the posterior weightbearing surface, at the microfracture site, now with a new 1.1 cm area of delamination immediately posterosuperior to the microfracture site.
3. Patellar chondral thinning and fissuring with osseous ridging, areas to bone, and edema, most likely showing interval worsening since the prior examination.

Assessment

Professional basketball player, 13 months status post left knee arthroscopy with chondroplasty, debridement and medial femoral condyle microfracture. He is doing well clinically and has no symptoms, but there is a new area of cartilage thinning and bone edema just posterior and superior to his medial femoral condyle microfracture.

Plan after first MRI: Since he is asymptomatic, the decision is made to continue physical therapy, and start gentle agility drills. Repeat MRI of the left knee is planned in 2–3 weeks to determine the stability of the findings.

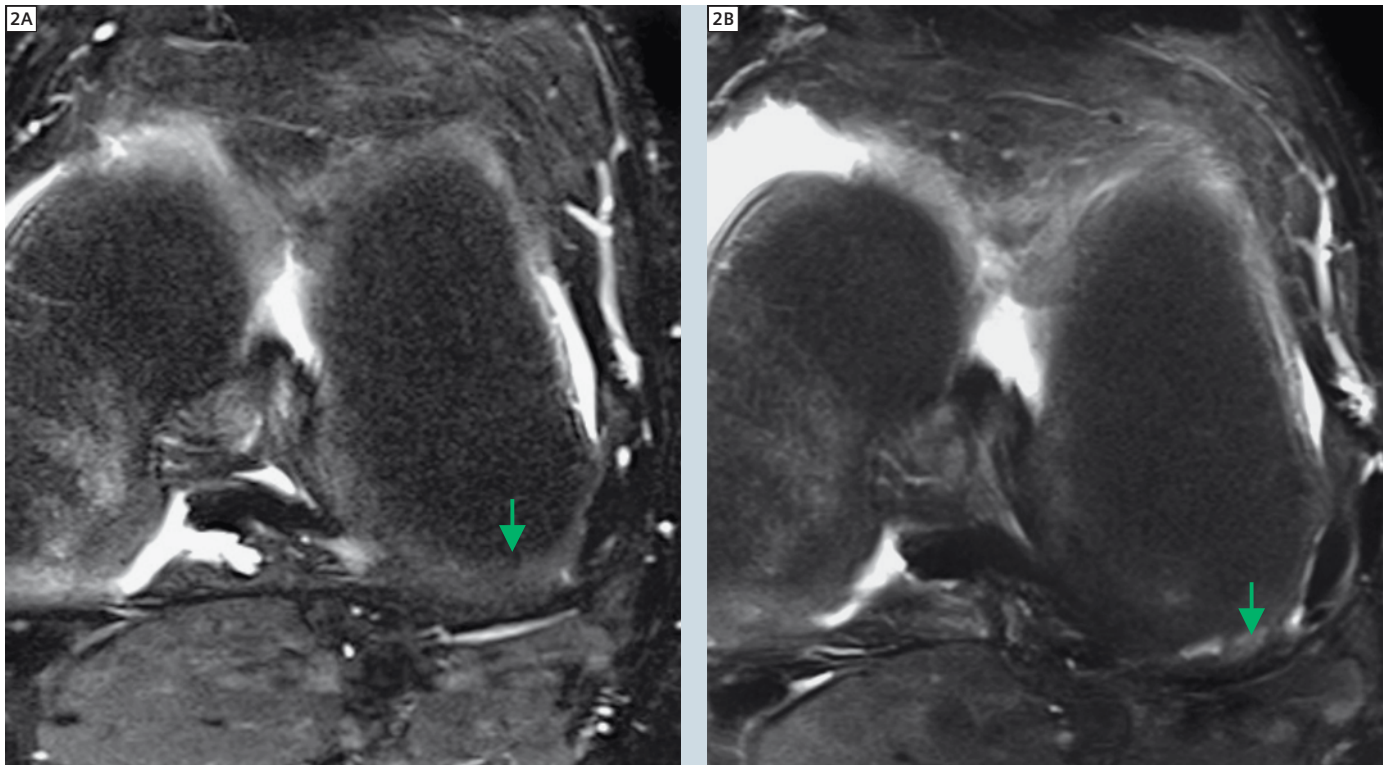
MRI 43 days later:

(Figs. 1B, 2B, 3, and Table 1)

1. Trochlea: 1.2 × 2.3 cm area of chondral thinning and fissuring with areas to bone, and underlying osseous edema, with more focal sharply marginated 1.0 cm full thickness chondral defect

and with areas of undermining and possible flaps. This appears more severe.

2. Lateral femoral condyle: New 5 mm area of heterogenous increased signal along the bone cartilage interface of the posterior weightbearing surface, possibly representing an area of softening and blistering, and/or undermining and delamination.
3. Medial femoral condyle: Little or no change involving the 1.1 cm area of high signal chondral undermining and delamination immediately posterosuperior to the microfracture site. There is irregularity and increased signal involving the microfracture site, possibly with slightly more severe increased signal and possible slight osseous pitting along the bone-cartilage interface of the microfracture site.
4. Patellar chondral thinning and fissuring with osseous ridging and areas to bone, as well as edema, slightly more severe than on the prior examination.



2 (2A) Initial Study: Axial fat suppressed proton density-weighted image showing no chondral defect (arrow) in the lateral femoral condyle. (2B) 43 days later: Axial fat suppressed proton density-weighted image, showing a new 5 mm area of heterogenous increased signal (arrow) along the bone cartilage interface of the posterior weight-bearing surface of the lateral femoral condyle, possibly representing an area of softening and blistering, and/or undermining and delamination.

Surgical findings after second MRI:

1. Approximately 1 × 1 cm medial femoral condyle chondral defect and delamination posterior to the previously microfractured defect. The microfractured area of the medial femoral condyle previously looked to be in very good condition.
2. Left knee trochlear defect, measuring approximately 1.5 cm × 5 mm.

Chondroplasty and microfracture performed: Unstable cartilage of the medial femoral condyle defect was debrided down to smooth, stable rims, with exposed subchondral bone. Similar debridement was performed about the trochlear defect. Microfracture was then performed at both sites.

Discussion

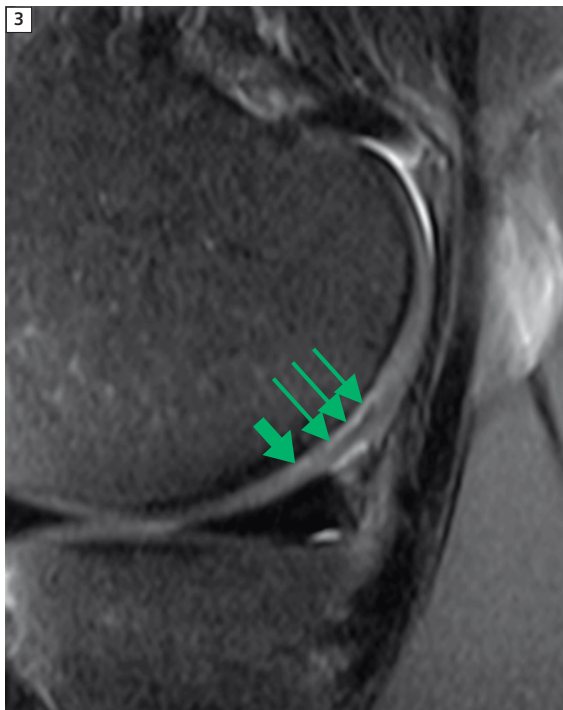
This case is a good example of progressive chondral degeneration and delamination in a professional athlete, with progression over time. This had a significant impact on the performance and career trajectory of this athlete. Although this documents the patient's left knee, there was similarly progressive chondral delamination disease in the right knee as well. Articular cartilage damage within joints

may result from chronic wear or acute injury. Chondral delamination refers to separation of the articular cartilage from the underlying cortical bone, parallel to the joint surface, and due to shear stress at the junction of the noncalcified and calcified cartilage. This process is often acute or acute-on-chronic. The overlying cartilage layer may be intact initially, but will often progress and develop fissuring and fragmentation, creating full thickness chondral defects. Untreated delaminated chondral flaps will tend to enlarge over time.

The degree of pain is often related to the presence and severity of subchondral bone edema. There may also be locking, catching, and grinding.

The prevalence and incidence of chondral delamination in the knee is not known. There is an association with other types of chondral degeneration including defects, fissuring, and thinning [1]. There is also an association with meniscal tears [2]. In the patellofemoral compartment, there may also be an association with patellar dislocation injuries. Plain film examination is not sensitive for chondral delamination. MRI does provide visualization of articular cartilage, and more recent high field tech-

niques may be more sensitive for chondral lesions due to their higher resolution and smaller field-of-view. Although a 1996 study demonstrated poor sensitivity with MRI [3], this has improved with better exam techniques and increased radiologist knowledge and experience. Images show linear T2-weighted signal near the intensity of joint fluid at the interface of the articular cartilage and subchondral bone. One study revealed higher interobserver agreement among radiologists than among orthopedists in the evaluation of chondral knee lesions by MRI [4]. The mainstay of treatment is surgical debridement, followed by cartilage restorative procedure. The restorative procedure can take different forms, depending on the specifics of the individual lesion, and this is beyond the scope of discussion of this report. Techniques include microfracture, osteochondral allograft (OATS), osteochondral allograft, and autologous cartilage implantation (ACI). A study reporting 19 consecutive patients with acetabular chondral delamination showed excellent results at one year after reattachment with fibrin adhesive [5], however similarly successful results have not been reported in the knee. Future techniques may include newer generation ACI, juvenile allograft cartilage, stem cells and scaffolds. Untreated chondral delamination carries a poor prognosis [3]. Delaminated chondral flaps will often enlarge over time due to ongoing stress at the bone-cartilage interface.



3 Sagittal fat suppressed proton density-weighted image showing increased signal, undermining and possible delamination (long arrows) immediately postero-superior to the microfracture site. This is new since a prior outside exam. There is irregularity and increased signal involving the microfracture site (wide arrow).

References

- 1 Kendell SD, et al. MRI Appearance of Chondral Delamination Injuries of the Knee. *AJR* May 2005;184(5):1486-1489.
- 2 Hopkinson WJ, Mitchell WA, Curl WW. Chondral fractures of the knee: cause for confusion. *Am J Sports Med* 1985;13:309-312.
- 3 Levy AS, et al. Chondral delamination of the knee in soccer players. *Am J Sports Med* 1996;24:634-639.
- 4 Cavalli F, et al. Interobserver Reliability among Radiologists and Orthopaedists in Evaluation of Chondral Lesions of the Knee by MRI. *Advances in Orthopedics* 2011;Article ID 743742, 4 pages.
- 5 Tzaveas AP, Villar RN. Arthroscopic repair of acetabular chondral delamination with fibrin adhesive. *Hip Int* 2010;20(1):115-119.

Table 1: MRI technique.

Weighting and planes	Field-of-view	TR	TE	Sequence	Slice thickness	GAP	Matrix size
T2-weighted axial	115	5320	100	Turbo Spin Echo	3.2 mm	0.3 mm	512 × 512
Proton Density-weighted axial fat suppressed	150	1200	45	Turbo Spin Echo fat suppressed	2 mm	0.0 mm	256 × 256
Proton Density-weighted sagittal	140	2570	41	Turbo Spin Echo	2 mm	0.0 mm	256 × 256
Proton Density-weighted sagittal fat suppressed	150	1200	45	Turbo Spin Echo fat suppressed	2 mm	0.0 mm	256 × 256
Proton Density-weighted coronal	120	2770	31	Turbo Spin Echo	3 mm	0.3 mm	640 × 640
Proton Density-weighted coronal fat suppressed	160	6040	41	Turbo Spin Echo fat suppressed	2 mm	0.3 mm	512 × 512

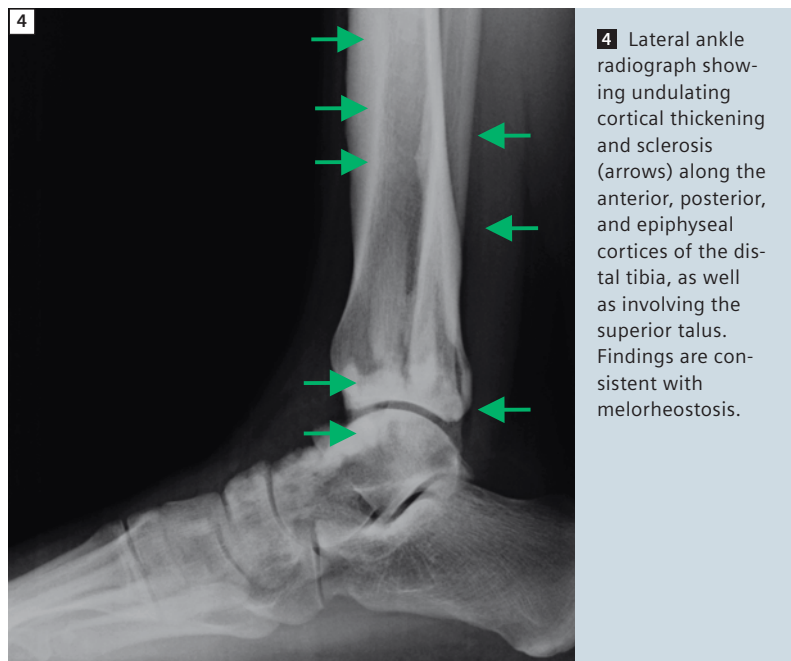
Case 2: Melorheostosis

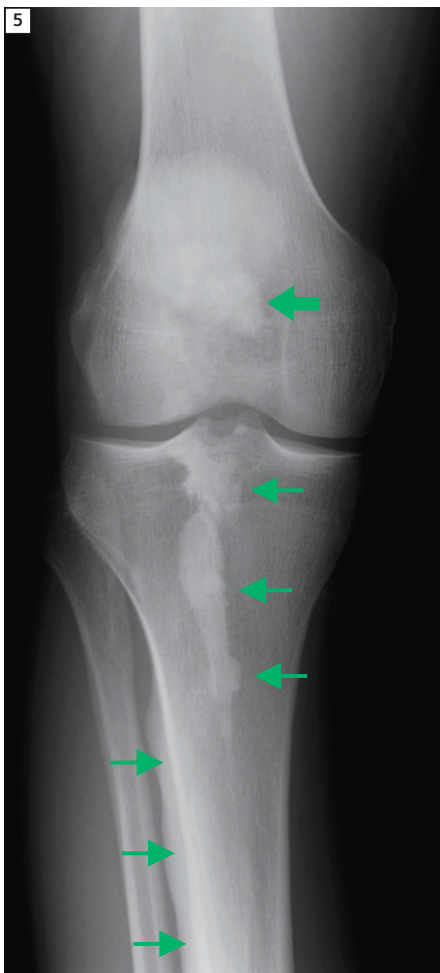
Patient history

25-year-old male with right knee pain, mainly along the medial border of his patella and posterior. He states he hyper-extended his right knee in 2006. He was evaluated and was diagnosed with melorheostosis and a possible fracture of the patella with migrating loose bodies and was treated conservatively. He states that his pain has been continuous since then. He notes locking, catching, giving way, popping and grinding.

Physical examination

Focal exam of right knee reveals no deformity. No lesions, erythema, ecchymosis or edema when compared to the contralateral limb. Flexion on his right 95 and on his left is 135 degrees. He has slight tenderness to palpation in the popliteal fossa as well as medial border of his patella.





5 AP right knee radiograph showing undulating sclerosis in the marrow space of the proximal tibia (arrows), sclerosis along the lateral cortex of the proximal tibial shaft (arrows). There is soft tissue ossification projecting over the femoral notch (wide arrow), corresponding to ossification in the popliteal fossa seen on the MRI image (see Figure 6). Findings are consistent with melorheostosis.

Imaging findings

Radiographs: (Figs. 4, 5)

1. Lateral right ankle view reveals undulating cortical thickening and sclerosis along the anterior, posterior, and epiphyseal cortices of the distal tibia, as well as the superior talus. Findings are consistent with melorheostosis.
2. AP right knee view reveals undulating sclerosis in the marrow space of the proximal tibia, and soft tissue ossification in the popliteal fossa. Findings are consistent with melorheostosis.

MRI: (Figs. 6, 7, Table 2)

1. Areas of bony sclerosis in patella, femur, and tibia, consistent with melorheostosis.
2. Infrapatellar fat pad edema, possibly related to bone dysplasia.
3. 2 cm low intensity mass in the posterior intercondylar notch.

Clinical course

Four months later, the patient returns reporting continued pain. He states the pain is worse than it was before. He does feel that his knee is more stable and more muscular due to therapy; however, he has pain with going down stairs and feels it is on the inferior border as well as posterior border of his knee when he flexes. He is non-tender to palpation. His available flexion on exam on the left is 130 degrees and on the right is 95 degrees. He is lacking approximately 1 cm off his thigh circumference on the right when compared to the left. Clinical impression was inflammation of the fat pad and patellofemoral syndrome, and he was injected with Kenalog and Marcaine.

One month later he reports no significant improvement. He has failed a maximal amount of non-operative management of this including intense physical therapy and anti-inflammatory medications. He is unchanged from his baseline in terms of pain and discomfort and with function. He has a small effusion in his knee. His range of flexion on the right is to 90 and on the left is to 135.

Clinical impression is that melorheostosis may be causing restricted motion in his patellofemoral joint and the remainder of his knee joint. Although surgical results are unpredictable, as his disease process makes him different than the general population, it is elected to proceed with anterior interval release, lysis of adhesions and synovectomy, in an effort to create more knee mobility. He subsequently underwent arthroscopy, adhesion lysis, anterior interval release, and intercondylar plica removal. He returned one month after surgery, and reported that his anterior pain was gone, but posterior discomfort was still present. There was a small effusion

present in posterior aspect of knee when compared to the collateral knee. Maximal flexion on the right was 121 degrees and 145 degrees on the left, with good patellar mobility.

Discussion

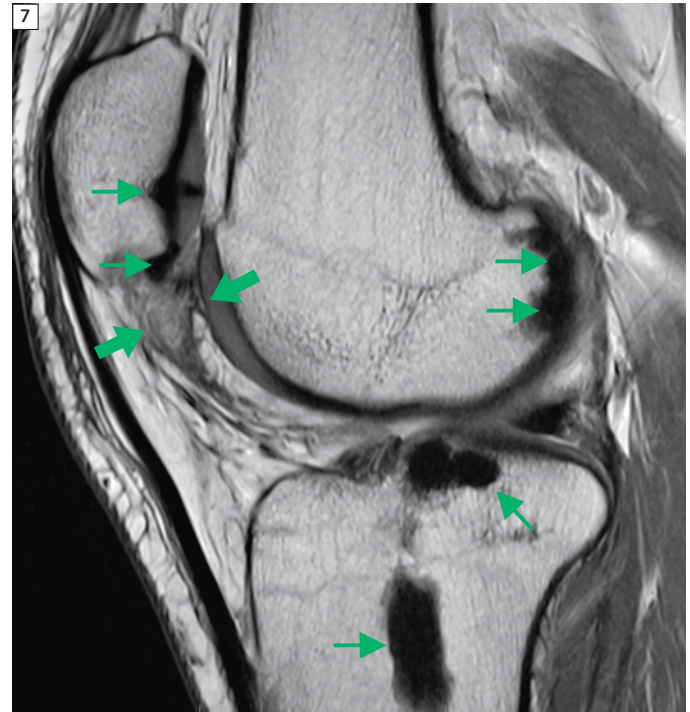
Melorheostosis is also known as Leri disease, and is a rare sclerosing bone dysplasia which exhibits sclerosis and hyperostosis, and is classically known for its 'dripping candle wax' radiographic appearance [1]. It can overlap within a spectrum of other sclerosing bone dysplasias including osteopoikilosis, osteopathia striata, and Buschke-Ollendorff syndrome (BOS). There is no apparent hereditary pattern, but it may share a genetic origin with several other bone dysplasias, related to chromosome 12q, resulting in disinhibition of a growth factor and bone morphogenic protein.

The most common presentation is incidental, in patients who are asymptomatic from the disease. When symptoms are present, stiffness and pain are the most common, due to limited motion and periosteal irritation [2]. The disease most commonly presents in late adolescents or young adults, but can be seen at any age. It has a slow but chronically progressive course, with periodic exacerbations. Progressive disability, limb length discrepancies, and even amputations may result [3]. If the spine is involved, fusions may occur.

The disease favors the appendicular skeleton, and is most often seen in the long bones of the extremities. It may monostotic or polyostotic, and can also tend to affect a single limb (monomelic) or sclerotome. Although the dripping candle wax sclerotic appearance is classic on radiographs, one series [3] showed it in only a minority of cases. Variable appearances resembling osteomas, myositis ossificans, and osteopathia striata have been described, as well as mixed appearances due to the tendency for overlap with other sclerosing syndromes. Skin changes resembling scleroderma have been reported overlying the affected bones [3], and can be seen at birth [2]. Hyperpigmented skin patches have also been described. Aside from the com-



6 Sagittal proton density-weighted image showing an ill-defined low signal mass, most likely partially calcified, in the popliteal fossa, with adjacent scarring and fibrosis (arrows). Sclerosis and thickening along the posterior tibial cortex (wide arrow) consistent with melorheostosis.



7 Sagittal proton density-weighted image showing an ill-defined low signal mass and fibrosis in the superior aspect of the infrapatellar fat pad (wide arrow). Multiple areas of osseous sclerosis (arrows) consistent with melorheostosis.

Table 2: MRI technique.

Weighting and planes	Field-of-view	TR	TE	Sequence	Slice thickness	GAP	Matrix size
T2-weighted axial	100	5250	93	Turbo Spin Echo	3 mm	0.3 mm	640 × 640
Proton Density-weighted axial fat suppressed	120	1200	43	Turbo Spin Echo fat suppressed	2 mm	0.3 mm	256 × 256
Proton Density-weighted sagittal	82.5	2910	41	Turbo Spin Echo	2 mm	0.3 mm	256 × 256
Proton Density-weighted sagittal fat suppressed	77.8	1200	43	Turbo Spin Echo fat suppressed	2 mm	0.3 mm	256 × 256
Proton Density-weighted coronal	100	5490	39	Turbo Spin Echo	3 mm	0.3 mm	640 × 640
Proton Density-weighted coronal fat suppressed	120	1200	35	Turbo Spin Echo fat suppressed	2 mm	0.3 mm	256 × 256

monly seen hyperostotic lesions, most patients also have soft tissue masses, often with infiltrative margins [2], either immediately adjacent to or distinct from bony lesions. Pathologically these represent vascularized fibrous tissue with variable collagen content. Biopsy can be avoided if these are recognized as part of the spectrum of melorheostosis findings [2]. Muscle atrophy may also be seen due to nerve involvement. There is also increased incidence of vascular tumors and malformations in melorheostosis patients, including hemangiomas, glomus tumors, and AVMs [4]. The characteristic undulating cortical hyperostosis exhibits wavy zones of thickening bony cortex with low signal

intensity on all MRI pulse sequences [5], and may encroach on and narrow the marrow space [6]. Soft tissue masses, associated vascular tumors and vascular malformations, and areas of fibrosis tend to enhance after gadolinium administration. Radionuclide bone scan reveals moderate and asymmetric increased uptake [6].

Biopsy is nondiagnostic. Treatment may consist of surgical tendon lengthening, contracture releases, osteotomies, fixation with corrective stretching, and rarely amputation. A case of symptom control following intravenous zoledronic acid, with treatment monitoring by the use of a specific bone resorption marker β cross-laps, has been reported [7].

References

- 1 Bansal A. The Dripping Candle Wax Sign. *Radiology* 2008; 246: 638-640.
- 2 Salmanzadeh A. Melorheostosis of the left foot. *Applied Radiology* 1998; 27(5).
- 3 Freyschmidt J. Melorheostosis: a review of 23 cases. *Eur Radiol* 2001; 11:474-479.
- 4 Kessler HB, Recht MP, Dalinka MK. Vascular anomalies in association with osteodystrophies: a spectrum. *Skeletal Radiol* 1983; 10: 95-101.
- 5 Meyers SP. *MRI of Bone and Soft Tissue Tumors and Tumorlike Lesions: Differential Diagnosis and Atlas*. Thieme 2008; pp. 816.
- 6 Judkiewicz AM, et al. Advanced imaging of melorheostosis with emphasis on MRI. *Skeletal Radiol* 2001; 30(8): 447-53.
- 7 Hollick RJ. Melorheostosis and its treatment with intravenous zoledronic acid. *BMJ Case Reports* 2010; 10: 1757.

Case 3: Glenohumeral Joint Dislocation

Patient history

A 20-year-old amateur snowboarder injured his right shoulder approximately 10 days ago, and anteriorly dislocated his right shoulder. He had the joint relocated in the emergency room. This was his only known instance of shoulder dislocation, and he has no history of prior injuries to the shoulder. On presentation his pain was approximately a 3/10 to 4/10, and at its worst was 7/10 to 8/10.

Musculoskeletal examination

There is no evidence of muscular atrophy. Range of motion is limited secondary to pain, with his forward elevation passively to approximately 90 degrees, abduction passively to approximately 50 degrees and external rotation to approximately 30 degrees. Strength with forward elevation and abduction is 4+/5. Internal and external rotation strength is -5/5. He is most tender over the supraspinatus. He is non-tender over his coracoid process and long biceps tendon. He has a positive apprehension sign with relocation.

Imaging findings

Radiographs: Three views of the right shoulder show well-reduced right shoulder, with no evidence of acute fracture.

MRI findings: (Figs. 8–10, Table 3)

1. There is near-circumferential labral undermining and tearing, most severe in the anterior to anteroinferior aspects, with labral stripping and detachment, periosteal and capsular stripping and tearing, with medial and inferior displacement of capsulolabral tissue. There is partial tearing of the glenoid attachment of the inferior glenohumeral ligament, and there is a focal 4–5 mm sharply marginated acute-appearing chondral defect and adjacent fragment along the anteroinferior glenoid rim. There is slight cortical flattening and possible slight impaction or avulsion of the anterior inferior glenoid margin.
2. Hill-Sachs impaction fracture deformity, 3.6 cm maximal AP dimension, 1.2 cm in vertical dimension, and 7 mm in depth. There is also fracture through the greater tuberosity of the humerus to the physeal scar and metaphysis, incomplete or with little or no displacement.

3. Supraspinatus tendinosis with partial tearing along distal deep margin, with retracted fibers.
4. Severe subacromial/subdeltoid bursitis.
5. Large effusion with synovitis.

Plan: Surgical intervention is recommended to retighten the shoulder.

Operative findings: Arthroscopy revealed normal-appearing humeral articular cartilage. There were grade 1 articular cartilage changes on the glenoid. There was a small Hill-Sachs lesion. There were some areas of chondral damage in the anteroinferior glenoid from the dislocation. There was a partial thickness articular surface tear of the supraspinatus tendon. This involved greater than 50% of the footprint. There was a complete anterior capsulolabral separation from the glenoid. This was an unusual pattern, since there was a radial tear through the anterosuperior labrum with the whole complex being retracted laterally towards the humeral head. The subscapularis and biceps tendon were intact.

Procedures performed:

1. Right shoulder arthroscopy and glenohumeral debridement.
2. Right shoulder anterior labral repair and capsulorrhaphy.
3. Right shoulder subacromial decompression with partial acromioplasty.
4. Right shoulder supraspinatus repair, trans-tendon double-row technique.

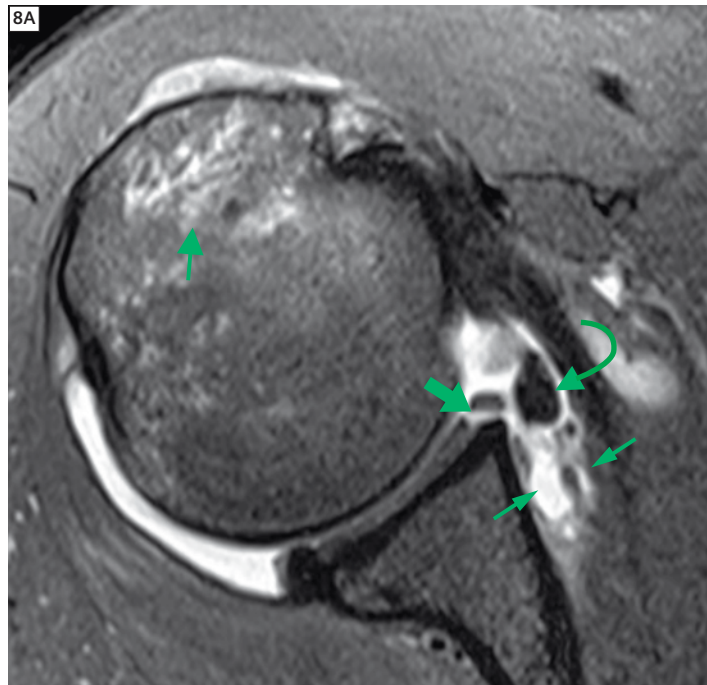
Discussion**Anatomy**

The shoulder joint is designed for a wide range of activities, including throwing, pushing, and pulling. The versatility of the joint must be balanced by stabilizing forces, and the dynamics are complex. Due to the large range of motion [1], stability of the joint must be provided by a range of anatomic structures, including bone, labrum, muscles, tendons, ligaments, and capsule.

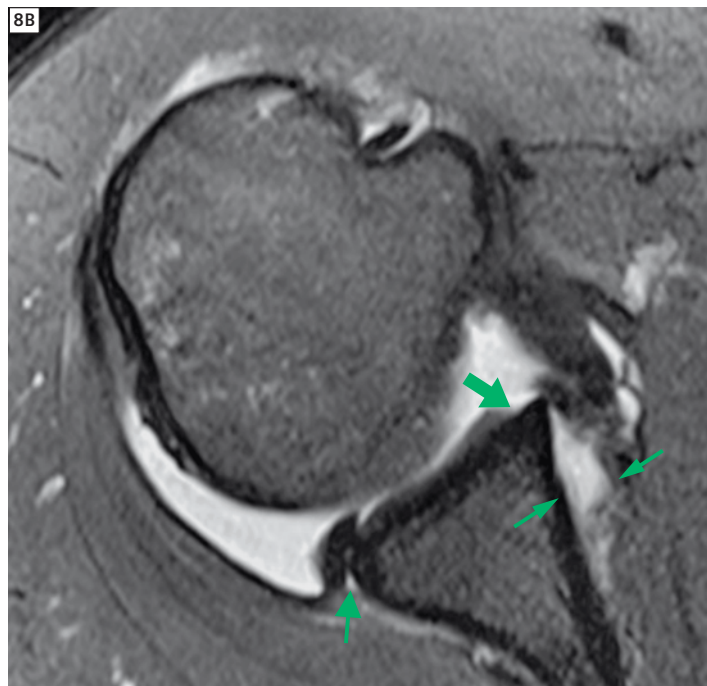
Numerous normal variants of labral shape, size, and position have been described by arthroscopy and MRI, and a complete discussion of these is beyond the scope of this report. The anterosuperior sublabral foramen is one of the more common variants, and has been described in up to 18% [2] of asymptomatic patients. However, this has not been clearly demonstrated to be congenital, and increases its prevalence with age [3], suggesting it may be an acquired finding, or possibly an asymptomatic labral tear. The Buford complex is a thickened and enlarged middle glenohumeral ligament in the absence of an anterosuperior labrum, seen in about 6% [2].

A superior sublabral recess extending from the 11-o'clock to 1-o'clock positions has been demonstrated in 73% of cadavers [4], with loosely attached and completely unattached superior labra documented in 45% and 36% respectively on autopsy [5].

The long biceps brachii tendon has an intra-articular origin, from the supraglenoid tubercle of the scapula and/or the superior to posterosuperior glenoid labrum. It travels laterally through the rotator interval and then extends inferiorly along the bicipital groove of the proximal humerus.



8A Axial fat suppressed proton density-weighted image shows medial and inferior displacement of stripped capsulo-labral tissue (curved arrow) with periosteal and capsular stripping and tearing (thin arrows). There is a focal sharply margined acute-appearing chondral defect and adjacent fragment along the anteroinferior glenoid rim (wide arrow). There is greater tuberosity edema from impaction fracture (standard arrow).



8B Axial fat suppressed proton density-weighted image shows periosteal and capsular stripping and tearing (thin arrows). There is a focal sharply margined acute-appearing chondral defect along the anteroinferior glenoid rim (wide arrow). There is posterior labral tearing and partial detachment (arrow).

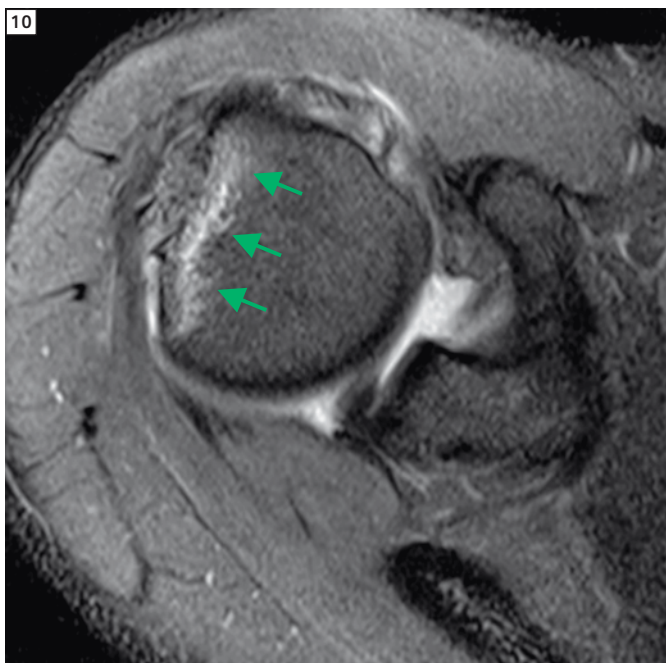
The glenohumeral ligaments are thickened bands of the joint capsule. The superior glenohumeral ligament originates from the anterosuperior labrum, the attachment of the long head biceps tendon, or the middle glenohumeral ligament [6]. It extends nearly perpendicular to the middle glenohumeral ligament and parallel to the coracoid process.

The middle glenohumeral ligament runs superomedial to inferolateral and is quite variable. It may be absent or quite thick, and its appearance changes with humeral head rotation [6].

The inferior glenohumeral ligament has anterior and posterior bands, as well as



9 Coronal fat-suppressed proton density-weighted image shows superior labral undermining and partial tearing (arrows). There is partial tearing of the glenoid attachment of the inferior glenohumeral ligament (wide arrow). There is supraspinatus tendinosis with partial tearing along distal deep margin, with retracted fibers (thin arrows).



10 Axial fat-suppressed proton density-weighted image shows a large Hill-Sachs impaction fracture deformity of the superolateral humeral head (arrows).

the axillary pouch [6]. It is an anterior stabilizer, and may tear along with the anterior labrum and capsule.

Clinical

Labral and capsular injuries can occur anywhere around the circumference of the glenohumeral joint, depending on mechanism of injury, and result in instability in a variety of directions. Aside from instability, patients may report pain, catching, and popping sensation. In the anterior, posterior, and superior regions, capsulolabral injuries have been classified and divided into different types, and are described with a variety of different eponyms and acronyms. Inferior labral tears are not discretely subdivided, but are not infrequently seen as extension from anterior and posterior capsulolabral lesions. It is important for the radiologist to be familiar with the many different types and classes of capsulolabral injuries, but also be aware that a great many clinical MRI cases exhibit overlapping imaging findings which describe partial or complete components of two or more different named injuries patterns, and do not fall into a single discrete category or pattern. For this reason, accurate description of imaging findings is very important, and of greater importance than categorization of the injury into a specific named or numbered entity. This case provides a good example of this.

Anterior lesions

The first 'essential lesion' of the anterior capsule was described by Bankart in 1923 [1]. He later broadened this to include traumatic shearing of the labrum off of its bony attachment. More than 85% of traumatic anterior dislocations result in anterior labral detachment, due to anterior displacement of the humeral head. The classic Bankart injury may also include tearing of the anterior joint capsule and periosteum. Anterior glenoid impaction or avulsion fracture, now known as a bony Bankart lesion, is also closely associated with this mechanism of injury, but was never described by Bankart himself. The Hill-Sachs lesion, named for two American radiologists,

Table 3: MRI technique.

Weighting and planes	Field-of-view	TR	TE	Sequence	Slice thickness	GAP	Matrix size
T2-weighted axial	120	650	7.5	Gradient Echo	3 mm	0.3 mm	512 × 512
Proton Density-weighted axial fat suppressed	120	3350	46	Turbo Spin Echo fat suppressed	3 mm	0.3 mm	512 × 512
Proton Density-weighted sagittal	120	4000	93	Turbo Spin Echo	2 mm	0.3 mm	640 × 640
Proton Density-weighted sagittal fat suppressed	120	3000	46	Turbo Spin Echo fat suppressed	2 mm	0.3 mm	512 × 512
Proton Density-weighted coronal	120	2510	34	Turbo Spin Echo	3 mm	0.3 mm	768 × 768
Proton Density-weighted coronal fat suppressed	120	3000	46	Turbo Spin Echo fat suppressed	2 mm	0.3 mm	512 × 512

refers to a bony impaction injury of the posterolateral humeral head against the anterior lip of the glenoid, and is also commonly seen with anterior dislocation. The Perthes lesion describes stripping of the anterior labroligamentous complex and periosteum, without displacement, and without tearing of partially stripped periosteum of the anterior scapula. Due to the lack of displacement, this lesion may be more difficult to appreciate than the other anterior lesions on MRI images, but the lack of anterior periosteal integrity predisposes these patients to laxity and instability.

A detached Perthes lesion describes a Perthes lesion in which the labrum is displaced from its attachment, and there

is detachment of the inferior glenohumeral ligament with anterior displacement, but the periosteum remains continuous.

The anterior labroligamentous periosteal sleeve avulsion (ALPSA) lesion [1] exhibits a torn anteroinferior labrum with inferomedial displacement, with the inferior glenohumeral ligament rolled up along the periosteum, like a sleeve. The anterior scapular periosteum remains continuous but may be partially stripped.

A glenolabral articular disruption (GLAD) lesion refers to an anteroinferior labral tear associated with adjacent injury to the glenoid articular cartilage [1]. This does not specifically lead to glenohumeral joint instability.

The glenoid labrum ovoid mass (GLOM) sign refers to a torn anterior labrum which is retracted superiorly, but should not be confused with a normal middle glenohumeral ligament.

A humeral avulsion of the glenohumeral ligament (HAGL) lesion [1], typically of the anterior band, can also occur with anterior glenohumeral joint dislocation or instability. It is more common in older patients. The GAGL lesion is similar, but the avulsion is of the glenoid attachment instead of the humeral. There may be bony fragment avulsions with these lesions as well, referred to as BHAGL and BGAGL lesions.

Superior lesions

Superior labral tears are important to recognize, due to the labrum itself, and also due to the association with long biceps tendon and tendon anchor tears, which may compromise anterior stability. Overhead throwing athletes are predisposed. Other proposed mechanisms include compression from fall on outstretched hand, and traction injuries. Superior labral tears commonly occur anterior and posterior to the long biceps tendon origin, and thus are termed superior labrum anterior/posterior, or SLAP, tears. Mechanism of injury has a role in tear type and morphology. Snyder first divided SLAP tears into four main types [8], and Maffet [9] subsequently added three more grades. Type I is marked free edge fraying. Type II is avulsion of the labral/bicipital complex from the glenoid, and is further subdivided into three groups. Type III is a displaced bucket handle labral tear with intact biceps anchor. Type IV is a bucket handle tear with extension into the substance of the biceps anchor. Type V is a Bankart lesion that extends superiorly to the biceps anchor. Type VI is an unstable radial or flap superior labral tear. Type VII is tear extension beneath the middle glenohumeral ligament. Labral SLAP tear types VIII – X have also been described [10], and additional types proposed

Posterior lesions

On MRI, findings related to posterior instability are typically the reverse of those for anterior instability, and posterior dislocation/instability is less common. Posterior labral tears with capsular detachment or stripping may be seen, as evidenced by disruption or stretching/laxity of the normal, well defined continuous low signal capsule line connecting the glenoid and labral margin to the humeral neck. There may be bony impaction or fragmentation of the posterior glenoid rim and the anterior humeral head, which are the characteristic reverse Bankart and reverse Hill-Sachs lesions.

There may be a tear or stripping avulsion of the posterior band of the inferior glenohumeral ligament, typically at the glenoid but also possibly at the humeral attachments. There is also an association with teres minor tears (may tear along with the posterior band of the IGHL), and internal bodies in the glenohumeral joint.

There may also be associated rotator cuff injury. Glenoid erosive changes, sclerosis, or heterotopic bone formation may be seen chronically. There may be soft-tissue findings of associated edema, hematoma, or extravasated joint fluid. The humeral head may be posteriorly subluxed in relation to the glenoid. In chronic cases, there may be bone loss and remodeling with retroversion of the glenoid, although there is a reported wide normal range of glenoid inclination from 25° retroversion to 8° anteversion. The Bennett lesion represents an enthesophyte arising from the posterior portion of the glenoid neck to rim, which is commonly seen in baseball pitchers. The posterior labrocapsular periosteal sleeve avulsion (POLPSA) lesion is the posterior analogue of the ALPSA (anterior labroligamentous periosteal sleeve avulsion). It is associated with posterior instability. Wherein the reverse Bankart lesion the periosteum is torn, the periosteum is stripped but continuous in a POLPSA lesion.

Paralabral cysts

Paralabral cysts are an important diagnostic clue strongly indicating an adjacent labral tear and capsulolabral tear, although the tear may not always be discretely visualized on MRI. These cysts can be unilocular, but are often multilocular, and can extend/dissect several cm away from the labrum tear from which they originate. This can result in symptoms related to mass effect, including extension into the suprascapular or spinoglenoid notches, with possible nerve entrapment and neuropathy, which may result in denervation atrophy of rotator cuff muscles.

References

- 1 Khan AN, Chew FS. Glenoid Labrum Injury MRI. <http://emedicine.medscape.com/article/401990-overview>. Updated 7/28/11, accessed 5/24/12.
- 2 Tuite MJ, et al. Sublabral foramen and Buford complex: inferior extent of the unattached or absent labrum in 50 patients. *Radiology* 2002; 223: 137-142.
- 3 DePalma AF, Gallery G, Bennett GA. Variational anatomy and degenerative lesions of the shoulder joint. In: Edwards JW. Instructional course lectures: the American Academy of Orthopedic Surgeons, vol. 6. St. Louis: Mosby, 1949 : 225–281.
- 4 Smith DK, et al. Sublabral recess of the superior labrum: study of cadavers with conventional non-enhanced MR imaging, MR arthrography, anatomic dissection and limited histologic examination. *Radiology* 1996; 201:251-256.
- 5 Cooper DE, et al. Anatomy, histology, and vascularity of the glenoid labrum: an anatomical study. *J Bone Joint Surg (Am)* 1992; 14:46-52.
- 6 De Maeseneer M, et al. CT and MR Arthrography of the Normal and Pathologic Anterosuperior Labrum and Labral-Bicipital Complex. *RadioGraphics* 2000; 20: S67-S81.
- 7 Bencardino JT et al. Superior Labrum Anterior-Posterior Lesions: Diagnosis with MR Arthrography of the Shoulder. *Radiology* 2000; 214: 267-271.
- 8 Snyder SJ, Karzel RP, Del Pizzo W, et al. SLAP lesions of the shoulder. *Arthroscopy* 1990; 6:274-279.
- 9 Maffet MW, Gartsman GM, Moseley B. Superior labrum-biceps tendon complex lesions of the shoulder. *Am J Sports Med* 1995; 23:93-98.
- 10 Mohana-Borges AVR, Chung CG, Resnick D. Superior Labral Anteroposterior Tear: Classification and Diagnosis on MRI and MR Arthrography. *AJR* 2003; 181: 1446-1449.

Contact

Charles P. Ho, Ph.D., M.D.
Steadman Philippon Research Institute
181 W. Meadow Dr. Suite 1000
Vail, CO 81657
USA
charles.ho@thesteadmanclinic.com

Tim 4G

High SNR and excellent iPAT performance for fast and high quality imaging

16-channel Hand/Wrist coil¹



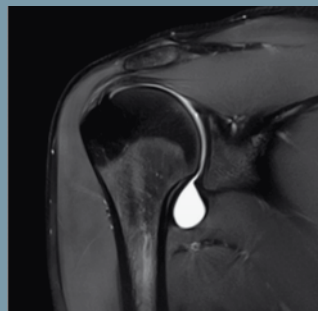
- Imaging the whole hand and wrist in a single measurement.
- Comfortable patient positioning with arms on the side.
- Improved ease of use with Slide Connect.

16-channel Foot/Ankle coil¹



- Imaging the whole foot and ankle in a single measurement.
- Tilting in head-foot direction in four positions for higher comfort.
- Direct Connect for fast and easy positioning.

16-channel Shoulder coils¹



- Large and small coils to match patient's needs.
- Improved ease of use with Slide Connect.

Image courtesy of Radiologisches Zentrum München-Pasing, Munich, Germany

¹Tim 4G coils are available for 1.5T MAGNETOM Aera as well as for 3T MAGNETOM Skyra and Spectra; the coils will be available for 1.5T MAGNETOM Avanto^{fit} as well as for 3T MAGNETOM Skyra^{fit}, Prisma and Prisma^{fit}. MAGNETOM Avanto^{fit}, Skyra^{fit}, Prisma and Prisma^{fit} are still under development and not commercially available yet. Their future availability cannot be ensured.

Discover our extensive coil portfolio for Musculoskeletal MRI:

www.siemens.com/redefine-MRI-with-coils



15-channel Tx/Rx Knee coil
14-channel Extremity coil²
18-channel Body coil
4-channel Flex coil small



²Available for 1.5T MAGNETOM ESSENZA

Case Report: Job's Syndrome

G. Hadjidekov¹; G. Georgieva¹; S. Hadjidekova²; M. Radeva¹; D. Stoyanova¹; G. Tonev¹

¹MC "Pro-Vita", Sofia, Bulgaria

²Department of Medical Genetics, Medical University, Sofia, Bulgaria

Introduction

First described in 1966, the hyperimmunoglobulin E (hyper-IgE or HIE) syndrome is a rare immunodeficiency disorder with autosomal dominant inheritance pattern. HIE syndrome has variable expressivity and is associated with multiple abnormalities. The most common findings are recurrent skin abscesses (hence the name "Job's Syndrome", that comes from the Old Testament Book of Job. Job was tormented with plagues of boils etc.), pneumonia with pneumatocele development, and high serum levels of IgE. Facial, dental, and skeletal features are also associated with this syndrome [1].

Patient history

37-year-old female patient with lumbar and pelvic pain, multiple hyper- and atrophic cicatrices due to surgical interventions and spontaneous suppuration presents for MR postoperative evaluation. The onset of the disease was shortly after birth with apparition of abscesses of the capilitium at the age of 7 months and eczematous skin of the body and the extremities with different aspect and density, accompanied by pus formation. Erythemo-papulous itchy rash with tendency to lichenification had unsuccessfully been treated as eczema. Job's Syndrome was diagnosed at the age of 3 years by histological and micro-

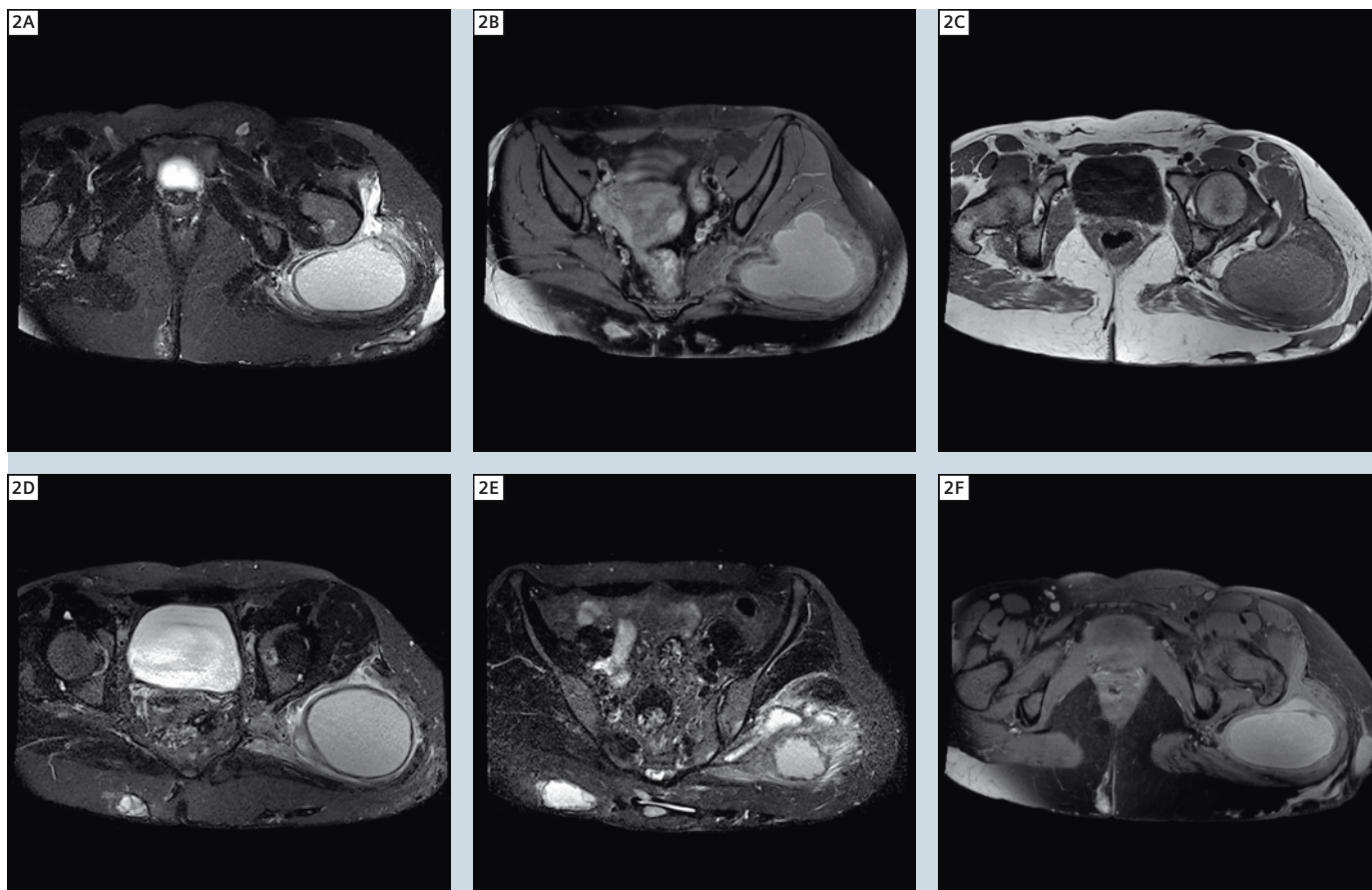
biological examination, and several skin resections, including incisions and necrectomies, were performed. Erythrocyte sedimentation rate (ESR) was 67 mm, C-reactive protein (CRP) 88, Hb 97 and total IgE > 4000 IU/ml (with normal values up to 120 IU/ml).

Sequence details

The following images were acquired on our 1.5T MAGNETOM ESSENZA using a 4-channel body matrix coil. The T2 sequence in axial and sagittal plains is using the following parameters: TR 2600 ms, TE 83 ms, matrix (300 x 448) px², FOV 380 mm, phase



1 Presenting an ovoid, capsulated formation at the level of the left m. gluteus maximus, passing between m. adductor magnus and m. vastus lateralis. (1A) coronal T1, (1B) sagittal T2, (1C) axial T2.



2 (2A) Shows a small amount of liquid close to the iliotibial tract; (2B) edematous m. gluteus maximus and m. piriformis; (2C) subcutaneous liquid collection in communication with the skin. (2D) shows the collection at the level of coccygeal bone; (2E) collection with fistula at the level of sacroiliac joint; (2F) collection behind the rectum with skin fistula formation. Axial TIRM (2A, F), axial PD fat sat (2B, D, E), Axial T1 (2C) images.

FOV 100%, bandwidth 260 Hz/px, flip angle 150°, base resolution 448, phase resolution 100%.

The T1 sequence in axial, sagittal and coronal plains is using the following parameters:

TR 680 ms, TE 8,5 ms, matrix (300 x 448) px², FOV 380 mm, phase FOV 100,0%, bandwidth 260 Hz/px, flip angle 150°, base resolution 448, phase resolution 100%.

The T2 TIRM sequence in the axial plain is using the following parameters:

TR 5560 ms, TE 80 ms, matrix (258 x 384) px², FOV 360 mm, phase FOV 67,2%, bandwidth 260 Hz/px, flip angle 150°, base resolution 384, phase resolution 100%.

The T1 VIBE sequence with fat suppression is using pre-and post contrast injection

with the following parameters:

TR 5.2 ms, TE 2.4 ms, matrix (319 x 384) px², FOV 340 mm, phase FOV 100%, bandwidth 410 Hz/px, base resolution 384, phase resolution 83%, slice resolution 67%.

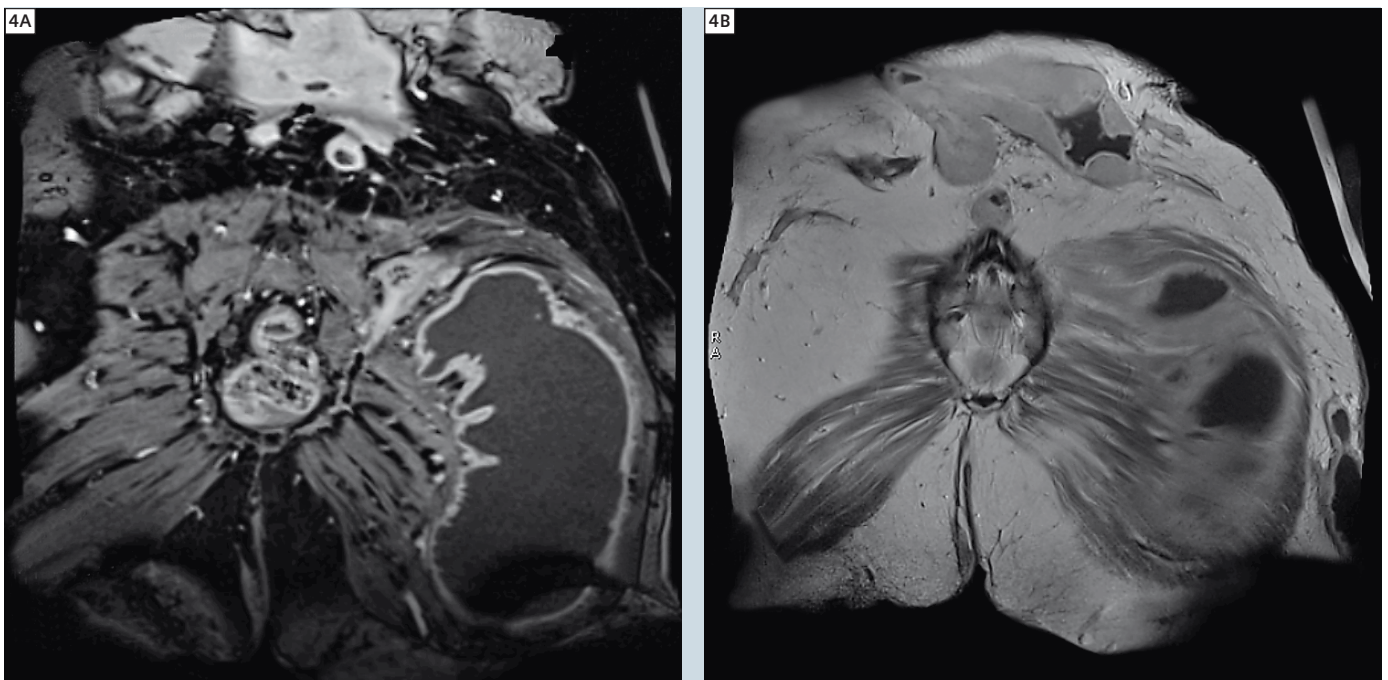
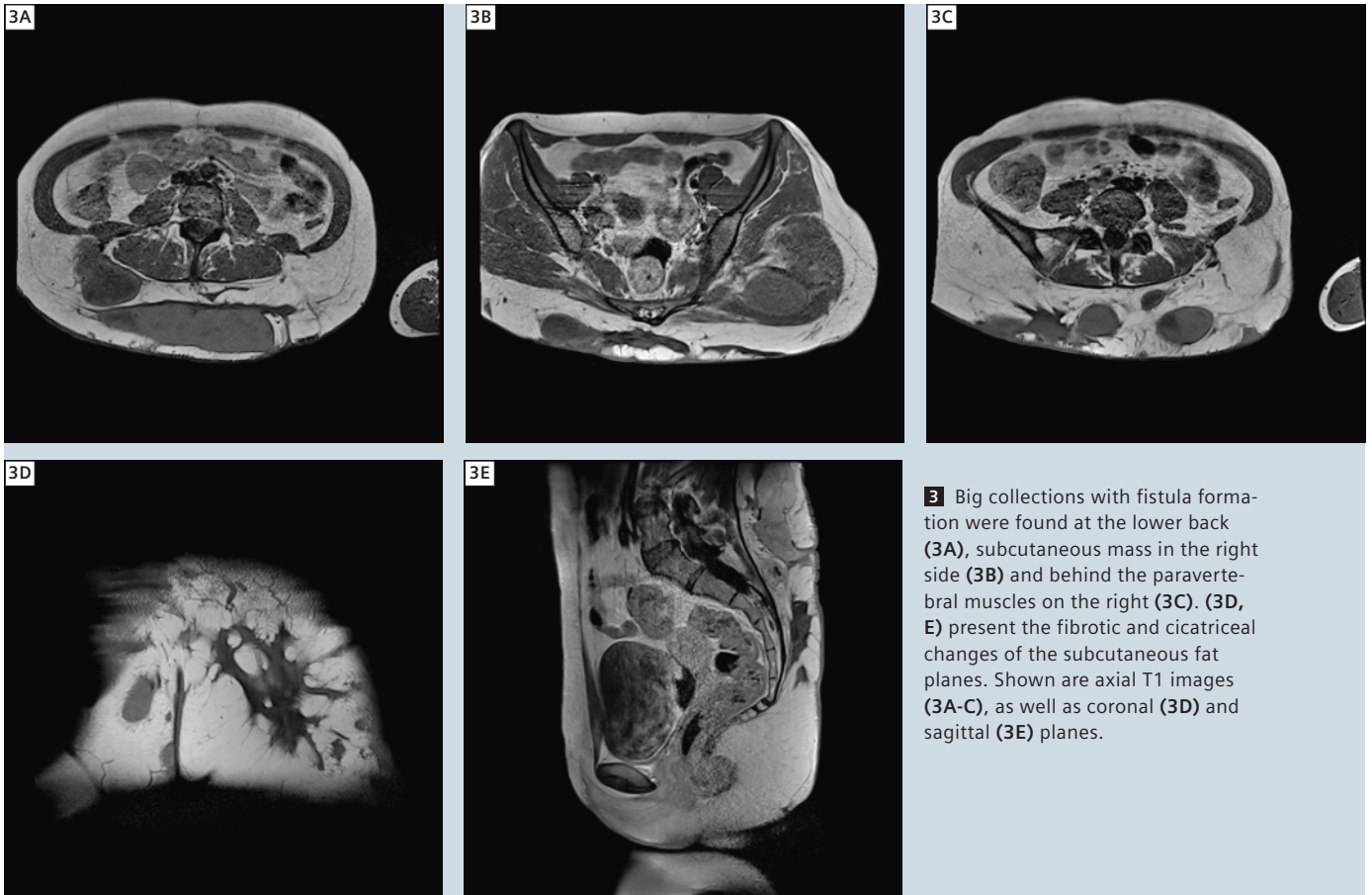
The PD sequence with fat suppression in axial plain was acquired using the following parameters:

TR 2200 ms, TE 12 ms, matrix (304 x 512) px², FOV 380 mm, phase FOV 50%, bandwidth 165 Hz/px, base resolution 512, phase resolution 100%.

Imaging findings

MRI examination (1.5T Siemens MAGNETOM ESSENZA) at the level of the lower back and pelvis revealed a huge, ovoid, capsulated formation at the level of the left musculus (m.) gluteus maxi-

mus measuring 18/10/5 cm. The mass propagates in caudal direction and is passing through the lateral femoral intermuscular septum, between m. adductor magnus and m. vastus lateralis and is located approximately 10 cm distal to the trochanter major. The content of the lesion presents with hyperintensity on T2 and hypointense on T1 images and corresponds to pus (Fig. 1A-C). There is also a small amount of liquid close to the iliotibial tract (Fig. 2A), accompanied by edematous m. gluteus maximus and m. piriformis. Figure 2B at the level of the trochanter major on the left side reveals two subcutaneous liquid collections with the same signal intensity, both in communication with the skin (Fig. 2C). Additional liquid collections are found on the right side, subcu-



taneously, at the level of the coccygeal bone (Fig. 2D), the sacroiliac articulation with fistula formation (Fig. 2E) and close to the rectum with again pararectal skin fistula formation (Fig. 2F).

Another distinctive collection with fistula formation was found at the lower back, at the level of the biiliac line subcutaneously at the left measuring 12/8/4 cm in the left and medially (Fig. 3A) and a smaller one measuring 4/3 cm in the right side (Fig. 3B). A mass measuring 6/3 cm has been found behind the paravertebral muscles in the fat tissues at the right side of the back (Fig. 3C). A massive fibrosis of the subcutaneous fatty tissues in addition to hyper- and atrophic cicatrices resulting from surgical interventions and spontaneous suppuration has been noted (Fig. 3D, E).

Following gadolinium injection there was significant contrast uptake from the capsules of the described lesions as well as from the inflammatory changes of the fatty planes (Figs. 4A, B).

Besides the described soft tissue lesions a small amount of liquid has been detected in the left sacroiliac joint with associated high signal intensity zones in T2 fat sat, corresponding to bone edema in the context of left side sacroileitis (Fig. 8).

Discussion

Autosomal dominant hyper IgE syndrome (AD-HIES), formerly known as 'Job's Syndrome', is a genetic disease affecting several body systems including the immune system. AD-HIES is characterized by abnormally high levels of an immune system protein called immunoglobulin E (IgE) in the blood. Some cases

of Job's Syndrome have been found to be due to a genetic defect in a protein called STAT3 and mutations in the STAT3 gene, but in many others, the cause is unknown [2, 3]. Job's Syndrome's STAT3 gene resides on chromosome 17 on the longer arm. HIES often appears early in life with recurrent staphylococcal and candidal infections, pneumonias, lymphadenitis, conjunctivitis and eczematoid skin. Characteristic facial, dental, and skeletal abnormalities have also been described. Patients with HIES have either delay of or failure in shedding of primary teeth. The characteristic coarse facial features are usually set by age 16. These include facial asymmetry, a prominent forehead, deep-set eyes, a broad nasal bridge, a wide, fleshy nasal tip, and mild prognathism. Additionally, facial skin could be rough with prominent pores. Finally, some patients have scoliosis, as well as bones that fracture easily [4]. A review of reported cases of lymphoma in Job's Syndrome indicates an increase in relative risk [7].

Our patient presented with recurrent suppurative skin infections, chronic eczematoid rash and large skin abscesses. Increased number of eosinophils in blood and high levels of total IgE was also present. People with Job's Syndrome tend also to have high levels of anxiety, depression, and guilt. Recurring pneumonias and fungal infections like infections of the mouth or of the nails were not present in our patient as well as bone fractures. As skin manifestations were dominant, we found the diagnostic value of MRI of utmost importance regarding the precise determination, localization and extent of the lesions,

the effect from previous resections and the fibrotic and cicatricial soft-tissue changes. Due to the excellent contrast resolution, MRI was also useful in our case in considering further surgical treatment, since it provides optimum contrast and high spatial resolution to visualize soft-tissue details demanded by the dermatologists. Fat suppression is often essential in musculoskeletal imaging to obtain superb contrast. We consider MRI a superior imaging modality to computer tomography (CT) in delineating the extent of the disease [5]. Necrotizing fasciitis and gas gangrene are more common necrotizing infections that also cause necrosis of skin, subcutaneous tissue, and muscle [6]. They present with different aspects and are easily differentiated by the cutaneous abscesses within the dermis and deeper skin and soft tissues in our patient.

Conclusion

Contrast-enhanced MRI is a particularly sensitive method for detecting soft-tissue masses, as well as their precise localization and extent. For this purpose different sequences are available nowadays. Our case is an example of the usefulness of MRI as a powerful non-invasive technique in medical diagnosis, applied here to analyze skin disorders and deeper soft-tissue masses with various localizations.

Contact

Georgi Hadjidekov, M.D.
MC "Pro-Vita"
Montevideo str. N66
Sofia 1632
Bulgaria
jordiman76@yahoo.com

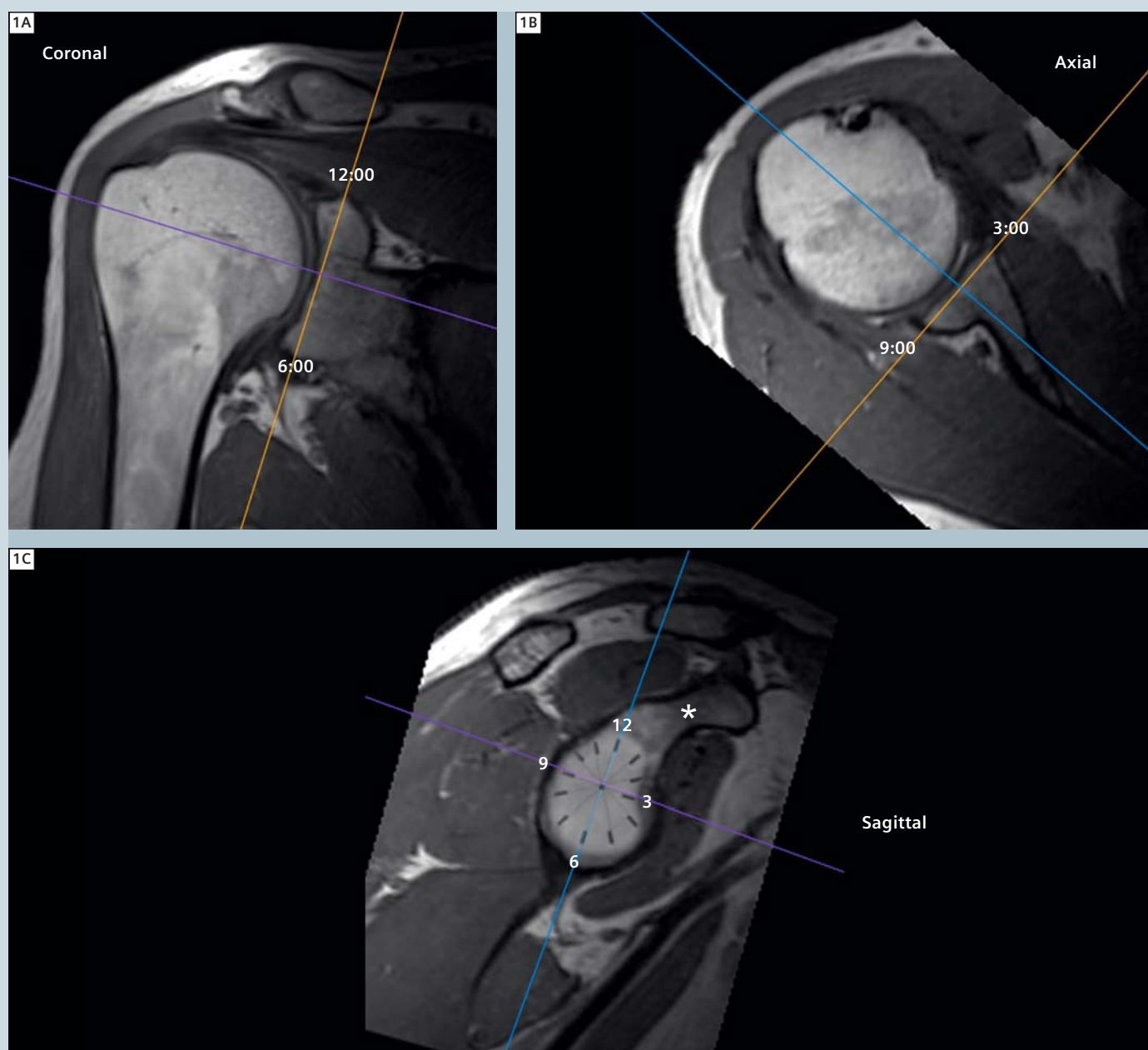
References

- Grimbacher B, Holland SM, Puck JM. Hyper-IgE syndromes. *Immunol Rev.* Feb 2005;203:244-50.
- Job syndrome. Genetics Home Reference (GHR). February 2008 Available at: <http://ghr.nlm.nih.gov/condition=jobsyndrome>. Accessed November 13, 2008.
- Holland SM, DeLeo FR, Elloumi HZ, Hsu AP, Uzel G, Brodsky N. STAT3 mutations in the hyper-IgE syndrome. *N Engl J Med.* Oct 18 2007;357(16):1608-19.
- Grimbacher B, Holland S, Gallin J, Greenberg F, Hill S, Malech H, Miller J, O'Connell A, Puck J. "Hyper-IgE syndrome with recurrent infections – an autosomal dominant multisystem disorder". *N Engl J Med* 1999; 340 (9): 692–702.
- Aisen AM, Martel W, Braunstein EM, McMillin KI, Phillips WA, Kling TF. MRI and CT evaluation of primary bone and soft-tissue tumors. *AJR* 1986; 146 (4): 749-756.
- Stevens DL, Bisno AL, Chambers HF, Everett ED, Dellinger P, Goldstein EJ, Gorbach SL, Hirshmann JV, Kaplan EL, Montoya JG, Wade JC. Practice Guidelines for the Diagnosis and Management of Skin and Soft-Tissue Infections. *Clin Infect Dis.* 2005; 41 (10): 1373-1406.
- Leonard G, Posadas E, Herrmann P, Anderson V, Jaffe E, Holland S, Wilson W. Non-Hodgkin's Lymphoma in Job's Syndrome: A Case Report and Literature Review. *Leukemia & Lymphoma* 2004; 45 (12): 2521-2525.

MRI of the Shoulder: Utilizing the Glenoid Clockface Orientation

Steven D. Needell, M.D.

Boca Radiology Group, P.A., Boca Raton, FL, USA



1 Orientation of coronal (orange line), sagittal (blue line) and axial (purple line) planes using glenoid clockface as reference.

Background

Orthopedic surgeons describe the glenoid fossa as the face of a clock, with the longitudinal axis defined by the supraglenoid tubercle marking the 12:00 position and the inferior margin of the glenoid marking the 6:00 position. Orienting the shoulder MRI exam relative to this clockface is ideal because it results in images which consistently correspond with the arthroscopists' perspective and optimally profiles the major anatomic structures of the glenohumeral joint.

Technique

After obtaining axial scouts, a three plane localizer should be prescribed medial enough to include the coracoid process in the sagittal plane, which is essential to orienting the exam to the glenoid clockface. In the sagittal plane, identify the coracoid process, which projects anterosuperiorly off the neck of the scapula and defines the 1:00 position of the glenoid clockface for a right shoulder and the 11:00 position for a left shoulder. Coronal sequences are prescribed parallel to a line bisecting the 12:00 superior and 6:00 inferior positions of the glenoid fossa on a sagittal image (Fig. 1). Axial sequences are prescribed perpendicular to the coronal plane, and bisect the 3:00 and 6:00 positions (Fig. 1). Sagittal sequences are prescribed perpendicular to the glenoid rim (Fig. 1).

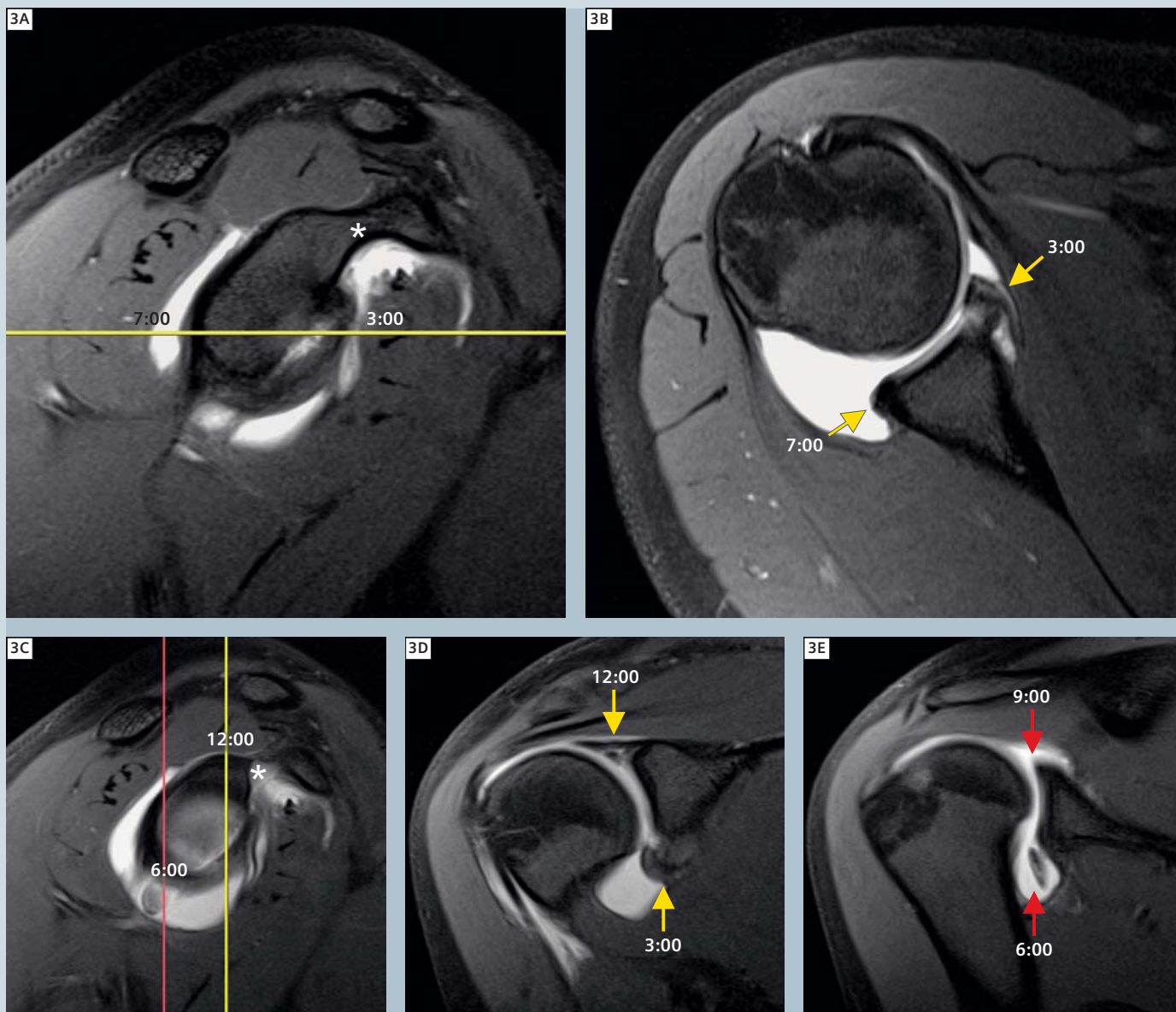
Discussion

With the shoulder placed in a neutral position, the osseous, tendinous and ligamentous structures supporting the glenohumeral joint are all anatomically oriented with respect to the glenoid clockface. Therefore, in addition to being an ideal presentation of the glenoid labrum, imaging the shoulder orthogo-



2 Using glenoid clockface orientation, proximal biceps tendon (arrows) is imaged along its length in the oblique coronal plane when patient is placed in neutral position.

nal to the glenoid clockface is also an optimal way to evaluate the biceps tendon (Fig. 2), rotator cuff tendons and sources of outlet impingement. When shoulder exams are prescribed without regard to the glenoid clockface, physicians reviewing the exam must rely on scout lines and interactive PACS tools to accurately determine the positions of the glenoid labrum on axial and coronal sequences. By utilizing the glenoid clockface orientation, the labrum is consistently and predictably presented in an orientation familiar to clinicians and radiologists.



Clinical Cases

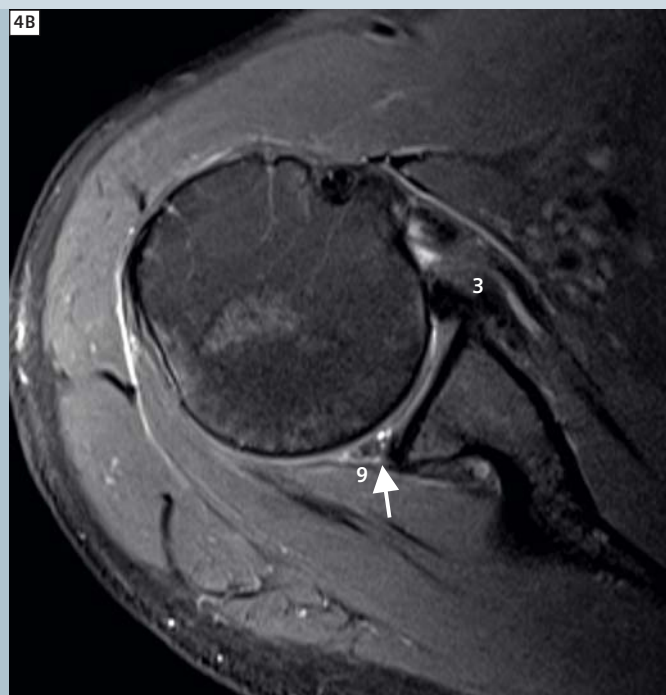
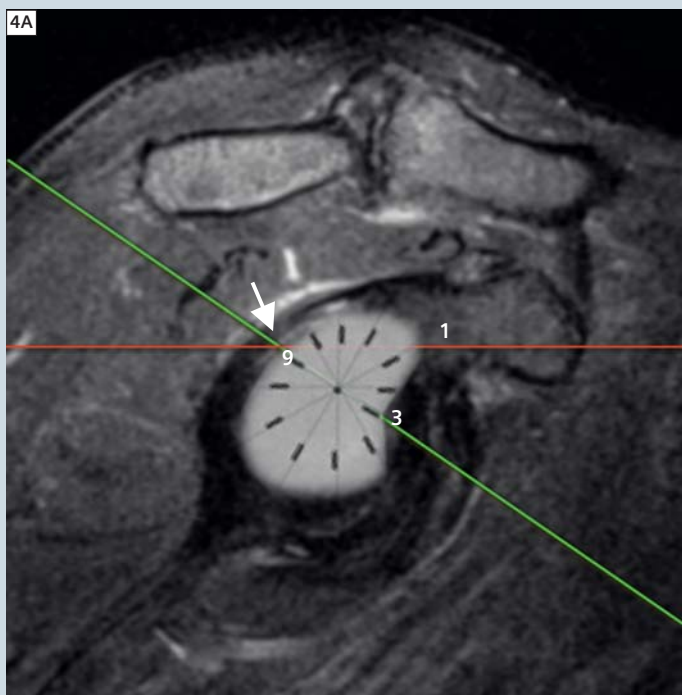
Case 1: Disadvantages of not using Glenoid Clockface Orientation

(A) MR Arthrogram of the right shoulder in an 18-year-old volleyball player with superior labral (SLAP) tear and inferiorly displaced tear of antero-inferior glenoid labrum. Straight coronal and axial prescriptions were utilized rather than orienting to the glenoid clockface (asterisk marks the 1:00 position of the acromion). Note how the straight axial prescription (Fig. 3A) results in the 3:00 anterior position

positioned opposite the 7:00 postero-inferior position on axial images (Fig. 3B), which is an unintuitive and unpredictable presentation.

(B) Straight coronal prescription in the same patient unnecessarily complicates identification of labral pathology. Had a glenoid clockface orientation been utilized, the 12:00 superior labral tear would have appeared on the same coronal image as the displaced tear of the 6:00 inferior labrum.

However, since straight prescriptions were used (Fig. 3C), the SLAP tear appears on the same image as the 3:00 anterior position (Fig. 3D) and the inferiorly displaced tear appears on the same image as the 9:00 posterior labral position (Fig. 3E).



Case 2: Advantages of using Glenoid Clockface Orientation

38-year-old male with tear (arrows) involving the 9:00 to 11:00 positions of the posterosuperior quadrant of the-glenoid labrum. Utilizing the glenoid clockface orientation on a sagittal image (**Fig. 4A, green line**), the torn 9:00 posterior labrum is opposite the

3:00 anterior labrum on an axial image (**Fig. 4B**), which is what one would intuitively expect. Had axials been prescribed without regard to the glenoid clockface, then the 9:00 posterior position would have appeared opposite the 1:00 anterosuperior position (**Fig. 4A, red line**), which would have resulted in an unintuitive presentation.



Steven D. Needell, M.D.

Contact

Steven D. Needell, M.D.
 Director Musculoskeletal Imaging
 Boca Radiology Group, P.A.
 951 NW 13th St, Suite 1C
 Boca Raton, FL 33486
 USA
 Phone: +1 561.391.1728
 Fax: +1 561.447.4316
sneedell@bocaradiology.com

Bone and Soft Tissue Tumor Imaging: An Overview

Marcus Pianta, MBBS MMed FRANZCR; Mark Lourensz; Nicholas Trost, MBBS FRANZCR

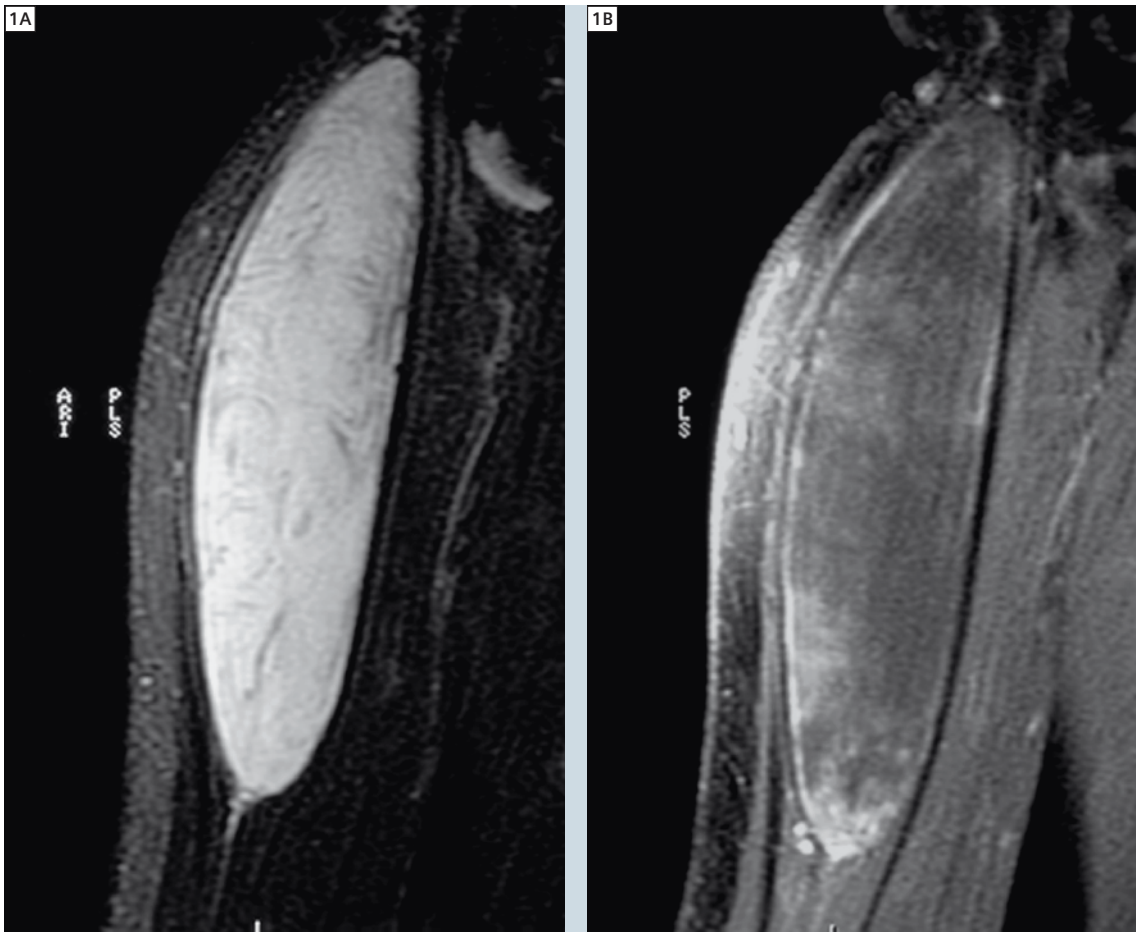
MRI Department, St Vincent's Hospital, Fitzroy, Victoria, Australia

Why?

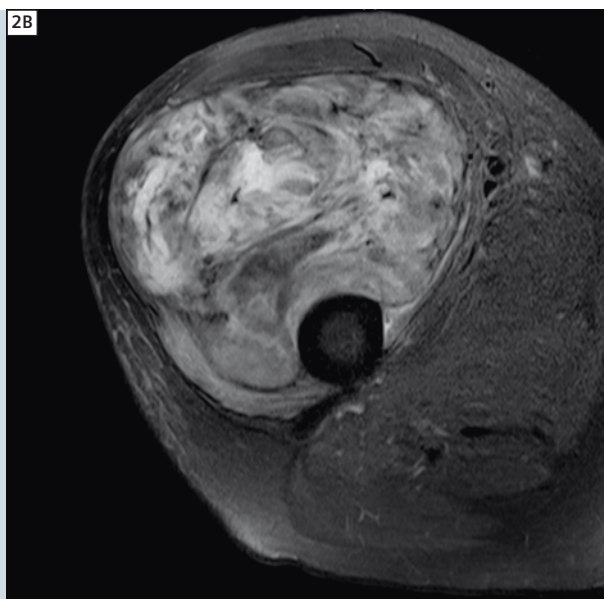
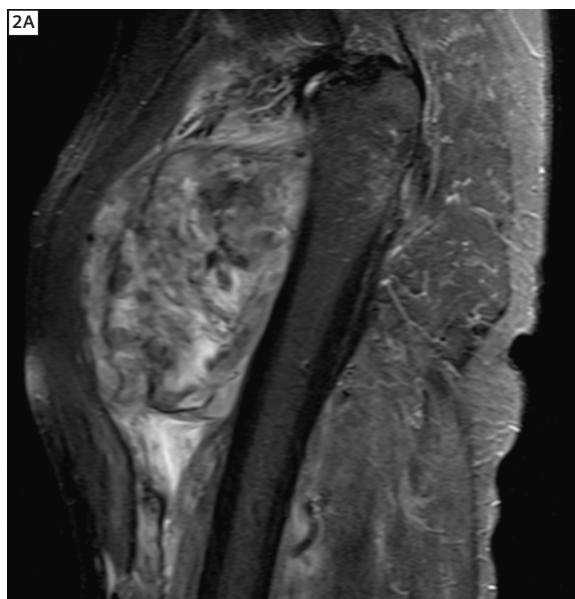
Imaging of bone and soft tissue tumors has progressed in line with technological developments in medical imaging equipment. Particularly with modern computed tomography (CT) and magnetic resonance imaging (MRI) scanners, multiplanar imaging is significantly quicker, more practical and of higher resolution than 10 years ago. As a benefit, it is now possible to very accurately define a suspected bone or soft tissue tumor in terms of its involvement of the surrounding small

neurovascular structures, breaching of fascial planes, deposits at distal sites and likely underlying histology (Fig. 1). Simultaneously, oncologic orthopedic surgical techniques have developed and progressed from limb amputation to many tumors now being resected in line with 'limb sparing surgery' [1]. This involves generally wide surgical margins around the entire tumor and adjuvant chemotherapy and/or radiotherapy in order to preserve the patient's

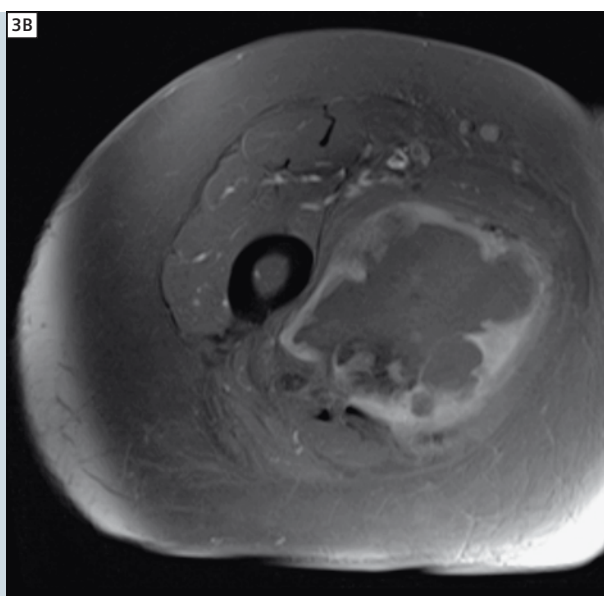
limb and as much function as possible. At our institution, all patients suspected of having a primary bone or soft tissue sarcoma are comprehensively imaged, discussed in a multi-disciplinary team meeting and most undergo pre-treatment percutaneous biopsy. Imaging is crucial to determine a preliminary diagnosis and prognosis, develop a treatment plan and prepare the approach for biopsy, surgery and chemo/radiotherapy. It is also essential in post-treatment progress monitor-



1 Soft-tissue mass of the right upper limb demonstrates a close neural association and ovoid shape with 'tail' suggesting neurofibroma. The markedly increased signal on T2-weighted imaging correlates with the histology of myxoid type neurofibroma. There is typical heterogeneous post contrast enhancement on the T1 fat-saturated sequence.



2 Anterior thigh compartment sarcoma is well appreciated on sagittal post-contrast T1 fat-saturated imaging, as well as axially where it wraps inseparably around the femur.



3 Adductor compartment high-grade spindle cell pleomorphic sarcoma, including relationship to the femur is well appreciated on both the coronal and axial post-contrast T1 fat-saturated imaging.

ing and in assessing for tumor recurrence and complications such as pathological fractures or infection.

How?

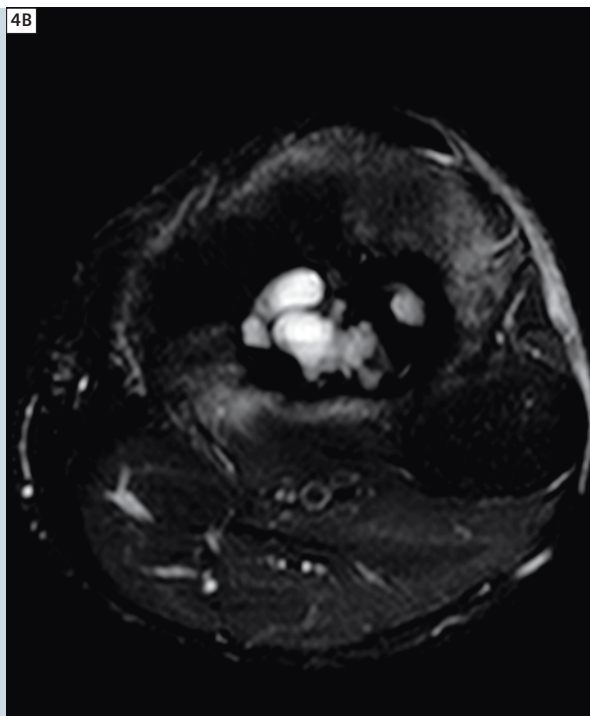
Whilst plain radiographs, ultrasound and CT are usually the initial investigations for 'lumps and bumps', soft tissue extent is most comprehensively assessed with MRI, which is best performed at the institution where the oncological treating team is based and where the surgery will be performed. Positron emission tomography (PET) and Thallium scans are also useful to assess for metabolic activ-

ity in a lesion, especially for targeting a percutaneous biopsy to yield an optimum diagnostic result and when determining treatment response.

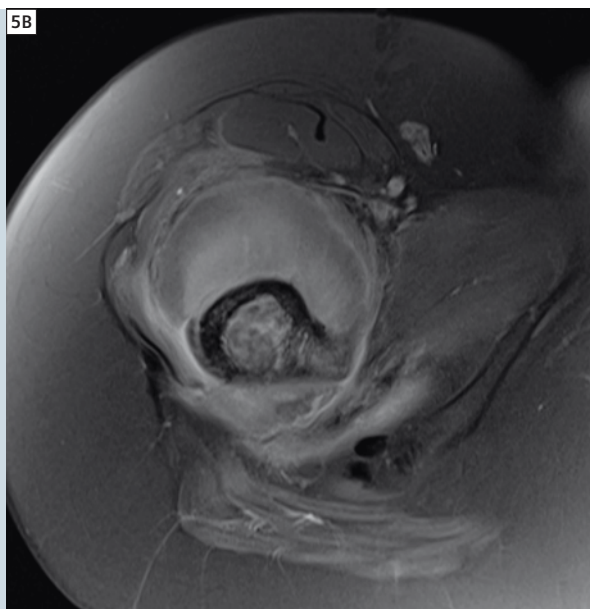
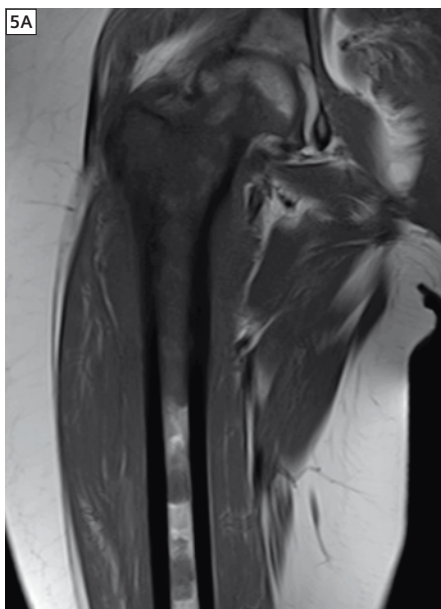
Whilst MRI yields excellent soft tissue contrast, the correct scan parameters and sequences are required to maximize the imaging outcome. At our institution the lesion is imaged in 3 orthogonal planes at high resolution with a combination of T1, T2-weighted, short T1/tau inversion recovery (STIR) and contrast-enhanced sequences [2]. Our routine protocol targeted to the lesion comprises T1 without fat saturation in all 3 planes,

T2 fat-saturated in the axial plane, STIR in a longitudinal plane and post-gadolinium fat-saturated T1 in the axial and longitudinal planes. The longitudinal plane (usually sagittal or coronal) for the STIR and post-gadolinium sequences is chosen to be perpendicular to the lie of the lesion so that it is imaged within the central slices of the acquisition e.g. a quadriceps mass will be longitudinally imaged in the sagittal plane (Fig. 2), and an adductor compartment mass in the coronal plane (Fig. 3).

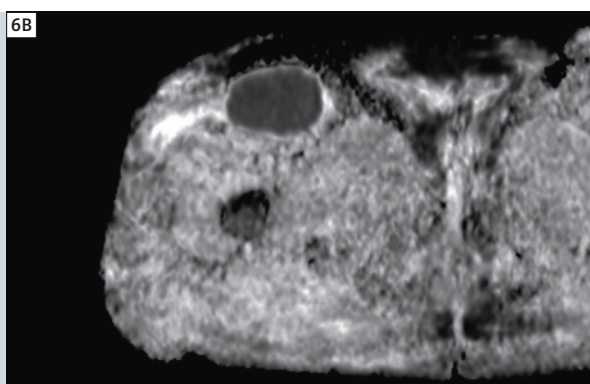
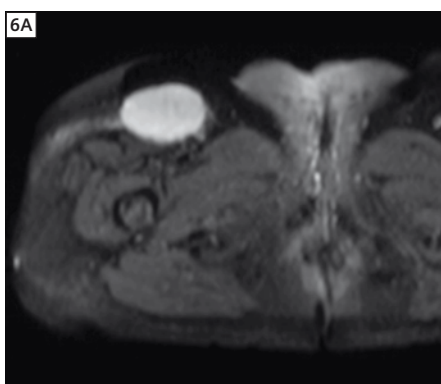
T1-weighted imaging best demonstrates the anatomy involved. Most solid com-



4 T2-weighted sequences show a giant cell tumor of the tibia, **(4B)** windowed to demonstrate the fluid-fluid levels. There is also low signal peripherally and throughout consistent with a combination of fibrous tissue and hemosiderin.



5 T1 and T1 fat-saturated post-contrast images show a Ewing's sarcoma replacing the proximal femoral medulla. There is bone destruction and a large, enhancing soft tissue component.



6 DWI and ADC map show restricted diffusion of a right groin lesion. When demonstrated, a high grade soft tissue sarcoma or lymphoma should be suspected.

ponents of tumors are of intermediate T1 signal similar to muscle. Pathological foci of fat, melanin, protein, methemoglobin, some calcifications and contrast can be seen with high T1 signal.

T2-weighted images are generally useful for determining fluid components, where bright signal corresponds with increased free water protons as seen in edema and fluid collections such as cysts and necrosis. Fluid layering, or 'fluid-fluid levels' may be seen in aneurysmal bone cysts, giant cell tumors of bone (Fig. 4), telangiectatic osteosarcoma, cystic degeneration, infection and hematomas. Whilst most solid tumors are of intermediate T2 signal, some specific pathological types may demonstrate high T2 signal such as cartilaginous and myxoid tumors, chordomas and nerve sheath tumors. Tumors with lower T2 signal compared to muscle may include those of high fibrous content and giant cell tumor of the tendon sheath.

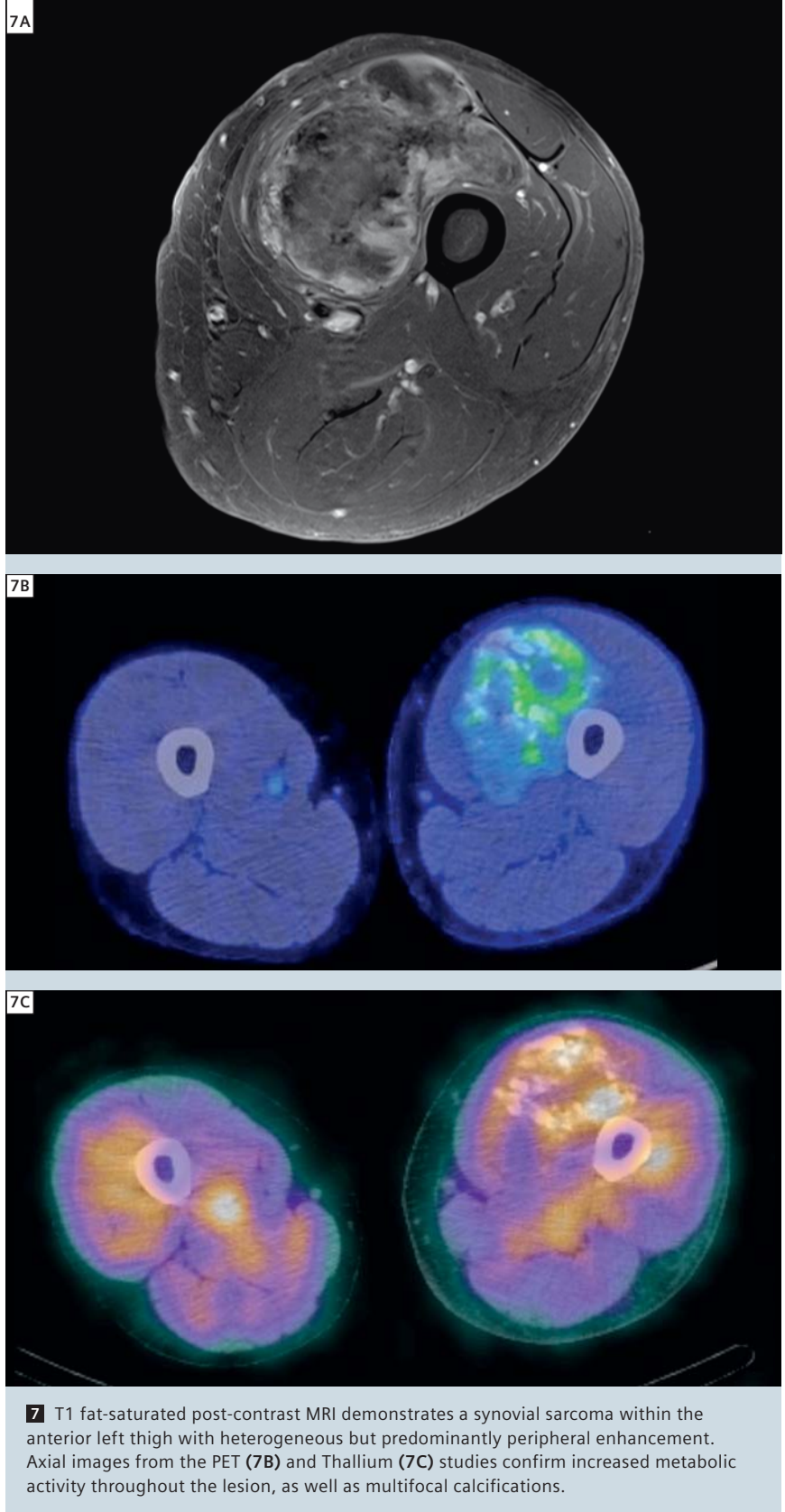
STIR sequences help highlight pathology by suppressing fat and allowing bright fluid signal in tumors and edema to be more conspicuous.

T1 post gadolinium contrast administration with fat saturation is also employed to better outline abnormal enhancement of a lesion or tumor by suppressing the surrounding T1-bright fat (Fig. 5). The pattern of enhancement can indicate vascular permeability or necrosis, and help differentiate tumor (rapid enhancement) compared to reactive edema or post-radiotherapy changes (more gradual enhancement) [3].

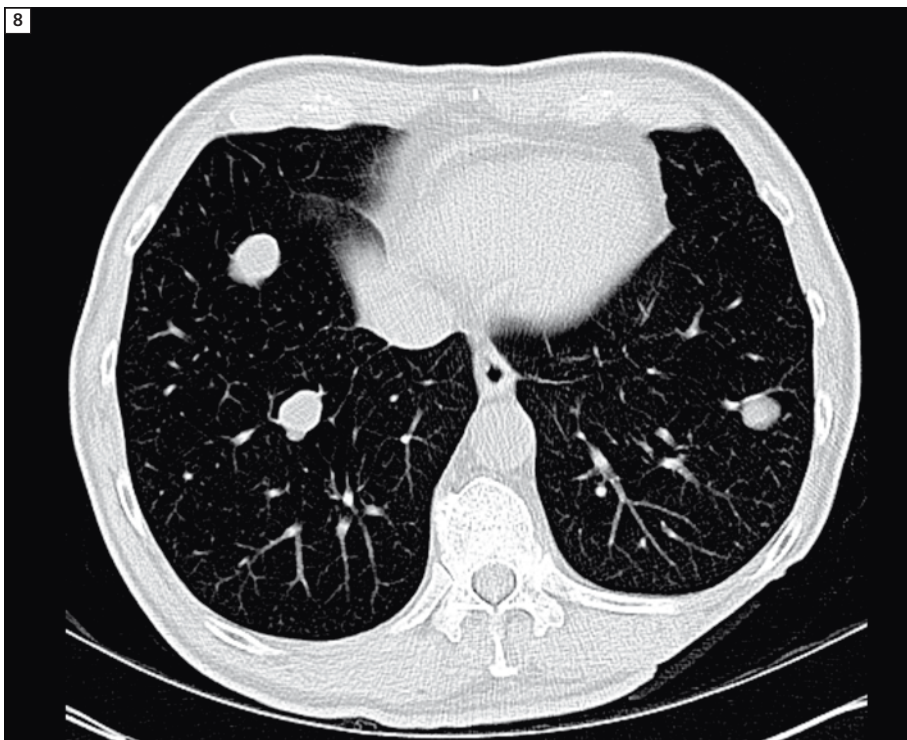
Fat saturation imaging is often suboptimal in the presence of a ferromagnetic prosthesis that causes local field inhomogeneities and susceptibility artifact [4]. In such cases, T1 pre and post contrast imaging is employed without fat saturation. Occasionally, a gradient echo sequence will be added to highlight differences in magnetic susceptibility for cases particularly suspected of containing calcification or blood products, such as pigmented villonodular synovitis, synovial chondromatosis or hemorrhagic metastasis. Whilst we do not routinely use diffusion-weighted imaging (DWI), solid components of higher-grade and poorly respon-

sive sarcomas can demonstrate a low apparent diffusion coefficient (ADC) and low/restricted diffusion (high diffusion-weighted signal) (Fig. 6). The clinical context needs to be carefully noted [5] however, as an abscess can result in a similar appearance.

Comprehensive imaging of a patient with a tumor includes whole-body thallium scan and PET to evaluate metabolic activity and multiplicity (Fig. 7) and CT of the thorax to assess for the presence of pulmonary metastasis (Fig. 8). Finally biopsy is performed in accordance with



7 T1 fat-saturated post-contrast MRI demonstrates a synovial sarcoma within the anterior left thigh with heterogeneous but predominantly peripheral enhancement. Axial images from the PET (7B) and Thallium (7C) studies confirm increased metabolic activity throughout the lesion, as well as multifocal calcifications.



8 Non contrast-enhanced CT of the thorax with lung windows demonstrates multiple lung lesions in keeping with metastasis. Such a finding drastically alters staging, prognosis and management in a patient with a bone or soft tissue tumor.

the planned surgical approach so that minimal tissue planes are contaminated and the biopsy tract can be excised. In addition to the targeted imaging of the primary lesion, further STIR and post-gadolinium fat-saturated T1 sagittal and coronal sequences with a wide field of view are acquired through the entire limb (Fig. 9) to evaluate for skip lesions. This saves time required in the scanner, for example axial scans through the entire limb are not required, whilst maintaining acceptable sensitivity for evaluating for skip pathology. In cases where the lower limb is involved, thick axial and coronal images are also acquired through the pelvis and lower lumbar spine to exclude skip lesions, metastasis and lymphadenopathy – all of which affect prognosis and management planning (Fig. 10).

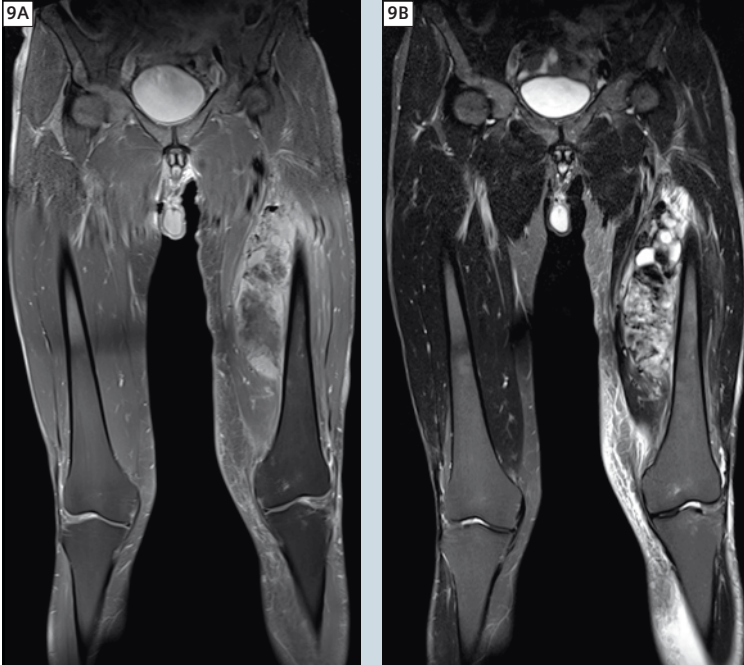
Reporting

It is important to foster a close relationship with the entire treating team of a patient with a soft tissue tumor – whether

benign or malignant. In this way, a feedback loop can be developed so that difficult cases are flagged early, and there is open and frequent communication amongst physicians, including the surgeons, radiologists and pathologists. When reporting, there are several key points that should be made clear to the referring physician in order to help stratify patients, particularly those at risk of aggressive or poorly responsive tumors. Deep compartment and larger sized soft tissue tumors should be considered aggressive [6] until proven otherwise (usually with biopsy). Poor definition and invasion of multiple compartments suggests malignancy, whereas confinement to a single muscular compartment with a well-defined capsule suggests a less aggressive, or even benign lesion. Peri-lesional increased T2 signal can indicate tumor spread or edema for which contrast enhancement can help differentiate, as well as determine cystic, solid and mixed components of lesions [7] (Fig. 11).

Bone lesions that cause aggressive periosteal reaction or destroy cortex, medulla and comprise a surrounding soft tissue mass should be considered malignant. Such a process can be seen with primary tumors such as Ewing's sarcoma (Fig. 5), or with osteochondromas that have undergone malignant change to chondrosarcomas. In this case, the often well organized foci of high T2 signal that reflect cartilage remnants will be more disorganized throughout a large soft tissue mass. In comparison, synovial cell sarcoma, which usually occurs around a joint can comprise multiple foci of low T2 signal in keeping with calcifications. In the appropriate clinical setting, a differential diagnosis for such an aggressive appearing lesion should include acute osteomyelitis.

Multiple lesions raise the possibility of a malignant tumor, including if seen within the lungs, which may be visible at the edge of the MRI field whilst imaging the shoulder or pelvis. Skip lesions within the same bone or limb should also be sought. Growth along neurovascular planes or into joints is also highly suggestive of a malignant lesion and indicates a poorer prognosis, including increased complexity of surgery. A location for biopsy is best evaluated in reference to the T1 and post contrast imaging where vividly enhancing regions of tumor, suggesting viability, may yield more success with a pathology diagnosis [8]. Non-enhancing regions of tumor can reflect internal lesion necrosis or cystic-appearing tumor components such as myxoid, which will demonstrate very high T2-weighted signal (Fig. 12). These findings can be correlated on PET or Thallium imaging, where increased tracer uptake is suggestive of viable tumor, and lack of uptake often correlates with lack of contrast enhancement on MRI. Post-radiotherapy changes may result in increased tumor size due to necrosis and hemorrhage, although a good response will also correlate with reduced or absent lesion enhancement (Fig. 13). Caution with non-enhancing cystic-appearing lesions is required if there is any increased T1 internal signal and irregular, thickened enhancing capsule that may indicate



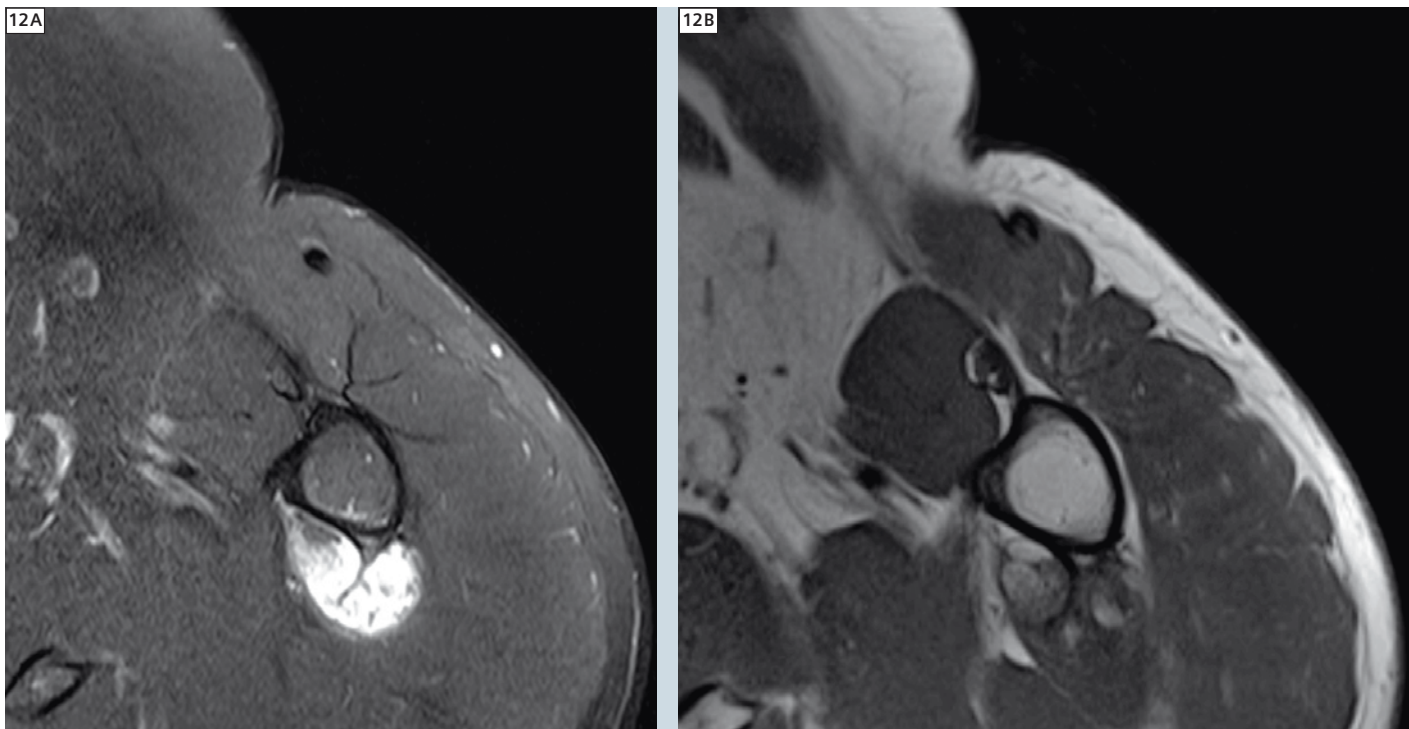
9 T1w fat saturated post-contrast and STIR imaging of the pelvis and bilateral lower limb demonstrate an extensive left thigh synovial sarcoma wrapping around the femur without evidence for pelvis or contralateral limb involvement.



10 Pelvis and lower limb STIR imaging demonstrates a high-grade pleomorphic sarcoma wrapping around the mid and proximal right femur with surrounding post-radiotherapy changes. There are metastatic right iliac nodes and a metastasis of the proximal left femoral diaphysis.



11 T2-weighted and T1 fat-saturated post-contrast imaging show an osteosarcoma which is predominantly cystic / necrotic, involving bone and with a soft tissue component.



12 Myxoid liposarcoma demonstrates high T2-weighted signal (myxoid) and portions of high T1 signal (fat) abutting the posterior aspect of the left proximal femur.

abscess formation – either super-infection of an underlying lesion, or as a result of intervention e.g. biopsy or surgery. Concluding the report should be concise and offer a brief differential if required. When appropriate, percutaneous biopsy can be recommended and specialist referral suggested. Concerning findings should be communicated at the time of reporting such as unexpected and new metastasis, post-operative complications (wound dehiscence, compressive hematoma) or pathological fractures.

Final thoughts

Tumor imaging can be daunting, given the relatively high stakes involved with a missed diagnosis or mis-diagnosis resulting in unnecessary further investigations, biopsies or even surgeries which carry additional morbidity and mortality. However, even the combined experience of specialist physicians is not infallible

and so systems must be in place to streamline patient work-up and maximize diagnostic accuracy and disease survival.

Standard MRI protocols developed by Radiology Departments in consultation with the treating oncologic orthopedic team ensure a consistent, reproducible service and high standard of imaging. Discussing a biopsy approach is also essential so that the subsequent surgery can include excision of the biopsy tract to avoid recurrence in the tract due to tumor seeding.

When imaging post-operatively, the surgical approach should be known and correlated with the expected skin and soft tissue changes. The tumor will have been excised (or in rare instances, debulked) with only faint, generalised post-contrast enhancement evident, suggesting post-surgical reaction and granulation formation rather than focal,

or nodular enhancement that suggests residual or recurrent tumor. In the short-term after surgery, a small seroma or hematoma can usually be discerned from tumor given its distinct fluid or blood signal, lack of internal enhancement and resolution over time.

MR Spectroscopy is not routinely performed at our institution but has been reported to assist in diagnoses that are not initially evident [9]. Often, patients have been on the scanner for close to 45 minutes with our standard protocols and we find at this time, image quality starts to decrease due to movement artifact.

Conclusion

Imaging of bone and soft tissue tumors can be very rewarding with a team approach, including use and continued development of reproducible imaging protocols and knowledge of what the



13 Pre and post radiotherapy: The initial T1 post contrast-enhanced scan (**13A**) demonstrates a large soft tissue, enhancing mass in the adductor compartment of the right thigh which is smaller and shows markedly reduced enhancement following radiotherapy (**13B**), in keeping with tumor necrosis and a good response.

referring physicians need to know. Open and frequent communication amongst the treating team is essential, with discussion regarding biopsy approaches and inter-physician feedback paramount to improving patient outcomes.

MRI sequencing of large primary tumors and metastasis can be time-consuming and so efficiency is required to maintain diagnostic image quality. Whilst there are some indicative features of tumors that correlate with certain components or likelihood of aggressiveness, ultimately biopsy is required to confirm tissue diagnosis prior to surgical planning, particularly in cases of potential tumor recurrence.

References

- 1 Liu et al., "Anatomically Based Guidelines for Core Needle Biopsy of Bone Tumors: Implications for Limb-Sparing Surgery." *RadioGraphics* (January 2007) 27:189–205.
- 2 Theodore Parsons III, Spencer Frink, and Scot Campbell, "Musculoskeletal Neoplasia: Helping the Orthopaedic Surgeon Establish the Diagnosis," *Seminars in Musculoskeletal Radiology* 11, no. 1 (March 2007): 003–015.
- 3 D Vanel et al., "MR Imaging in the Follow-Up of Malignant and Aggressive Soft-Tissue Tumors: Results of 511 Examinations," *Radiology* 190, no. 1 (January 1994): 263–268.
- 4 Kenneth Buckwalter, "Optimizing Imaging Techniques in the Postoperative Patient," *Seminars in Musculoskeletal Radiology* 11, no. 3 (September 2007): 261–272.
- 5 Oliver Dudeck et al., "Diffusion-Weighted Magnetic Resonance Imaging Allows Monitoring of Anticancer Treatment Effects in Patients with Soft-Tissue Sarcomas," *Journal of Magnetic Resonance Imaging: JMIR* 27, no. 5 (May 2008): 1109–1113.
- 6 P Gustafson, "Soft Tissue Sarcoma. Epidemiology and Prognosis in 508 Patients," *Acta Orthopaedica Scandinavica. Supplementum* 259 (June 1994): 1–31.
- 7 Catherine Roberts Guest Ed, "What the Orthopaedic Doctor Needs to Know," *Seminars in Musculoskeletal Radiology* 11, no. 1 (March 2007): 001–001.
- 8 P T Liu et al., "Anatomically Based Guidelines for Core Needle Biopsy of Bone Tumors: Implications for Limb-Sparing Surgery," *Radiographics* 27, no. 1 (January 1, 2007): 189–205.
- 9 L M Fayad et al., "Characterization of Musculoskeletal Lesions on 3-T Proton MR Spectroscopy," *American Journal of Roentgenology* 188, no. 6 (June 1, 2007): 1513–1520.

Contact

Marcus Pianta, MBBS MMed FRANZCR
MRI Department
St Vincent's Hospital
41 Victoria Pde
Fitzroy, Vic
Australia 3065
marcus.pianta@svhm.org.au

MSK Imaging Tips and Tricks

Mark Lourensz; Nicholas Trost, MBBS MMed FRANZCR; Marcus Pianta, MBBS FRANZCR

MRI Department, St Vincent's Hospital, Fitzroy, Victoria, Australia

Our MRI centre performs a wide range of MSK examinations ranging from standard joint work to whole limb tumor evaluation. These tips can be applied equally to both groups depending on clinical indications. Much of this is common sense, but it doesn't hurt to revisit the basics occasionally.

- Preparation is very important. Make sure you have your examination planned, previous imaging available for tumor cases, and relevant patient history.
- Always speak to the patient before the examination to determine the mechanism of injury, identify the area of injury, or to identify the relevant pathology under investigation. Ask the patient to show you the 'lump' they may be concerned about and identify any previous surgical sites or biopsy sites related to the lesion. This seems like a basic point, but maybe sometimes overlooked in a busy department, and is the key to providing an efficient and targeted MRI examination.
- Always mark the lesion of interest with a vitamin E capsule or similar MRI visible marker for all tumor studies. This is particularly important for small lesions, which may be very difficult to identify once imaging has commenced. If the patient has had a previous resection or biopsy of the lesion, mark each end of the scar or the biopsy site.
- Pre-cannulate patients who need contrast. This is particularly important for those patients who are difficult to position or have to lie in an awkward position for their scan. This will minimise patient time on the table, reduce scheduling hold ups due to difficult cannulations and minimize change in patient position between pre and post contrast scans.
- Make sure the patient is positioned comfortably to reduce the chances of patient movement during the scan. Do not get too caught up in trying to place the joint or limb in the anatomically correct position – this is pointless if the patient moves on every sequence.
- The beauty of MRI is its multiplanar capability, so use this to its full advantage when producing scout images. After your first scout, take a minute to scout again using your first scouts as a baseline, this time positioning your slices to produce orthogonal images which cover the full extent of the joint or tumor, and show any potential problems such as sources of aliasing etc. An extra few minutes spent here can save you a lot of time during the examination.
- Always position coils to cover the full extent of the area of interest in tumor cases – usually including both joints. This is very easy with Tim systems where a combination of body array coils and the peripheral array coil can be used for long bones, and specific joint coils are available for all other areas. The body array coils or flex coils can also be used for patients who, either due to body habitus or disease process, are unable to be accommodated with the standard joint coils.
- Talk to your radiologist and have a set of consistent protocols saved for use with all of your cases. This may be different for every joint, but should be the same for a specific joint and a specific clinical question. These should be well labelled and saved with any specific notes in your protocol tree. Make sure you know how much signal-to-

noise latitude you have in each sequence i.e. for tumor cases can you drop your field-of-view (FOV) from 250 mm to 200 mm to look at a smaller lesion without degrading your image too much. This will allow you to produce consistently high quality results.

- It is very important (for all MR imaging) to use the same slice position, thickness and gap, for the differently weighted sequences (e.g. T1, T2, T1 post Gd) in each plane of an anatomical area. This will allow better characterisation and localisation of normal anatomical structures and pathology.
- All sites will have their own protocol set for bone and soft tissue tumors, but it helps to identify the full extent of a lesion at the outset of the examination. We find that for tumor cases after running the scouts that a wide field-of-view (wfov) STIR series, usually in the coronal plane, helps to plan the rest of the examination. This is particularly true in lower limb cases where, by using Tim planning, we can cover the whole limb or joint to joint (for example from above the hip to below the knee or to below the ankle) to show the full extent of related

edema, identify skip lesions and demonstrate potential lymph node involvement.

- We always run all sequences to cover the whole lesion. It is important that these slices, particularly the transverse T2 fatsat, also cover the full extent of the edema not just the identified mass lesion. The transverse T1 and post contrast transverse fatsat T1 scans should cover the same area. This is important to accurately identify the tumor margins prior to surgical intervention or radiotherapy. This is also true for non-tumor MSK imaging involving muscle tears, where the extent of edema or haemorrhage should be identified and the extent of muscle retraction should be well demonstrated. Usually contrast is not needed in these cases unless an underlying lesion is suspected.

- Ensure that the basic protocol is tailored to the specific clinical question and size of the lesion being evaluated as well as the patient's ability to cooperate for the length of the examination. This may involve modifying the FOV, resolution and time for each sequence to obtain the best imaging outcome. This is not usually an issue for routine joint imaging where standard protocols are the norm, but it is basis for MSK tumor patients.
- We always finish our MSK tumor cases with a post contrast wfov fatsat T1 to match our original wfov STIR sequence to identify and characterize lesions outside the scope of the primary examination.

Contact

Mark Lourensz
MRI Department
St Vincent's Hospital
41 Victoria Pde
Fitzroy, Vic
Australia 3065
mark.lourensz@svhm.org.au

Whole-Body Diffusion-Weighted MRI of the Bone Marrow in Health and Disease

Anwar R. Padhani¹; Hassan Douis²; Peter Gall³

¹Paul Strickland Scanner Centre, Mount Vernon Cancer Centre, Northwood, Middlesex, UK

²Department of Radiology, Royal Orthopaedic Hospital, Birmingham, UK

³Siemens Healthcare, Erlangen, Germany

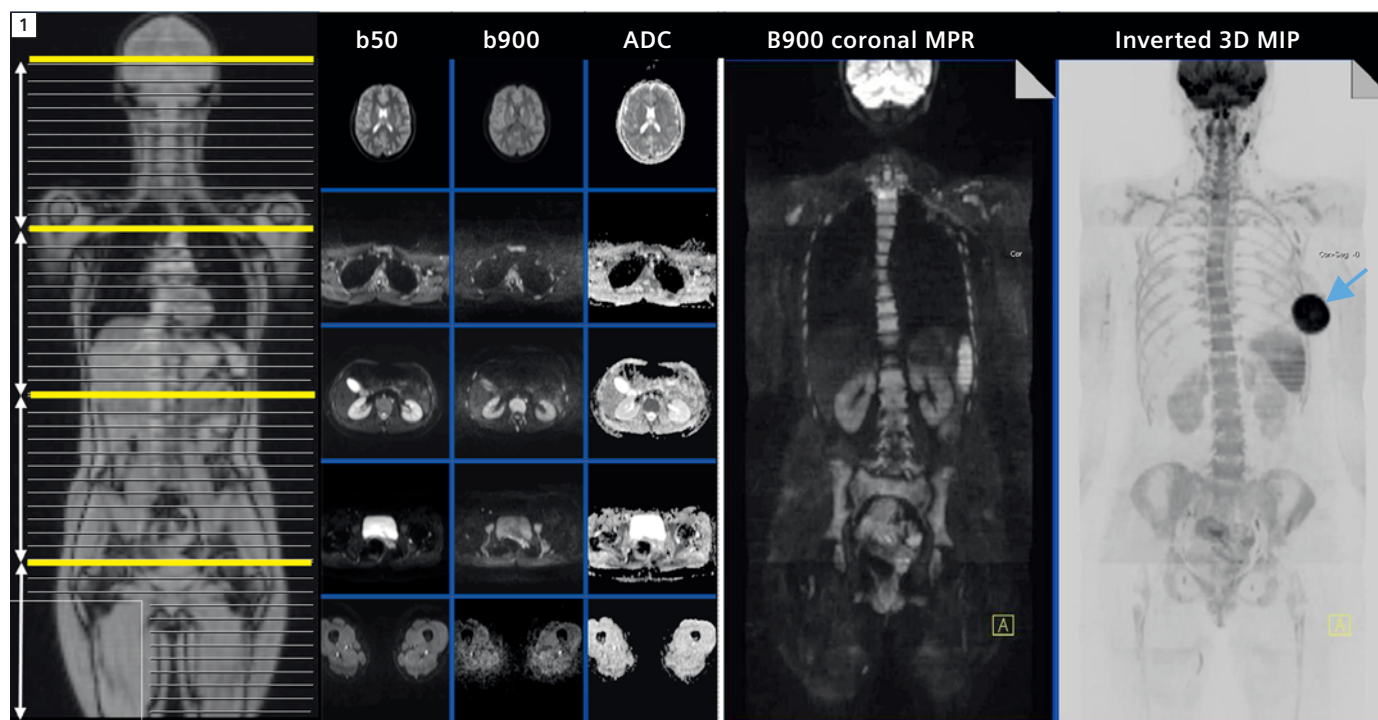
Background

A comprehensive imaging assessment of the skeletal bone marrow requires a multimodal approach because no one technique is able to evaluate all aspects of bone health. Thus, ^{99m}Tc-MDP skeletal scintigraphy and ¹⁸F-Na PET evaluate osteoblastic function, ultrashort TE and CT scans evaluate the structural properties of bone and the osteolytic activity of osteoclasts. Non-specific PET tracers can evaluate bone marrow/tumor membrane transporters and metabolism. Relevant

tracers include ¹⁸F-fluorodeoxyglucose (FDG) for glucose metabolism, ¹¹C/¹⁸F-thymidine (FLT) for DNA synthesis, ¹¹C/¹⁸F-acetate for fatty acid synthesis, ¹¹C-methionine for protein synthesis and ¹¹C/¹⁸F-choline for cell membrane synthesis and degradation [1]. Tumor specific tracers include ¹⁸F-FES (fluoro-estradiol for breast cancer), ¹⁸F-FDHT (fluorodihydrotestosterone for prostate cancer) and engineered antibody fragments that target tumor cell-surface targets such as HER-2/neu (for breast

cancer) and prostate specific membrane antigen (PSMA) [2]. Dynamic contrast-enhanced MRI (DCE-MRI) can evaluate the vascularisation of bone marrow and its cellular content can be assessed using Dixon and diffusion MRI techniques. These techniques have variable clinical availability and whole-body imaging capability.

In recent years, whole-body MRI has emerged as an excellent imaging modality for the evaluation of normal bone, of bone marrow infiltration and the detec-



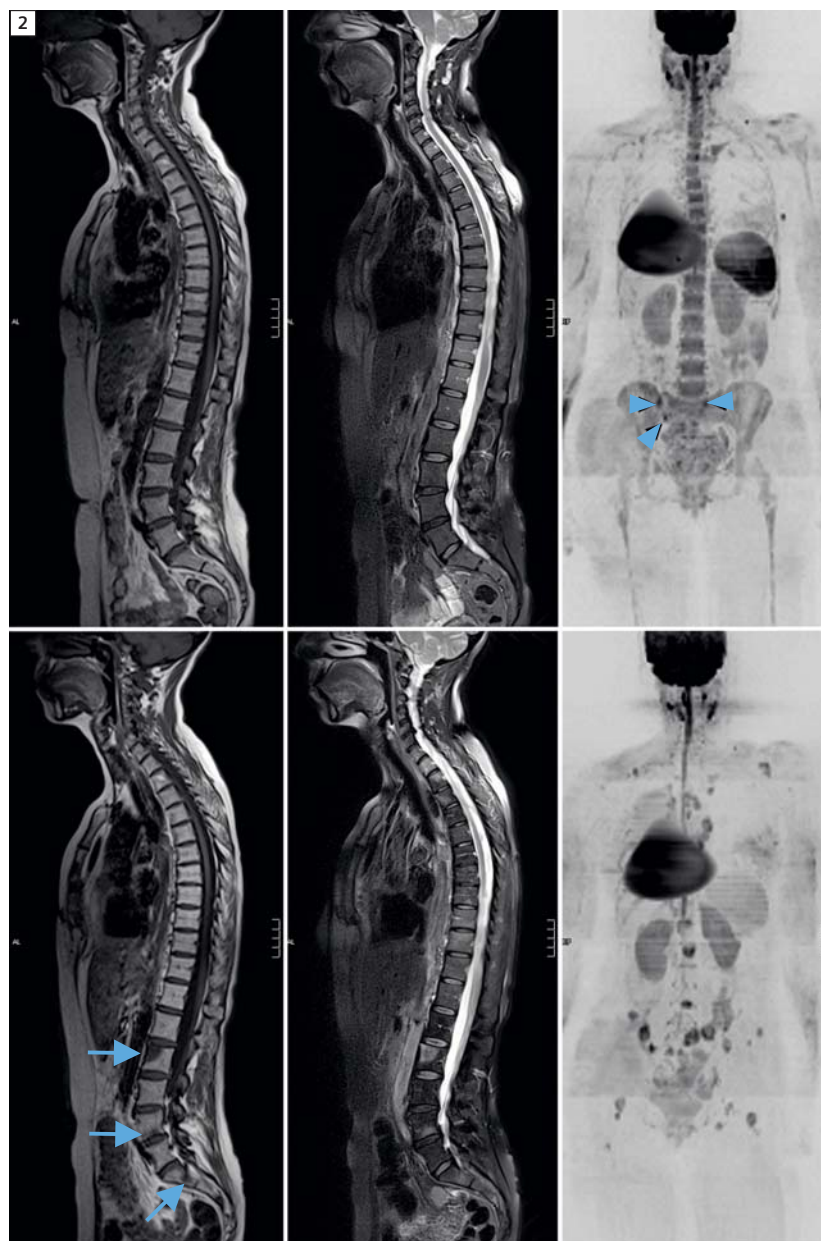
1 WB-DWI workflow. 27-year-old-woman with sarcomatoid left breast cancer (arrow). The bone marrow pattern is normal for this age. Axial DWI from the skull base to the mid-thigh is performed using 2 b-values (50 and 900 s/mm²) with a slice thickness of 5 mm in 4 stations. The b900 images are reconstructed into the coronal plane (5 mm) and displayed as thick 3D MIPs (inverted grey scale). ADC images are computed inline with mono-exponential fitting of b50 and b900 signal intensities.

tion of skeletal metastases due to its exquisite soft tissue contrast, high spatial resolution and lack of ionizing radiation [3]. Whole-body MRI is particularly attractive for children* and young adults because it lacks ionizing radiation. Despite its high sensitivity and high specificity for the detection of skeletal metastases, whole-body MRI has not been widely adopted into daily clinical practice. This is predominantly due to the fact, that whole-body MRI performed with conventional sequences has to be tailored for each tumor type, has long examination times, often requires the administration of intravenous contrast and importantly, it is time consuming to analyse and report [4]. However, there is a strong clinical need for whole-body tumor assessments particularly for cancer patients.

Whole-body diffusion-weighted MRI (WB-DWI) is a new powerful adjunct to anatomical whole-body MRI because it provides a functional assessment of disease burden, can quantify disease extent, does not require the administration of exogenous contrast medium and can be performed in reasonably short examination times. Furthermore, WB-DWI can improve the reading and test performance of anatomical whole-body MR examinations because areas of increased cellularity are depicted as regions of high signal-intensity, therefore allowing an 'at-a-glance' assessment of disease burden and distribution [5]. Whole-body DWI is emerging as a particularly promising imaging technique in the detection, assessment of extent and therapy monitoring of skeletal metastases [6] because it is sensitive to bone marrow cellular density, the relative proportion of fat and marrow cells, water content and bone marrow perfusion.

Technique of whole-body DWI

Most modern high-field MRI systems possess echo-planar and parallel imaging capabilities and allow the use of high-performance gradients which together with phased-array multichannel surface coils, make it feasible for WB-DWI to be implemented into clinical practice. Currently we find that WB-DWI

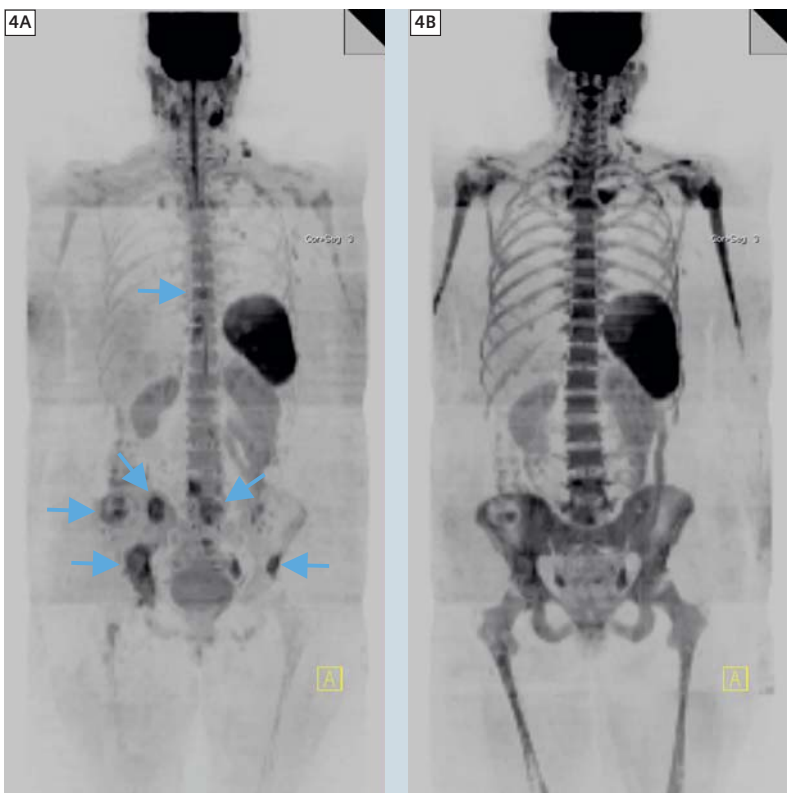


2 Bone marrow hypoplasia due to chemotherapy with disease progression. 49-year-old woman with metastatic breast cancer before and after 3 cycles of carboplatin chemotherapy. Both rows left-to-right: spine T1-weighted spin-echo, spine T2-weighted spin-echo with spectral fat saturation and b900 3D MIP (inverted scale) images. Top row before chemotherapy shows normal background bone marrow pattern with superimposed small volume bone metastases (arrow heads). Bottom row after chemotherapy shows marked disease progression with enlarging and new bony metastases (arrows). Note that bone marrow hypoplasia has developed in the ribs, spine and pelvis. Note reductions of signal intensity of the spleen secondary to iron deposition due to blood transfusions. There is a right sided silicone containing breast enhancement bra pad in place on both examinations.

*MR scanning has not been established as safe for imaging fetuses and infants under two years of age. The responsible physician must evaluate the benefit of the MRI examination in comparison to other imaging procedures.



3 Bone marrow hypoplasia due to aromatase inhibitor therapy. 56-year-old post-menopausal woman with estrogen receptor positive breast cancer on long term anastrozole therapy. Long term therapy of aromatase inhibitors such as anastrozole put women at greater risk for osteoporosis which in turn leads to increased bone marrow fat. Left-to-right: spinal T1-weighted GRE sequence (from the scout views), T1-weighted spin-echo, T2-weighted spin-echo with spectral fat saturation and b900 3D MIP (inverted scale) images. There is some loss of vertebral height of the D9 vertebral body. Note the visibility of the entire length of the spinal cord on the 3D inverted MIP images and ready visibility of the dorsal nerve root ganglia of the brachial and lumbar plexuses. Focal high-signal lesions over the left chest are due to an acneiform rash on the skin.



4 Bone marrow hyperplasia induced by chemotherapy with G-CSF therapy. 50-year-old woman with metastatic breast cancer before and after 3 cycles of erubulin chemotherapy with growth-colony stimulating factor (G-CSF) given to prevent neutropenia. b900 3D MIP (inverted scale) images. Left image shows multiple bone metastases (arrows). Right image after 3 cycles of chemotherapy shows increases in signal intensity of the bone marrow leading to the decreased visibility of the bone metastases. The splenic size has also increased. The increased signal intensity of the background bone marrow should not be misinterpreted as malignant progression.

is best performed at 1.5T using multiple surface coils for signal reception which allows uniform fat-suppression over large fields-of-view. Although imaging at 3T increases the signal-to-noise ratio, WB-DWI remains challenging because of increased susceptibility artifacts and poorer fat suppression.

A multiple-averaged, free-breathing technique is most commonly used for data acquisition. In general, the use of two diffusion sensitizing gradients is sufficient to enable good quality, clinically useable images to be acquired. Low b-value black-blood (50 s/mm^2) combined with high b-value ($800\text{--}1000 \text{ s/mm}^2$) images are used in combination for anatomic depiction, disease detection and for the calculation of apparent diffusion coefficient (ADC) values [5, 7]. Our preferred method for fat suppression uses inversion recovery because it allows uniform fat suppression over large fields-of-view [8].

Our institutional protocol combines whole-body MRI and whole-body DWI done on a 1.5T MAGNETOM Avanto scanner (Siemens Healthcare, Erlangen, Germany) equipped with a continuous moving table option and total imaging matrix (Tim) body surface coils. First, conventional sagittal T1-weighted and T2-weighted fat-suppressed images of the spine are obtained. Subsequently, axial T1-weighted and STIR images from the skull vault to the mid-thigh are acquired using continuous table movement employing multiple breath-holds for image acquisitions of the chest, abdomen, pelvis and upper thighs. Axial DWI from the skull vault to the mid-thigh is then performed using b-values of 50 s/mm^2 and a b-value of 900 s/mm^2 with a slice thickness of 5 mm. The axial DWI acquisition is usually achieved in 4 contiguous stations using a free-breathing technique, with each station taking approximately 6 minutes to acquire. The high b-value images are then reconstructed in orthogonal planes as thin multiplanar reconstructions (5 mm) and as thick 3D maximum intensity projections (MIPs) which are usually displayed using an inverted grey scale. ADC maps are computed inline with system soft-

ware using mono-exponential fitting in which each voxel reflects the tissue diffusivity (units: $\mu\text{m}^2/\text{s}$) (Fig. 1).

Bone marrow imaging on WB-DWI

In order to be able to utilize WB-DWI in the detection, characterization and treatment assessment of skeletal metastases, it is vital to be familiar with the signal distribution of normal bone marrow on high b-value images. Normal adult bone marrow distribution becomes established by the age of 25 years with mixed red bone marrow found in the axial skeleton, the humeral and femoral proximal metaphyses whilst yellow marrow is found in the appendicular skeleton. Thereafter, conversion of red marrow regions to yellow marrow occurs at a slow rate, the speed of conversion being dependent on patient gender and underlying medical conditions [9]. It is thought that the reduced water content [9], the larger-sized fat cells, the hydrophobic nature of fat and poorer perfusion all contribute to lower signal intensities and ADC values of the yellow bone marrow. On the other hand, with increasing cellularity and water content and greater perfusion, mixed yellow-red bone marrow returns higher signal intensities and paradoxically higher ADC values [5, 10–12]. The changing distribution of the normal marrow is exquisitely demonstrated on WB-DWI (Fig. 1). Similarly, both bone marrow hypo- and hypercellularity are also well depicted on WB-DWI. Common causes for bone marrow hypocellularity include chemotherapy (Fig. 2), radiotherapy, myeloproliferative disorders (e.g. myelofibrosis, myelodysplasia), non-malignant marrow disorders (e.g. aplastic anemia), old age and osteoporosis (including drug induced), chronic disease (e.g. renal failure, chronic liver disease, rheumatoid arthritis) and prolonged immobility. In contrast, relative bone marrow hypercellularity is observed in children and adolescents, chronic anaemia, in smokers, chronic cardiac failure, in pregnancy and in patients treated with hematopoietic growth factors such as granulocyte-colony stimulating factors (G-CSF). On



5 Poor visibility of treated metastases and osteoblastic metastases. 69-year-old man with metastatic prostate cancer on long term, third line hormonal therapy with abiraterone being evaluated for rising serum prostate specific antigen (PSA) levels. He has had an excellent response to 2 years of treatment with residual abnormalities in his bone marrow visible on T1-weighted (5A) and T2-weighted (5B with fat suppression) spinal images. No hyperintensity is seen on the b900 3D MIP (inverted scale) image (5C) indicating the absence of osteolytic disease. Bone scan (5D) shows a focal area of osteoblastic uptake in the intertrochanteric region of the left femur (arrow) which is not visible as a discrete region on the b900 3D inverted MIP image.

WB-DWI, bone marrow hypocellularity demonstrates decreased signal intensity on high b-value images with the increased visibility of the spinal cord (Fig. 3). Marrow hypercellularity presents as diffuse increases in signal intensity on high b-values [5, 6]. Changes in background bone marrow cellularity can affect the visibility of bone marrow metastases. Bony metastases can become less conspicuous against increasing background signal intensities when growth colony stimulating factor (G-CSF) is used to prevent chemotherapy induced neutropenia (Fig. 4). On the other hand, the detection of bone metastases is improved in bone marrow that is relatively hypocellular, for example in the older patient or after chemotherapy (Fig. 2).

Skeletal metastases detection

On WB-DWI, skeletal metastases appear as focal or diffuse areas of high signal intensity on high b-values (Figs. 2, 4, 5). It is, however, important to emphasize

that WB-DWI should not be performed nor interpreted in isolation but rather has to be considered as a valued adjunct to anatomical whole-body MRI and therefore needs to be interpreted in conjunction with conventional WB-MRI studies [13]. This assertion has been highlighted in a recent meta-analysis which demonstrated that the high sensitivity of WB-DWI to detect metastases was at the expense of specificity [3]. Causes for false-positive findings are bone marrow edema caused by fractures, osteoarthritis, infection, bone infarcts, vertebral hemangiomas, isolated bone marrow islands and bone marrow hyperplasia due to G-CSF (Fig. 4). However, many of these false-positive findings can be overcome by correlating high b-value DW images with ADC maps and anatomical sequences [5].

In contrast, causes for false-negative findings are low levels of bone marrow infiltration such as in smoldering multiple myeloma or when background bone marrow hyperplasia obscures the pres-

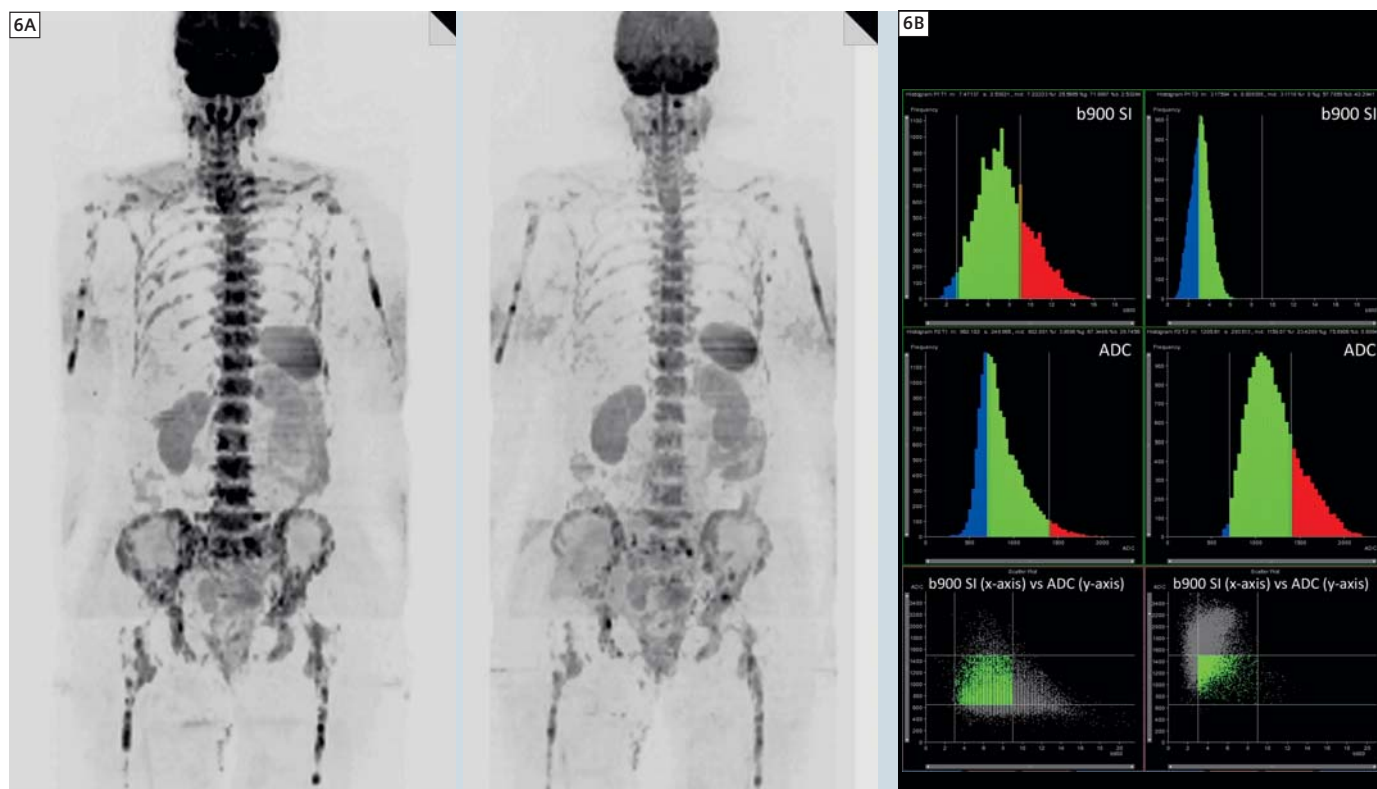
ence of metastases. Similarly, the detection of skeletal metastases on WB-DWI may be impaired in areas of macroscopic movement such as the anterior ribs and sternum. Visibility of skull vault infiltrations can be impaired because of the adjacent high signal of the brain. The visibility of skull base disease is impaired because of susceptibility effects. Another important cause for false-negative findings is successfully treated malignant disease and sclerotic metastases (Fig. 5). In general, lytic lesions are better detected than sclerotic or treated lesions on WB-DWI. This is due to the lower

water and cellular content of sclerotic and treated metastases [10, 14]. Diffusion-weighted MRI is better at detecting skeletal lesions from smaller cancer cell size infiltrations such as those due to breast cancer, myeloma, lymphoma and small cell tumors such as neuroendocrine tumors compared to bony metastases from clear cell cancers of the kidneys.

Therapy assessment of skeletal metastases on WB-DWI

Successful treatment of skeletal metastases is characterized by tumor cell death which results in increased water

diffusivity. On WB-DWI, this leads to marked increases of ADC values. The extent of ADC increases after successful therapy is thought to be related to mechanism of tumor cell death. It has been proposed that therapies which result in necrotic cell death may result in higher ADC values than treatment regimes which result in non-necrotic tumor cell death. This is thought to be due to the fact that necrotic cell death is associated with an inflammatory response which results in increased tissue water. Signal intensity changes on high b-values images after successful therapy are more



6 Therapy response in metastatic breast cancer. Serial changes in a 64-year-old woman with metastatic breast cancer responding to treatment with FEC (Fluorouracil (5FU), epirubicin and cyclophosphamide) chemotherapy with bisphosphonates. **(6A)** b900 3D MIP (inverted scale) images before (left column) and after 3 cycles of treatment (right column). A diffuse pattern of metastatic bone disease is seen pre-treatment that decreases in extent and signal intensity indicating disease response. There are a few focal areas of persistent signal hyperintensity post-therapy indicating likely active disease. **(6B)** Histogram analysis of a pelvic volume of interest defined on b900 images of the pre-treatment examination and applied to the second examination after robust image registration. Threshold histograms of muscle normalized b900 signal intensity (top row) and ADC values (middle row), and pixel scatter plots (bottom row) of normalized b900 signal intensity (x-axis) and ADC values (y-axis). The control lines on the histograms and scatter plots are placed on 3 and 9 for normalized b900 signal intensity and 650 and 1500 $\mu\text{m}^2/\text{s}$ for ADC values. The histograms show reductions in signal intensity (more blue pixels and less overall spread) on top row accompanied by increases in ADC values (more green and red pixels). Note how the pixel scatter plot moves to the top left. Analyses were done using OncoTreat* software (Works-in-progress, Siemens Healthcare, Erlangen, Germany).

*This information about this product is preliminary. The product is under development and not commercially available in the U.S., and its future availability cannot be ensured.

varied, but in most cases decreases in signal intensity are seen (Fig. 6).

Occasionally, successful treatment response may demonstrate persistent high signal intensity on high b-value images but with an associated increase in ADC-values. This appearance is termed 'T2 shine-through' and is due to tumor necrosis. It is thus prudent to always correlate high b-value images with ADC values when interpreting WB-DWI in order to avoid misinterpreting persistent high signal intensity on high b-value images as non-responding disease. Another pattern is a decrease in signal intensity on high b-values associated with unchanged ADC values or slight decreases in ADC values. Our experience from comparison with CT examinations, Dixon images and anatomical MRI studies suggests that this pattern may be due to sclerosis or fibrosis. We have classified this pattern as indeterminate and therefore take into account other radiological and clinical findings for response assessment. By contrast, patients who fail to respond to therapy usually demonstrate persistent or increasing bone marrow hyperintensity on high b-value images. In the context of disease progression, a decrease or no change in ADC values can be observed because of increasing in tumor cell density within the confines of a fixed bone marrow space. Small increases in ADC values can also be observed in progressive disease (but of a much smaller magnitude compared to responding lesions). For this reason we use an upper ADC cut-off value derived from untreated patients in order to differentiate responders from non-responders. This cut-off value is likely to be dependent on the choice of b-values utilized and the tumor type [5, 6].

Clinical indications

At our institution, we have performed more than 1,200 WB-MRI examinations incorporating diffusion MRI in the last four years using it for bone marrow metastasis detection and therapy monitoring for a variety of cancer types – principally in breast and prostate cancer and multiple myeloma. It is increasingly

being used for the evaluation of patients with melanoma, lymphoma and renal cancer. We have also found it valuable for the examination of children* and young adults, pregnant* women with cancer and in patients with impaired renal function or allergies when there is a contraindication to the intravenous injection of contrast medium.

Conclusions

WB-DWI has emerged as a powerful imaging tool in the detection, characterization and for monitoring of treatment response of tumors. It particularly excels in the detection and disease extent assessment of bone marrow lesions as well as in the evaluation of therapy response of skeletal lesions. It is however important to emphasize the fact that WB-DWI has to be interpreted in conjunction with conventional whole-body MRI sequences in order to avoid pitfalls in diagnoses. There is an urgent need to better understand the biologic basis of treatment-related changes. Furthermore response criteria need to be established and tested in prospective clinical studies. Nevertheless, WB-DWI demonstrates great potential in the evaluation of bone marrow lesions because it is quick to perform, can be incorporated into standard clinical protocols and can potentially answer clinical questions regarding tumor response more reliably than conventional imaging modalities.

*MR scanning has not been established as safe for imaging fetuses and infants under two years of age. The responsible physician must evaluate the benefit of the MRI examination in comparison to other imaging procedures.

Contact

Prof. Anwar R. Padhani, MBBS FRCP FRCR
Paul Strickland Scanner Centre
Mount Vernon Cancer Centre
Rickmansworth Road
Northwood
Middlesex HA6 2RN
United Kingdom
Phone: +44-(0) 1923-844751
Fax: +44-(0) 1923-844600
anwar.padhani@stricklandscanner.org.uk

References

1. Jadvar H. Prostate cancer: PET with 18F-FDG, 18F- or 11C-acetate, and 18F- or 11C-choline. *J Nucl Med* 2011;52:81-89.
2. Mankoff DA, Link JM, Linden HM, Sundarajan L, Krohn KA. Tumor receptor imaging. *J Nucl Med* 2008;49 Suppl 2:149S-163S.
3. Wu LM, Gu HY, Zheng J, et al. Diagnostic value of whole-body magnetic resonance imaging for bone metastases: a systematic review and meta-analysis. *J Magn Reson Imaging* 2011;34:128-135.
4. Schmidt GP, Reiser MF, Baur-Melnyk A. Whole-body MRI for the staging and follow-up of patients with metastasis. *Eur J Radiol* 2009;70:393-400.
5. Padhani AR, Koh DM, Collins DJ. Whole-body diffusion-weighted MR imaging in cancer: current status and research directions. *Radiology* 2011;261:700-718.
6. Padhani AR, Gogbashian A. Bony metastases: assessing response to therapy with whole-body diffusion MRI. *Cancer Imaging* 2011;11 Spec No A:S129-145.
7. Padhani AR. Diffusion magnetic resonance imaging in cancer patient management. *Semin Radiat Oncol* 2011;21:119-140.
8. Koh DM, Blackledge M, Padhani AR, et al. Whole-Body Diffusion-Weighted MRI: Tips, Tricks, and Pitfalls. *AJR Am J Roentgenol* 2012;199:252-262.
9. Hwang S, Panicek DM. Magnetic resonance imaging of bone marrow in oncology, Part 1. *Skeletal Radiol* 2007;36:913-920.
10. Messiou C, Collins DJ, Morgan VA, Desouza NM. Optimising diffusion weighted MRI for imaging metastatic and myeloma bone disease and assessing reproducibility. *Eur Radiol* 2011;21:1713-1718.
11. Hillengass J, Bauerle T, Bartl R, et al. Diffusion-weighted imaging for non-invasive and quantitative monitoring of bone marrow infiltration in patients with monoclonal plasma cell disease: a comparative study with histology. *Br J Haematol* 2011;153:721-728.
12. Nonomura Y, Yasumoto M, Yoshimura R, et al. Relationship between bone marrow cellularity and apparent diffusion coefficient. *J Magn Reson Imaging* 2001;13:757-760.
13. Lecouvet FE, El Mouedden J, Collette L, et al. Can whole-body magnetic resonance imaging with diffusion-weighted imaging replace Tc 99m bone scanning and computed tomography for single-step detection of metastases in patients with high-risk prostate cancer? *Eur Urol* 2012;62:68-75.
14. Eiber M, Holzapfel K, Ganter C, et al. Whole-body MRI including diffusion-weighted imaging (DWI) for patients with recurring prostate cancer: Technical feasibility and assessment of lesion conspicuity in DWI. *J Magn Reson Imaging* 2011;33:1160-1170.

Case Report: Knee MR Imaging of an Osteochondroma in Combination with Melorheostosis

Paul Flechsig, M.D.; Marc-André Weber, M.D.

University Hospital Heidelberg, Department of Diagnostic and Interventional Radiology, Heidelberg, Germany

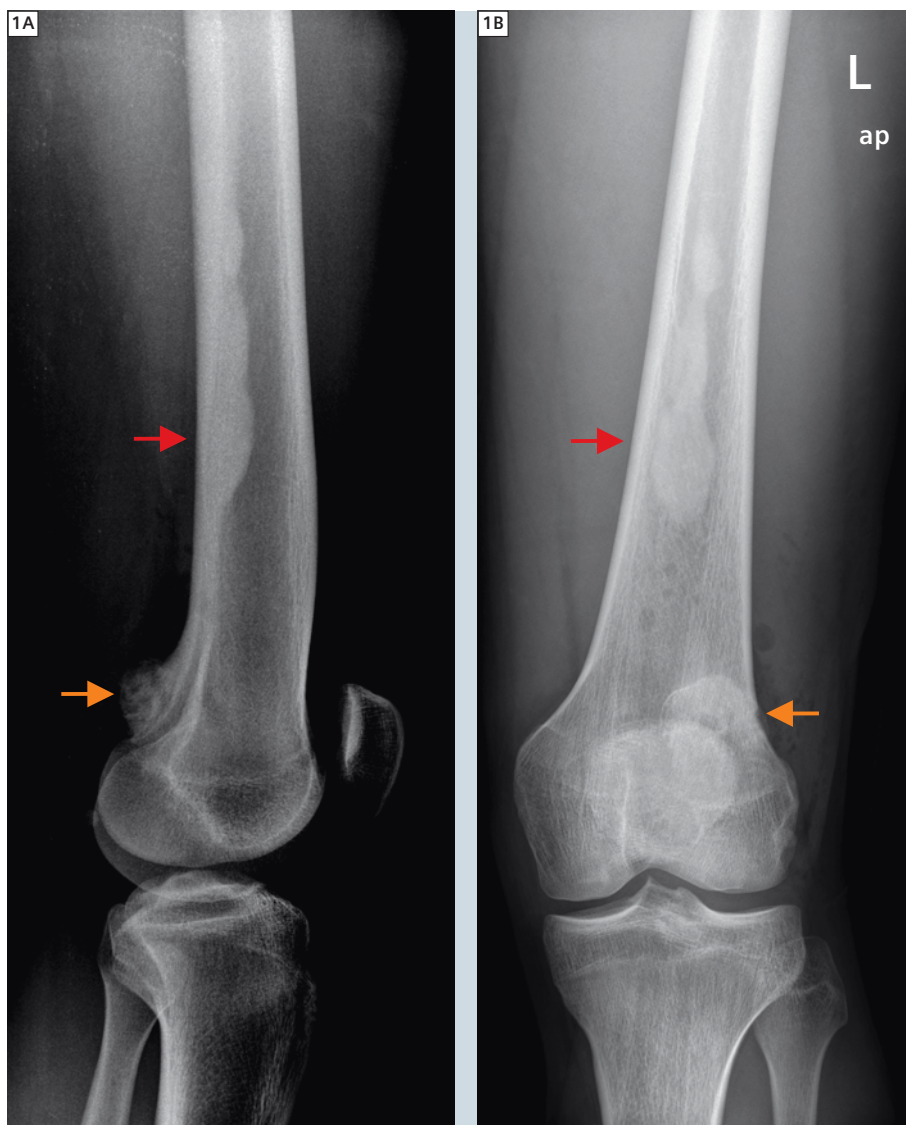
Background

The evaluation of muscular and skeletal pathologies is the domain of MRI with its excellent soft tissue contrast. This allows the evaluation of early changes in bone structure and soft tissue and makes the MRI an irreplaceable tool to rule out benign and malignant processes. In daily patient care imaging speed and high resolution are key elements that are in direct conflict. Therefore the combination of 3 Tesla MR and multi-channel coils is recommended to reduce the acquisition time and still reach excellent quality.

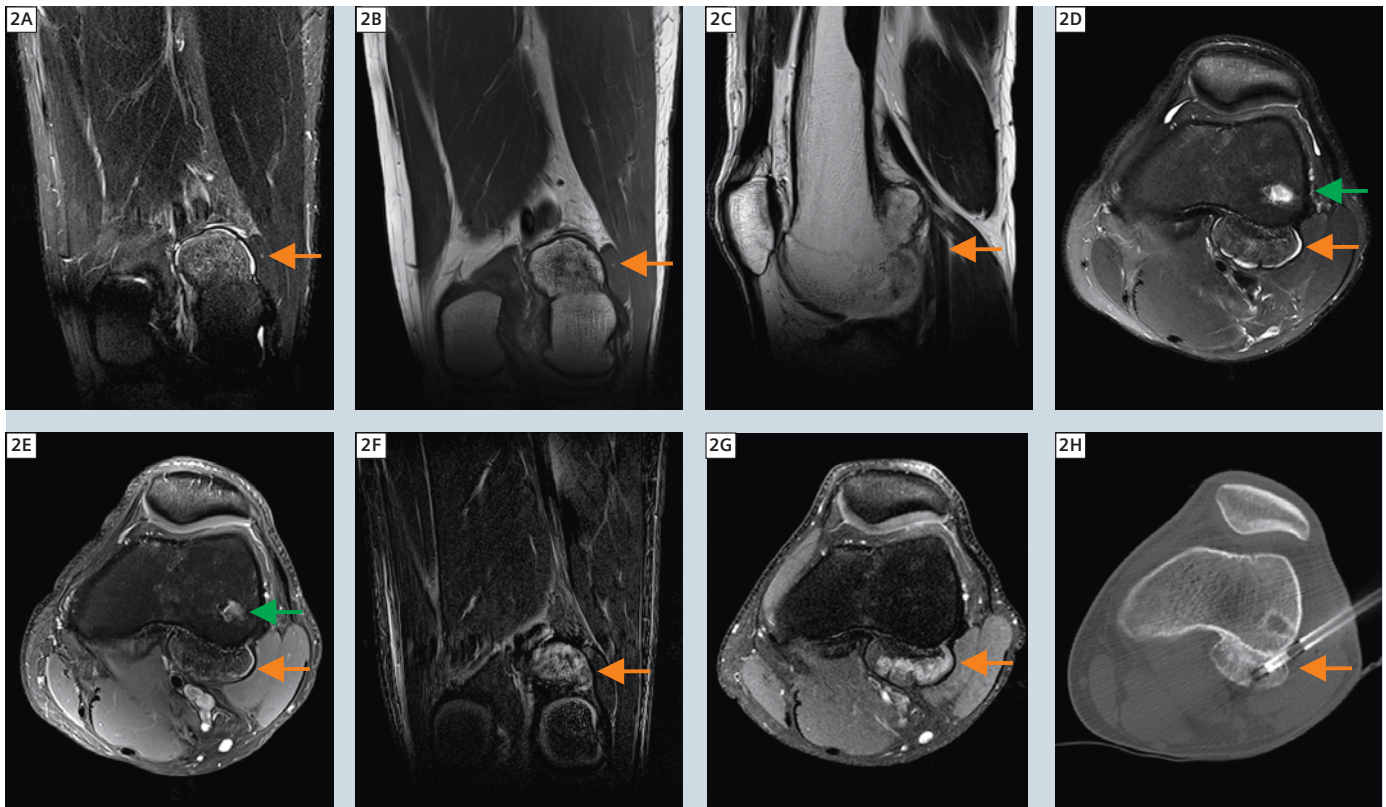
Patient history

In this case we report on the imaging findings of a 20-year-old woman with an unclear bone lesion at the dorsal part of the left distal femur that presented in the ambulance of our orthopedic department. The lesion became symptomatic 6 months earlier, so that an external MR-investigation was performed (Siemens 1.5T MAGNETOM Espree). Here, a bone lesion at the dorsal part of the distal femur was found measuring 20 x 37 mm with a concomitant bone oedema. The differential diagnoses comprise parosteal osteosarcoma, low-grade chondrosarcoma or osteochondroma (cartilaginous exostosis).

After X-ray and MR imaging at the University Hospital Heidelberg the lesion was suspected to be a cartilaginous exostosis measuring 37 mm with a thin coat of cartilage, measuring 2 mm. No soft tissue reaction was found. As an incidental finding a melorheostosis was detected in the dorsal part of the middle and distal third of the femur. In an open biopsy to



1 Conventional X-ray of the left knee (5 days before MRI) with an unclear bordered lesion at the lateral condyle of the distal femur (orange arrow). Intramedullary, corticalis associated lesion at the dorsal part of the middle up to the distal third of the femur (red arrow).



2 MRI of the left knee. **(2A)** Coronal T2w STIR showing the tumor at the lateral femur condyle with a thin coat of cartilage (orange arrow). **(2B)** Coronal T1w SE with bone isointense tumor (orange arrow). **(2C)** Sagittal T2w TSE without soft tissue reaction (orange arrow). **(2D)** Transversal T2w with fat saturation showing the tumor measuring 37 mm at the maximal diameter (orange arrow). Bone defect after open, fluoroscopy guided surgical biopsy that missed the lesion (green arrow). No femoral bone marrow oedema or soft tissue reaction as an argument against a malignant lesion. **(2E)** Transversal ce T1w TSE with fat saturation showing contrast enhancement of the thin coat of cartilage (orange arrow). Biopsy canal (green arrow). **(2F)** Coronal T1w SE images were subtracted from coronal ce T1w SE images. Resulting image shows heterogeneous contrast enhancement of the cartilage (orange arrow). **(2G)** External MRI of the left knee (Siemens 1.5T MAGNETOM Espree): Transversal T1w with fat saturation and contrast enhancement showing the 37 mm measuring bone lesion with enhancing bone marrow oedema. This might indicate active reorganisation or growth (orange arrow). **(2H)** CT-guided biopsy of the bone lesion with proof of intratumoral biopsy sampling (orange arrow).

rule out parosteal osteosarcoma only healthy bone was acquired for histopathological analysis so that CT-guided biopsy was necessary. After biopsy the lesion was proven to be a benign cartilaginous exostosis (osteochondroma) by the pathologists.

Cartilaginous exostoses (osteochondromas) are one of the most common type of benign bone tumors. Every bone can be affected. Nevertheless, distal femur and proximal tibia are the most common locations. Osteochondromas peak in the 2nd to 3rd decade. They have a thin coat of cartilage, but no soft tissue reaction. Low-grade chondrosarcomas have a thicker coat of cartilage (typically 2 cm or more). However, also few cases of parosteal osteosarcomas show a thin

coat of cartilage. Parosteal osteosarcomas are rare, low malignant tumors at the surface of hollow bones, especially at the distal metaphysis of the femur. The tumor peaks in the 3rd and 4th decade. Metastases are rare. Patients show a five year survival of nearly 90% after radical tumor resection.

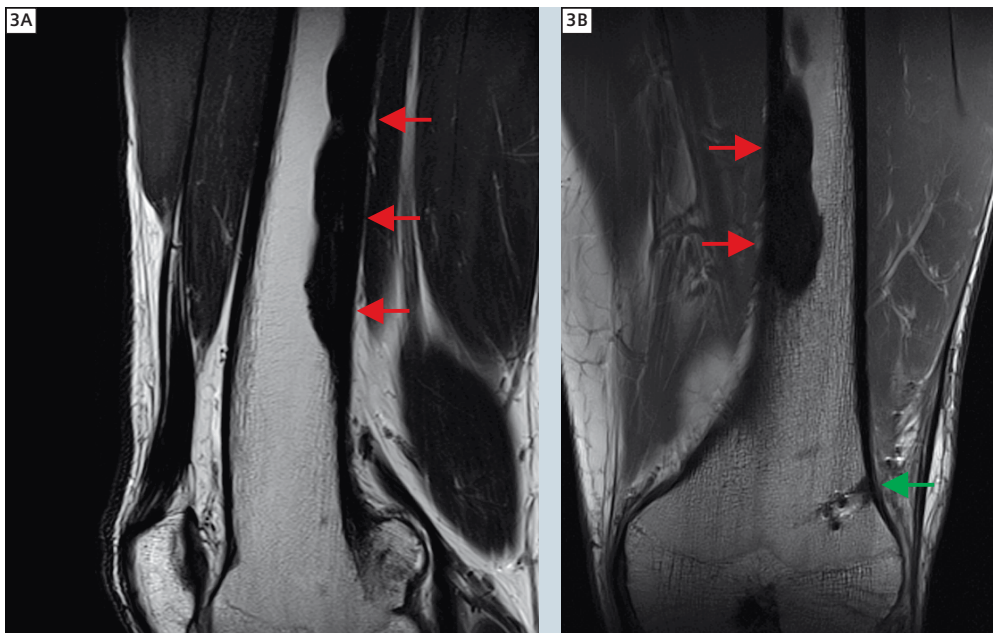
Sequence details

Examination was performed on a 3T open-bore MR-system (MAGNETOM Verio), equipped with 18-channels (Tim [102 x 18] configuration) in combination with a dedicated 15-channel knee coil.

Imaging protocol included:

- coronal T2w STIR (TR 3710 ms, TE 54 ms, pixel spacing (0.558 x

- 0.558) mm², matrix (448 x 400) px², slice thickness 3 mm, bandwidth 243 Hz/px, one average, TA 4:21 min)
- coronal T1w SE (TR 945 ms, TE 11 ms, pixel spacing (0.488 x 0.488) mm², matrix (512 x 512) px², slice thickness 3 mm, bandwidth 150 Hz/px, one average, TA 3:41 min)
- sagittal T2w TSE (TR 7060 ms, TE 92 ms, pixel spacing (0.488 x 0.488) mm², matrix (512 x 346) px²; slice thickness 3 mm, bandwidth 181 Hz/px, two averages, TA 4:51 min)
- transversal T2w with fat saturation (TR 4890 ms, TE 77 ms, pixel spacing (0.246 x 0.246) mm², matrix (448 x 402) px²; slice thickness 3 mm, bandwidth 181 Hz/px, two averages, TA 3:51 min)



3 Additional findings:
(3A) Sagittal T2w TSE with melorheostosis (red arrows).
(3B) Coronal ce T1w SE without fat saturation showing the biopsy canal with little contrast enhancement (green arrow) and the melorheostosis at the dorsal corticalis (red arrows).

- coronal contrast enhanced (ce) T1w SE without fat saturation (TR 945 ms, TE 11 ms, pixel spacing (0.488 x 0.488) mm², matrix (512 x 512) px²; slice thickness 3 mm, bandwidth 181 Hz/px, two averages, TA 3:41 min)
- coronal T1w SE images were subtracted from coronal ce T1w SE images resulting in subtraction images showing only the tissue's contrast enhancement (see Figure 2F).
- transversal ce T1w TSE with fat saturation (TR 917 ms, TE 12 ms, pixel spacing (0.573 x 0.573) mm², matrix (384 x 340) px²; slice thickness 3 mm, bandwidth 181 Hz/px, two averages, TA 4:31 min)

Imaging findings

In X-ray an unclear bordered lesion at the dorsal surface of the distal femur is visible. No calcification of soft tissue. Additionally you see a thickening of the dorsal corticalis in the middle and distal third of the femur, typical for a melorheostosis.

In MRI a 37 x 19 mm measuring, broad based, T1 bone isointense tumor was found at the dorsal part of the distal femur with a thin, T2 signal enhanced coat that had positive contrast enhancement. No reaction of the periosteum and soft tissue. These are typical fea-

tures of an exostosis cartilaginea with a thin coat of cartilage. Nevertheless, corresponding aspects are found in parosteal osteosarcomas, therefore biopsy should be forced. Concerning another potential differential diagnosis of the osteochondroma, a cartilage coat measuring more than 20 mm with increased signal intensity in bone scintigraphy has to be suspected for G1 chondrosarcoma. The biopsy canal of the open biopsy that has missed the tumor is still visible at the lateral femur condyle. Moreover an intramedullary, corticalis associated lesion at the dorsal part of the middle third of the femur is partially pictured, suspected for melorheostosis.

Conclusion

In this case of cartilaginous exostosis (osteochondroma) the combination of high-field strength MRI (3T) and dedicated high-density coils is an irreplaceable tool for the fast and confident evaluation of malignant and benign aspects and helps to raise arguments against a parosteal osteosarcoma or a low-grade chondrosarcoma as differential diagnoses. Also, 3T is beneficial for the evaluation of skip metastases, local lymph-node- and soft tissue involvement including the potential infiltration of vessels and nerves [1]. These pieces of information effect

clinical treatment and, as a consequence, patient's life time and quality of life [2]. Therefore, the usage of MR imaging techniques in patients with unclear bone lesions is under permanent evaluation and its amelioration an ongoing process [3]. The implementation of our 3T open-bore-system in the department is a decisive step in order to advance imaging speed and quality for patients and referring physicians.

References

- 1 Davies AM. [Imaging of primary osteosarcoma]. *Radiologe* 1998 Jun; 38(6):492-501.
- 2 Funovics PT, Bucher F, Toma CD, Kotz RI, Dominkus M. Treatment and outcome of parosteal osteosarcoma: biological versus endoprosthetic reconstruction. *J Surg Oncol* 2011 Jun; 103(8):782-789.
- 3 Murphey MD, Jelinek JS, Temple HT, Flemming DJ, Gannon FH. Imaging of periosteal osteosarcoma: radiologic-pathologic comparison. *Radiology* 2004 Oct; 233(1):129-138.

Contact

Marc-André Weber, M.D., M.Sc.
 Professor of Radiology
 Heidelberg University
 Diagnostic and Interventional Radiology
 Im Neuenheimer Feld 110
 69120 Heidelberg
 Germany
 Phone: +49 6221 966601
 MarcAndre.Weber@med.uni-heidelberg.de

Product News

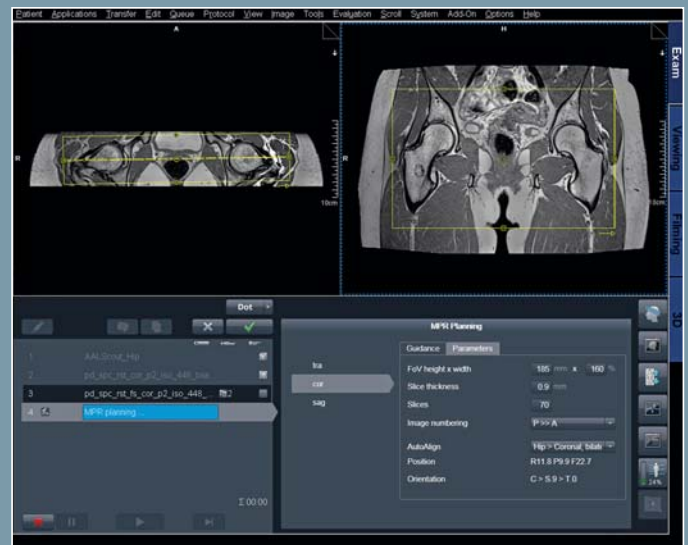
Large Joint Dot Engine

Consistency, standardization and increased productivity in large joint examinations

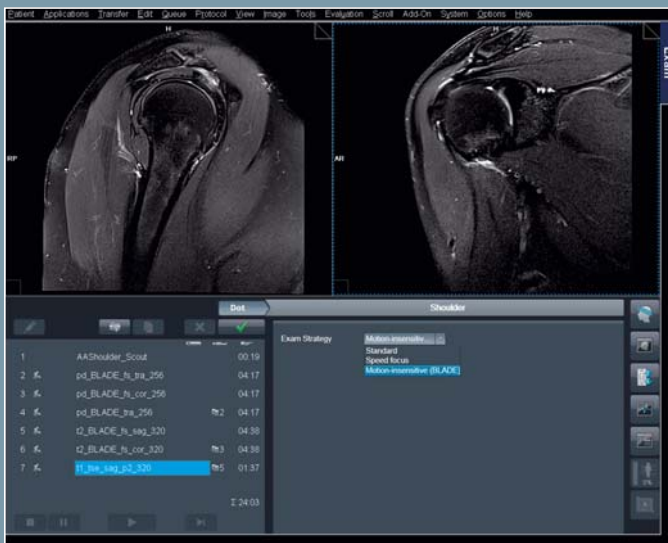
- A single product covering 70 %* of MSK examinations (without spine).
- Standardized examinations and reproducible positioning with AutoCoverage and AutoAlign.
- Personalized exams for individual patient conditions with dedicated exam strategies.
- Advanced *syngo* WARP** functionality for reduction of susceptibility artifacts, such as from MR conditional metal implants
- Preconfigurable automatic reconstructions of 2D images from high resolutions 3D acquisitions

*IMV, 2010

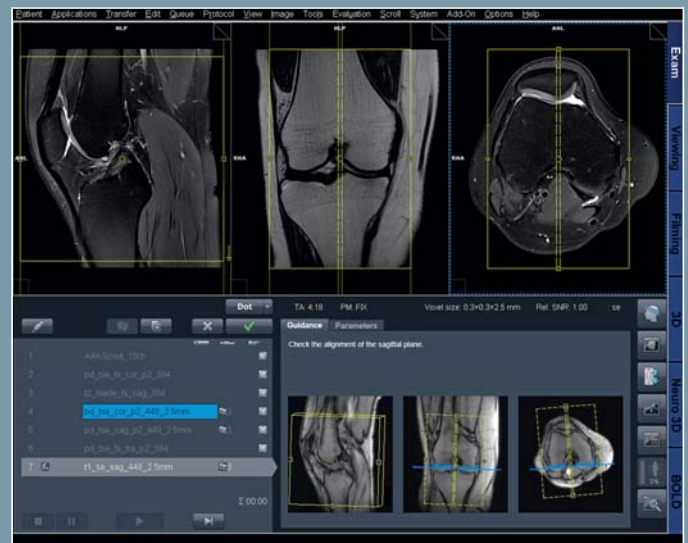
**510(k) pending. Not for sale in the U.S. and in other countries.



MRA planning (Hip)



Exam Strategies (Shoulder)



Guidance View (Knee)

Experience a Dot workflow yourself and hear about other user's favourite Dot feature at:
www.siemens.com/Dot

Case Report:

Sinding-Larsen-Johansson Disease

Axel Goldmann, M.D.

Orthopedic Center Erlangen, Germany

Patient history

An 11-year-old female patient presented with pain in the left knee during extension and flexion manoeuvres of the knee following horseback exercises (maximum extension and abduction of the left lower extremity). Based on physical examination, a partial rupture of the left patellar ligament was suspected. No direct trauma to the patella was reported and mobility of the whole extremity as well as the knee was preserved. The patient was referred to MRI to confirm /

further evaluate the finding. No X-ray examination was conducted.

Material and methods

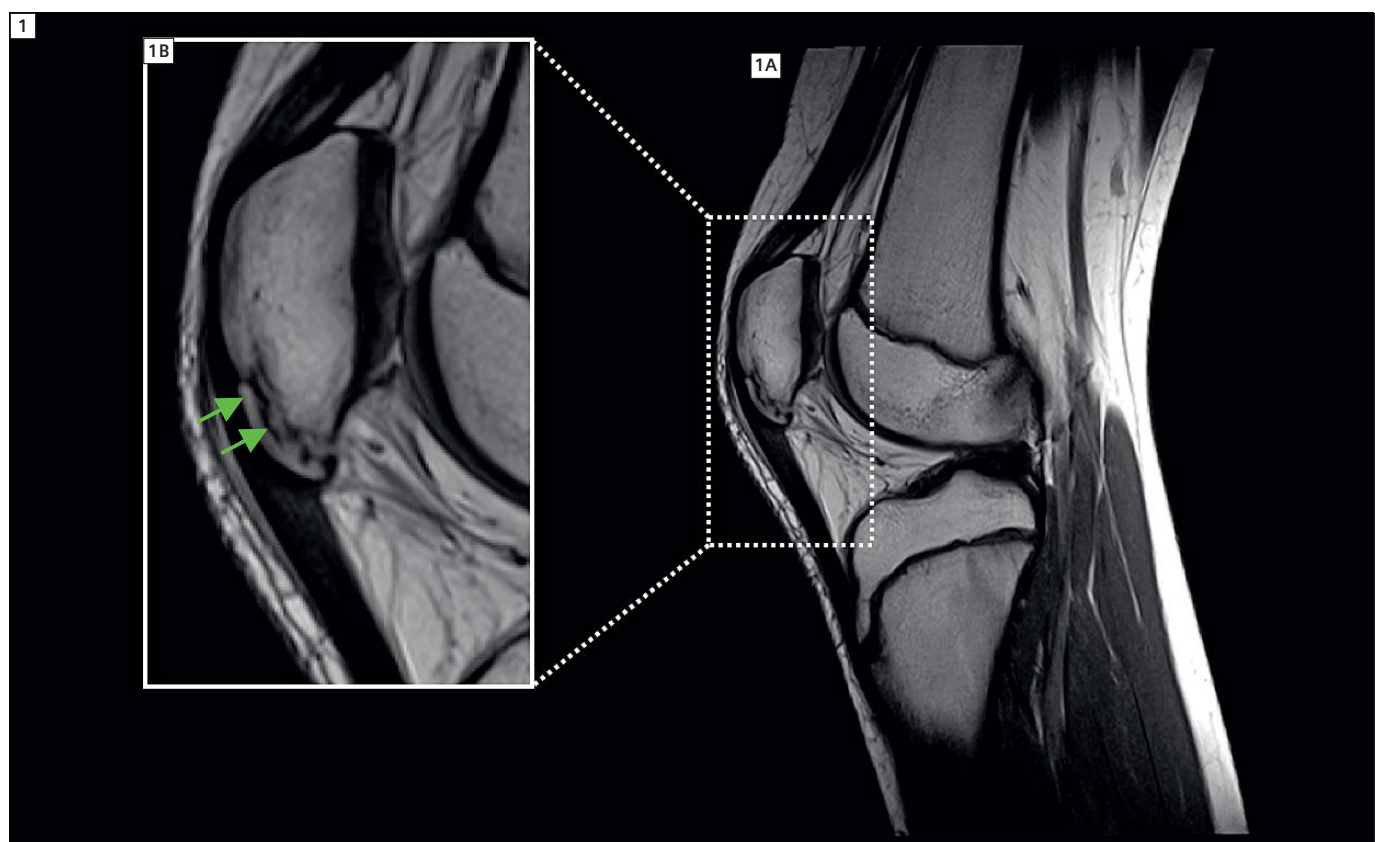
MRI of the knee was conducted at 1.5 Tesla (MAGNETOM Espree; open bore system) in combination with a transmit / receive knee coil. To reduce total imaging time, the imaging protocol consisted of proton density-weighted sequences only. Sequence details were:

■ Transversal PD-weighted TSE with spectral fat saturation:

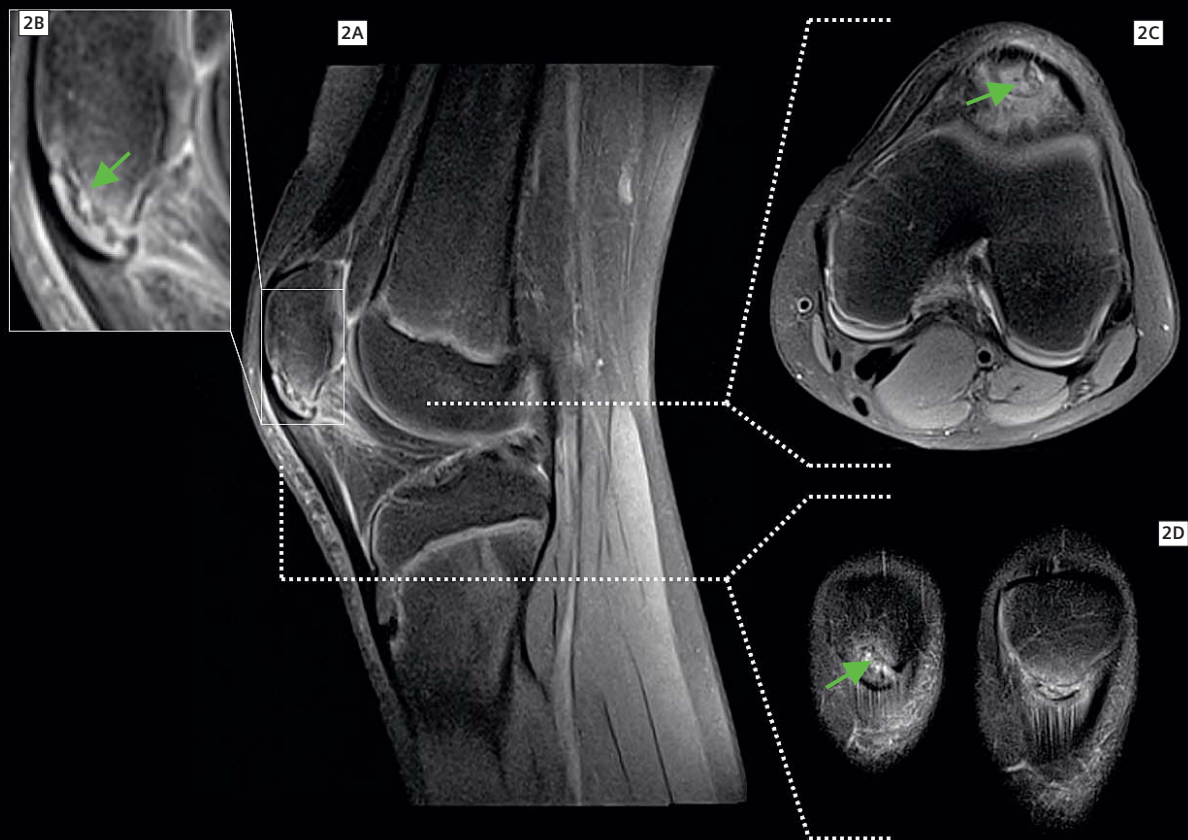
TR / TE = 2000 / 48 ms, SL = 4 mm, FOV = 160 mm², matrix = 320 px², number of slices n = 19, averages n = 1, acquisition time = 2:26 min:s

■ Coronal PD-weighted TSE with spectral fat saturation:

TR / TE = 2000 / 48 ms, SL = 4 mm, FOV = 180 mm², matrix = 384 px², number of slices n = 16, averages n = 1, acquisition time = 2:46 min:s



1 Sagittal PD-weighted TSE of the left knee of an 11-year-old girl.



2 Corresponding sagittal, coronal and transversal PD-weighted TSE images of the left knee in a case of Sinding-Larsen-Johansson disease.

■ **Sagittal PD-weighted TSE with spectral fat saturation:**

TR / TE = 2250 / 39 ms, SL = 3.5 mm, FOV = 189 mm², matrix = 326 x 384 px², number of slices n = 19, averages n = 1, acquisition time = 2:53 min:s

■ **Sagittal PD-weighted TSE:**

TR / TE = 2180 / 46 ms, SL = 3.5 mm, FOV = 189 mm², matrix = 358 x 448 px², number of slices n = 15, averages n = 1, acquisition time = 2:18 min:s

Imaging findings

Sagittal PD-weighted MRI shows an irregular formation of the bone of the lower patellar pole; an irregular line giving the impression of a 'fracture line' is also shown (compare arrows in Fig. 1) and consequently, irregular shape and appearance of the lower patella is demonstrated. In addition, edema of the lower pole of the patella and therefore edema of the insertion of the patellar tendon is demonstrated in all fat saturated sequences (Fig. 2) All other findings were normal and age-related.

Discussion

Due to the nature of the event (no direct trauma), the age of the patient and the imaging findings, MRI has to be interpreted as demonstrating a case of Sinding-Larsen-Johansson disease (SLJD). In 1921 and 1922 the Swedish doctor Sven Christian Johansson and his Norwegian colleague Christian M. F. Sinding-Larsen independently published the first case studies on this overuse injury. SLJD is a painful inflammation of the patellar ligament at the tip of the patella, where the tendon from the tibia attaches. Symptoms are swelling or tenderness at the base of the patella. The condition occurs in active teens who participate in sports that involve running, twisting, and jumping, such as basketball, football, volleyball, soccer, tennis, figure skating, gymnastics or – in our case – exercises on horseback. SLJD belongs to osteonecrosis, since parts of the patella can become necrotic. The prognosis is good and SLJD is considered to be a self-limiting disease, however (conservative) treatment is longterm. In the presented case, the

patient was advised to stop horseback exercises and related training for at least half a year.

References

- 1 Gottsegen CJ, Eyer BA, White EA, Leach TJ, Forrester D. Avulsion fractures of the knee: imaging findings and clinical significance. *Radiographics*. 2008 Oct;28(6):1755-70. Review.
- 2 Peace KA, Lee JC, Healy J. Imaging the infrapatellar tendon in the elite athlete. *Clin Radiol*. 2006 Jul;61(7):570-8. Review.

Contact

Axel Goldmann, M.D.
Orthopädisches Centrum Erlangen
Nägelsbachstraße 49
91052 Erlangen
Germany
Phone: +49 9131 7190-0
goldmann@orthopaeden.com

MRI of the Fetal Skeleton: Tips for Sequence Parameters and Post-Processing Protocol

Marcio Bernardes; Thomas Doring; Heron Werner; Renata Nogueira; Taisa Gasparetto; Tatiana Fazecas; Pedro Daltro; Romeu Cortes Domingues

Clínica de Diagnóstico por Imagem (CDPI, DASA), Rio de Janeiro, Brazil

Fetal¹ skeletal dysplasias are a complex group of developmental bone and cartilage disorders, which usually result from mutated genes. Symptoms can include abnormal growth of the limbs, absence of a limb, duplication of fingers or toes and many other deformities.

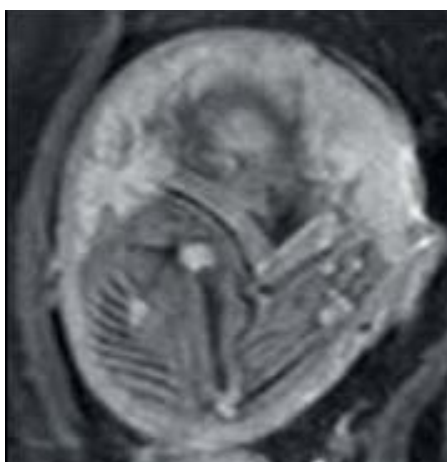
In general, three main technologies are used to obtain images within the uterus during pregnancy: ultrasonography (US), magnetic resonance imaging (MRI) and computed tomography (CT) [1, 4–6]. US is currently the primary method for fetal assessment during pregnancy because it is patient friendly, useful, cost-effective and considered to be safe. When US yields equivocal

results, MRI is generally used, because it provides additional information about fetal¹ abnormalities and conditions in situations where US cannot provide high-quality images [6]. Ultrafast T2-weighted sequences (HASTE) are commonly used in fetal¹ MRI [2, 3, 6]. For further investigation of the fetal¹ skeleton currently 2D echo planar imaging (EPI) sequences are used for the visualization of the skeleton [3]. One limitation of this 2D sequence is that it delivers only images in the acquisition plane. 3D sequences have the advantage that images can be reconstructed in every desired plane. Also multiplanar reconstructions (MPR),

minimum intensity projections (MIP) and volume rendering (VRT) can be created that help for the visualization and identification of the skeleton. For this reason a T2*-weighted 3D TurboFLASH sequence can be applied.

The main interest here is to show in two cases the MRI sequence parameters and post-processing protocol of the fetal¹ skeleton.

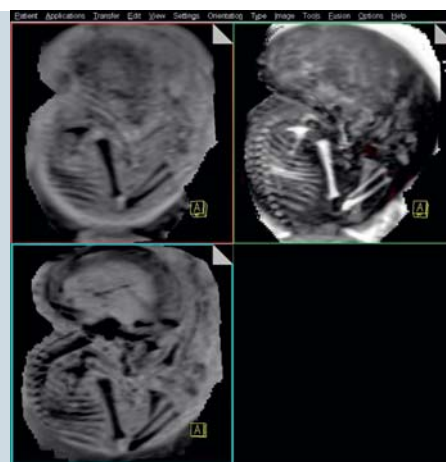
¹MR scanning has not been established as safe for imaging fetuses and infants under two years of age. The responsible physician must evaluate the benefit of the MRI examination in comparison to other imaging procedures.



1A 27-week-old fetus¹ in oligohydramnios. Sagittal oblique T2*-weighted echo planar image: The skeleton appears hypointense and the cartilage as hyperintense.



1B Same fetus¹. T2*-weighted 3D FLASH sequence. The bones appear hypointense whereas the cartilage appears hyperintense (less than in the EPI sequence) to the surrounding tissue.



1C Same fetus¹. Upper left: MPR. Upper right: VRT. Lower left: MinIP.



2A 35-week-old fetus¹ with platyspondilia. T2*-weighted 3D FLASH sequence (sagittal view). The femur and tibia can be clearly identified.



2B T2*-weighted 3D FLASH sequence. The humerus, ulna and radius can be clearly identified.



2C T2*-weighted 3D FLASH sequence. Note the platyspondilia of vertebral body.

MRI protocol

The MRI was performed on the 1.5T MAGNETOM Aera (software version syngo MR D11) using the 18-channel body phase array.

Sequence	epse2d	fl3d
Type	epi	gre
Scan time	27 seg	21 seg
Res [mm ³]	1.7 x 1.7 x 3.5	2 x 2 x 2
TR [ms]	2280	11.1
TE [ms]	46	9.53
FOV [mm]	300	380
Slices	24	60
Gap	0	0
Average	8	1
Concatenations	1	1
Flip angle	90	4
Slice thickness	3.5	2
Bandwidth	1050	475
ETL	46	n/a

References

1. Cassart M, Massez A, Cos T, Tecco L, Thomas D, Van Regemorter N, Avni F. Contribution of three-dimensional computed tomography in the assessment of fetal skeletal dysplasia. *Ultrasound Obstet Gynecol* 2007; 29: 537–543.
2. Nemec U, Nemec SF, Krakow D, Brugger PC, Malinger G, Graham, Jr JM., Rimoin DL, Prayer D. The skeleton and musculature on foetal MRI. *Insights Imaging*. 2011; 2(3): 309–318.
3. Prayer D, Brugger PC, Prayer L. Fetal MRI: techniques and protocols. *Pediatr Radiol* 2004; 34: 685–693.
4. Steiner H, Spitzer D, Weiss-Wichert PH, Graf AH, Staudack A. Three-dimensional ultrasound in prenatal diagnosis of skeletal dysplasia. *Prenat Diagn* 1995; 15: 373–377.
5. Werner H, dos Santos JR, Fontes R, Gasparetto EL, Daltro PA, Kuroki Y, Domingues RC. The use of rapid prototyping didactic models in the study of fetal malformations. *Ultrasound Obstet Gynecol* 2008; 32: 955–956.
6. Werner H, dos Santos JRL, Fontes R, Daltro P, Gasparetto E, Marchiori E, Campbell S. Additive manufacturing models of fetuses built from three-dimensional ultrasound, magnetic resonance imaging and computed tomography scan data. *Ultrasound Obstet Gynecol* 2010; 36: 355–361.

Contact

Thomas Doring
Clínica de Diagnóstico por Imagem
(CDPI, DASA)
Rio de Janeiro
Brazil
thomas.doring@gmail.com

Implementation of Quantitative MRI Evaluation of Tissue Health into Clinical Practice

Erin P. Lucas, M.Sc.; Rachel K. Surowiec, M.Sc.; Charles P. Ho, M.D., Ph.D.

Steadman Philippon Research Institute, Vail, CO, USA



1 Arthroscopic image of patellar cartilage damage. Surface fibrillation is visualized and cartilage stiffness can be assessed, however biochemical integrity cannot be determined.

Introduction

Currently non-surgical and surgical techniques exist which are thought to improve cartilage health. Based on clinical evaluation of pain symptoms, it appears that these preventative and repair strategies are successful. However, there are limited clinical tools available which are sensitive enough for assessing changes in cartilage associated with early osteoarthritis (OA). There is a clinical need for a non-invasive tool to visualize and quantify early cartilage degeneration to assist with treatment planning, longitudinal patient follow-up, and comparison between treatment methods.

Radiographs are commonly used to assess decreased joint space associated with cartilage thinning [1]. However, this approach is limited to moderate to severe diffuse cartilage loss before joint space narrowing will be manifested radiographically [2]. Arthroscopy is currently the gold standard for *in vivo* diagnosis of cartilage degeneration as it allows for the direct assessment of the surface integrity and qualitative assessment and grading of the cartilage stiff-

ness [3], but the internal structure of the cartilage cannot be directly visualized (Fig. 1) [4]. Additionally, subjecting the patient to a second surgery to assess cartilage health and treatment response is avoided. Conventional MR imaging (MRI) allows for non-invasive macroscopic anatomic assessment of the cartilage but is less sensitive to the biochemical changes associated with early cartilage degeneration and developing OA (Fig. 2) [5].

Early degeneration of cartilage starts with biochemical changes (proteoglycan depletion, changes in water content and collagen content, and collagen organization) that cannot be seen with these clinical approaches since there is little macroscopic change [6]. Since the prevention, delay and the potential reversal of cartilage damage has been established as the goals of OA treatment, the development of an appropriate method of assessing early OA is imperative. The ability for fine detection of the biochemical changes in cartilage would allow detection of early OA and response of cartilage to treatment of the joint, including progression of cartilage repair after surgery. Quantitative MR techniques including morphological measurements and biochemical measurements have shown promise for detecting early cartilage damage. This article will review the current state of quantitative MRI for assessment of cartilage health and challenges to be addressed before implementation into standard clinical routine.

Methods for assessing early cartilage degeneration

Quantitative morphological measurements can be measured using conventional MRI sequences and have been shown to vary with OA [6]. Cartilage volume and thickness have been shown to be a more sensitive predictor of OA progression than validated qualitative scor-

ing methods in MRI [7]. Significant changes in cartilage thickness have been observed between one and two-year follow-ups of OA patients [8]. It has also been reported that MRI based volumetric measurements of the knee can demonstrate change that is undetectable via radiographs [9]. However, total volume may not reflect chondral fraying, fissuring, or even small chondral defects. Assessing cartilage surface roughness by means of curvature quantification has been proposed as a method of evaluating damage [6, 10]. The method depends on mathematical descriptions of cartilage surface topography which is derived by fitting B-spline surfaces to segmented cartilage data [11, 12]. This technique would be highly influenced by resolution and contrast between cartilage and joint fluid. Congruency of cartilage surfaces such as the tibio-femoral articular surfaces has also been shown to a predictor of OA [13]. While morphological measurements have clinical usefulness for longitudinal tracking of cartilage health, biochemical changes occur before gross tissue loss, thus morphologic measures are not sensitive to the earliest signs of OA.

Quantitative cartilage MRI sequences such as T2, T2*, dGEMRIC¹, Sodium, CEST, Diffusion-Weighted Imaging (DWI), and T1_{rho}-mapping have been shown to be sensitive to biochemical changes in cartilage [14]. Studies in the knee, hip, shoulder, and ankle have shown significant changes in mapping values associated with various stages of OA, surgical repair techniques, and various pathologies [15–19]. Of these sequences, T2-mapping and dGEMRIC¹ are currently the most widely used in the clinical setting.

dGEMRIC¹ is sensitive to the proteoglycan content, which is one of the earliest changes associated with cartilage degeneration [20]. Studies have shown that dGEMRIC¹ can be used to differentiate between different grades of cartilage degeneration and healthy cartilage and may be a viable option to monitor changes in cartilage quality following intervention [21–24]. Mamisch et al. reported patients with femoral acetabu-

lar impingement exhibited significantly lower dGEMRIC¹ values compared to the control [25]. dGEMRIC¹ imaging does require the use of contrast agent, which has associated morbidity. Additionally, the detailed imaging protocol including exercising after contrast agent injection and the time between administration of the contrast and the image acquisition presents potential sources of variability between centers. When protocols are strictly followed, the test re-test has been shown to be high [26] but the additional time and resources required with this technique may not be feasible in all clinical settings.

T2-mapping is a non-invasive imaging technique that has also been shown to be sensitive to cartilage water content and structural organization [27]. Using the Osteoarthritis Initiative (OAI) dataset, it has been shown that OA subjects, subjects with risk factors for OA, and healthy individuals without known risk factors for OA have significantly different T2 values [28]. T2-mapping has also been used to track cartilage healing after cartilage repair surgery such as matrix-associated autologous chondrocyte transplantation (MACT), osteochondral autograft transplantation (OATS), and microfracture therapy [29–31]. Welsh et al. showed that mean T2 values vary between techniques, and that cartilage repair after microfracture does not return to normal zonal organization, while with MACT there is a zonal organization [30]. In an equine study, White et al. showed T2 values were significantly different between histological findings of fibrocartilage and hyaline cartilage [31].

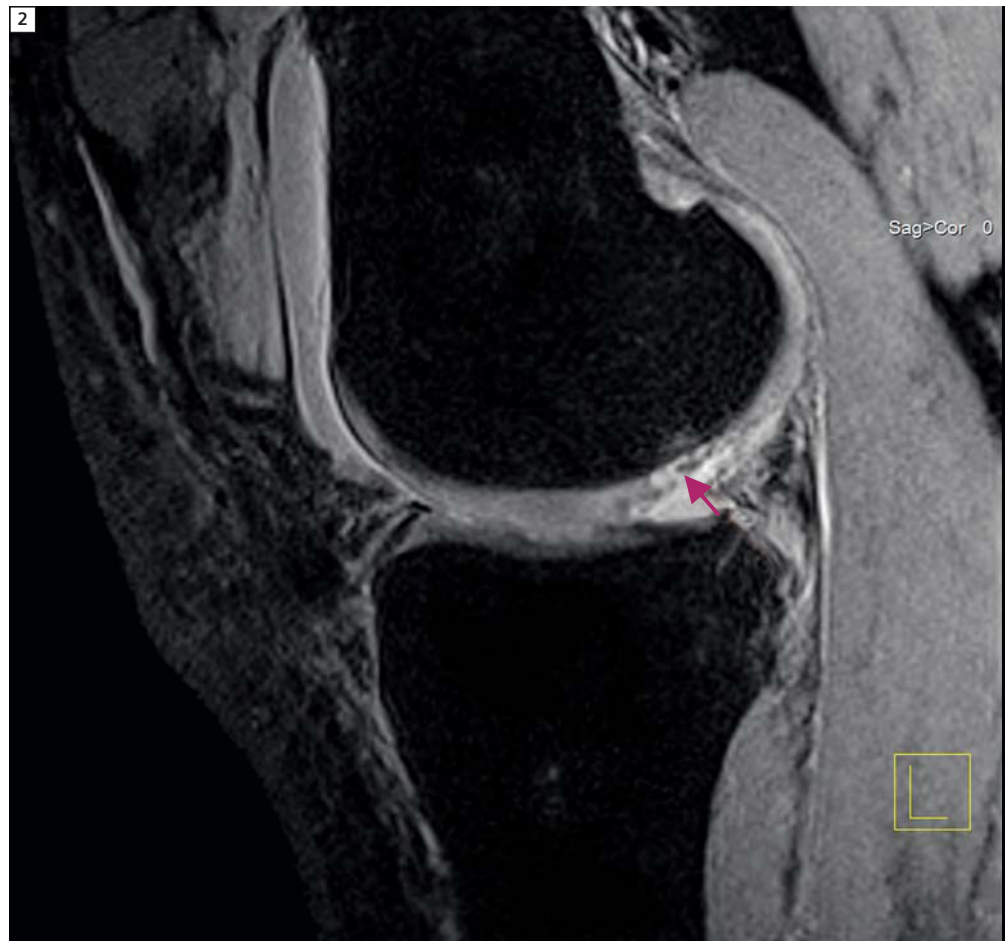
Current limitations of quantitative MRI mapping

While many researchers have shown differences in various quantitative MRI techniques between healthy populations and those with OA, quantitative cartilage mapping is still not commonly used in the clinical setting. There is a need to document specific values associated with healthy cartilage, cartilage repair tissue, and various grades of cartilage damage. Such values have been

¹A licensed physician may choose to use FDA-approved contrast agents in conjunction with an MRI exam, based on his/her medical opinion and discretion and in accordance with the instructions for use and indications for use supplied by the pharmaceutical manufacturer for the contrast agents.

reported, however, there is large variation in these values across literature. T2-mapping values, for example, are highly affected by external factors such as the environment, scanning hardware, sequence parameters, joint loading, calculation technique, and post-processing techniques [28, 32–37]. Typically differences in T2 values of healthy cartilage and cartilage with OA are 2–12 ms [18, 30, 38, 39]. Koff et al. reported the average difference in T2 values between different calculation methods to be approximately 5 ms which highlights the difficulty of comparing different studies and implementing results into clinical practice [32]. Some authors have proposed other analysis to reduce variability such as normalization of values to adjacent cartilage and quantification of the spatial distribution of values rather than analyzing absolute values [28, 29, 40–42].

Some investigational studies have been conducted measuring reproducibility of quantitative mapping techniques performed at a single site [26, 43]. These studies have the potential to overestimate the reliability and thus multicenter studies are needed. Mosher et al. evaluated the reproducibility of morphologic and biochemical (T2 and $T1_{\rho}$) MRI biomarkers across five sites using two different vendors [44]. Reproducibility of morphologic measurements were found to be high; however, T2 reproducibility ranged from good to high and $T1_{\rho}$ ranged from poor to fair [44]. It was reasoned that the lower in-plane resolution of the $T1_{\rho}$ source images may have accentuated the lower reproducibility of the $T1_{\rho}$ measurements. The Osteoarthritis Initiative (OAI) has created a public resource of imaging data associated with knee OA using a single protocol acquired at four study sites [45]. Quality assurance measures were assessed with a goal of ensuring that image data acquired from each of the four sites MR systems could be pooled accurately and reliably [46]. With the use of a phantom, T2 values were generally comparable between sites and, except for one site, the values were relatively stable over time. A limitation of this study was that



2 Sagittal proton density-weighted fat suppressed MR image showing advanced cartilage damage. Morphologic damage can be visualized, but biochemical state is unknown.

T2 measurements were assessed by means of a phantom and not assessed *in-vivo* or evaluated between healthy and degenerated cartilage. Currently analysis of cartilage voxel values (such as T2 values) requires manual or semi-automatic segmentation of the cartilage which is time intensive and adds potential variability [33, 47–50]. Raters must be trained to perform manual segmentation to ensure accuracy and to reduce variability. The time required for manual segmentation is not feasible in clinical routine. Semi-automated segmentation has been developed, although the processing time is still too long for a fast paced clinical setting [51]. The most accurate cartilage segmentation is performed on 3D sequences with isotropic voxels such as DESS, FLASH, and SPACE sequences. The

segmentation must then be registered to the quantitative sequences to acquire the quantitative data. The segmentation accuracy is highly dependent on the sequences used [52]. Delineation between cartilage and bone is most accurate performed on gradient-echo sequences [53]; however, gradient echo sequences have a smaller dynamic range within the cartilage and bone compared to turbo-spin echo sequences which reduces the sensitivity to cartilage degeneration and bone edema. Currently there is no universal sequence for cartilage segmentation, biochemical analysis, and clinical diagnosis. There have been attempts to use 3D DESS sequences to segment the cartilage and calculate 'T2d' values using the two DESS echoes, but this needs further validation, and again, uses a gradient echo

sequence with clinical limitations.

Requirements for practical clinical application of quantitative MRI mapping

In order for quantitative MRI cartilage mapping to become more clinically useful, reproducibility of the quantitative mapping technique and values is essential. The causes for variability between time points and between centers need to be more clearly understood and addressed. An imaging protocol for cartilage health quantification should then be agreed upon within the clinical community. This protocol must fit within the routine clinical imaging time and include the images needed for cartilage quantification without taking away from clinical diagnostic ability. Additionally the optimal method of quantitative cartilage analysis should be determined such as which sequence to use and how to analyze the values (mean, zonal variation, ratios, and/or texture analysis) [28, 41, 44]. Once these standardized protocols are developed, additional studies are needed to determine specific values or distribution of values which are associated with healthy and damaged cartilage.

Finally, automated segmentation of the full cartilage volume is needed for quantitative analysis of the mapping results and tracking patient progress over time. Current FDA approved T2-mapping software packages require manual segmentation of each slice which is not clinically practical and requires the MRI technologist to select the slices to segment. The cartilage should also be automatically divided into clinically relevant subregions using reproducible landmarks to allow for correlation with surgical findings and longitudinal tracking of cartilage health. There have been several different subregions used for analysis in literature [49, 54, 55], but a standardized set of clinically relevant subregions needs to be agreed upon. If automated segmentation is performed on a separate scan other than the mapping scan, automated registration is needed in

order to extract the values associated with cartilage. The scan on which auto-segmentation is performed must also be of clinical value and fit within the allotted patient scan time.

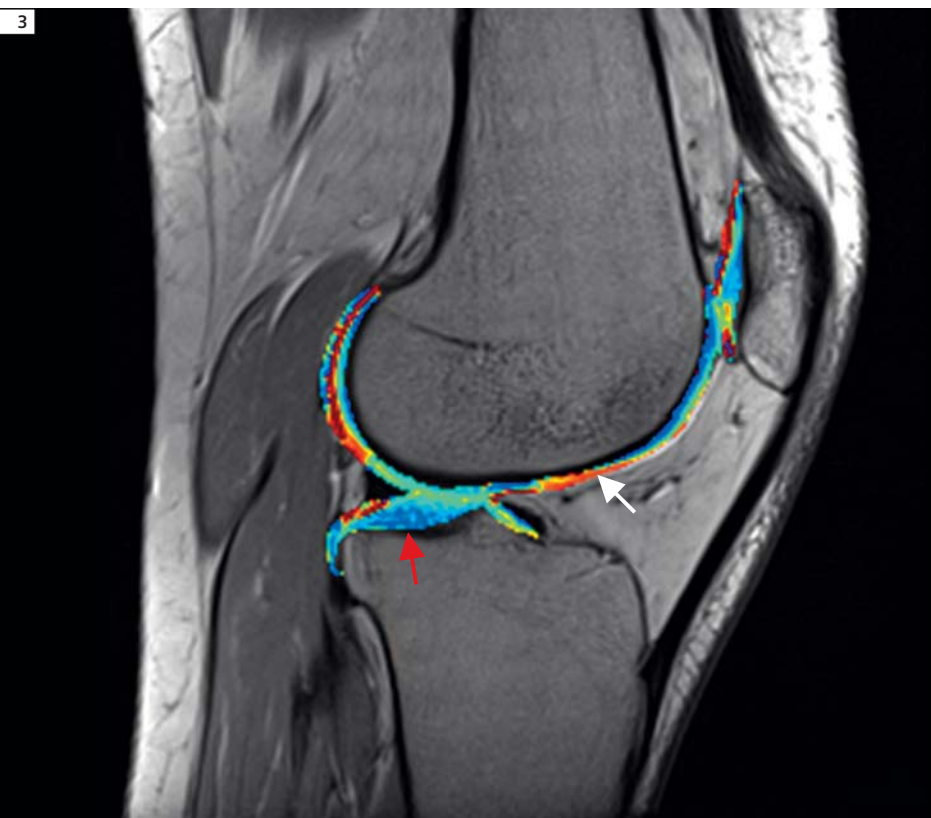
Clinical applications of quantitative MRI mapping

If quantitative cartilage mapping could be successfully implemented into the clinical workflow there are many clinical applications. Clinically meaningful color scales could be applied to cartilage mapping overlays for qualitative assessment (shown in Figure 3), and quantitative data could be analyzed to help in clinical decision making. Quantitative mapping could be used for treatment planning and tracking a patient's progress over time. Cartilage thickness is already used for clinical decision making. In the hip, joint space of less than 2 mm has been correlated with poor success rates after surgery [56]. The current biochemical state of the cartilage may also be related to clinical outcome; however this has yet to be determined. Additionally, the health of the cartilage may help determine whether a conservative approach such as physical therapy can be attempted or if a surgical approach is needed. The cartilage health can then be quantitatively monitored over time to determine the response to treatment and the treatment can be adjusted based on the results. This could also be used to monitor the affect that surgical or nonsurgical intervention of other joint tissues has on the health of cartilage. For example, it has been shown that removal of the meniscus causes early progression to OA [57]. Additionally, non-anatomic joint reconstruction could lead to abnormal loading within the joint and early cartilage degeneration [58]. The cartilage health could be monitored over time in these cases, and early intervention before gross cartilage damage occurs may be possible. Treatment strategies also exist in attempts to stabilize or even reverse cartilage damage but it is currently difficult to determine their effectiveness since there are no clinical tools sensitive enough to track biochemical changes in cartilage.

For example physical therapy rehabilitation techniques such as muscle strengthening and bracing are thought to reduce pressure within joint compartments [59]. Additionally, surgical approaches such as FAI surgery are thought to stabilize and even reverse the progression of cartilage damage but this has not been evaluated non-invasively. Response to intervention strategies such as PRP injections, stem cell injections, or other pharmaceutical interventions could also be investigated with the use of quantitative mapping.

Currently quantitative MRI mapping within the MSK system has been focused on cartilage within the knee and hip. There have been limited studies in other joints and there are equal clinical applications in these joints [60–62]. Additionally, quantitative mapping is not limited to cartilage and also has great application for tracking the health of other tissues. Quantitative analysis of the muscle has shown promise as it has been able to accurately distinguish muscle injury, even at early time points where edema is present [63] and to monitor disease severity such as in Duchene muscular dystrophy [36, 64]. Several prospective parameters such as T2*, T1_{rho}, and T2-mapping have been investigated in the degenerative Achilles tendon [65]. Early sensitivity to meniscus degeneration has been shown with various techniques, with further work needed to understand how the quantitative parameters are related to the structural components of the meniscus [66]. Current spine research has used T2, T2*, and T1_{rho}-mapping of the intervertebral disc evaluating early degeneration and the effects of acute spinal unloading [67–70].

The clinical applications of quantitative mapping are vast, but before the clinical community can fully take advantage of this tool, it must be automated, standardized, validated, and reproducible to be implemented into the clinical care routine.



3 Cartilage T2-mapping image overlaid on sagittal knee MRI. With validation studies of T2 values associated with healthy and damaged cartilage, clinically meaningful color-scales can be adopted. The red arrow depicts an area of potentially healthy cartilage and the white arrow depicts an area of potentially damaged cartilage.

Acknowledgements

The authors gratefully acknowledge the contributions of Jurgen Fripp, Ph.D., ICT Centre, Commonwealth Scientific Industrial Research Organization (CSIRO), for his imaging analysis expertise and suggestions with this paper.

References

- Shelbourne, K.D., et al., *Loss of Normal Knee Motion After Anterior Cruciate Ligament Reconstruction Is Associated With Radiographic Arthritic Changes After Surgery*. The American Journal of Sports Medicine, 2012. **40**(1): p. 108-113.
- Guermazi, A., et al., *Why radiography should no longer be considered a surrogate outcome measure for longitudinal assessment of cartilage in knee osteoarthritis*. Arthritis Research & Therapy, 2011. **13**(6): p. 247.
- Galea, A., et al., *The Accuracy of Magnetic Resonance Imaging Scanning and Its Influence on Management Decisions in Knee Surgery*. Arthroscopy: The Journal of Arthroscopic & amp; Related Surgery, 2009. **25**(5): p. 473-480.
- Acebes, C., et al., *Correlation between arthroscopic and histopathological grading systems of articular cartilage lesions in knee osteoarthritis*. Osteoarthritis and Cartilage, 2009. **17**(2): p. 205-212.
- Wang, Y.X., J.F. Griffith, and A.T. Ahuja, *Non-invasive MRI assessment of the articular cartilage in clinical studies and experimental settings*. World J Radiol, 2010. **2**(1): p. 44-54.
- Dam, E.B., et al., *Automatic morphometric cartilage quantification in the medial tibial plateau from MRI for osteoarthritis grading*. Osteoarthritis and Cartilage, 2007. **15**(7): p. 808-818.
- Sharma, L., et al., *Relationship of meniscal damage, meniscal extrusion, malalignment, and joint laxity to subsequent cartilage loss in osteoarthritic knees*. Arthritis Rheum, 2008. **58**(6): p. 1716-26.
- Wirth, W., et al., *Comparison of 1-year vs 2-year change in regional cartilage thickness in osteoarthritis results from 346 participants from the Osteoarthritis Initiative*. Osteoarthritis Cartilage, 2011. **19**(1): p. 74-83.
- Raynauld, J.P., et al., *Quantitative magnetic resonance imaging evaluation of knee osteoarthritis progression over two years and correlation with clinical symptoms and radiologic changes*. Arthritis Rheum, 2004. **50**(2): p. 476-87.
- Ghosh, S., et al., *Investigation of techniques for the measurement of articular cartilage surface roughness*. Micron, 2012.
- Hohe, J., et al., *Surface size, curvature analysis, and assessment of knee joint incongruity with MRI in vivo*. Magnetic Resonance in Medicine, 2002. **47**(3): p. 554-561.
- Ateshian, G.A., *A B-spline least-squares surface-fitting method for articular surfaces of diarthrodial joints*. J Biomech Eng, 1993. **115**(4A): p. 366-73.
- Tummala, S., et al., *Automatic quantification of tibio-femoral contact area and congruity*. IEEE Trans Med Imaging, 2012. **31**(7): p. 1404-12.
- Crema, M.D., et al., *Articular cartilage in the knee: current MR imaging techniques and applications in clinical practice and research*. Radiographics, 2011. **31**(1): p. 37-61.
- Maizlin, Z.V., et al., *T2 mapping of articular cartilage of glenohumeral joint with routine MRI correlation--initial experience*. HSS J, 2009. **5**(1): p. 61-6.
- Krause, F.G., et al., *Biochemical T2* MR quantification of ankle arthrosis in pes cavovarus*. Journal of Orthopaedic Research, 2010. **28**(12): p. 1562-1568.
- Welsch, G., et al., *Evaluation and comparison of cartilage repair tissue of the patella and medial femoral condyle by using morphological MRI and biochemical zonal T2 mapping*. European Radiology, 2009. **19**(5): p. 1253-1262.
- Li, X., et al., *In vivo T(1rho) and T(2) mapping of articular cartilage in osteoarthritis of the knee using 3 T MRI*. Osteoarthritis Cartilage, 2007. **15**(7): p. 789-97.
- Oneto, J., J. Ellermann, and R. LaPrade, *Longitudinal evaluation of cartilage repair tissue after microfracture using T2-mapping: a case report with arthroscopic and MRI correlation*. Knee Surgery, Sports Traumatology, Arthroscopy, 2010. **18**(11): p. 1545-1550.
- Jazrawi, L.M., et al., *Advances in magnetic resonance imaging of articular cartilage*. J Am Acad Orthop Surg, 2011. **19**(7): p. 420-9.
- Zilkens, C., et al., *Three-dimensional delayed gadolinium-enhanced magnetic resonance imaging of hip joint cartilage at 3T: A prospective controlled study*. Eur J Radiol, 2012.
- Lattanzi, R., et al., *A new method to analyze dGEMRIC measurements in femoroacetabular impingement: preliminary validation against arthroscopic findings*. Osteoarthritis Cartilage, 2012.
- McAlindon, T.E., et al., *Change in knee osteoarthritis cartilage detected by delayed gadolinium enhanced magnetic resonance imaging following treatment with collagen hydrolysate: a pilot randomized controlled trial*. Osteoarthritis Cartilage, 2011. **19**(4): p. 399-405.
- Rutgers, M., et al., *dGEMRIC as a tool for measuring changes in cartilage quality following high tibial osteotomy: a feasibility study*. Osteoarthritis Cartilage, 2012.
- Mamisch, T.C., et al., *Delayed gadolinium-enhanced magnetic resonance imaging of cartilage (dGEMRIC) in Femoroacetabular impingement*. J Orthop Res, 2011. **29**(9): p. 1305-11.
- van Tiel, J., et al., *Reproducibility of 3D delayed gadolinium enhanced MRI of cartilage (dGEMRIC) of the knee at 3.0 T in patients with early stage osteoarthritis*. Eur Radiol, 2012.
- Mosher, T.J. and B.J. Dardzinski, *Cartilage MRI T2 relaxation time mapping: overview and applica-*

- tions. *Semin Musculoskelet Radiol*, 2004. **8**(4): p. 355-68.
- 28 Joseph, G., et al., *Texture analysis of cartilage T2 maps: individuals with risk factors for OA have higher and more heterogeneous knee cartilage MR T2 compared to normal controls – data from the osteoarthritis initiative*. *Arthritis Research & Therapy*, 2011. **13**(5): p. R153.
 - 29 Welsch, G.H., et al., *Evaluation of Cartilage Repair Tissue After Matrix-Associated Autologous Chondrocyte Transplantation Using a Hyaluronic-Based or a Collagen-Based Scaffold With Morphological MOCART Scoring and Biochemical T2 Mapping*. *The American Journal of Sports Medicine*, 2010. **38**(5): p. 934-942.
 - 30 Welsch, G.H., et al., *Cartilage T2 assessment at 3-T MR imaging: in vivo differentiation of normal hyaline cartilage from reparative tissue after two cartilage repair procedures – initial experience*. *Radiology*, 2008. **247**(1): p. 154-61.
 - 31 White, L.M., et al., *Cartilage T2 assessment: differentiation of normal hyaline cartilage and reparative tissue after arthroscopic cartilage repair in equine subjects*. *Radiology*, 2006. **241**(2): p. 407-14.
 - 32 Koff, M.F., et al., *Bias of cartilage T2 values related to method of calculation*. *Magnetic Resonance Imaging*, 2008. **26**(9): p. 1236-1243.
 - 33 Raya, J.G., et al., *T2 measurement in articular cartilage: Impact of the fitting method on accuracy and precision at low SNR*. *Magnetic Resonance in Medicine*, 2010. **63**(1): p. 181-193.
 - 34 Apprigh, S., et al., *Quantitative T2 mapping of the patella at 3.0T is sensitive to early cartilage degeneration, but also to loading of the knee*. *European Journal of Radiology*, 2010(0).
 - 35 Juras, V., et al., *Regression error estimation significantly improves the region-of-interest statistics of noisy MR images*. *Medical Physics*, 2010. **37**(6): p. 2813-2821.
 - 36 Gold, G.E., et al., *Musculoskeletal MRI at 3.0 T: Relaxation Times and Image Contrast*. *American Journal of Roentgenology*, 2004. **183**(2): p. 343-351.
 - 37 Pai, A., X. Li, and S. Majumdar, *A comparative study at 3 T of sequence dependence of T2 quantitation in the knee*. *Magnetic Resonance Imaging*, 2008. **26**(9): p. 1215-1220.
 - 38 Zarins, Z.A., et al., *Cartilage and meniscus assessment using T1rho and T2 measurements in healthy subjects and patients with osteoarthritis*. *Osteoarthritis and Cartilage*, 2010. **18**(11): p. 1408-1416.
 - 39 Mamisch, T.C., et al., *Quantitative T2 Mapping of Knee Cartilage: Differentiation of Healthy Control Cartilage and Cartilage Repair Tissue in the Knee with Unloading – Initial Results*. *Radiology*, 2010. **254**(3): p. 818-826.
 - 40 Dunn, T.C., et al., *T2 relaxation time of cartilage at MR imaging: comparison with severity of knee osteoarthritis*. *Radiology*, 2004. **232**(2): p. 592-8.
 - 41 Domayer, S.E., et al., *T2 mapping in the knee after microfracture at 3.0 T: correlation of global T2 values and clinical outcome – preliminary results*. *Osteoarthritis Cartilage*, 2008. **16**(8): p. 903-8.
 - 42 Haralick, R.M., Shanmugam, K., Dinstein, I., *Textural Features for Image Classification*. *IEEE Trans Biomed Eng*, 1973. **SMC-3**(6): p. 610-621.
 - 43 Newbould, R.D., et al., *T2* measurement of the knee articular cartilage in osteoarthritis at 3T*. *J Magn Reson Imaging*, 2012. **35**(6): p. 1422-9.
 - 44 Mosher, T.J., et al., *Knee articular cartilage damage in osteoarthritis: analysis of MR image biomarker reproducibility in ACRIN-PA 4001 multicenter trial*. *Radiology*, 2011. **258**(3): p. 832-42.
 - 45 Eckstein, F., W. Wirth, and M.C. Nevitt, *Recent advances in osteoarthritis imaging-the Osteoarthritis Initiative*. *Nat Rev Rheumatol*, 2012.
 - 46 Schneider, E., et al., *The osteoarthritis initiative (OAI) magnetic resonance imaging quality assurance methods and results*. *Osteoarthritis Cartilage*, 2008. **16**(9): p. 994-1004.
 - 47 Koff, M.F., et al., *Examiner repeatability of patellar cartilage T2 values*. *Magnetic Resonance Imaging*, 2009. **27**(1): p. 131-136.
 - 48 Stehling, C., et al., *Patellar Cartilage: T2 Values and Morphologic Abnormalities at 3.0-T MR Imaging in Relation to Physical Activity in Asymptomatic Subjects from the Osteoarthritis Initiative*. *Radiology*, 2010. **254**(2): p. 509-520.
 - 49 Pan, J., et al., *Knee Cartilage T2 Characteristics and Evolution in Relation to Morphologic Abnormalities Detected at 3-T MR Imaging: A Longitudinal Study of the Normal Control Cohort from the Osteoarthritis Initiative*. *Radiology*, 2011. **261**(2): p. 507-515.
 - 50 Stahl, R., et al., *T1rho, T2, and focal knee cartilage abnormalities in physically active and sedentary healthy subjects versus early OA patients – a 3.0-Tesla MRI study*. *European Radiology*, 2009. **19**(1): p. 132-143.
 - 51 Stehling, C., et al., *A novel fast knee cartilage segmentation technique for T2 measurements at MR imaging – data from the Osteoarthritis Initiative*. *Osteoarthritis and Cartilage*, 2011. **19**(8): p. 984-989.
 - 52 Frupp, J., et al., *Automatic Segmentation and Quantitative Analysis of the Articular Cartilages From Magnetic Resonance Images of the Knee*. *Medical Imaging, IEEE Transactions on*, 2010. **29**(1): p. 55-64.
 - 53 Friedrich, K.M., et al., *High-resolution cartilage imaging of the knee at 3T: basic evaluation of modern isotropic 3D MR-sequences*. *Eur J Radiol*, 2011. **78**(3): p. 398-405.
 - 54 Goto, H., et al., *A preliminary study of the T1rho values of normal knee cartilage using 3T-MRI*. *European Journal of Radiology*, 2012. **81**(7): p. e796-e803.
 - 55 Hovis, K.K., et al., *Physical activity is associated with magnetic resonance imaging-based knee cartilage T2 measurements in asymptomatic subjects with and those without osteoarthritis risk factors*. *Arthritis & Rheumatism*, 2011. **63**(8): p. 2248-2256.
 - 56 Philippon, M.J., et al., *Outcomes 2 to 5 Years Following Hip Arthroscopy for Femoroacetabular Impingement in the Patient Aged 11 to 16 Years*. *Arthroscopy*, 2012.
 - 57 Bedi, A., et al., *Dynamic contact mechanics of radial tears of the lateral meniscus: implications for treatment*. *Arthroscopy*, 2012. **28**(3): p. 372-81.
 - 58 Prisk, V.R., et al., *Lateral ligament repair and reconstruction restore neither contact mechanics of the ankle joint nor motion patterns of the hindfoot*. *J Bone Joint Surg Am*, 2010. **92**(14): p. 2375-86.
 - 59 Chew, K.T., et al., *Current evidence and clinical applications of therapeutic knee braces*. *Am J Phys Med Rehabil*, 2007. **86**(8): p. 678-86.
 - 60 Domayer, S.E., et al., *Cartilage repair of the ankle: first results of T2 mapping at 7.0 T after microfracture and matrix associated autologous cartilage transplantation*. *Osteoarthritis and Cartilage*, 2012. **20**(8): p. 829-836.
 - 61 Maizlin, Z., et al., *T2 Mapping of Articular Cartilage of Glenohumeral Joint with Routine MRI Correlation—Initial Experience*. *HSS Journal®*, 2009. **5**(1): p. 61-66.
 - 62 Lazovic-Stojkovic, J., et al., *Interphalangeal Joint Cartilage: High-Spatial-Resolution in Vivo MR T2 Mapping—A Feasibility Study*. *Radiology*, 2004. **233**(1): p. 292-296.
 - 63 McMillan, A.B., et al., *Diffusion tensor MRI to assess damage in healthy and dystrophic skeletal muscle after lengthening contractions*. *J Biomed Biotechnol*, 2011. **2011**: p. 970726.
 - 64 Kim, H.K., et al., *Quantitative assessment of the T2 relaxation time of the gluteus muscles in children with Duchenne muscular dystrophy: a comparative study before and after steroid treatment*. *Korean J Radiol*, 2010. **11**(3): p. 304-11.
 - 65 Trattinnig, S., et al., *Advanced MR methods at ultra-high field (7 Tesla) for clinical musculoskeletal applications*. *Eur Radiol*, 2012.
 - 66 McWalter, E.J. and G.E. Gold, *UTE T2 * mapping detects sub-clinical meniscus degeneration*. *Osteoarthritis Cartilage*, 2012. **20**(6): p. 471-2.
 - 67 Stelzeneder, D., et al., *Quantitative in vivo MRI evaluation of lumbar facet joints and intervertebral discs using axial T2 mapping*. *Eur Radiol*, 2011.
 - 68 Zobel, B.B., et al., *T1rho magnetic resonance imaging quantification of early lumbar intervertebral disc degeneration in healthy young adults*. *Spine (Phila Pa 1976)*, 2012. **37**(14): p. 1224-30.
 - 69 Hoppe, S., et al., *Axial T2* mapping in intervertebral discs: a new technique for assessment of intervertebral disc degeneration*. *Eur Radiol*, 2012. **22**(9): p. 2013-9.
 - 70 Trattinnig, S., et al., *Lumbar intervertebral disc abnormalities: comparison of quantitative T2 mapping with conventional MR at 3.0 T*. *European Radiology*, 2010. **20**(11): p. 2715-2722.

Contact

Charles P. Ho, M.D., Ph.D.
 Steadman Philippon Research Institute
 181 W Meadow Dr, Suite 1000
 Vail, CO, 81657
 USA
 Phone: +1 (970) 479-5888
 Fax: +1 (970) 479-9753
 charles.ho@sprivail.org

T1_ρ MRI: A Potential Biomarker of Cartilage Physiology

Arijitt Borthakur, Ph.D.¹; Walter R. T. Witschey, Ph.D.¹; Anup Singh, Ph.D.¹; Hari Hariharan, Ph.D.¹; Tiejun Zhao, Ph.D.²; Niels Oesingmann, Ph.D.²; Ravinder Reddy, Ph.D.¹

¹Center for Magnetic Resonance & Optical Imaging, Department of Radiology, Perelman School of Medicine at the University of Pennsylvania, Philadelphia, PA, USA

²Siemens Medical Solutions, Pittsburgh and Malvern, PA, USA

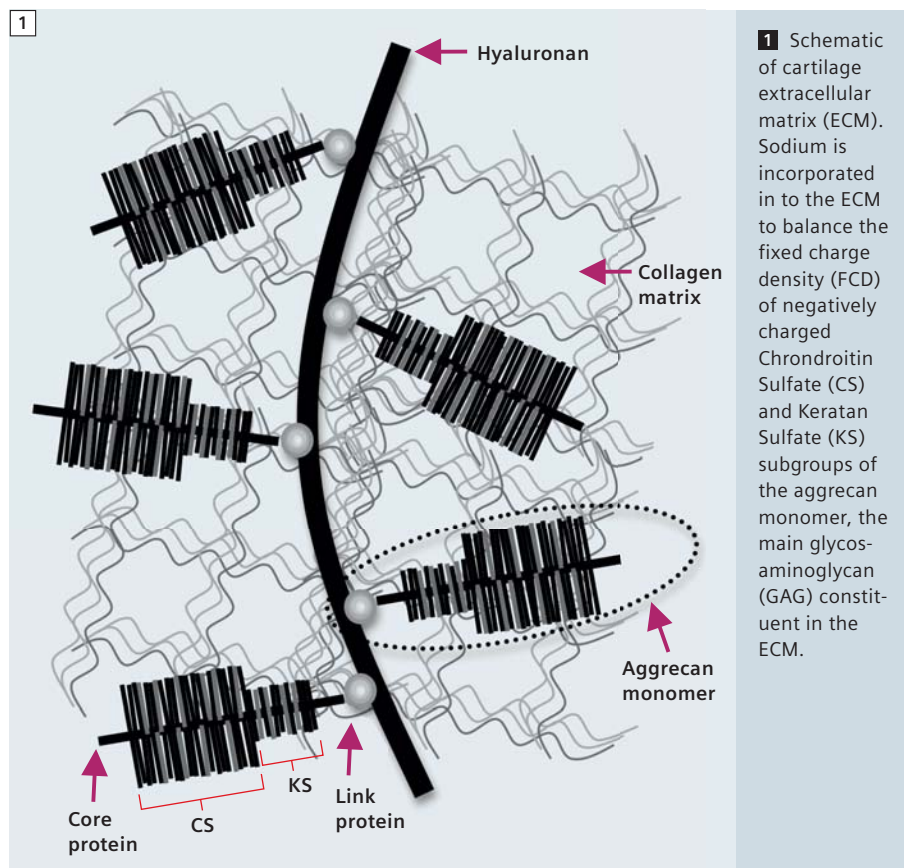
Introduction

Osteoarthritis (OA) affects more than half of the population above the age of 65 and has a significant negative impact on the quality of life of elderly individuals. The economic costs in the US from OA have been estimated to be more than 1% of the gross domestic product. Imaging the physiology of cartilage tissue holds promise for an early detection of OA, the most common joint disease whose prevalence will only increase due to an aging population [1]. The disease

is characterized by focal cartilage damage, changes in the subchondral bone, mild synovitis, and thickening of the joint capsule in synovial joints. Key to understanding the pathology of the disease is to appreciate that the biochemistry of cartilage tissue underlies its special purposes of control over joint loading and motion. Only a small fraction of the volume of cartilage is occupied by cells (chondrocytes) that facilitate construction, repair and

degradation of the extracellular matrix (ECM) in response to stimuli. Water occupies 70% of the volume of the ECM [1] while the major solid constituents (Fig. 1) are aggrecan (5% w/v) and type II collagen (20% w/v).

The early stage of OA is associated with an increase in enzymatic degradation by matrix metalloproteinases resulting in depletion of glycosaminoglycan (GAG) of aggrecan as well as degradation of the collagen network. In cartilage, GAG side chains are made of continuously repeating disaccharides containing carboxyl and sulfate functional groups and are both negatively charged under physiological conditions. The negative charge GAG confers on cartilage is the fixed charge density (FCD). Gorton originally proposed a model for the physiology of connective tissues in which a high polysaccharide content induces an osmotic pressure that is resisted by the network of collagen [2]. In this model, the presence of highly electronegative and immobile GAG macromolecules results in an influx of sodium ions to maintain electro-neutrality. Since then, Maroudas extended this model by introducing the Donnan equilibrium to describe the flux of charged ions across a semi-permeable membrane in the presence of a charged but non-exchanging GAG restricted to a single compartment [3, 4]. In this model, the low hydraulic permeability of GAG counterbalances resistive loads by its swelling pressure while collagen provides tensile and shear strength. Therefore, GAG loss in early OA initiates a cascade by which osmotic pressure is

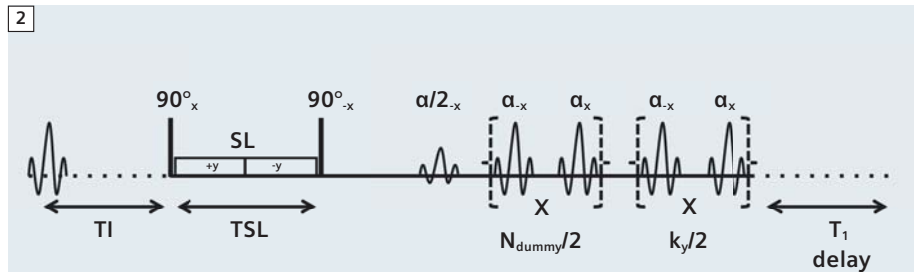


reduced and joint compression permanently disrupts the cartilage leading to thinning, fracturing and subsequently pain [5, 6].

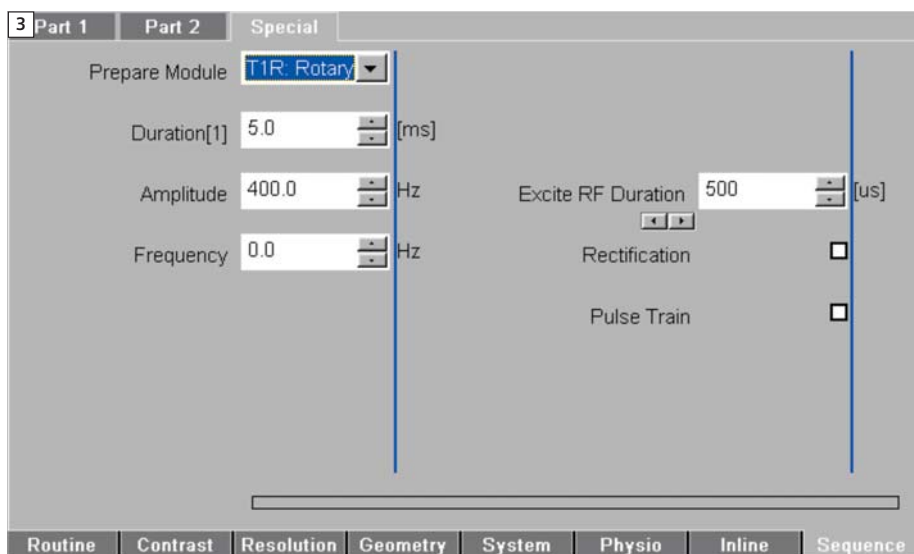
Current imaging methods for OA

Radiographic imaging is the current gold standard in imaging technology to detect advanced stages of OA. Lacking sensitivity to soft tissues, this X-ray based technique measures joint space narrowing (JSN) to indirectly gauge the extent of damage to cartilage. In addition, outcome instruments for assessment of OA in patients such as the Knee injury and Osteoarthritis Outcome Score (KOOS), an extension of the Western Ontario and McMaster Universities Osteoarthritis Index (WOMAC), is also used to determine mobility and pain in a specific joint [7, 8]. However, radiography, along with nuclear medicine scans, arthrography, and computed tomography (CT) scans, are limited in their use because they are unable to detect early cartilage abnormalities [9]. Conventional T1-weighted and T2w MRI can directly visualize all diarthrodial tissues, including cartilage, bone, synovium, menisci, and ligaments and has substantial advantages over radiography [10–12]. Due to the high morbidity of OA, therapeutic interventions are particularly necessary but current methods are restricted to management of pain and surgical interventions [13]. However, improving outcomes require development of more effective interventions that can slow or reverse the course of the disease. In this context, there is a requirement for strong diagnostic information sensitive to the early stages of the disease, where cartilage appears intact on radiographs. Furthermore, because of the long natural history of OA (10–20 years in humans), sensitive imaging biomarkers are expected to significantly accelerate the drug development process by assessing the therapeutic potential in terms of efficacy at the early stages of the disease and thereby lowering the cost and duration of clinical trials.

The aim of this review is to highlight T1_ρ (T1_{-rho}) MRI, a technique that has been developed to specifically detect the



2 Pulse sequence diagram for inversion-prepared T1_ρ MRI with a 3D balanced-GRE readout [38]. TI is the inversion time, TSL is the duration of two phase-alternating spin-lock pulses inserted between two 90° RF pulses, which is followed by a half-α pulse that begins the centric-encoded balanced-GRE readout. A delay time is inserted at the end of the α pulse train for T1 recovery.



3 The MRI console's Sequence Special tab showing the user controllable variables and typical values associated with the T1_ρ pulse sequence in figure 2. In this particular case, a Rotary Echo T1_ρ preparation is employed with TSL times in multiples of 5 ms. The number of distinct TSL data sets acquired is 5 (entered on Part 2 tab). The γB₁ spin-lock amplitude is set to 400 Hz for a body-coil transmit and 500 Hz for knee-coil transmit. The duration of the 90° hard pulses in the T1_ρ preparation is 500 μs.

GAG component of cartilage, which is the more important element due to the ostensibly limited contribution of collagen to the initiating steps of OA [14]. Only the salient features of this method are described here with a limited review of the literature.

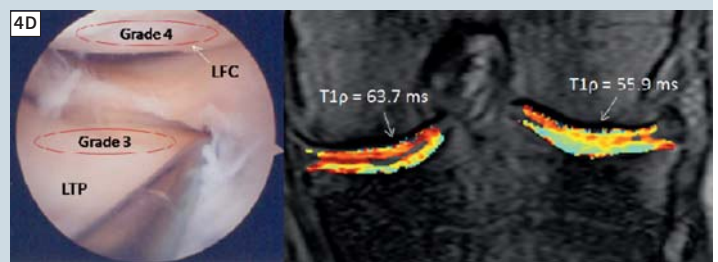
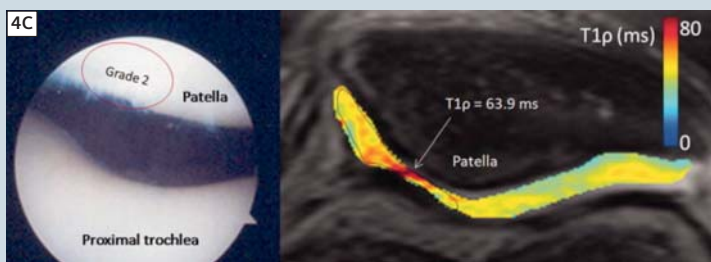
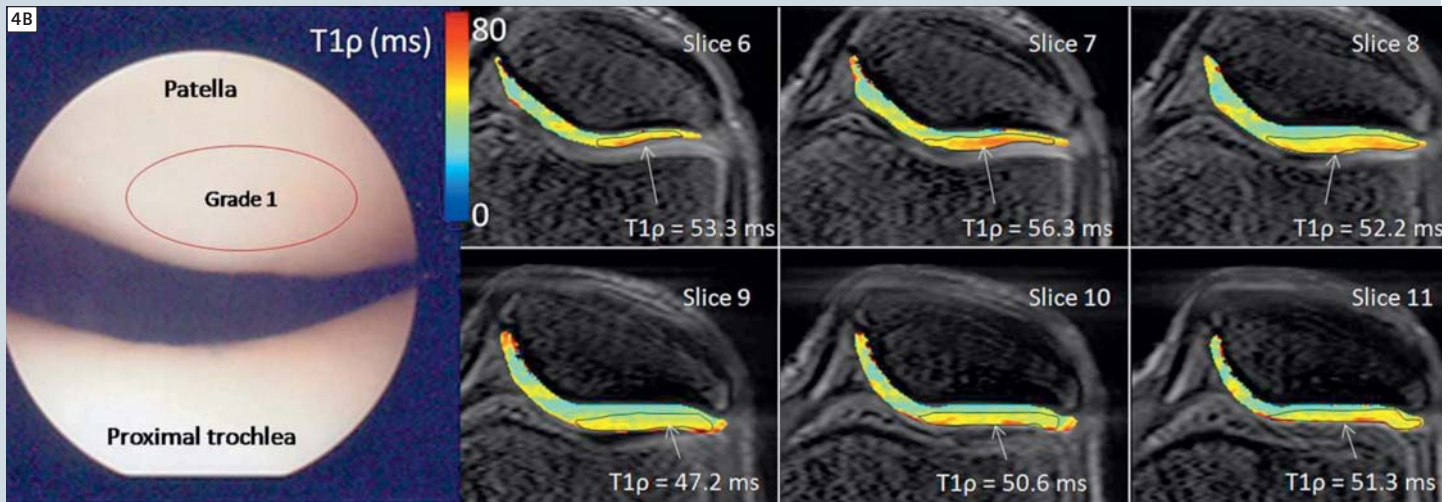
T1_ρ MRI

T1_ρ MRI is an alternative to conventional T1w and T2w MRI [15] by its use of a long-duration, low-power radiofrequency (RF) referred to as spin-lock (SL) pulse applied to the magnetization in the transverse plane. The magnetization

is effectively spin-locked around an effective B₁ field created by the vector sum of the applied B₁ and any off-resonant component. The spin-locked magnetization will relax with a time constant T1_ρ, the spin-lattice relaxation in the rotating frame, during the RF field. The B₁ field attenuates the effect of dipolar relaxation, static dipolar coupling, chemical exchange and background gradients on the signal resulting in a T1_ρ that is always greater than T2. T1_ρ was shown to be influenced by the exchange of hydroxyl (–OH) and amide (–NH) protons on the GAG [16]. There has been consid-



4 (4A) $T_{1\rho}$ relaxation map from a 30-year-old male with no history of knee injury and no knee pain. Patellar cartilage is homogeneously, smoothly varying and has a characteristic increase in $T_{1\rho}$ from the deep cartilage adjacent to the subchondral bone to the superficial cartilage adjacent to the synovium. The ROI drawn at the cartilage surface had a $T_{1\rho} = 41.7$ ms.



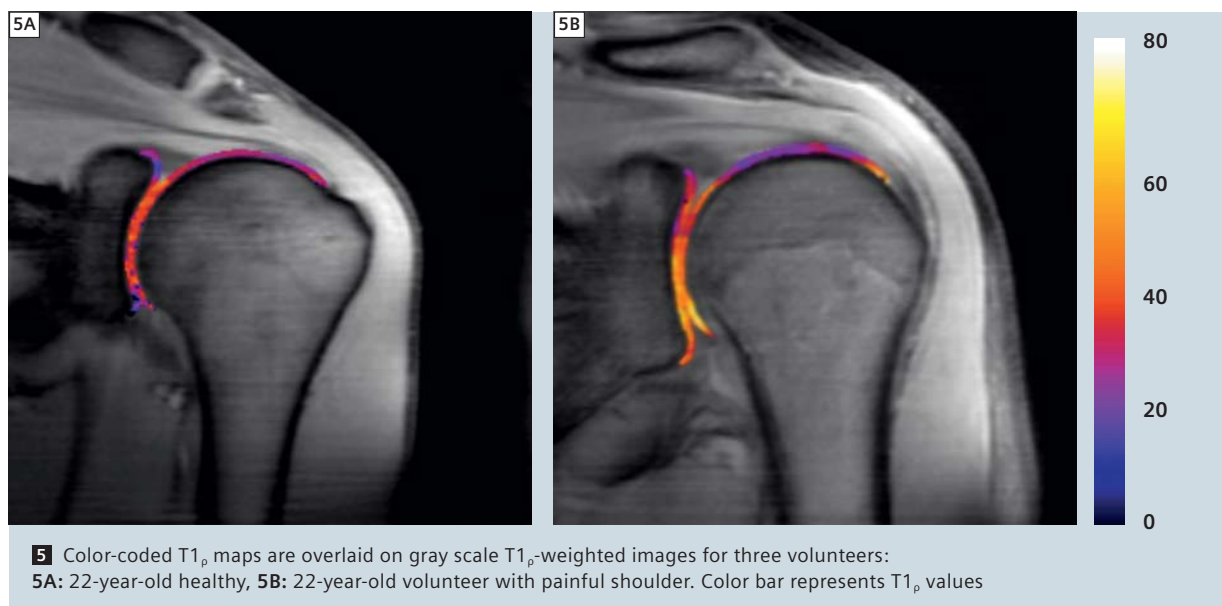
A 76-year-old patient with grade 1 chondromalacia of the lateral patellar facet and grade 2 chondromalacia of the medial patellar facet is shown (4B) with elevated focal $T_{1\rho}$ lesions. Another patient was observed at arthroscopy to have grade 2 patellar chondromalacia and a torn left medial meniscus, for which a partial medial meniscectomy was performed (4C). Similar images are provided to show correspondence between arthroscopic image and $T_{1\rho}$ maps for grade 3 (4D) and grade 4 (E) chondromalacia [33].

erable amount of work on biological tissues using $T_{1\rho}$ -spectroscopy and imaging dealing with tumors, muscle, myocardium, blood flow and cartilage [17–27].

Quantitative $T_{1\rho}$ MRI relaxation relaxometric images can reflect the biochemical composition of cartilage. These $T_{1\rho}$ 'maps' are created by fitting the signal intensity of $T_{1\rho}$ -weighted MR images as a function of the SL pulse duration with fixed amplitude ($\gamma B_1 = 500$ Hz). In this manner, spatial maps of $T_{1\rho}$ values related to macromolecular composition

of tissues can be visualized and analyzed. The current protocol for $T_{1\rho}$ MRI uses a 3D balanced gradient echo readout to detect the $T_{1\rho}$ prepared magnetization (Fig. 2) that is developed in our lab. Typical user-controllable values for the customer-made pulse sequence are shown in figure 3. This imaging protocol is under 15 minutes for acquiring five $T_{1\rho}$ -weighted 3D data sets for computing color-coded $T_{1\rho}$ maps showing the spatial distribution of cartilage matrix elements, GAG, water, and collagen. The non-averaged dipolar interaction

between water protons associated with collagen is the predominant contributor to relaxation in cartilage [28]. $T_{1\rho}$ -dispersion MRI, where the amplitude of the SL pulse amplitude is also varied, can be used to detect spectral density components in cartilage that are in the neighborhood of γB_1 . The effect of spin-locking reduces the laminar appearance in cartilage as demonstrated by Akella et al. in an orientation-dependent MRI experiment of cartilage plugs [29]. In this study, a typical laminar appearance was present in T2 MRI when the normal



to the surface of cartilage was parallel to B_0 but absent in $T1\rho$ MRI of the same cartilage specimen. In addition, $T1\rho$ values were consistently greater than T2 at all orientations throughout the cartilage layers, a result of spin-locking the magnetization.

$T1\rho$ in clinical OA research

Several studies have demonstrated the efficacy of $T1\rho$ MRI in detecting early tissue pathology with increasing values in OA-affected cartilage compared to normal tissue [30]. $T1\rho$ MRI was also demonstrated to quantitatively evaluate meniscus and cartilage matrix in animal models as well as in patients with acute anterior cruciate ligament (ACL) injuries [31, 32]. Studies on arthroscopically-confirmed early grades of chondromalacia have demonstrated the potential of a rapid MRI pulse sequence (Fig. 4) for $T1\rho$ mapping in order to detecting earliest molecular changes in cartilage *in vivo* [33].

Another potential application of $T1\rho$ MRI is in the shoulder joint. Glenohumeral arthritis is a disabling condition, which severely affects the quality of life and activities of recreation and daily living [34]. Primary glenohumeral osteoarthritis predominantly occurs in older individuals; however, a younger cohort of patients has been recently described with end stage glenohumeral arthritis after shoulder arthroscopy [35]. With shoulder injuries, the integrity of the cartilage may

become compromised due to several factors such as abnormal loading conditions and repeated stresses. Routine clinical care of shoulder joint is limited to morphologic and structural changes but the sensitivity of $T1\rho$ to early changes due to arthritis may help in the diagnosis and treatment of the disease. To this end, the $T1\rho$ mapping technique was applied to normal and shoulder pain subjects on a Siemens clinical 3T scanner with the vendor-supplied shoulder coil. $T1\rho$ map of the shoulder joint of a healthy volunteer is displayed alongside a patient with shoulder joint pain (Fig. 5). Elevated $T1\rho$ values in the glenoid compartment cartilage in the latter individual could indicate early cartilage degradation resulting from arthritis. Further research is ongoing on individuals with traumatic shoulder joint injury to quantify early onset of degeneration of cartilage in the joint.

Summary

MRI based on conventional T1 and T2 contrast is able to provide excellent images of cartilage morphology, but could be insensitive to detect changes in cartilage biochemistry and physiology. While OA progression is multi-factorial and slow progressing disease, its early stages involve the breakdown and loss of GAG and collagen from the extracellular matrix. There are other MRI-based methods targeting macromolecules as biomarkers of OA disease progression

besides $T1\rho$ MRI. Chemical Exchange Saturation Transfer (CEST) MRI is sensitive to proton exchange between $-OH$ groups in GAG and water and hence highly specific to GAG content. The feasibility of CEST MRI to detect GAG *in vivo* (gagCEST) was recently demonstrated in cartilage of the knee joint by experiments on 7T* whole-body Siemens MRI scanners [36]. This study also demonstrated that gagCEST values obtained from images without correcting for B_0 inhomogeneity (0.6 ppm) could lead to some inaccuracy of the final quantifications [37]. $T1\rho$ MRI has already been applied to clinical research by several groups and was shown to be a promise method in evaluating early OA by demonstrating its sensitivity and specificity to cartilage physiology and biochemistry as well as its ability to detect progression of the disease. Larger multi-center studies will be required to develop standard protocols in order for these methods to be translated to clinical practice.

Acknowledgements

This work was performed at a Biomedical Technology Research Center supported by NCR (P41 RR002305) and NIBIB (P41 EB015893) and grants R01AR45404, R01AR051041 from NIAMS.

*The 7T system is an investigational device. Limited by U.S. federal law to investigational use. The product is still under development and not commercially available yet. Its future availability cannot be ensured.

References

- 1 Brandt KD, Doherty M, Lohmander S. Osteoarthritis. Oxford ; New York: Oxford University Press; 2003. xii, 511 p. p.
- 2 Ogston A. The biological functions of the glycosaminoglycans. In: Balazs E, editor. Chemistry and Molecular Biology of the Intercellular Matrix. Volume 3. New York: Academic Press; 1970. p 1231-1240.
- 3 Maroudas AI. Balance between swelling pressure and collagen tension in normal and degenerate cartilage. *Nature* 1976;260(5554):808-809.
- 4 Maroudas A. Physicochemical properties of articular cartilage. In: Freeman MAR, editor. Adult articular cartilage. 2nd ed. Kent, England: Pitman Medical; 1979. p 215-290.
- 5 Glasson SS, Askew R, Sheppard B, Carito B, Blanchet T, Ma HL, Flannery CR, Peluso D, Kanki K, Yang Z, Majumdar MK, Morris EA. Deletion of active ADAMTS5 prevents cartilage degradation in a murine model of osteoarthritis. *Nature* 2005;434(7033):644-648.
- 6 Stanton H, Rogerson FM, East CJ, Golub SB, Lawlor KE, Meeker CT, Little CB, Last K, Farmer PJ, Campbell IK, Fourie AM, Fosang AJ. ADAMTS5 is the major aggrecanase in mouse cartilage *in vivo* and *in vitro*. *Nature* 2005;434(7033):648-652.
- 7 Bellamy N, Buchanan WW, Goldsmith CH, Campbell J, Stitt LW. Validation study of WOMAC: a health status instrument for measuring clinically important patient relevant outcomes to antirheumatic drug therapy in patients with osteoarthritis of the hip or knee. *J Rheumatol* 1988;15(12):1833-1840.
- 8 Roos EM, Roos HP, Lohmander LS, Ekdahl C, Beynnon BD. Knee Injury and Osteoarthritis Outcome Score (KOOS)--development of a self-administered outcome measure. *J Orthop Sports Phys Ther* 1998;28(2):88-96.
- 9 Blackburn WD, Jr., Chivers S, Bernreuter W. Cartilage imaging in osteoarthritis. *Seminars in Arthritis & Rheumatism* 1996;25(4):273-281.
- 10 Heron CW. Review article: MRI of the knee. *British Journal of Radiology* 1993;66(784):292-302.
- 11 Potter HG, Linklater JM, Allen AA, Hannafin JA, Haas SB. Magnetic resonance imaging of articular cartilage in the knee - An evaluation with use of fast-spin-echo imaging. *Journal of Bone and Joint Surgery* 1998;80A(9):1276-1284.
- 12 Recht M, Bobic V, Burstein D, Disler D, Gold G, Gray M, Kramer J, Lang P, McCauley T, Winalski C. Magnetic resonance imaging of articular cartilage. *Clin Orthop* 2001(391 Suppl):S379-396.
- 13 Zhang W, Moskowitz RW, Nuki G, Abramson S, Altman RD, Arden N, Bierma-Zeinstra S, Brandt KD, Croft P, Doherty M, Dougados M, Hochberg M, Hunter DJ, Kwok K, Lohmander LS, Tugwell P. OARSI recommendations for the management of hip and knee osteoarthritis, Part II: OARSI evidence-based, expert consensus guidelines. *Osteoarthritis Cartilage* 2008;16(2):137-162.
- 14 Dijkgraaf LC, de Bont LG, Boering G, Liem RS. The structure, biochemistry, and metabolism of osteoarthritic cartilage: a review of the literature. *J Oral Maxillofac Surg* 1995;53(10):1182-1192.
- 15 Borthakur A, Mellon E, Niyogi S, Witschey W, Kneeland J, Reddy R. Sodium and T1rho MRI for molecular and diagnostic imaging of articular cartilage. *NMR Biomed* 2006;19(7):781-821.
- 16 Duvvuri U, Goldberg AD, Kranz JK, Hoang L, Reddy R, Wehrli FW, Wand AJ, Englander SW, Leigh JS. Water magnetic relaxation dispersion in biological systems: The contribution of proton exchange and implications for the noninvasive detection of cartilage degradation. *Proc Natl Acad Sci U S A* 2001;98(22):12479-12484.
- 17 Santyr GE, Henkelman RM, Bronskill MJ. Spin locking for magnetic resonance imaging with application to human breast. *Magn Reson Med* 1989;12(1):25-37.
- 18 Lamminen AE, Tantt JI, Sepponen RE, Pihko H, Korhola OA. T1rho dispersion imaging of diseased muscle tissue. *Br J Radiol* 1993;66(789):783-787.
- 19 Dixon WT, Oshinski JN, Trudeau JD, Arnold BC, Pettigrew RI. Myocardial suppression *in vivo* by spin locking with composite pulses. *Magn Reson Med* 1996;36(1):90-94.
- 20 Charagundla SR, Stolpen AH, Leigh JS, Reddy R. Off-resonance proton T1r dispersion imaging of 17O-enriched tissue phantoms. *Magn Reson Med* 1998;39(4):588-595.
- 21 Mlynarik V, Trattnig S, Huber M, Zembsch A, Imhof H. The role of relaxation times in monitoring proteoglycan depletion in articular cartilage. *J Magn Reson Imaging* 1999;10(4):497-502.
- 22 Grohn OHJ, Kettunen MI, Makela HI, Penttonen M, Pitkanen A, Lukkari JA, Kauppinen RA. Early detection of irreversible cerebral ischemia in the rat using dispersion of the magnetic resonance imaging relaxation time, T1rho. *J Cereb Blood Flow Metab* 2000;20(10):1457-1466.
- 23 Poptani H, Duvvuri U, Miller CG, Mancuso A, Charagundla S, Fraser NW, Glickson JD, Leigh JS, Reddy R. T1rho imaging of murine brain tumors at 4 T. *Acad Radiol* 2001;8(1):42-47.
- 24 Duvvuri U, Poptani H, Feldman M, Nadal-Desbarats L, Gee MS, Lee WM, Reddy R, Leigh JS, Glickson JD. Quantitative T(1rho) magnetic resonance imaging of RIF-1 tumors *in vivo*: detection of early response to cyclophosphamide therapy. *Cancer Research* 2001;61(21):7747-7753.
- 25 Borthakur A, Wheaton A, Gougoutas A, Akella S, Regatte R, Charagundla S, Reddy R. *In vivo* measurement of T1rho dispersion in the human brain at 1.5 tesla. *J Magn Reson Imaging* 2004;19(4):403-409.
- 26 Wheaton A, Dodge G, Borthakur A, Kneeland J, Schumacher H, Reddy R. Detection of changes in articular cartilage proteoglycan by T(1rho) magnetic resonance imaging. *J Orthop Res* 2005;23(1):102-108.
- 27 Li X, Han ET, Ma CB, Link TM, Newitt DC, Majumdar S. *In vivo* 3T spiral imaging based multi-slice T(1rho) mapping of knee cartilage in osteoarthritis. *Magn Reson Med* 2005;54(4):929-936.
- 28 Xia Y, Farquhar T, Burton-Wurster N, Lust G. Origin of cartilage laminae in MRI. *Journal of Magnetic Resonance Imaging* 1997;7(5):887-894.
- 29 Akella S, Regatte R, Wheaton A, Borthakur A, Reddy R. Reduction of residual dipolar interaction in cartilage by spin-lock technique. *Magn Reson Med* 2004;52(5):1103-1109.
- 30 Majumdar S, Li X, Blumenkrantz G, Saldanha K, Ma CB, Kim H, Lozano J, Link T. MR imaging and early cartilage degeneration and strategies for monitoring regeneration. *J Musculoskelet Neuronal Interact* 2006;6(4):382-384.
- 31 Lozano J, Saadat E, Li X, Majumdar S, Ma CB. Magnetic resonance T(1 rho) imaging of osteoarthritis: a rabbit ACL transection model. *Magn Reson Imaging* 2009;27(5):611-616.
- 32 Bolbos RI, Link TM, Ma CB, Majumdar S, Li X. T1rho relaxation time of the meniscus and its relationship with T1rho of adjacent cartilage in knees with acute ACL injuries at 3 T. *Osteoarthritis Cartilage* 2009;17(1):12-18.
- 33 Witschey W, Borthakur A, Fenty M, Kneeland B, Lonner J, McArdle E, Sochor M, Reddy R. T1rho MRI quantification of arthroscopically confirmed cartilage degeneration. *Magn Reson Med* 2010;63(5):1376-1382.
- 34 de Beer JF, Bhatia DN, van Rooyen KS, Du Toit DF. Arthroscopic debridement and biological resurfacing of the glenoid in glenohumeral arthritis. *Knee Surg Sports Traumatol Arthrosc* 2010;18(12):1767-1773.
- 35 McNickle AG, L'Heureux DR, Provencher MT, Romeo AA, Cole BJ. Postsurgical glenohumeral arthritis in young adults. *Am J Sports Med* 2009;37(9):1784-1791.
- 36 Singh A, Haris M, Cai K, Kassey VB, Kogan F, Reddy D, Hariharan H, Reddy R. Chemical exchange saturation transfer magnetic resonance imaging of human knee cartilage at 3 T and 7 T. *Magn Reson Med* 2012;68(2):588-594.
- 37 Ling W, Regatte R, Navon G, Jerschow A. Assessment of glycosaminoglycan concentration *in vivo* by chemical exchange-dependent saturation transfer (gagCEST). *Proc Natl Acad Sci U S A* 2008;105(7):2266-2270.
- 38 Witschey W, Borthakur A, Elliott M, Fenty M, Sochor M, Wang C, Reddy R. T1rho-prepared balanced gradient echo for rapid 3D T1rho MRI. *J Magn Reson Imaging* 2008;28(3):744-754.

Contact

Ari Borthakur, Ph.D.
Associate Director
Center for Magnetic Resonance &
Optical Imaging
Perelman School of Medicine
at the University of Pennsylvania
B1 Stellar-Chance Laboratories
422 Curie Boulevard
Philadelphia, PA 19104-6100
USA
Phone: +1 (215) 573-8482
Fax: +1 (215) 573-2113
borthaku@upenn.edu
Web: <http://med.cmroi.upenn.edu>

Save the Date

Heidelberg Summer School

Musculoskeletal Cross Sectional Imaging 2013

July 5th / 6th 2013
Heidelberg, Germany

The Heidelberg Summer School offers advanced learning opportunities and promotes the academic exchange of knowledge, ideas, and experiences by bringing together physicians and professional staff from all over the world. Excellent speakers will cover a wide range of medical, physical, and technical topics in musculoskeletal imaging. All lectures are in English.

Course director

Marc-André Weber, M.D., M.Sc.

Professor of Radiology, Section Head Musculoskeletal Radiology at the University Hospital Heidelberg

CME Accreditation

The symposium will be accredited by the 'Landesärztekammer Baden-Württemberg' with CME credits (category A).

Also, the symposium is accredited for 1 category 3 credit point for the ESSR diploma by the European Society of Musculoskeletal Radiology.

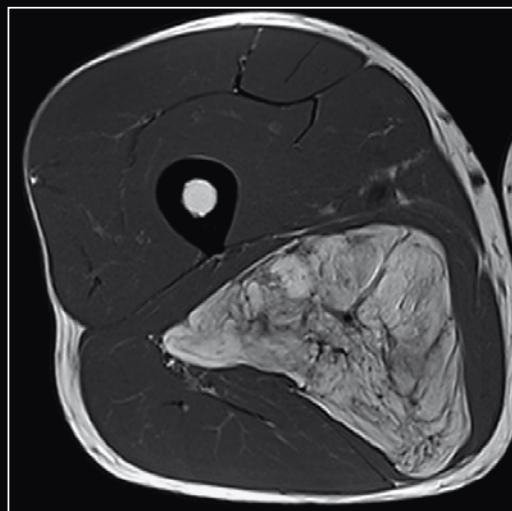
Registration

Mrs. Marianne Krebs, Secretary of the Section Musculoskeletal Radiology

Marianne.Krebs@med.uni-heidelberg.de

For further information please visit:

www.heidelbergsummerschool.de



Biochemical MRI in Musculoskeletal Applications

Siegfried Trattnig; Štefan Zbýň; Vladimír Juras; Pavol Szomolanyi; Stephan Domayer; Iris-Melanie Noebauer-Huhmann; Goetz Welsch; Benjamin Schmitt

MR Centre – High field MR, Department of Radiology, Medical University of Vienna/Vienna General Hospital, Vienna, Austria

1. Biochemical MRI assessment of cartilage and cartilage repair

To visualize the constitution of articular cartilage and cartilage repair tissue, a variety of different MRI methods are available. Considering the composition of healthy hyaline articular cartilage, these methods can depict relatively specifically either one component of cartilage or a combination of different components. Although some more recent techniques, in particular CEST, have not yet been validated sufficiently, studies have shown promising initial results. Articular cartilage is complex, dense, connective tissue that relies on the diffusion of solutes for nutrition [1]. Responsible for the biomechanical properties of articular cartilage is the extracellular matrix, mainly composed of water (~75%), collagen (~20%), and proteoglycan aggregates (~5%) [1, 2]. Water either freely moves throughout the matrix or is bound to macromolecules. Collagen in hyaline cartilage is largely type II, which creates a stable network throughout the cartilage. The negatively-charged proteoglycans are composed of a central core protein to which glycosaminoglycans (GAG) are bound.

1.1) Proteoglycan-sensitive MRI techniques

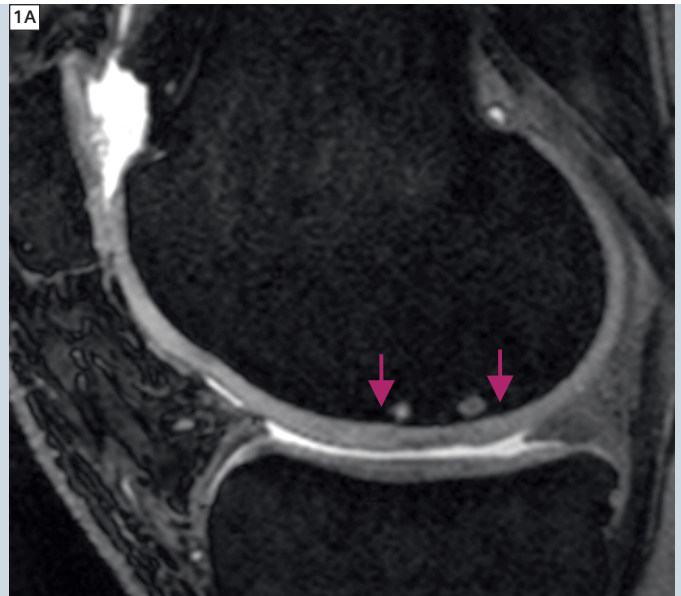
Although no MRI sequence is really 100% specific for only proteoglycans or collagens, there are MRI methods that reportedly focus mainly on one component of articular cartilage. The negatively-charged proteoglycan, composed of a central core protein to which GAG are bound, can be visualized by delayed gadolinium-enhanced MRI of cartilage (dGEMRIC*) [3], sodium MR imaging [4, 5], and, very recently, chemical

exchange-dependent saturation transfer (CEST) [6]. Of these techniques, only dGEMRIC has so far become clinically useful in cartilage repair imaging.

a) Delayed gadolinium-enhanced MRI of cartilage (dGEMRIC*)

GAG are important to the cartilage tissue's biochemical and biomechanical function. GAG are the main source of fixed charge density (FCD) in cartilage, and are often decreased in the early stages of cartilage degeneration [7], or in repar-

1 (1A) Shows a sagittal 3D GRE image in a patient after microfracturing at 3T. In the area of microfracture only slight thinning of the cartilage layer can be seen. (1B) Precontrast* T1-map shows no difference in T1 relaxation times in the repair tissue; however, in the postcontrast* image (1C) a significant drop in T1 values in the repair tissue can be seen, which corresponds to a low glycosaminoglycan content.

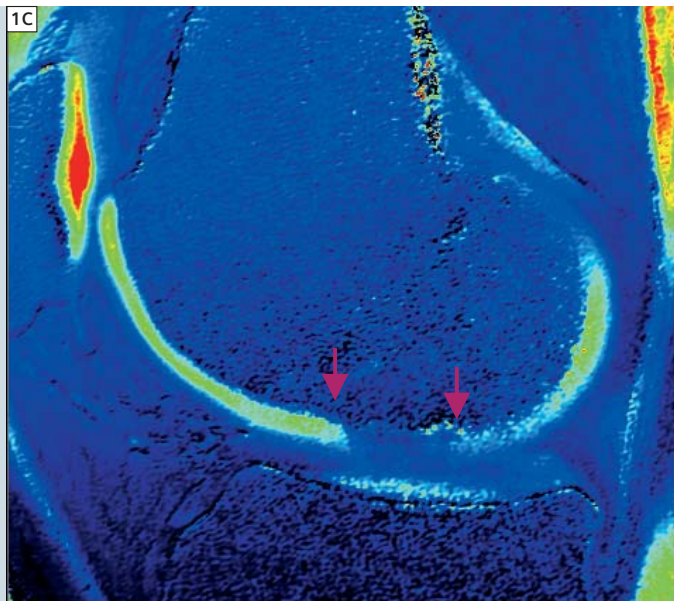
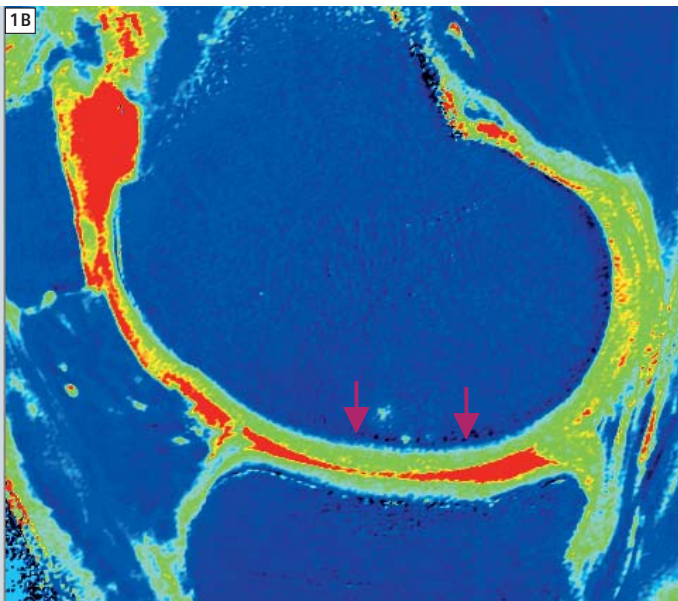


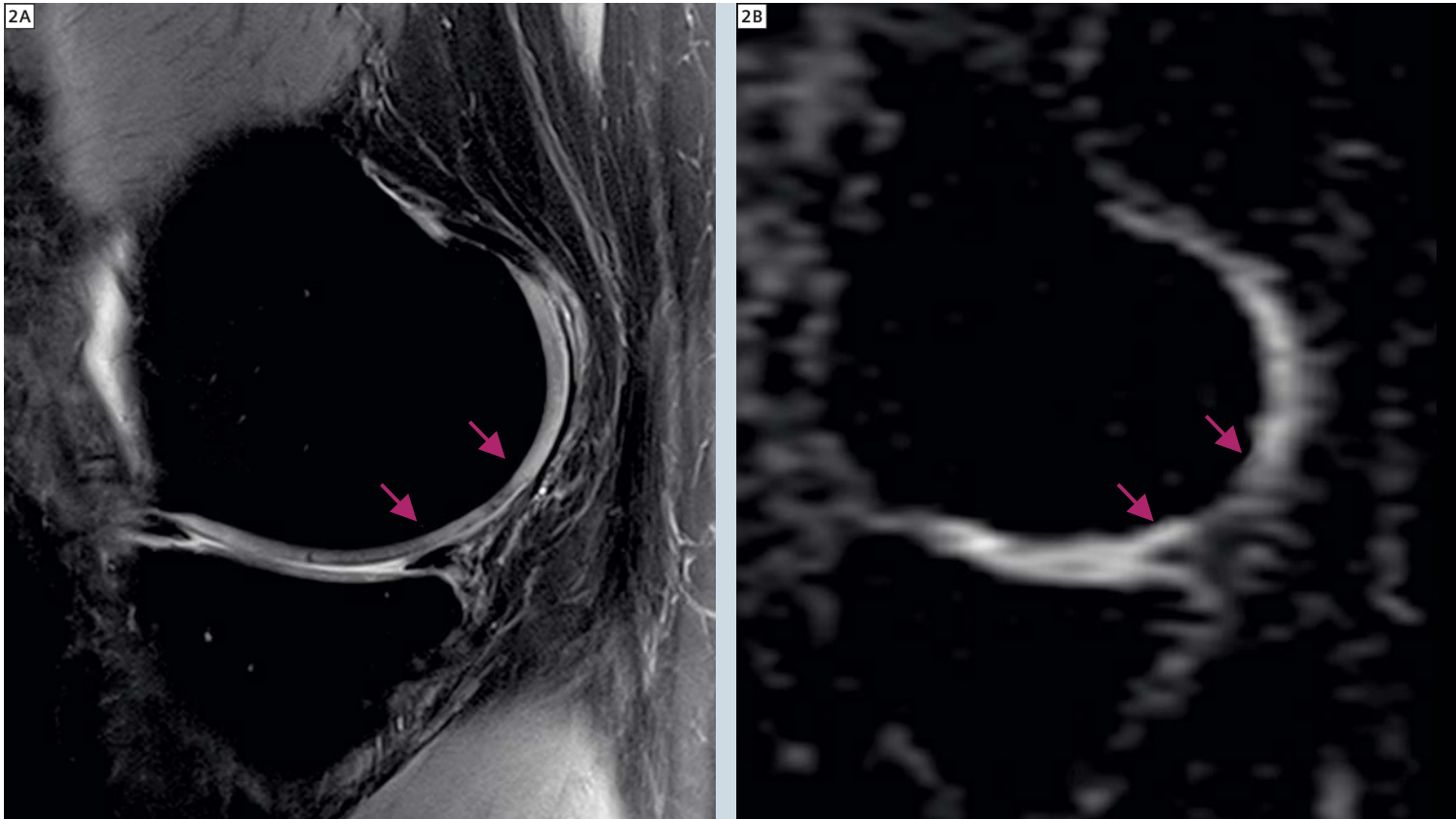
ative cartilage after cartilage repair [8]. Intravenously administered gadolinium diethylenetriamine pentaacetate anion, (Gd-DTPA^{2-}) penetrates the cartilage through both the articular surface and the subchondral bone. The contrast equilibrates in inverse relation to the FCD, which is, in turn, directly related to the GAG concentration. Therefore, T1, which is determined by the Gd-DTPA^{2-} concentration, becomes a specific measure of tissue GAG concentration, suggesting that Gd-DTPA^{2-} enhanced MRI has the potential to monitor the GAG content of cartilage in vivo [9]. Thus, T1-mapping, enhanced by delayed administration of Gd-DTPA^{2-} (T1 dGEMRIC*), can be considered the most widely used methodology for detecting proteoglycan depletion in articular cartilage (Fig. 1), and has shown promising results [10, 11]. As differences in pre-contrast values between cartilage repair tissue and normal hyaline cartilage are larger compared to early cartilage degeneration, in cartilage repair tissue, the pre-contrast T1 values must also be calculated [8]. The concentration of GAG is represented by ΔR_1 , i.e., the difference in relaxation rate ($R_1 = 1/T_1$) between $T_{1\text{precontrast}}$ and $T_{1\text{postcontrast}}$. Thus, the sequence must be performed twice, for pre-contrast and delayed post-contrast T1-mapping. This increases the total scan time, and

requires a break in between the two MRI scans, where the contrast agent must be administered and a delay of at least 90 minutes after injection is needed for penetration of the contrast agent into the cartilage. Scan time reduction, compared to the standard inversion recovery (IR) evaluation, has been achieved with a new approach using fast T1-mapping based on GRE-technique [12]. Although the 90-minute delay is still required, this might increase the clinical applicability of the dGEMRIC* technique. Other drawbacks of dGEMRIC* are the use of i. v. contrast agent administration, the necessity of a double dose of contrast agent, and the fact that uptake and distribution of contrast agent is not only dominated by GAG. Since GAG content is responsible for cartilage function, particularly its tensile strength, the monitoring of the development of GAG content in cartilage repair tissues may provide information about the quality of the repair tissue. A study by our group showed that dGEMRIC* was able to differentiate between different cartilage repair tissues with higher ΔR_1 values, and thus, lower GAG content, in cartilage repair tissue after MFX, compared to MACT [13]. The applicability of this technique has also been shown in regions other than the knee joint [14–16].

b) ^{23}Na (Sodium) imaging of cartilage

The major advantage of sodium MRI in musculoskeletal applications is that it is highly specific for glycosaminoglycan content, and, since the sodium from surrounding structures in the joint is low ($< 50 \text{ mM}$), cartilage can be visualized with very high contrast without the requirement for any exogenous contrast agent, such as with dGEMRIC*. The recent proliferation of 7T¹ whole-body MRI scanners in clinical research centers has had a significant impact on sodium MRI and its potential for clinical use. Since signal-to-noise (SNR) scales linearly with increasing field strength, and because of the lack of B_1 penetration and B_0 susceptibility that pose problems with proton imaging, sodium MRI can be particularly advantageous at higher fields. The low gyromagnetic ratio of sodium also means significantly lower power deposition compared with proton imaging, which thus reduces SAR problems at 7T¹. It is, therefore, very likely that the improved SNR sodium MRI at 7T¹ can provide a robust tool for quantitative imaging of MSK structures in particular cartilage. Although sodium MRI has high specificity and does not require any exogenous contrast agent, it does require special hardware capabilities (multinuclear) and specialized RF coils [5].





With the application of a 7T whole-body system and a modified 3D GRE optimized for sodium imaging and dedicated multi-element sodium coils, we performed a series of clinical studies. In a small group of 12 patients after matrix-associated autologous chondrocyte transplantation (MACT), sodium imaging enabled the differentiation between sodium content, and thus GAG in the transplants, compared to native, healthy cartilage. In all patients, the sodium SNR was lower in the repair tissue compared to healthy cartilage. A good correlation between sodium imaging and dGEMRIC* in the quantification of GAG content was found in patients after MACT [17].

In another study, 18 patients who had different cartilage repair surgeries (nine bone marrow stimulation (BMS) and nine MACT patients), age-matched, with similar postoperative intervals and defect locations, were examined with sodium imaging. Sodium SNR was significantly lower in BMS ($p < .001$) and

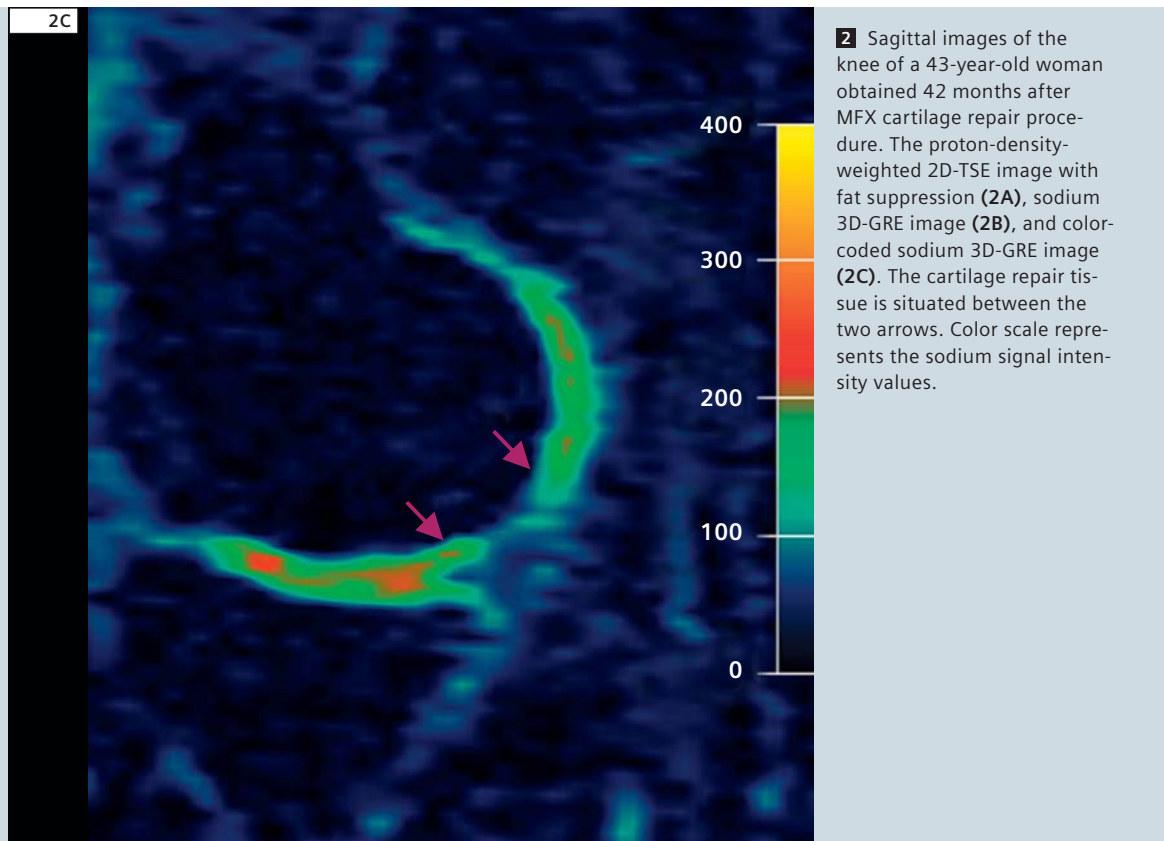
MACT ($p = .002$) repair tissue, compared to reference cartilage. These differences were influenced by surgery type, but not by age and follow-up interval. Although sodium SNR was not different between the reference cartilage in the MACT and BMS patients ($p = .528$), it was significantly higher in MACT than in BMS repair tissue ($p = .002$). There was no difference between the magnetic resonance observation of cartilage repair tissue (MOCART) scores for MACT and BMS patients ($p = .889$). No correlation was observed between the MOCART score and repair tissue SNR with sodium imaging ($R = .111$). Our results suggest that MACT provides higher GAG content and, therefore, higher-quality repair tissue compared to the BMS techniques. Sodium MR imaging at 7T¹ (Fig. 2) might be beneficial in the non-invasive evaluation of cartilage repair procedure efficacy in the knee [18].

Similar studies in patients after long-term autologous osteochondral transplantation (AOT) in which hyaline cartilage

is transplanted, and in patients after patella dislocation, have demonstrated the potential of sodium imaging in the detection of early stages of cartilage degeneration [19].

c) Chemical Exchange Saturation Transfer (CEST)

Chemical exchange between bulk water protons and protons bound to solutes can be visualized with MR imaging [20] by using the saturation transfer (ST) technique, a common approach in nuclear magnetic resonance (NMR) [21]. Consequently, the corresponding MR imaging scheme is referred to as CEST MRI [22, 23]. In principle, CEST MRI relies on a reduction of bulk water MR signal as a consequence of selective saturation of off-resonant (solute) spins and subsequent chemical transfer of the saturation to spins of bulk water [24]. A prerequisite for observation of CEST phenomena within a chemical environment is the abundance of sufficiently labile solute protons that are in contact



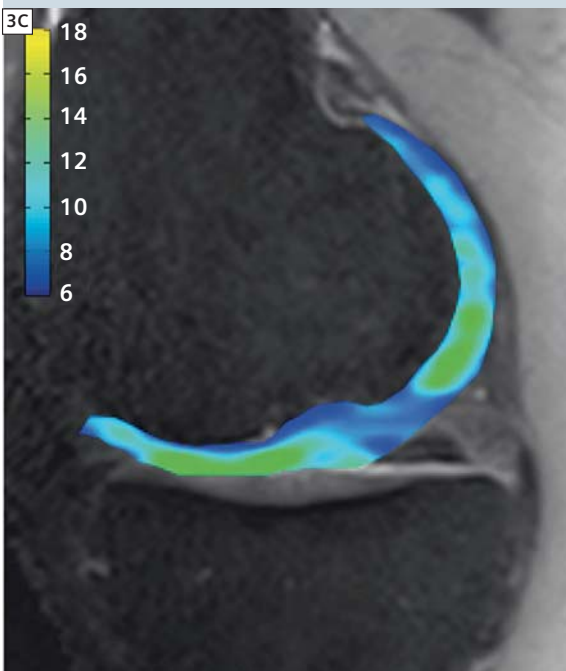
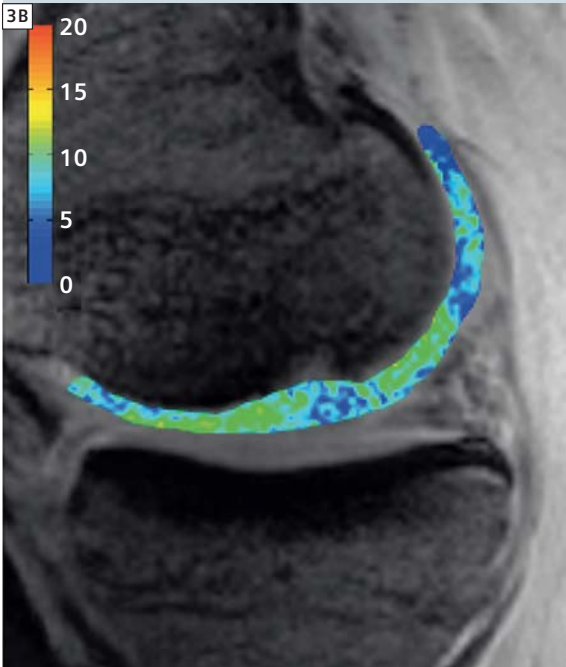
with bulk water. The offset of the resonance frequency of the labile protons ($\Delta\omega$) in Hz must be greater than the exchange rate (k) to provide CEST effects that can be distinguished from direct water saturation. For example, hydroxyl and amide protons of GAG were shown to be suited for CEST experiments (gagCEST) due to their chemical exchange properties [25]: GAG -OH protons resonate at frequency offsets of 1 and 1.5–2 ppm downfield from bulk water, and k can be on the order of up to 1000 s^{-1} [26]. This means that magnetic field strengths greater than 3 Tesla are beneficial for gagCEST experiments, as the condition $\Delta\omega > k$ will be increasingly fulfilled. At higher fields, i.e., with increasing frequency differences, the confounding direct water saturation (RF spillover) decreases. In combination with longer T1 relaxation times, this factor makes ultra high field strengths, such as 7T^1 , potentially favorable for CEST experiments. Consequently, gagCEST imaging was first demonstrated to be

a sensitive biomarker for cartilage GAG content in *in vitro* studies of bovine cartilage at 11.7T^1 [25]. Since the introduction of the gagCEST imaging, more studies have been performed on animal and human subjects to assess the feasibility of gagCEST imaging *in vivo* [27–29], and a large palette of imaging sequences for fast and reliable detection of CEST effects have been proposed [27, 30–32]. The vast majority of techniques is based on repetitive image acquisition with pre-saturation at different offset frequencies ($\Delta\omega$), which allows plotting of the remaining bulk water signal (M_{Sat}), normalized to a reference (M_{Ref}), against the RF pre-saturation offset (z-spectrum). In the z-spectrum, CEST effects appear asymmetric with respect to the water resonance and, thus, calculation of the asymmetry of the magnetization transfer ratio, (Eq. 1) ($\text{MTR}_{\text{asym}}(\Delta\omega) = (M_{\text{Sat}}(-\Delta\omega) - M_{\text{Sat}}(+\Delta\omega)) / M_{\text{Ref}}$), provides a positive measure of CEST effects. In first order, the magnitude of MTR_{asym} values in cartilage

scales linearly with the ratio of GAG protons to bulk water protons. gagCEST imaging (Fig. 3) was shown to be a valuable tool for the non-invasive assessment of GAG content *in vivo*. For example, we could demonstrate that gagCEST can be used to reliably detect GAG in the knee cartilage of patients after cartilage repair surgery [33]. In this study, which was performed at 7T^1 , a 3D GRE-based gagCEST measurement technique was used, and results from ^{23}Na MRI served as a reference for GAG measurements. Moreover, the potential of gagCEST for GAG evaluation in intervertebral discs (IVD) at 3T has been demonstrated in healthy volunteers [34, 35] and in patients with lower back pain [36]. Given the results from the latter studies on IVDs from our group, it is reasonable to assume that gagCEST can also be used to assess cartilage GAG content at 3T. Thus, the indicated potential of gagCEST for the clinical routine is tremendous because it also offers advantages compared to other GAG-sen-



3 High-spatial-resolution (3A) morphologic, (3B) gagCEST, and (3C) ^{23}Na MR images of the knee joint cartilage of a patient after MFX in the medial femoral condyle. Color bars on (3B) and (3C) represent MTR asym values summed over offsets from 0 to 1.3 ppm (gagCEST) and sodium SNRs, respectively. Both techniques show decreased signals in repair tissue compared to surrounding native tissue.



sitive imaging techniques, such as dGEMRIC* and sodium imaging. These advantages include the relatively short acquisition time, which covers the entire volume of a knee joint in ~10 minutes [33], no administration of contrast agent, and simple implementation into a standard imaging protocol.

1.2) Collagen and water-sensitive MRI techniques

Although the differentiation of particular components of articular cartilage that are visualized by a specific sequence is not entirely possible, the classic biochemical MR methodology that focuses on the collagen content of articular cartilage is T2-mapping [37]. In addition to the transverse relaxation time (T2) of articular cartilage, recently, T2* relaxation is being discussed for the depiction of the collagen matrix [38]. Magnetization transfer contrast (MTC) might also play a more important role in future approaches [39].

T2 relaxation time mapping

The transverse relaxation time (T2) of cartilage is a sensitive parameter for the evaluation of changes in water and collagen content and tissue anisotropy [37]. Cartilage T2 reflects the interaction of water and the extracellular matrix on a molecular level. The collagen fiber orientation defines the layers of articular cartilage. Thus, the three-dimensional organization and curvature of the collagen network, influenced by water mobility, the proteoglycan orientation, and the resulting magic angle at 55° (with respect to the main magnetic field B_0) influence the appearance of T2 [40, 41]. In healthy articular cartilage, an increase in T2 values from deep to superficial cartilage layers can be observed, based on the anisotropy of collagen fibers running perpendicular to cortical bone in the deep layer of cartilage [42]. Histologically validated animal studies have shown this zonal increase in T2 values as a marker of hyaline or hyaline-like cartilage structure after cartilage repair procedures in the knee [43, 44]. To visualize this zonal variation *in vivo*, high spatial resolution

is essential, which can already be achieved with high-field MR, together with dedicated multi-channel coils in clinical approaches (Fig. 4). In cartilage repair tissue, global (bulk) T2 values, as well as line profiles, have shown an increase in the early post-operative follow-up period, which might enable visualization of cartilage repair maturation [45]. Another study by our group further showed the ability of zonal T2 evaluation to differentiate cartilage repair tissue after microfracture (MFX) and MACT [46]. Whereas cartilage repair tissue after MFX – histologically seen as fibrocartilage – shows no zonal increase from deep to superficial cartilage aspects, repair tissue after MACT – histologically reported as hyaline-like – shows a significant stratification.

The current evidence shows that the quality of the repair tissue is the key to success in the long term. Patients with repair tissue similar to the native articular cartilage are more likely to have good mid-term results, and in the knee, cell-based techniques result more often in hyaline-like repair tissue than does microfracturing.

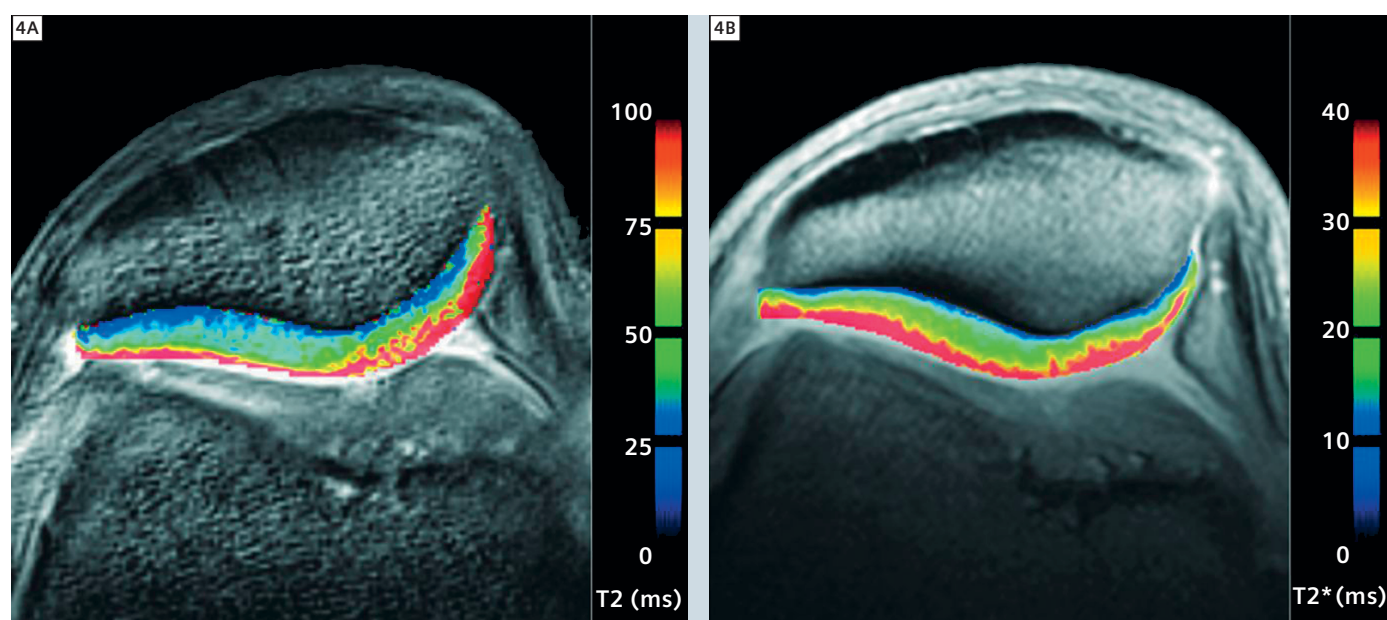
In addition to the knee joint, studies have been performed to analyze different repair surgery techniques in the ankle joint. The initial results at 3T were highly surprising; the average T2 value of the repair tissue after microfracture did not differ significantly from the repair tissue after matrix associated autologous chondrocyte transplantation (MACT). These results were very different from the analyses in the knee, but did, however, agree with the clinical evidence in the literature.

A major drawback of T2-mapping in the ankle was that the SNR even at 3T was not sufficient to perform a zonal analysis of the very thin cartilage layer of the talus. Based on the results in the knee, this might be crucial for characterizing the quality of cartilage repair tissue, as the zonal T2 variation correlates with the degree of organization of the collagen network, and therefore, with the general quality of the repair tissue.

The optimization of the multi-echo spin echo T2-mapping algorithm for 7T yielded a high SNR, better resolution within a clinically feasible scan time, and enabled us to perform an initial comparison of

20 cases after microfracture and MACT of the ankle joint cartilage. The analysis confirmed that there was no significant difference between the average T2 values of the repair tissue after either technique. The major advance was, however, the possibility of a zonal analysis of the healthy cartilage in asymptomatic volunteers, and in patients after cartilage repair [47].

The values of the superficial layer of the repair tissue were comparable to those of articular cartilage; however, there was a substantial difference in the deep layer. A significantly higher T2 was demonstrated for the repair tissue when compared to the healthy reference. Again, there was no difference between the cartilage repair techniques. T2-mapping yielded repair tissue with comparable properties in the MR analysis, which further substantiates the notion that cartilage repair of the ankle cannot be compared to the knee. Bone marrow stimulation techniques are less invasive and less costly than MACT, and might yield a comparable or even better outcome for this joint. It should be noted that the evidence does not allow for



4 Axial T2-maps (4A) and T2*-map (4B) of the cartilage layer of the patella at 7 Tesla¹ nicely demonstrate the zonal variation in the collagen fiber network in cartilage in this volunteer.

a conclusion at this time; however, biochemical MRI can be of substantial help in determining future treatment algorithms in this field.

In osteoarthritis, however, T2-mapping has shown varying results [48–50] and the role of T2 as an absolute quantification parameter must be further analyzed. Thus, it is not yet totally clear whether a slight increase or decrease in T2 relaxation times can be correlated to morphological changes. Nevertheless, T2-mapping seems to offer potential in this area as well. Conclusions would be more easily derived, however, from a longitudinal evaluation of the same subject, with MRI performed at the same time of day.

2. Biochemical MRI assessment of the intervertebral disc

For biochemical MR imaging of the intervertebral disc (IVD), the following MR methods and techniques were optimized by our group: T2-mapping; T2*-mapping; diffusion-weighted imaging at 3 Tesla; and recently, sodium imaging at 7 Tesla; and Chemical Exchange Saturation Transfer (CEST) at 3 Tesla (Fig. 5). In an initial trial on 34 patients with lower back pain but without radicular symptoms we compared standard morphological MRI at 3T with T2-mapping [51, 52]. For T2-mapping, all discs of the lumbar spine were analyzed by classification into five equally-sized regions-of-interest (ROI) (20% each) in the sagittal plane, where the anterior and posterior 20% were defined anatomically as the annulus fibrosus (AF) and the 60% area in between the anterior and posterior represented the nucleus pulposus (NP) of the IVD. We found a good correlation between the morphological Pfirrmann classification and T2 relaxation time values. To further increase the sensitivity of the analysis, the posterior annulus fibrosus was further subdivided into two 10% ROIs to consider the axial load on the posterior column of the spine. This analysis provided a possible marker for the early stage of disc degeneration [51].

Furthermore, a comparison of quantitative T2 values of the IVD with conven-

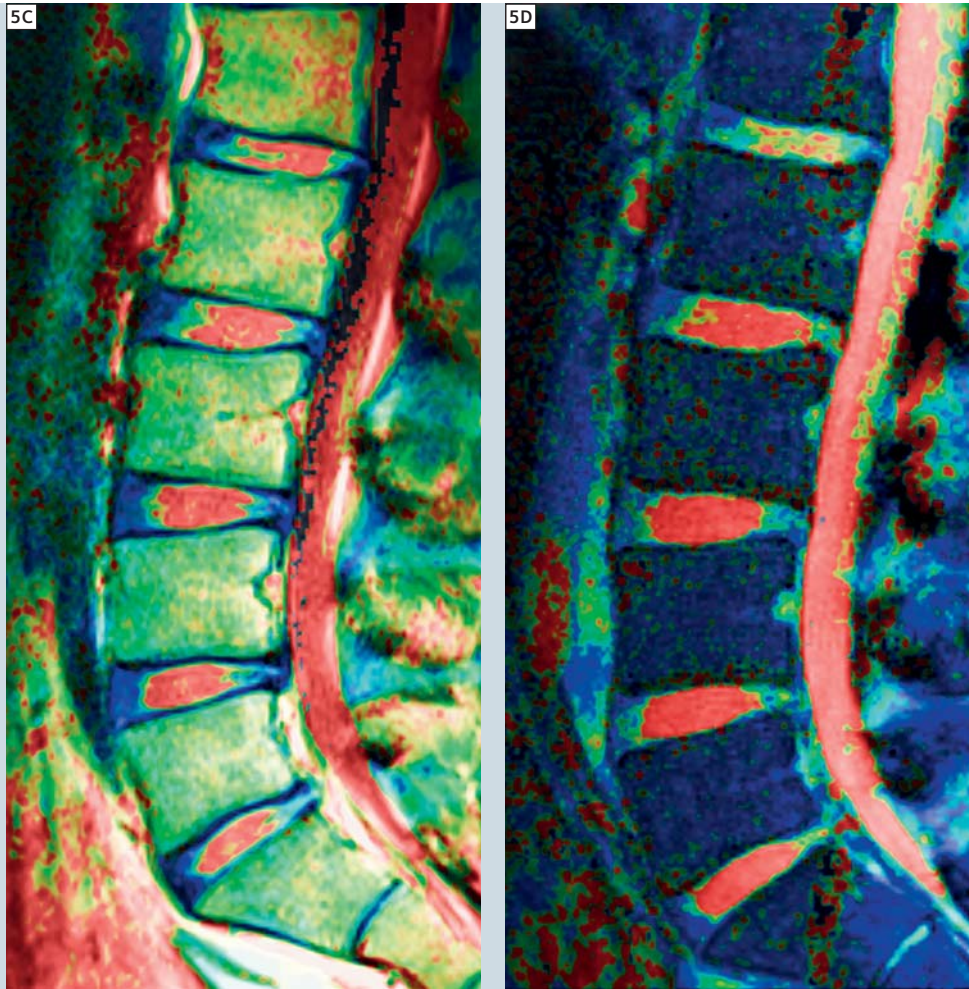


5 Comparison of morphological and biochemical imaging of the intervertebral discs of the lumbar spine in a healthy volunteer using T2 FSE (5A), T1 FSE (5B), T2-map (5C), and T2*-map (5D).

tional MRI findings of the spine at 3T was performed [53]. In a total of 265 discs, there were 39 focal herniations, 10 annular tears, 123 disc bulgings, and 103 normal discs. We found a statistically significant difference between the nucleus pulposus T2 values in discs with annular tears and all other groups with the discs with annular tears, showing significantly lower T2 values compared to discs without annular tears. The difference in NP T2 values between discs with focal herniations and normal discs was also significant. However, no significant difference was found between NP T2 values between disc bulging and disc herniation. Thus, for the first time, quantitative T2-mapping of the NP at

3 Tesla demonstrated significant differences in T2 values between different dislocations of the discs of the lumbar spine.

In addition, methodologically, T2-mapping of the IVD was compared to T2*-mapping at 3 Tesla in 30 patients with lower back pain [54]. The highest variation with an increase of T2 and T2* values from the AF to NP was found in Pfirrmann grade I and decreased with higher Pfirrmann grades II-IV. In addition to T2-mapping, T2*-mapping revealed further changes in the posterior annulus fibrosus. The correlation between T2 and T2*-mapping showed a moderate correlation of 0.21 to 0.356. The clear differentiation between different stages



of disc degeneration and the possibility of quantification by T2 and T2*-mapping may provide a new tool for a more sensitive monitoring of different therapies in patients with lower back pain. In a preliminary study, sodium imaging of the IVD of the lumbar spine at 7 Tesla was compared with T2-mapping and morphological grading by the Pfirrmann classification. No correlation was found between sodium imaging and T2-mapping, confirming that both methods detect different components of the IVD [55].

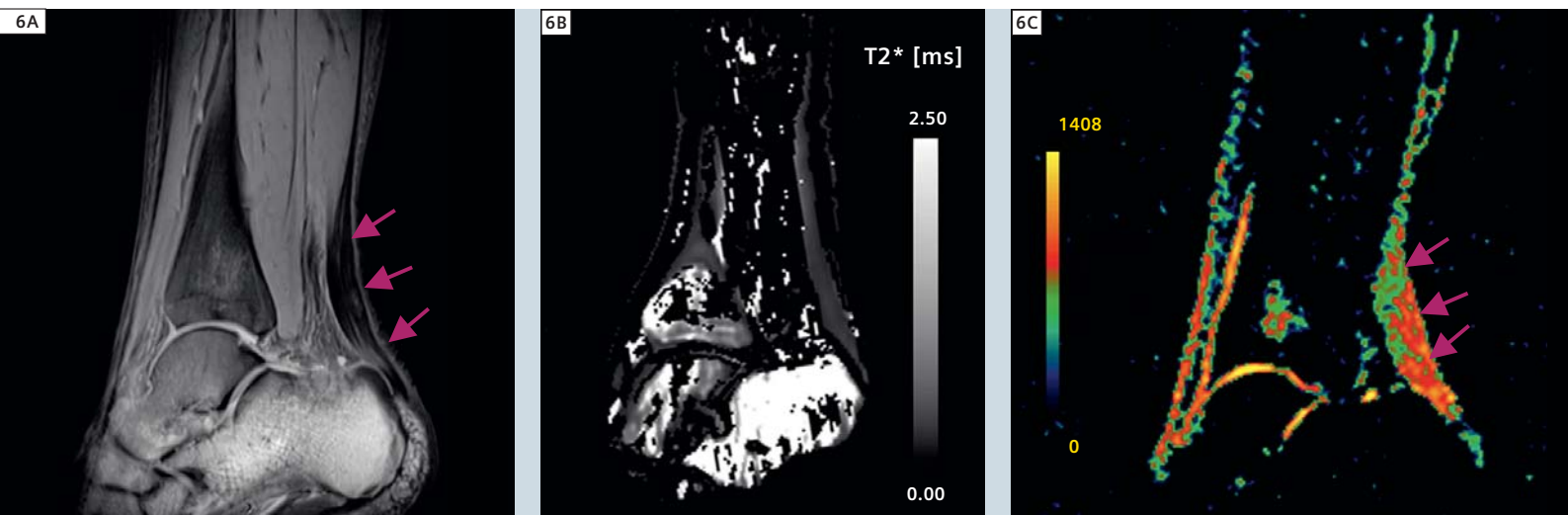
3. Biochemical MRI assessment of tendons

3.1) Sodium imaging of tendons

Tendons, which are dense, fibrous connective tissues, are often affected by tendinopathy. This clinical condition is defined as a syndrome of tendon pain, tenderness, and swelling that affects tendon function. Morphologically, degeneration of the Achilles tendon, for example, leads to thickening of the tendon [56]. Tendinopathy is accompanied by a disaggregation of the microfibrillar bundles due to the greater quantities of water and proteoglycan macromolecules. In chronic Achilles tendinopathy, biochemical alterations presage macro-

scopic changes [57]. Glycosaminoglycan (GAG) content was observed to be doubled in pathologic tendons in biochemical studies [58]. In a study our group, the feasibility of sodium magnetic resonance imaging at 7T¹ for the diagnosis of Achilles tendinopathy was investigated [59]. The cohort comprised twenty healthy volunteers with no history of pain in the Achilles tendon and eight patients with clinical findings of chronic Achilles tendinopathy. We used a three-dimensional gradient-echo sequence optimized for sodium imaging. The parameters were as follows: TR 17 msec, TE 8.34 msec, FOV 199 x 199 mm, section thickness 3 mm, flip angle 50°; 12 signals acquired, acquisition matrix 224 x 224 pixels. The total measurement time for sodium imaging, including flip angle calibration and localizers, was about 32 minutes. Moreover, five fresh human cadaver lower legs from four different subjects (mean age of 48 ± 8 years) were used as a reference for sodium signal and GAG content relation. These samples were analyzed biochemically to obtain GAG and water content. The study found that the mean bulk sodium SNR was 4.9 ± 2.1 in healthy control subjects and 9.3 ± 2.3 in patients with Achilles tendinopathy, and that the difference between the means was statistically significant. The correlation between sodium SNR values acquired from three regions of five cadaver Achilles tendons and GAG content was found to be high, with a Pearson coefficient of 0.71.

This study showed a statistically significant increase in sodium SNR in patients with Achilles tendinopathy, compared with healthy tendons (Fig. 6C). Moreover, the study also revealed abnormal sodium signal values in the whole tendon, although morphologically focal abnormalities with focal thickening were seen. This suggests that the Achilles tendon is affected diffusely in tendinopathy rather than focally. Sodium signal values mostly correspond to GAG content in the Achilles tendon, which, as shown in *in vitro* studies, is increased with tendinopathy [59]. It has been shown that, despite the relatively challenging techni-



6 Morphological image (**6A**), T2*-map measured by 3D-UTE multi-echo sequence (**6B**) acquired at different echo times (minimal TE 0.07 ms, maximal TE 9.0 ms), sodium image (**6C**) of a patient with chronic Achillotendinitis. Sodium image shows increased sodium SNR and thus higher GAG content.

cal requirements of sodium MRI, it is possible to clinically use sodium MRI for diagnostic purposes in the Achilles tendon *in vivo*.

3.2) Quantitative analysis of T2* in the Achilles tendon at 7 Tesla¹

With the recent hardware and software developments, MRI is still more often used clinically for the evaluation of the Achilles tendon. Modern MRI methods provide direct access to signal from fast-relaxing tissues, such as tendons. Since the relaxation times in the AT are on the order of 1 ms, a very short echo time (TE) must be used to acquire signal from the tendon. These methods were successfully used to detect partial or total tendon rupture or even the degenerative processes in the tendon tissue [56]. Pathological and consecutive repair processes may lead to collagen fiber alterations, and thus, relaxation properties may be changed [60]. This results in signal alterations and changes in relaxation properties of the bound and free water molecules. Quantitative analysis of the relaxation and/or diffusion constants of the AT, such as T1, T2*, T1ρ, or ADC, may provide additional information about the tendon condition. On conventional high-field MR systems, several parameters have been investigated in the past as prospective markers for Achilles tendon

degeneration, such as T2, T2*, T1ρ, ADC, and magnetization transfer [61–65]. It was shown spectroscopically that T2* decay in the Achilles tendon demonstrates a multi-component nature [66]. The MR signals from the second, third, and fourth components are difficult to acquire on conventional clinical MR systems, since these have a relatively small component ratio compared to the first component. The first component has the highest ratio, but it is in the submillisecond range and can therefore hardly be acquired with conventional echo times (~5 ms). Recent sequence development allows the acquisition of a signal from these tissues. The most important sequences used in MR imaging of highly organized tissues are two- and three-dimensional ultra-short echo time sequences (2D- and 3D-UTE), variable echo time sequences (VTE), and an acquisition-weighted stack of spirals (AWSOS) sequence. Du and colleagues observed a T2* of 0.78 ± 0.07 ms at 3T, using a 2D-UTE sequence [67]. Regional dependencies of T2* within the Achilles tendon were described by Robson et al. [61]. Ultra high field MRI provides a substantial increase in the SNR ratio of fast-relaxing tissue types [68]. In a recent study, we used a 3D-UTE sequence at 7T¹ to estimate T2* in tendons in order to investigate the potential feasibility

of using this parameter as a marker for Achilles tendinopathy [69]. An SNR increase between 3 and 7T¹ was observed in this study as well. T2* was acquired by fitting bi-component exponential functions, and both short (T2*s) and long (T2*I) components were evaluated. With regard to the comparison of patients and volunteers at 7T¹, the bulk T2*s was significantly higher in patients, although the bulk T2*I difference was not statistically significant. This study suggests that ultra-short bi-component T2* measurements in the human Achilles tendon *in vivo* are feasible using a 3D-UTE sequence, with high accuracy at 7T¹ (Fig. 6B). Although it is difficult to separate the water and collagen fibers in the Achilles tendon; T2* reflects the overall condition of AT as an interplay between the amount of water and the organization of collagen macromolecules. The observed differences between T2*s in healthy and pathological tendons suggest that advanced quantitative imaging of the human Achilles tendon may provide additional information to standard clinical imaging in reasonably short MR data acquisition times. Quantitative analysis of T2* may be a promising marker for the diagnosis of early tendinopathy in the Achilles tendon [69].

In conclusion, ultra high field MRI at 7T¹ offers the advantage of higher resolution imaging for morphological information, and improves spatial resolution in T2-mapping, which enables an evaluation of the zonal variation of even thin cartilage layers and significantly improves sensitivity for other nuclei, such as ²³Na. This plays an important role in MSK imaging, since sodium correlates directly with GAG content. In addition, the GAG-specific CEST technique also benefits from the ultra high field. This will provide new insights into the normal and abnormal physiology of musculoskeletal tissues, and will, therefore, provide new in vivo clinical applications.

Acknowledgment

The authors would like to thank the Editorial office of **European Radiology, Osteoarthritis and Cartilage and Radiology** for permissions to use figures from previously published articles.

* A licensed physician may choose to use FDA-approved contrast agents in conjunction with an MRI exam, based on his/her medical opinion and discretion and in accordance with the instructions for use and indications for use supplied by the pharmaceutical manufacturer for the contrast agents.

¹Works in Progress in the USA. The information about this product is preliminary. The product is under development and is not commercially available in the U.S. and its future availability cannot be ensured. The 7T system is an investigational device. Limited by U.S. federal law to investigational use. This research system is not cleared, approved or licensed in any jurisdiction for patient examinations. This research system is not labelled according to applicable medical device law and therefore may only be used for volunteer or patient examinations in the context of clinical studies according to applicable law.

References

- Buckwalter JA, Mankin HJ (1998) *Articular cartilage: Degeneration and osteoarthritis, repair, regeneration, and transplantation*. Instructional Course Lectures, Vol 47 – 1998 **47**, 487-504.
- Poole AR, Kojima T, Yasuda T, et al (2001) *Composition and structure of articular cartilage – A template for tissue repair*. Clinical Orthopaedics and Related Research, **S26-S33**.
- Burstein D, Velyvis J, Scott KT, et al (2001) *Protocol issues for delayed Gd(DTPA)(2-)-enhanced MRI: (dGEMRIC) for clinical evaluation of articular cartilage*. Magnetic Resonance in Medicine **45**, 36-41.
- Bashir A, Gray ML, Burstein D (1996) *Gd-DTPA(2-) as a measure of cartilage degradation*. Magnetic Resonance in Med. **36**, 665-673.
- Borthakur A, Shapiro EM, Beers J, et al (2000) *Sensitivity of MRI to proteoglycan depletion in cartilage: comparison of sodium and proton MRI*. Osteoarthritis and Cartilage **8**, 288-293.
- Ling W, Regatte RR, Navon G, et al (2008b) *Assessment of glycosaminoglycan concentration in vivo by chemical exchange-dependent saturation transfer (gagCEST)*. Proceedings of the National Academy of Sciences of the United States of America **105**, 2266-2270.
- Burstein D, Bashir A, Gray ML (2000) *MRI techniques in early stages of cartilage disease*. Investigative Radiology **35**, 622-638.
- Watanabe A, Wada Y, Obata T, et al (2006) *Delayed gadolinium-enhanced MR to determine glycosaminoglycan concentration in reparative cartilage after autologous chondrocyte implantation: Preliminary results*. Radiology **239**, 201-208.
- Bashir A, Gray ML, Boutin RD, et al (1997) *Glycosaminoglycan in articular cartilage: In vivo assessment with delayed Gd(DTPA)(2-)-enhanced MR imaging*. Radiology **205**, 551-558.
- Tiderius CJ, Olsson LE, Leander P, et al (2003) *Delayed gadolinium-enhanced MRI of cartilage (dGEMRIC) in early knee osteoarthritis*. Magnetic Resonance in Medicine **49**, 488-492.
- Williams A, Gillis A, McKenzie C, et al (2004) *Glycosaminoglycan distribution in cartilage as determined by delayed gadolinium-enhanced MRI of cartilage (dGEMRIC): Potential clinical applications*. American Journal of Roentgenology **182**, 167-172.
- Trattinig S, Marlovits S, Gebetsroither S, et al (2007) *Three-dimensional delayed gadolinium-enhanced MRI of cartilage (dGEMRIC) for in vivo evaluation of reparative cartilage after matrix-associated autologous chondrocyte transplantation at 3.0T: Preliminary results*. Journal of Magnetic Resonance Imaging **26**, 974-982.
- Trattinig S, Mamisch TC, Pinker K, et al (2008) *Differentiating normal hyaline cartilage from post-surgical repair tissue using fast gradient echo imaging in delayed gadolinium-enhanced MRI (dGEMRIC) at 3 Tesla*. European Radiology **18**, 1251-1259.
- Kim YJ, Jaramillo D, Millis MB, et al (2003) *Assessment of early osteoarthritis in hip dysplasia with delayed gadolinium-enhanced magnetic resonance imaging of cartilage*. Journal of Bone and Joint Surgery-American Volume **85A**, 1987-1992.
- Vaga S, Raimondi MT, Caiani EG, et al (2008) *Quantitative assessment of intervertebral disc glycosaminoglycan distribution by gadolinium-enhanced MRI in orthopedic patients*. Magnetic Resonance in Medicine **59**, 85-95.
- Williams A, Shetty SK, Burstein D, et al (2008) *Delayed gadolinium enhanced MRI of cartilage (dGEMRIC) of the first carpometacarpal (1CMC) joint: a feasibility study*. Osteoarthritis and Cartilage **16**, 530-532.
- Trattinig S, Welsch GH, Juras V, et al (2010) (23) *Na MR Imaging at 7 T after Knee Matrix-associated Autologous Chondrocyte Transplantation: Preliminary Results*. Radiology **257**, 175-184.
- Zbyn S, Stelzeneder D, Welsch GH, et al *Evaluation of native hyaline cartilage and repair tissue after two cartilage repair surgery techniques with (23)Na MR imaging at 7 T: initial experience*. Osteoarthritis Cartilage **20**, 837-45.
- Krusche-Mandl I, Schmitt B, Zak L, et al *Long-term results 8 years after autologous osteo-chondral transplantation: 7 T gagCEST and sodium magnetic resonance imaging with morphological and clinical correlation*. Osteoarthritis Cartilage **20**, 357-63.
- Guivel-Scharen V, Sinnwell T, Wolff SD, et al (1998) *Detection of proton chemical exchange between metabolites and water in biological tissues*. Journal of Magnetic Resonance **133**, 36-45 DOI: S1090-7807(98)91440-9 [pii] 10.1006/jmre.1998.1440.
- Forsen S, Hoffman RA (1963) *Study of Moderately Rapid Chemical Exchange Reactions by Means of Nuclear Magnetic Double Resonance*. Journal of Chemical Physics **39**, 2892.
- Ward KM, Aletras AH, Balaban RS (2000) *A new class of contrast agents for MRI based on proton chemical exchange dependent saturation transfer (CEST)*. Journal of Magnetic Resonance **143**, 79-87 DOI: 10.1006/jmre.1999.1956 S1090-7807(99)91956-0 [pii].
- Ward KM, Balaban RS (2000) *Determination of pH using water protons and chemical exchange dependent saturation transfer (CEST)*. Magnetic Resonance in Medicine **44**, 799-802 DOI: 10.1002/1522-2594(200011)44:5<799::AID-MRM18>3.0.CO;2-S [pii].
- Zhou JY, van Zijl PCM (2006) *Chemical exchange saturation transfer imaging and spectroscopy*. Progress in Nuclear Magnetic Resonance Spectroscopy **48**, 109-136 DOI: DOI 10.1016/j.pnmrs.2006.01.001.
- Ling W, Regatte RR, Schweitzer ME, et al (2008) *Characterization of bovine patellar cartilage by NMR*. Nmr in Biomedicine **21**, 289-295 DOI: Doi 10.1002/Nbm.1193.
- Ling W, Regatte RR, Navon G, et al (2008) *Assessment of glycosaminoglycan concentration in vivo by chemical exchange-dependent saturation transfer (gagCEST)*. Proc Natl Acad Sci U S A **105**, 2266-70 DOI: 0707666105 [pii] 10.1073/pnas.0707666105.
- Schmitt B, Bock M, Stieltjes B, et al. *A new, 3D GRE based CEST imaging method for clinical application and verification with gagCEST in articular cartilage*. in Proceedings 18th Scientific Meeting, International Society for Magnetic Resonance in Medicine. 2010. Stockholm.
- Vinogradov E, Ivanishev A, Grant AK, et al. *CEST and Sodium Imaging of Glycosaminoglycans in-vivo in the 3T: Preliminary Results*. in Proceedings 18th Scientific Meeting, International Society for Magnetic Resonance in Medicine. 2010. Stockholm.
- Fenty M, Kassey V, Kogan F, et al. *Feasibility of CEST imaging on the guinea pig stifle at 9.4 T*. in Proceedings 19th Scientific Meeting, International Society for Magnetic Resonance in Medicine. 2011. Montreal.

- 30 Vinogradov E, Lenkinski RE. *Detection of Glycosaminoglycans using Positive CEST approach*. in *Proceedings 18th Scientific Meeting, International Society for Magnetic Resonance in Medicine*. 2010. Stockholm.
- 31 Varma G, Alsop DC, Lenkinski RE, et al. *Optimization of pulsed-gagCEST at 3.0T*. in *Proceedings 19th Scientific Meeting, International Society for Magnetic Resonance in Medicine*. 2011. Montreal.
- 32 Varma G, Lenkinski RE, Vinogradov E. *Keyhole Chemical Exchange Saturation Transfer*. in *Proceedings 19th Scientific Meeting, International Society for Magnetic Resonance in Medicine*. 2011. Montreal.
- 33 Schmitt B, Zbyn S, Stelzeneder D, et al (2011) *Cartilage quality assessment by using glycosaminoglycan chemical exchange saturation transfer and (23)Na MR imaging at 7 T*. *Radiology* **260**, 257-64 DOI: 10.1148/radiol.11101841.
- 34 Ling W, Saar G, Regatte R, et al. *Assessing the Invertebral Disc via gagCEST*. in *Proceedings 17th Scientific Meeting, International Society for Magnetic Resonance in Medicine*. 2009. Honolulu.
- 35 Kim M, Chan Q, Anthony MP, et al (2011) *Assessment of glycosaminoglycan distribution in human lumbar intervertebral discs using chemical exchange saturation transfer at 3 T: feasibility and initial experience*. *NMR in Biomedicine* **24**, 1137-44 DOI: 10.1002/nbm.1671.
- 36 Haneder S, Apprich S, Schmitt B, et al (2012) *Glycosaminoglycan content in intervertebral discs using chemical exchange saturation transfer at 3T MRI: preliminary results in patients with low back pain*. *European Radiology Accepted for Publication*.
- 37 Mosher TJ, Dardzinski BJ (2004) *Cartilage MRI T2 relaxation time mapping: Overview and applications*. *Seminars in Musculoskeletal Radiology* **8**, 355-368.
- 38 Welsch GH, Mamisch TC, Hughes T, et al (2008) *In vivo biochemical 7.0 Tesla magnetic resonance - Preliminary results of dGEMRIC, zonal T2, and T2* mapping of articular cartilage*. *Investigative Radiology* **43**, 619-626.
- 39 Welsch GH, Trattnig S, Scheffler K, et al (2008) *Magnetization transfer contrast and T2 mapping in the evaluation of cartilage repair tissue with 3T MRI*. *Journal of Magnetic Resonance Imaging* **28**, 979-986.
- 40 Goodwin DW, Zhu HQ, Dunn JF (2000) *In vitro MR imaging of hyaline cartilage: Correlation with scanning electron microscopy*. *American Journal of Roentgenology* **174**, 405-409.
- 41 Goodwin DW, Wadghiri YZ, Dunn JF (1998) *Micro-imaging of articular cartilage: T2, proton density, and the magic angle effect*. *Academic Radiology* **5**, 790-798.
- 42 Smith HE, Mosher TJ, Dardzinski BJ, et al (2001) *Spatial variation in cartilage T2 of the knee*. *Journal of Magnetic Resonance Imaging* **14**, 50-55.
- 43 Watrin-Pinzano A, Ruaud JP, Cheli Y, et al (2004) *Evaluation of cartilage repair tissue after biomaterial implantation in rat patella by using T2 mapping*. *Magnetic Resonance Materials in Physics Biology and Medicine* **17**, 219-228.
- 44 White LM, Sussman MS, Hurtig M, et al (2006) *Cartilage T2 assessment: Differentiation of normal hyaline cartilage and reparative tissue after arthroscopic cartilage repair in equine subjects*. *Radiology* **241**, 407-414.
- 45 Trattnig S, Mamisch TC, Welsch GH, et al (2007) *Quantitative T-2 mapping of matrix-associated autologous chondrocyte transplantation at 3 Tesla - An in vivo cross-sectional study*. *Investigative Radiology* **42**, 442-448.
- 46 Welsch GH, Mamisch TC, Domayer SE, et al (2008) *Cartilage T2 assessment at 3-T MR imaging: In vivo differentiation of normal hyaline cartilage from reparative tissue after two cartilage repair procedures - Initial experience*. *Radiology* **247**, 154-161.
- 47 Domayer SE, Apprich S, Stelzeneder D, et al *Cartilage repair of the ankle: first results of T2 mapping at 7.0 T after microfracture and matrix associated autologous cartilage transplantation*. *Osteoarthritis Cartilage* **20**, 829-36.
- 48 David-Vaudey E, Ghosh S, Ries M, et al (2004) *T-2 relaxation time measurements in osteoarthritis*. *Magnetic Resonance Imaging* **22**, 673-682.
- 49 Dunn TC, Lu Y, Jin H, et al (2004) *T2 relaxation time of cartilage at MR imaging: Comparison with severity of knee osteoarthritis*. *Radiology* **232**, 592-598.
- 50 Burstein D, Gray ML (2006) *Is MRI fulfilling its promise for molecular imaging of cartilage in arthritis? Osteoarthritis and Cartilage* **14**, 1087-1090.
- 51 Stelzeneder D, Welsch GH, Kovacs BK, et al *Quantitative T2 evaluation at 3.0T compared to morphological grading of the lumbar intervertebral disc: a standardized evaluation approach in patients with low back pain*. *Eur J Radiol* **81**, 324-30.
- 52 Stelzeneder D, Messner A, Vlychou M, et al *Quantitative in vivo MRI evaluation of lumbar facet joints and intervertebral discs using axial T2 mapping*. *Eur Radiol* **21**, 2388-95.
- 53 Trattnig S, Stelzeneder D, Goed S, et al *Lumbar intervertebral disc abnormalities: comparison of quantitative T2 mapping with conventional MR at 3.0 T*. *Eur Radiol* **20**, 2715-22.
- 54 Welsch GH, Trattnig S, Paternostro-Sluga T, et al *Parametric T2 and T2* mapping techniques to visualize intervertebral disc degeneration in patients with low back pain: initial results on the clinical use of 3.0 Tesla MRI*. *Skeletal Radiol* **40**, 543-51.
- 55 Noebauer-Huhmann IM, Juras V, Pfirrmann C, et al (in press) *Sodium Imaging of the Lumbar Intervertebral Disc at 7T: Correlation with T2 Mapping and Modified Pfirrmann Score at 3T*. *Preliminary results*. *Radiology*.
- 56 Schweitzer ME, Karasick D (2000) *MR imaging of disorders of the Achilles tendon*. *AJR Am J Roentgenol* **175**, 613-25.
- 57 Samiric T, Parkinson J, Ilic MZ, et al (2009) *Changes in the composition of the extracellular matrix in patellar tendinopathy*. *Matrix Biol* **28**, 230-6.
- 58 Fu SC, Chan KM, Rolf CG (2007) *Increased deposition of sulfated glycosaminoglycans in human patellar tendinopathy*. *Clin J Sport Med* **17**, 129-34.
- 59 Juras V, Zbyn S, Pressl C, et al (2012) *Sodium MR Imaging of Achilles Tendinopathy at 7 T: Preliminary Results*. *Radiology* **262**, 199-205.
- 60 Gelberman RH, Manske PR, Vande Berg JS, et al (1984) *Flexor tendon repair in vitro: a comparative histologic study of the rabbit, chicken, dog, and monkey*. *J Orthop Res* **2**, 39-48.
- 61 Robson MD, Benjamin M, Gishen P, et al (2004) *Magnetic resonance imaging of the Achilles tendon using ultrashort TE (UTE) pulse sequences*. *Clin Radiol* **59**, 727-35.
- 62 Hodgson RJ, Evans R, Wright P, et al (2011) *Quantitative magnetization transfer ultrashort echo time imaging of the Achilles tendon*. *Magn Reson Med* **65**, 1372-6.
- 63 Du J, Carl M, Diaz E, et al (2010) *Ultrashort TE T1rho (UTE T1rho) imaging of the Achilles tendon and meniscus*. *Magn Reson Med* **64**, 834-42.
- 64 Fechete R, Demco DE, Eliav U, et al (2005) *Self-diffusion anisotropy of water in sheep Achilles tendon*. *NMR Biomed* **18**, 577-86.
- 65 Henkelman RM, Stanisz GJ, Kim JK, et al (1994) *Anisotropy of NMR properties of tissues*. *Magn Reson Med* **32**, 592-601.
- 66 Peto S, Gillis P (1990) *Fiber-to-field angle dependence of proton nuclear magnetic relaxation in collagen*. *Magn Reson Imaging* **8**, 705-12.
- 67 Du J, Chiang AJT, Chung CB, et al (2010) *Orientation analysis of the Achilles tendon and entheses using an ultrashort echo time spectroscopic imaging sequence*. *Magnetic Resonance Imaging* **28**, 178-184.
- 68 Regatte RR, Schweitzer ME (2007) *Ultra-high-field MRI of the musculoskeletal system at 7.0T*. *J Magn Reson Imaging* **25**, 262-9.
- 69 Juras V, Zbyn S, Pressl C, et al (2012) *Regional Variations of T2* in Healthy and Pathologic Achilles Tendon In Vivo at 7 Tesla: Preliminary Results*. *Magnetic resonance in Medicine In Press*.

Contact

Prof. Siegfried Trattnig, M.D.
MR Center – High field MR
Department of Radiology
Medical University of Vienna/Vienna
General Hospital
Lazarettgasse 14
A-1090 Vienna
Austria
Phone: +43 1 40 400 6460
Fax: +43 1 40 400 6475
siegfried.trattnig@meduniwien.ac.at

The magazine of MR

MAGNETOM Flash

turns 50...



*...and says thank you to all
authors and readers.*

With the first issue published in 1993 we are not celebrating our 50th birthday, but issue no. 50. From the very beginning, MAGNETOM Flash was a cooperation between Siemens Healthcare and MAGNETOM users. The first editor of the newspaper sized publication was Christine Harris, R.T. at Children's Hospital of Philadelphia, USA and the focus of the 'newsletter' was a communication network between Technologists and the Siemens Corporation. As the newsletter developed into a magazine the target group grew to include radiologists, physicists, cardiologists and researchers. What did not change is the involvement of you - our readers. Being part of the MAGNETOM World, the community for all Siemens MR users worldwide, the magazine is affording you a platform to contribute and expand your knowledge. We welcome your feedback, questions and comments – please contact us at magnetomworld.med@siemens.com.
www.siemens.com/magnetom-world – communications keeping you up-to-date.

Ultra High Field (7 Tesla) MRI for Musculoskeletal Applications

Siegfried Trattning; Štefan Zbýň; Vladimír Juras; Pavol Szomolanyi; Stephan Domayer; Iris-Melanie Noebauer-Huhmann; Goetz Welsch; Benjamin Schmitt

MR Centre - High field MR, Department of Radiology, Medical University of Vienna/Vienna General Hospital, Vienna, Austria

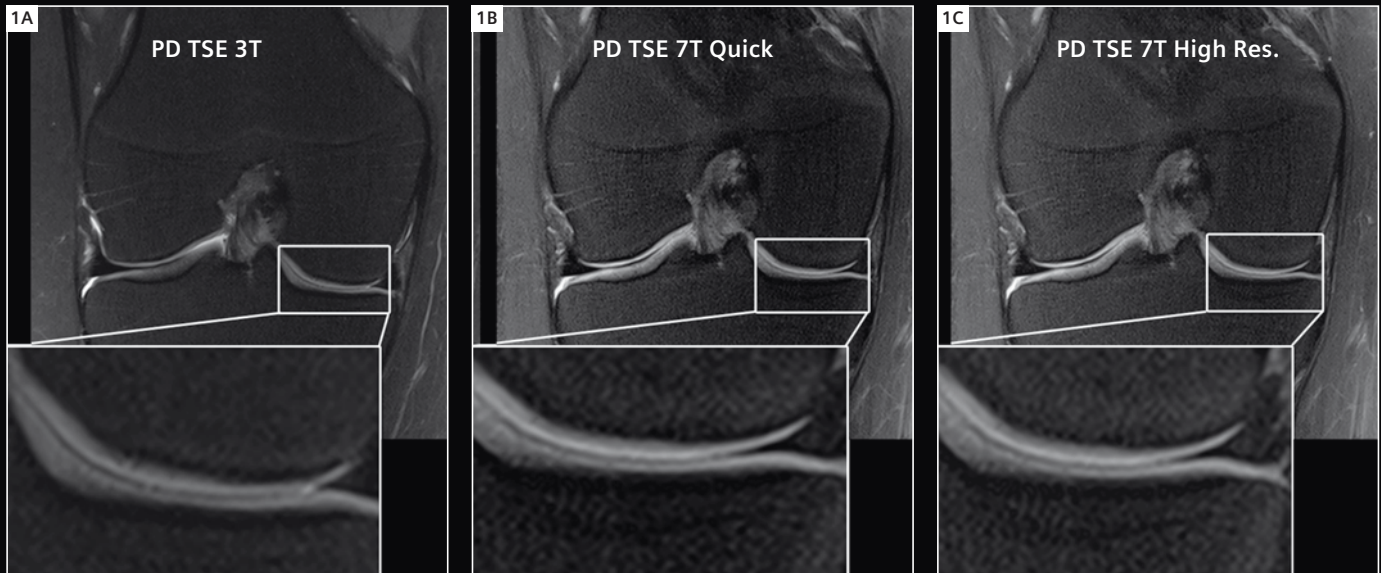
Since the end of the 1990s, high field MRI operating at 3 Tesla has become the benchmark for routine clinical applications, as well as for clinical MRI research. The clinical benefits of the double signal-to-noise ratio (SNR) compared to standard 1.5 Tesla MRI lie predominantly in the possibility of combining morphological and functional high-field MR methods, such as functional MR, metabolic imaging, and diffusion-weighted imaging.

In the early 2000s, the MRI field strength was again increased by another factor of approximately two and at least three major MR vendors currently provide commercial 7 Tesla systems for human clinical research under approved ethical permission. During the last several years, the number of 7 Tesla installations finalized or under preparation has increased to about 50.

While clinical MR research centers operating at 7 Tesla mostly focus on neurological applications, only a few 7 Tesla sites perform whole-body clinical research. This is because of the limited availability of suitable coils for 7 Tesla, which have to be transmit and receive coils, and because of the higher B1 heterogeneity related to the ultra high field. Other limitations relate to the safety issues, particularly the increased specific absorption rate (SAR).

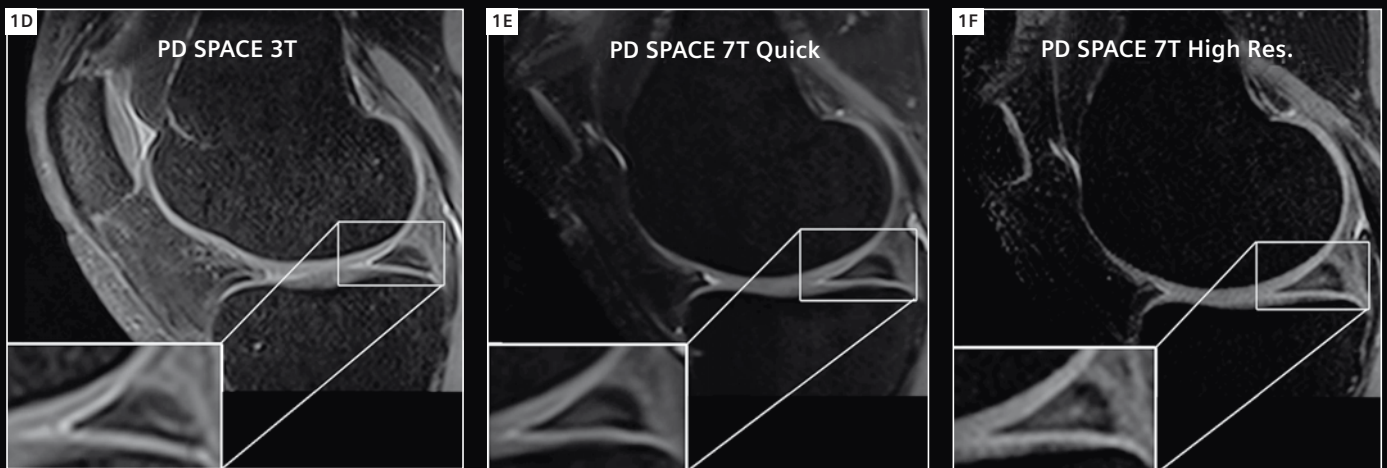
Due to the relatively small volumes of joints in comparison to brain or abdomen for example, a higher B_0 and B_1 homogeneity is easier to study in musculoskeletal applications. While in morphological imaging the spatial resolution can be increased within the same scan time compared to 3 Tesla, compositional or biochemical MR of cartilage and other joint structures benefit from the higher SNR at 7 Tesla. Moreover, nuclei other than protons can be used at 7 Tesla. Sodium values which correlate directly with the glycosaminoglycan content of cartilage, as well as other MSK structures such as the tendons and the intervertebral disc, have been used in clinical applications for the first time [1]. The same is true for Chemical Exchange Saturation Transfer (CEST), which is a very modern glycosaminoglycan (GAG)-specific technique [2]. This image gallery gives an overview of musculoskeletal applications at 7 Tesla.

CAUTION: The 7T system is an investigational device. Limited by U.S. federal law to investigational use. The products mentioned herein are still under development and not commercially available yet. Its future availability cannot be ensured. This research system is not cleared, approved or licensed in any jurisdiction for patient examinations. This research system is not labelled according to applicable medical device law and therefore may only be used for volunteer or patient examinations in the context of clinical studies according to applicable law.

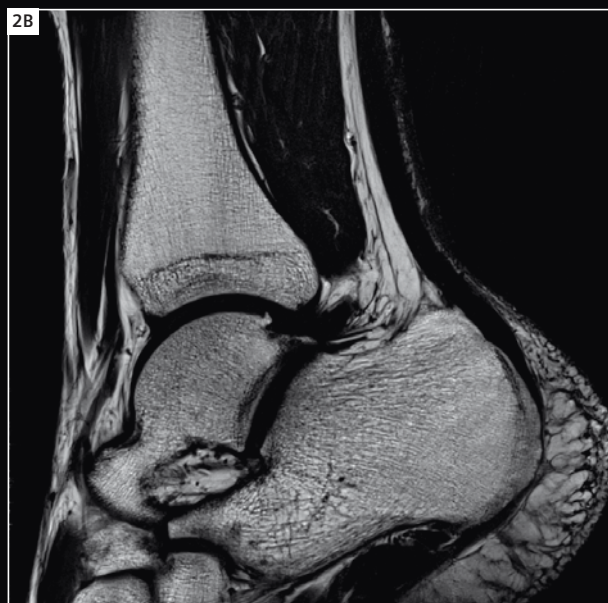
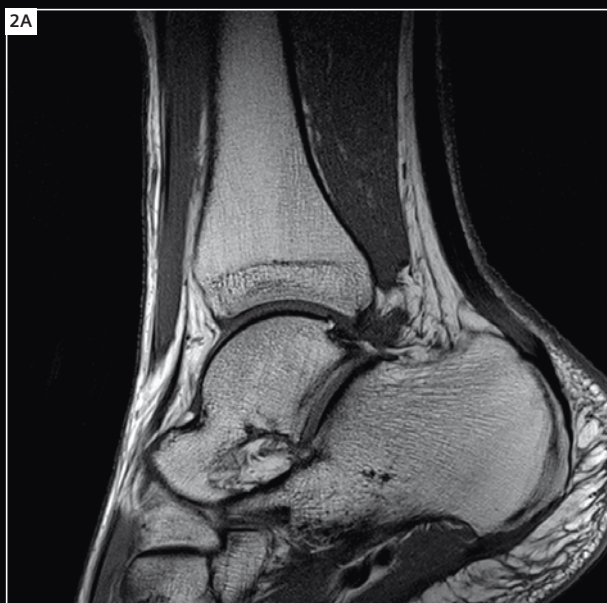


Case 1

Coronal fat-saturated (fs) 2D proton density-weighted turbo spin echo (PD TSE) sequence for 3T (**1A**), 7T quick (same resolution compared to 3T, but shorter scan time at 7T) (**1B**) and 7T high-resolution (same scan time compared to 3T, but higher resolution at 7T) (**1C**) measurements. The medial femoral condyle with the medial meniscus is enlarged for better visualisation of the image quality.



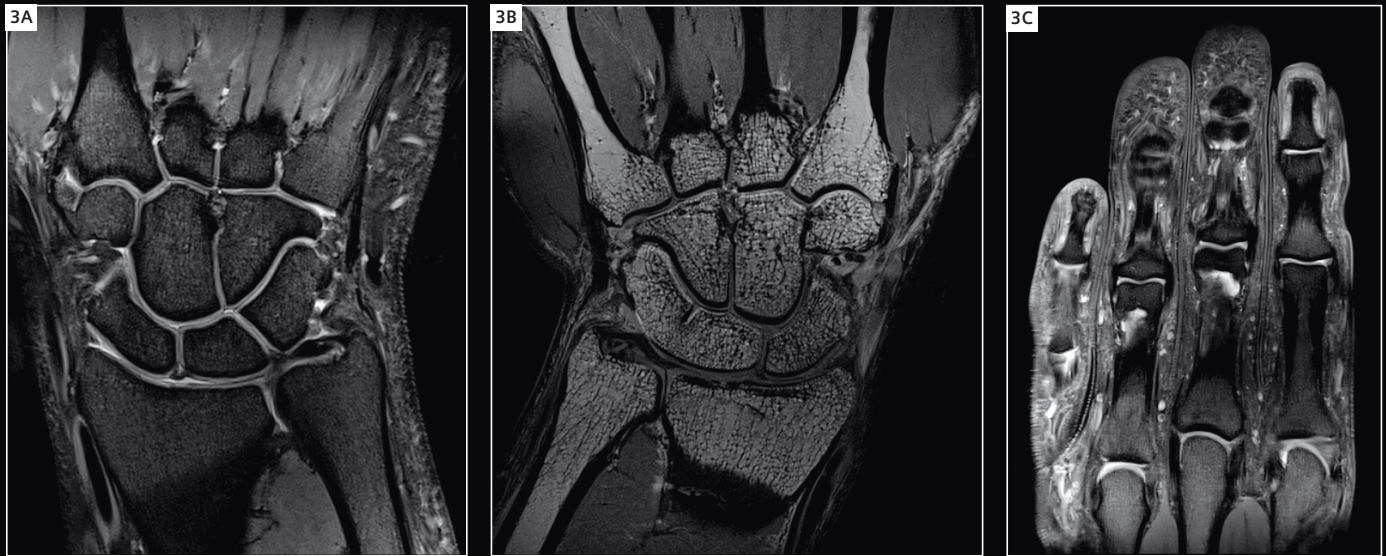
The sagittal fat-saturated isotropic 3D PD-TSE sequence, called PD SPACE (sampling perfection with application-optimised contrasts using different flip angle evolutions), is shown for the 3T and two 7T protocols (see above).



Case 2

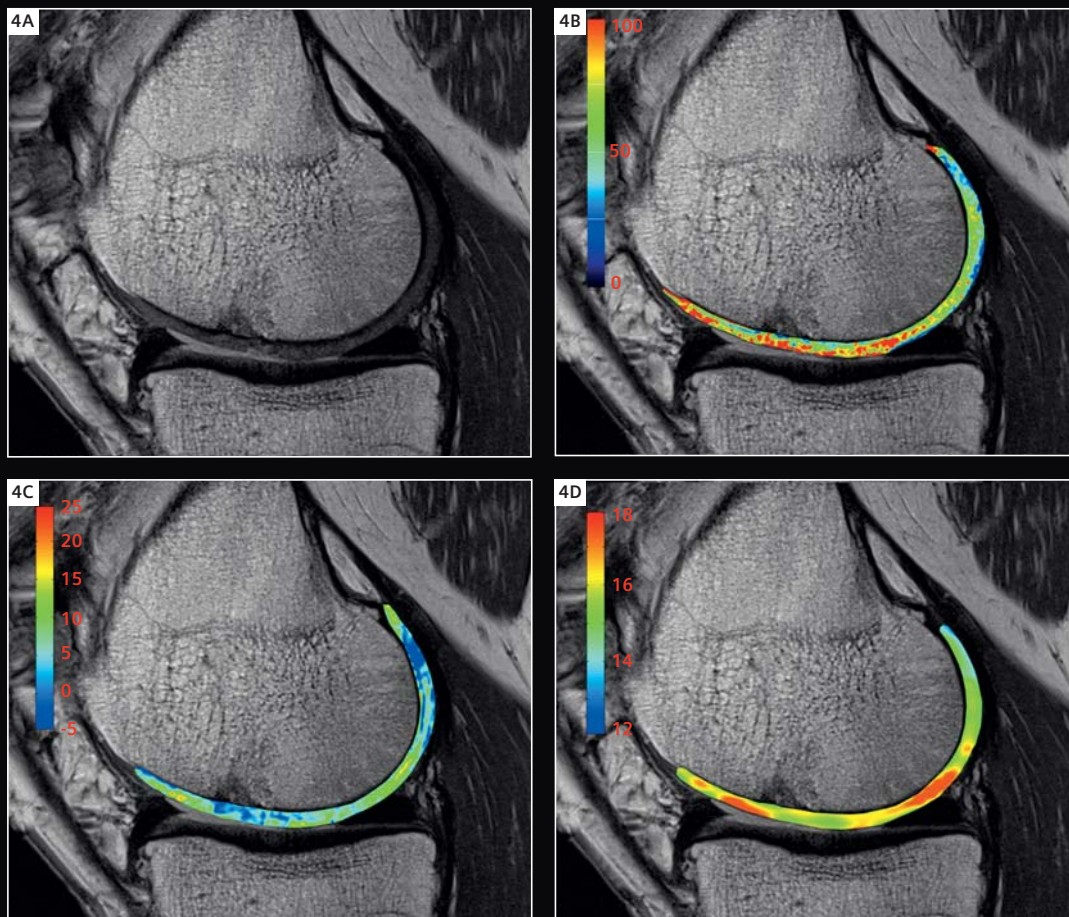
Sagittal 2D SE of the healthy ankle of a 25-year-old volunteer at 3T (**2A**) and 7T (**2B**).

Coronal 2D TSE of the healthy ankle of a 25-year-old volunteer at 3T (**2C**) and at 7T (**2D**).



Case 3

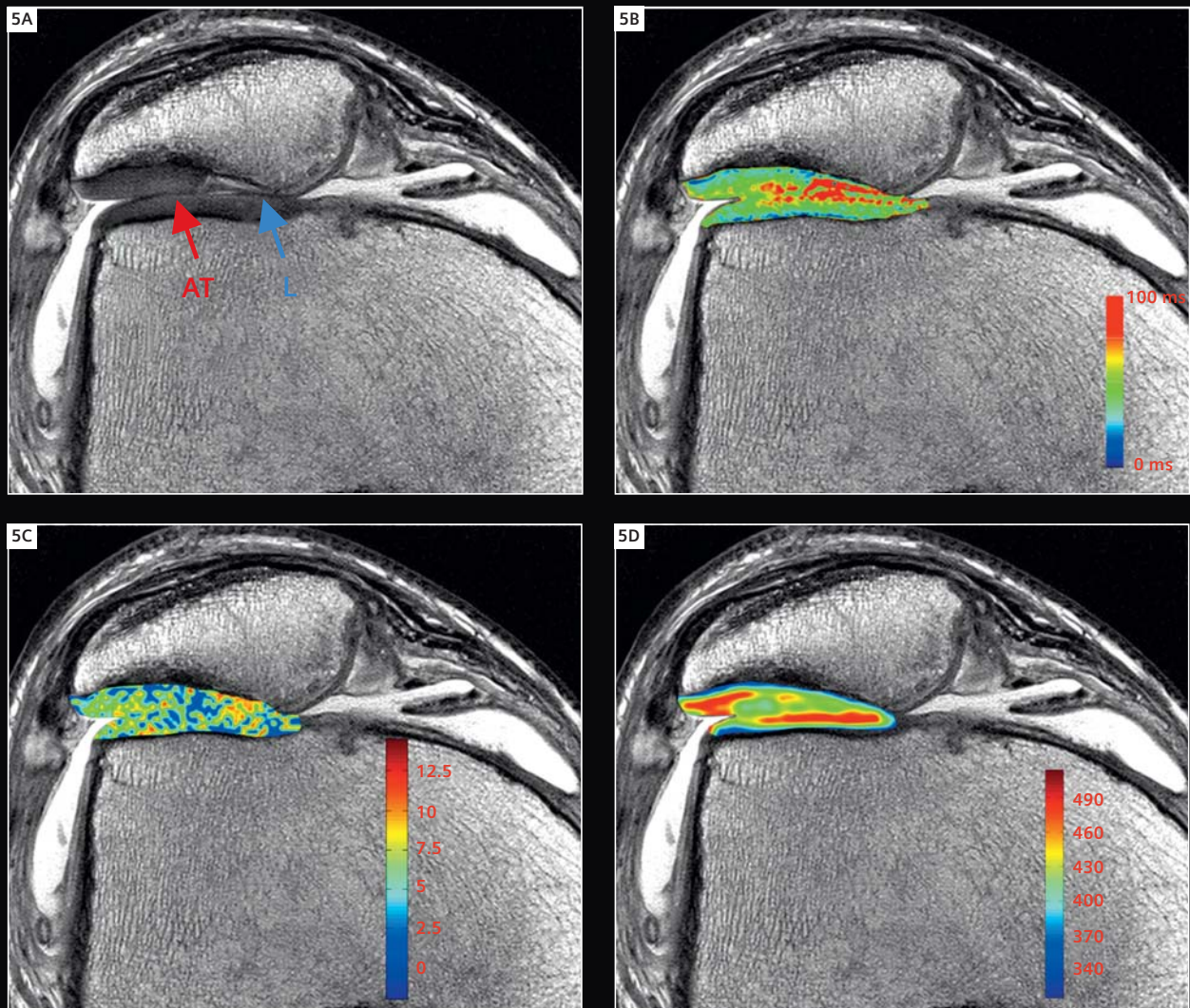
PD fs grayscale image of the wrist (**3A**), T1-weighted wrist image (**3B**) and image of fingers, showing cartilage of small joints (**3C**).



Case 4

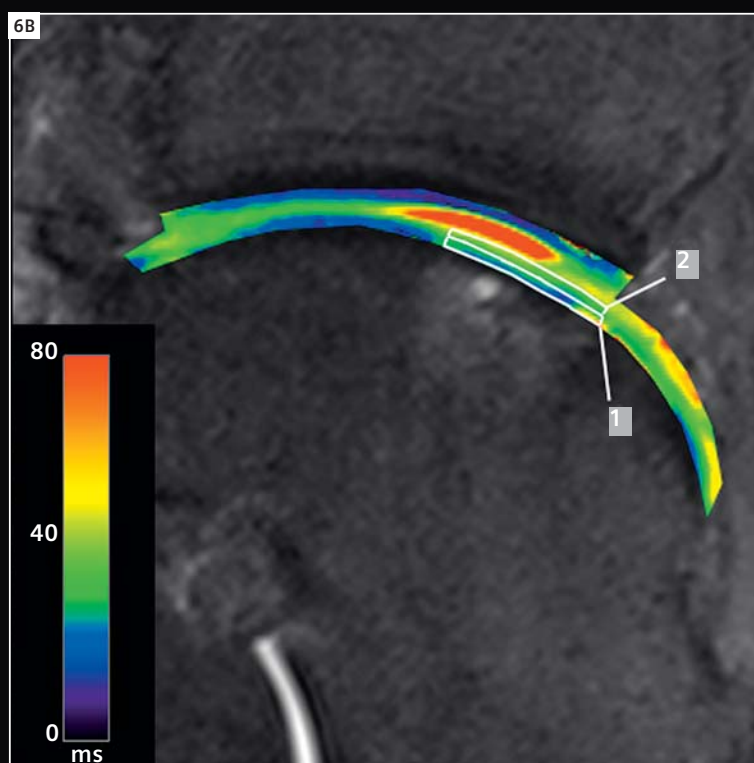
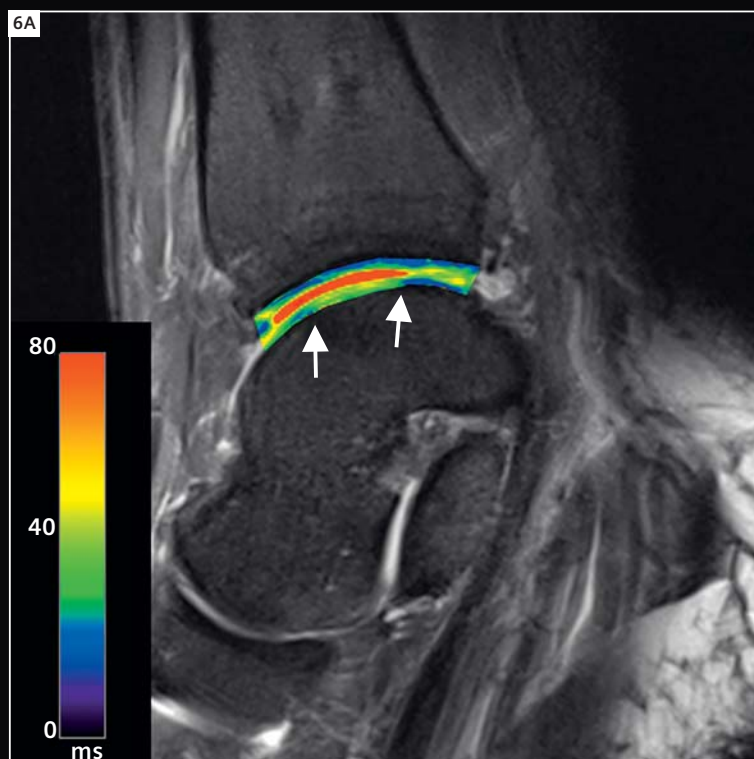
Sagittal knee image of a 58-year-old male patient, 9.4 years after Autologous Osteochondral Transplantation (AOT) at the medial femoral condyle.

(**4A**) Morphologic PD-TSE image. (**4B**) Graphical overlay with T_2 -map. Colorbar represents relaxation times in [ms]; higher values = more water, disturbed collagen architecture. (**4C**) Graphical overlay with gagCEST image. Colorbar represents gagCEST asymmetries in [%]; lower values, less PG content. (**4D**) Graphical overlay with Sodium image. Colorbar represents the Sodium SNR values; lower values, less PG content. Note, that with all modalities degenerative changes are seen in the area of AOT.



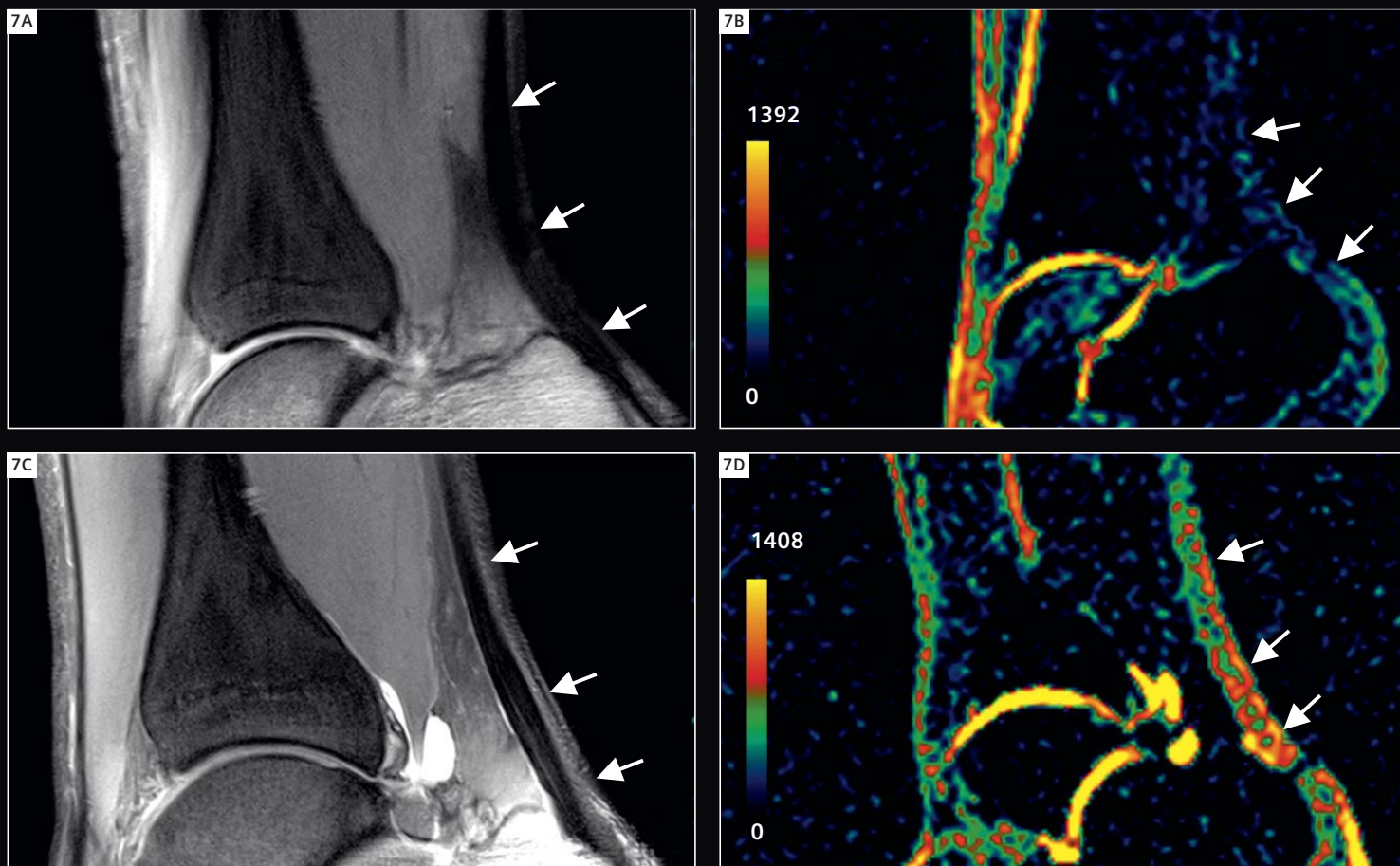
Case 5

Axial knee images from a 25-year-old male patient after matrix-associated chondrocyte transplantation (MACT) in the retropatellar cartilage (L). Cartilage adjacent to the lesion (AT) appears morphologically intact on PD-TSE image (**5A**) and appears normal on the color-coded overlay of T2-map (**5B**). However on color-coded overlay of gagCEST (**5C**) and color-coded overlay of Sodium image (**5D**) lower values in adjacent cartilage is seen, corresponding to a lower GAG content.



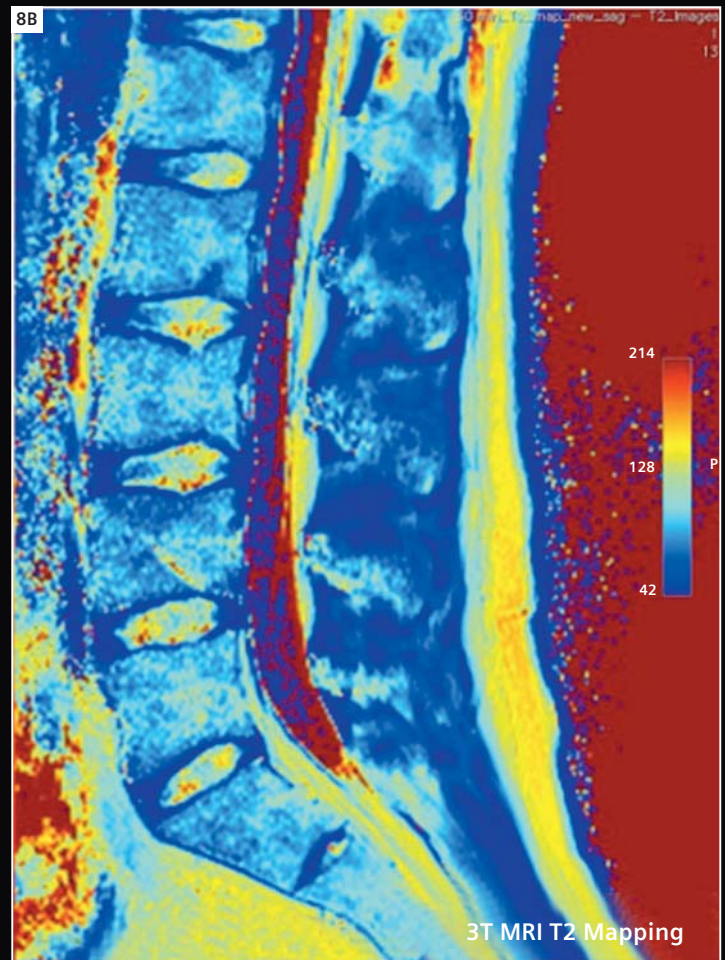
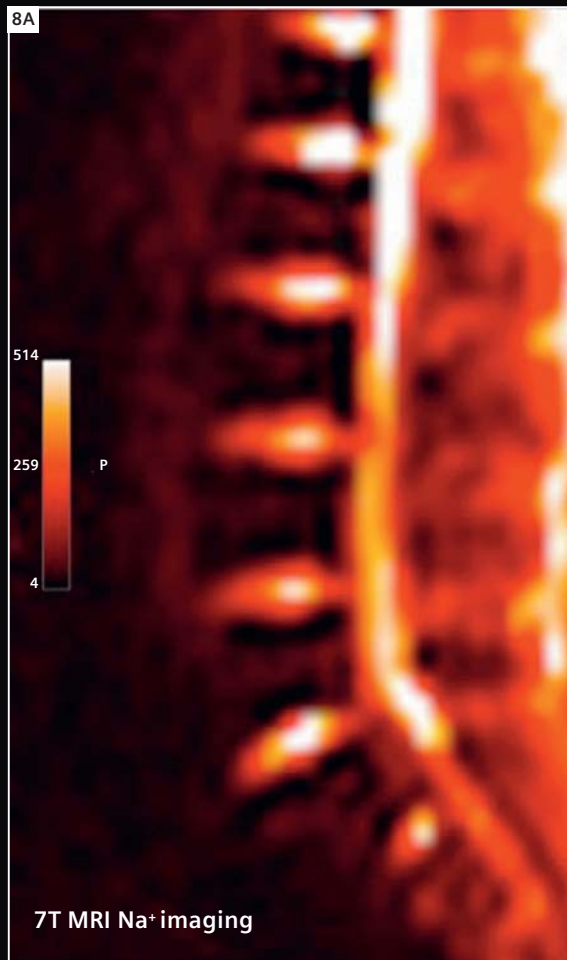
Case 6

T₂-mapping of the ankle joint cartilage layer at 7T (6A). In (6B) the regions-of-interest for the zonal analysis are superimposed onto the cartilage layer of the talus.



Case 7

The comparison of the sodium signal in a healthy volunteer (**7B**) and in a patient with Achilles tendinopathy (**7D**). Corresponding morphological images are on the left-hand side, **7A** and **7C** respectively. Higher sodium image intensity (white arrows) in case of the patient with chronic Achilles tendinopathy corresponds to the higher GAG content found in such patients (**7D**) in comparison to healthy tendons (**7B**).



Case 8

7T Sodium imaging (8A) and 3T color-coded image of T2-mapping (8B) in a volunteer without disc degeneration.

References

- 1 Juras V, Zbyn S, Pressl C, et al (2012) Regional Variations of T2* in Healthy and Pathologic Achilles Tendon In Vivo at 7 Tesla: Preliminary Results. Magnetic Resonance in Medicine, In Press.
- 2 Schmitt B, Zbyn S, Stelzeneder D, et al (2011) Cartilage quality assessment by using glycosaminoglycan chemical exchange saturation transfer and (23)Na MR imaging at 7T. Radiology 260, 257-64 DOI: 10.1148/radiol.11101841.

Contact

Prof. Siegfried Trattnig, M.D.
MR Center – High field MR
Department of Radiology
Medical University of Vienna/Vienna
General Hospital
Lazarettgasse 14
A-1090 Vienna
Austria
Phone: +43 1 40 400 6460
Fax.: +43 1 40 400 6475
siegfried.trattnig@meduniwien.ac.at

Siemens Healthcare Publications

Our publications offer the latest information and background for every healthcare field. From the hospital director to the radiological assistant – here, you can quickly find information relevant to your needs.



Medical Solutions
Innovations and trends in healthcare. The magazine is designed especially for members of hospital management, administration personnel, and heads of medical departments.



eNews
Register for the global Siemens Healthcare News-letter at www.siemens.com/healthcare-eNews to receive monthly updates on topics that interest you.



AXIOM Innovations
Everything from the worlds of interventional radiology, cardiology, fluoroscopy, and radiography. This semi-annual magazine is primarily designed for physicians, physicists, researchers, and medical technical personnel.



MAGNETOM Flash
Everything from the world of magnetic resonance imaging. The magazine presents case reports, technology, product news, and how-to articles. It is primarily designed for physicians, physicists, and medical technical personnel.



SOMATOM Sessions
Everything from the world of computed tomography. With its innovations, clinical applications, and visions, this semiannual magazine is primarily designed for physicians, physicists, researchers, and medical technical personnel.



Imaging Life
Everything from the world of molecular imaging innovations. This bi-annual magazine presents clinical case reports, customer experiences, and product news and is primarily designed for physicians, hospital management and researchers.

For current and past issues and to order the magazines, please visit www.siemens.com/healthcare-magazine.

Siemens Healthcare Publications

Our publications offer the latest information and background for every healthcare field. From the hospital director to the radiological assistant – here, you can quickly find information relevant to your needs.



Medical Solutions
Innovations and trends in healthcare. The magazine is designed especially for members of hospital management, administration personnel, and heads of medical departments.



eNews
Register for the global Siemens Healthcare News-letter at www.siemens.com/healthcare-eNews to receive monthly updates on topics that interest you.



AXIOM Innovations
Everything from the worlds of interventional radiology, cardiology, fluoroscopy, and radiography. This semi-annual magazine is primarily designed for physicians, physicists, researchers, and medical technical personnel.



MAGNETOM Flash
Everything from the world of magnetic resonance imaging. The magazine presents case reports, technology, product news, and how-to articles. It is primarily designed for physicians, physicists, and medical technical personnel.



SOMATOM Sessions
Everything from the world of computed tomography. With its innovations, clinical applications, and visions, this semiannual magazine is primarily designed for physicians, physicists, researchers, and medical technical personnel.



Imaging Life
Everything from the world of molecular imaging innovations. This bi-annual magazine presents clinical case reports, customer experiences, and product news and is primarily designed for physicians, hospital management and researchers.

For current and past issues and to order the magazines, please visit www.siemens.com/healthcare-magazine.

The entire editorial staff at Johns Hopkins University and at Siemens Healthcare extends their appreciation to all the radiologists, technologists, physicists, experts and scholars who donated their time and energy – without payment – in order to share their expertise with the readers of MAGNETOM Flash.

MAGNETOM Flash – Imprint

© 2012 by Siemens AG,
Berlin and Munich,
All Rights Reserved

Publisher:

Siemens AG
Medical Solutions
Business Unit Magnetic Resonance,
Karl-Schall-Straße 6, D-91052 Erlangen,
Germany

Guest Editor:

John A. Carrino, M.D., M.P.H.
Associate Professor of Radiology and
Orthopedic Surgery, Section Chief
Musculoskeletal Radiology, Johns Hopkins
University School of Medicine, Baltimore,
MD, USA

For the Neurography Supplement to
this issue:

Avneesh Chhabra, M.D.
Assistant Professor of Radiology and
Orthopedic Surgery, Johns Hopkins
University School of Medicine, Baltimore,
MD, USA

Associate Editor:

Antje Hellwich
(antje.hellwich@siemens.com)

Editorial Board:

John A. Carrino, M.D., M.P.H.; Avneesh
Chhabra, M.D.; Antje Hellwich; Milind
Dhamankar, M.D.; Ferdinand Lipps, Ph.D.;
Ignacio Vallines, Ph.D.; Wellesley Were;
Ralph Strecker; Matthias Lichy, M.D., M.Sc.;
Gary R. McNeal; Peter Kreisler, Ph.D.

Production: Norbert Moser, Siemens AG,
Medical Solutions, Erlangen, Germany

Layout: independent Medien-Design
Widenmayerstrasse 16, D-80538 Munich,
Germany

Printer: Mediahaus Biering GmbH,
Freisinger Landstr. 21, 80939 Munich,
Germany

Note in accordance with § 33 Para.1 of
the German Federal Data Protection Law:
Despatch is made using an address file
which is maintained with the aid of an
automated data processing system.

MAGNETOM Flash with a total circulation
of 35,000 copies is sent free of charge
to Siemens MR customers, qualified phy-
sicians, technologists, physicists and
radiology departments throughout the
world. It includes reports in the English
language on magnetic resonance:
diagnostic and therapeutic methods and
their application as well as results and
experience gained with corresponding
systems and solutions. It introduces from
case to case new principles and proce-
dures and discusses their clinical poten-
tial.

The statements and views of the authors
in the individual contributions do not
necessarily reflect the opinion of the
publisher.

The information presented in these
articles and case reports is for illustration
only and is not intended to be relied
upon by the reader for instruction as to
the practice of medicine. Any health care
practitioner reading this information is
reminded that they must use their own
learning, training and expertise in deal-
ing with their individual patients. This
material does not substitute for that duty
and is not intended by Siemens Medical
Solutions to be used for any purpose

in that regard. The drugs and doses
mentioned herein are consistent with
the approval labeling for uses and/or
indications of the drug. The treating
physician bears the sole responsibility for
the diagnosis and treatment of patients,
including drugs and doses prescribed in
connection with such use. The Operating
Instructions must always be strictly
followed when operating the MR system.
The sources for the technical data are the
corresponding data sheets. Results may
vary.

Partial reproduction in printed form of
individual contributions is permitted,
provided the customary bibliographical
data such as author's name and title of
the contribution as well as year, issue
number and pages of MAGNETOM Flash
are named, but the editors request that
two copies be sent to them. The written
consent of the authors and publisher is
required for the complete reprinting of
an article.

We welcome your questions and com-
ments about the editorial content of
MAGNETOM Flash. Please contact us at
magnetomworld.med@siemens.com.
Manuscripts as well as suggestions,
proposals and information are always
welcome; they are carefully examined
and submitted to the editorial board for
attention. MAGNETOM Flash is not
responsible for loss, damage, or any other
injury to unsolicited manuscripts or other
materials. We reserve the right to edit
for clarity, accuracy, and space. Include
your name, address, and phone number
and send to the editors, address above.

MAGNETOM Flash is also available on the internet:

www.siemens.com/magnetom-world

MAGNETOM Flash

The Magazine of MRI

Issue Number 2/2012
RSNA Edition

SIEMENS

Artifact Reduction

3D MSK MRI with syngo SPACE
Page 6

Oncology

Bone and soft tissue tumor imaging
Page 50

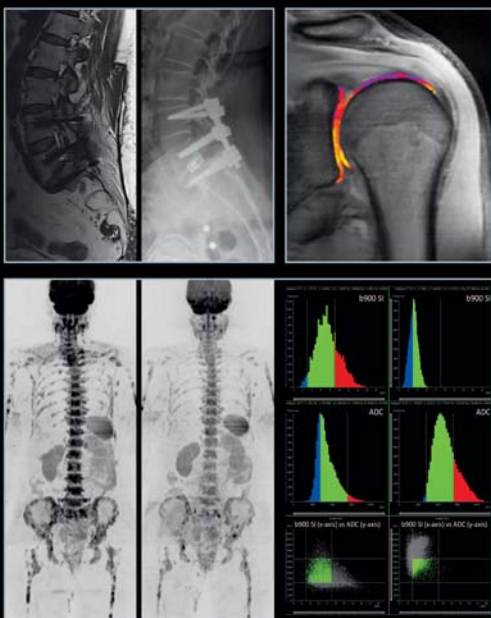
Whole-body DWI of Bone Marrow
Page 60

How I do it

MSK imaging
Tips and Tricks
Page 58

Technology

7T MRI for MSK
Applications
Page 98



Please enter your business address

Institution

Department

Function

Title

Name

Street

Postal Code

City

State

Country

MR system used

Please include me in your mailing list for the following Siemens Healthcare customer magazine(s):

☐ Medical Solutions

☐ MAGNETOM Flash

☐ SOMATOM Sessions

☐ AXIOM Innovations

Stay up to date with the latest information
Register for:

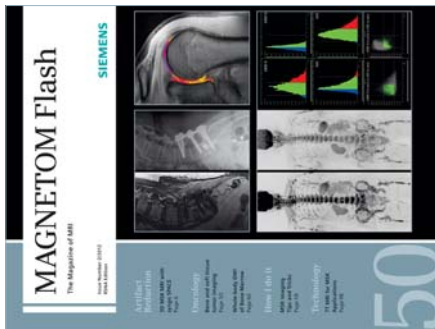
E-mail

☐ Yes, I consent to the above information being used for future contact regarding product updates and other important news from Siemens.

☐ unsubscribe from info service

Please print clearly!

MAGNETOM Flash



Siemens AG
Medical Solutions
Magnetic Resonance
Antje Hellwich - Marketing
P.O. Box 32 60
D-91050 Erlangen
Germany



→ Visit www.siemens.com/magnetom-world
for case reports,
clinical methods,
application tips,
talks and much more
clinical information.

SUBSCRIBE NOW!

– and get your free copy of future
MAGNETOM Flash! Interesting information from
the world of magnetic resonance – gratis to your
desk. Send us this postcard, or subscribe online at
www.siemens.com/MAGNETOM-World

Global Siemens Headquarters

Siemens AG
Wittelsbacherplatz 2
80333 Muenchen
Germany

Global Siemens Healthcare Headquarters

Siemens AG
Healthcare Sector
Henkestrasse 127
91052 Erlangen
Germany
Phone: +49 9131 84-0
www.siemens.com/healthcare

www.siemens.com/healthcare-magazine

Order No. A91MR-1000-87C-7600 | Printed in Germany | CC 170 111225. | © 11.12, Siemens AG

On account of certain regional limitations of sales rights and service availability, we cannot guarantee that all products included in this brochure are available through the Siemens sales organization worldwide. Availability and packaging may vary by country and is subject to change without prior notice. Some/All of the features and products described herein may not be available in the United States.

The information in this document contains general technical descriptions of specifications and options as well as standard and optional features which do not always have to be present in individual cases.

Siemens reserves the right to modify the design, packaging, specifications and options described herein without prior notice.
Please contact your local Siemens sales representative for the most current information.

Note: Any technical data contained in this document may vary within defined tolerances. Original images always lose a certain amount of detail when reproduced.

Global Business Unit

Siemens AG
Medical Solutions
Magnetic Resonance
Henkestr. 127
DE-91052 Erlangen
Germany
Phone: +49 9131 84-0
www.siemens.com/healthcare

Local Contact Information

Asia

Siemens Pte Ltd
The Siemens Center
60 MacPherson Road
Singapore 348615
Phone: +65 6490-8096

Canada

Siemens Canada Limited
Medical Solutions
2185 Derry Road West
Mississauga ON L5N 7A6
Canada
Phone: +1 905 819-5800

Europe/Africa/Middle East

Siemens AG
Medical Solutions
Henkestr. 127
91052 Erlangen
Germany
Phone: +49 9131 84-0

Latin America

Siemens S.A.
Medical Solutions
Avenida de Pte. Julio A. Roca No 516,
Piso 7
C1067ABN Buenos Aires
Argentina
Phone: +54 11 4340-8400

USA

Siemens Medical Solutions U.S.A., Inc.
51 Valley Stream Parkway
Malvern, PA 19355-1406
USA
Phone: +1-888-826-9702